Solar Energetic Particles at Mars

by

Rebecca Dawn Jolitz

B.A., University of California, Berkeley, 2014

M.A., University of Colorado, Boulder, 2018

A thesis submitted to the

Faculty of the Graduate School of the

University of Colorado in partial fulfillment

of the requirement for the degree of

Doctor of Philosophy

Department of Physics

2022

Committee Members:

Daniel Baker

David Brain

Patricia Rankin

Robert Ergun

Mihaly Horanyi

Jolitz, Rebecca Dawn (Physics)

Solar Energetic Particles at Mars

Thesis directed by Prof. David Brain

Solar energetic particles (SEPs) are both a hazard to human spaceflight and a source of energy to planetary atmospheres. Since Mars lacks a global magnetic field, Mars may be more susceptible to this type of radiation than Earth. This thesis investigates the precipitation of SEPs at Mars via a combination of model predictions and observation.

First, a 3-D Monte Carlo test particle and energy degradation simulation called ASPEN (Atmospheric Scattering of Protons, Electrons, and Neutrals) was developed to describe SEP transport in inhomogeneous magnetic fields and precipitation into an atmosphere. ASPEN was applied to predict ionization above Martian crustal fields, finding that crustal fields attenuated the low-energy range of the spectra measured at the peak of the 2003 “Halloween” SEP event.

Next, ASPEN was used to study the transport of 10-200 keV electrons in the near Mars environment, from the solar wind to atmospheric entry. While precipitation was predicted to be favored into magnetic cusps, the simulation predicted a fraction of energetic electrons can enter closed field regions. This is because the particles are affected by non-adiabatic mechanisms as well as curvature and gradient drifts, which are proportional to particle energy.

Finally, the total energy flux incident on Mars from EUV, solar wind, and SEPs was calculated using MAVEN spacecraft data during the declining solar cycle. On average, the energy flux from extreme ultraviolet radiation (EUV) exceeded that of solar wind, and solar wind energy flux exceeded SEP energy flux. Solar wind ion energy flux could sporadically become comparable to EUV energy flux, but not exceed it by a margin sufficient to displace EUV as the dominant source of the dayside ionosphere. On the other hand, SEP ions did reach an intensity comparable to solar wind electrons and are possibly sufficient to increase nightside ionization. These observations were contextualized with seasonal and solar cycle variation, and compared to predictions of energy fluxes at ancient Mars.

Acknowledgements

I have been very fortunate to have had significant support in my career and have many people to thank.

Thank you to everyone who helped me get started in research: Yvonne Pendleton, for continued correspondence and encouragement since I was in fourth grade; the American Chemical Society, for the third place science fair prize that brought me to Chris McKay's perchlorates-on-Mars talk; Chris, for mentoring and giving me the opportunity to work at Ames; Donna Sakima, for the chance meeting and introducing me to Rob Lillis; Rob, for taking the risk of hiring a fresh-out-of-community-college undergraduate to do a proton version of your electron-based thesis code (it took a decade, but here we are!).

Thank you to everyone who has supported me through grad school. Thanks to the committee for your thoughts and suggestions as this thesis has been assembled. Thank you Dave for your continued guidance and patience, especially given the difficult circumstances during which this work was completed. Many thanks to the Brain group for many thoughtful discussions, and the occasional bout of paper-airplane-throwing insanity. Additional thanks to Andrea Hughes for the opportunity to put the simulation developed in this thesis to good use for modeling proton aurora. Thank you also to my many research collaborators at SSL for many fruitful and fun discussions when I'd visit for the summer: Christina Lee, Shannon Curry, Ali Rahmati, Shaosui Xu, and Gwen Hanley.

Thank you to the Jolitz team. To Autumn, the best sister I could ask for. Thank you for helping me learn Python many years ago so I didn't have to get stuck with IDL. Thank you also for spontaneously converting my single-thread simulation into a parallel one, even though you were *supposed* to be recovering in bed.

To William and Lynne, thank you. You have never wavered in your support for my career. From giving me my own C-5 telescope in fourth grade when I'd first declared I wanted to become an astrophysicist, to finding me a way out of middle school and spending up to three hours a day in traffic so I could attend classes at Ohlone College instead. You taught me how to invent, pitch, and challenge the way things are done, and most of all to have the determination to see a project through. Your entrepreneurial spirit has and will continue to drive me.

Finally, thank you Nitin for being with me on the road to thesis Kal'Hyah. I'm incredibly fortunate to have you in my life.

Contents

Tables

Figures

Chapter 1

Introduction

The sun radiates considerable energy through the solar system as light and plasma. At times, additional plasma is violently ejected and can produce extremely energetic charged particles in "solar storms". This energy can be destructive to life as we know it. Ultraviolet light and energetic charged particles can ionize and dissociate molecules, disrupting biological processes and presenting a hazard to human spaceflight. Ionizing radiation can also drive and influence planetary atmospheres. Since the intensity of solar radiation and frequency of solar storms varies over time depending on the magnetic activity of the sun, it is thought ionizing radiation could have been much more intense in the past based on observations of similar stars to the sun. Could solar storms have shaped the evolution of planetary atmospheres? While Mars is an arid and desiccated planet today, multiple spacecraft have found evidence that water used to flow on the surface of Mars billions of years ago. Despite uncertainty over whether the climate of ancient Mars was cold or warm, there is increasing evidence that Mars once had a thicker atmosphere that was lost to space. How much of this loss to space is owed to the more frequent solar storms of a young sun?

In this Introduction, I will briefly discuss solar emissions associated with space weather. Next I discuss how the search for life on Mars transformed into the search for water, and how we know that Mars used to have a thicker atmosphere and an active dynamo. Then I present a detailed discussion of the current state of Mars' atmosphere, ionosphere, and interaction with the solar wind, followed by a description of the current and past atmospheric escape processes. Finally, I review observations of increased atmosphere escape during space weather events, and describe how the role of SEPs in these events is ambiguous. In this context, I present a roadmap of the work done in this thesis to investigate the role of SEPs at Mars.

1.1. Space weather: A summary

Solar emissions can be described as constant or episodic, depending on the source, and vary depending on the solar cycle. The term "space weather" refers to these emissions and the overall conditions of the heliosphere that can affect any object in the solar system. Steady emissions like extreme ultraviolet (EUV) radiation and charged particles in the solar wind can ionize the constituents of planetary atmospheres to produce an ionosphere. Episodic solar transients like flares, coronal mass ejections (CMEs), and stream interaction regions (SIRs) can drive rapid changes in EUV and the solar wind, as well as releasing high-energy solar energetic particles (SEPs). As a plasma, the solar wind is interleaved with the interplanetary magnetic field (IMF) and serves as the medium through which solar transients propagate. Variations in the solar wind and IMF can influence transport of solar transients in the heliosphere, and the overall solar wind interaction with ambient or absent planetary magnetic fields.

I will now summarize the solar drivers. Solar EUV is the part of the solar spectrum with wavelengths between 10 nm and 120 nm. The solar wind is a stream of electrons, protons, and alpha particles released from the sun into the interplanetary environment. It originates as coronal plasma that is accelerated to supersonic speeds via an effective radial de Laval nozzle from the declining gravitational force over heliocentric distance [Parker 1958]. Solar wind density and velocity is variable depending on coronal source and may be classified into "slow" and "fast" solar wind streams.

Solar transients like flares, CMEs, and SIRs can drive changes in the solar wind and EUV, and release SEPs. Solar flares cause sporadic rapid increases in EUV and soft X-rays (0.1-10 nm). CMEs, boluses of plasma ejected from the sun, can propagate outwards from the sun as an interplanetary coronal mass ejection (ICME). SIRs are the compressed plasma formed from when a fast solar wind stream overtakes a slow solar wind stream, and are also called corotating interaction regions (CIRs) if they are observed for multiple solar rotations. Each of these transients can produce SEPs, which are mainly protons and electrons with energies from tens of keVs to up to several GeV. SEPs may be accelerated by the moving shock source ahead of a CME or the local shock source at a solar flare or SIR site. While they are related to CMEs and SIRs, observations of SEPs (SEP events) do not necessarily coincide with observing these phenomena. SEPs can travel along the IMF far from the acceleration source. Occasionally SEP events may be sufficiently energetic to be measured on the Earth's surface, leading to an increase in neutron detector counts. These are called "ground-level enhancements" (GLEs) and they usually follow intense flares and extremely fast CMEs (e.g. Nitta et al. [2011]).

All solar emissions are controlled by the solar cycle, the 11-year period during which the solar magnetic fields reverse polarity. When the sun is in "solar minimum", there are few sunspots, more polar coronal holes to supply high speed solar wind, and accordingly more frequent SIRs [Schwenn 2006]. Few CMEs and even fewer GLEs occur. EUV emissions are at their lowest. As the solar magnetic axis begins to shift in the "rising" phase of the solar cycle, the quadrupole terms in the magnetic field become significant and more sunspots appear. The waviness of the heliospheric current sheet increases, suppressing GCR flux in the solar system [Potgieter 2013]. The polar coronal holes become less prevalent and the solar wind becomes dominated by the slow solar wind and CMEs. Coronal heating increases, leading to increased EUV and soft X-ray irradiance. The solar cycle peaks at "solar maximum", before entering the declining phase and eventually approximating a dipole at solar minimum again, although inverted relative to the initial orientation.

Sunspot number is a useful proxy to track the solar cycle (Figure 1.1). The occurrence rate of solar flares and CMEs correlate with the sunspot number, but this correlation becomes poor at high sunspot numbers (SSN > 100) and the coefficient varies for different solar cycles and solar cycle phases (e.g. Gopalswamy et al. [2020]).

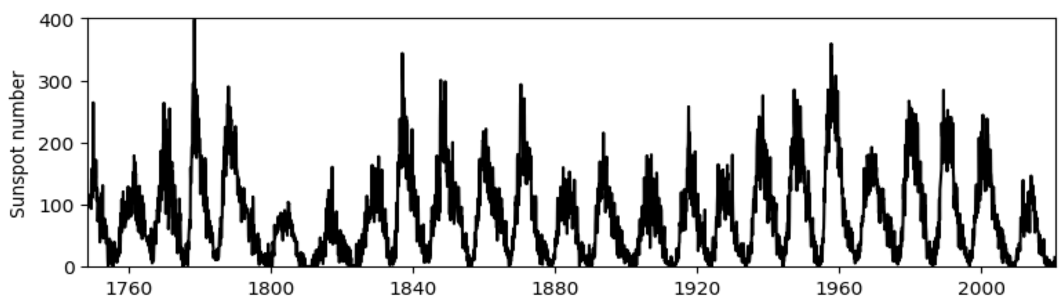

Figure 1.1: The sunspot number from 1750 to the present. Credit: SILSO.

1.2. Mars: From habitability to absent magnetic fields

Mars has been a premier target for the search for life on other worlds. However, six decades of research has revealed a frozen desert world with signs of an ancient water cycle that expired approximately three billion years ago. The atmosphere is thin compared to Earth, having a surface pressure of ~6 millibar, and consists of carbon dioxide followed by trace quantities of nitrogen, argon, monatomic oxygen, diatomic oxygen, and carbon monoxide [Nier et al. 1976]. While remnants of an ancient magnetic field are embedded in the crust, there is no active dynamo to currently sustain an intrinsic magnetic field like Earth's. This section will describe the astrobiological context of Mars, from life-detection and evidence of water on the surface, to evidence for ancient climates that suggest a thicker atmosphere lost to space, to the magnetic field that was lost early in Mars history.

1.2.1. Search for life

The pair of Viking landers tested Mars soil for signs of organic molecules and metabolism, but the results were ambiguous [Klein 1978]. Only water, carbon dioxide, and chlorine-bearing organic molecules were detected by the Gas Chromatograph-Mass Spectrometer (GC-MS) instrument. Measured chlorohydrocarbons were attributed to cleaning agents, while tests for photosynthetic and heterotrophic respiration were suspicious for abiotic reactions [Biemann et al. 1976]. These discoveries quenched the likelihood of even bacterial life and powered speculation that the Martian soil was rich in metal hydroxides or "superoxides". However, the required concentration and production rate of superoxides would have to be unreasonably high to both explain the results and overcome UV destruction rates [Levin and Straat 1981]. This mystery wasn't solved until the Phoenix Lander accidentally discovered significant perchlorates, anions commonly used in rocket fuel [Hecht et al. 2009]. Reanalysis of the Viking results suggests that heated perchlorate could have rapidly reacted with ambient organics within the instrument to produce dichloromethane (Figure 1.2) [Navarro-Gonzalez et al. 2010]. Unambiguously Martian organic molecules have since been found by the Mars Curiosity rover [Freissnet et al. 2015] and in the original Viking results [Guzman et al. 2018].

Figure 1.2: A demonstration of the likely fate of organic molecules in the Viking GC-MS. Snapshots from a personal video recording of sodium perchlorate decomposing when exposed to heat. Credit: R. Jolitz.

1.2.2. Search for water

Following the Viking results, there was a cooling of interest in Mars exploration. Aside from the Phobos-2 mission that lasted eight months, there was no successful return to Mars until the formation of the Mars Exploration Program in 1993. Given the low likelihood of active biology on the surface of Mars, the program goal was to seek signs of past life. The foremost theme of this search was embodied by the log line, “follow the water”.

The evidence for flowing water at Mars is manifold. It can be helpful to organize by geological era: Noachian (4.1-3.7 Gya), Hesperian (3.7-3 Gya), and Amazonian (3.7 Gya to present). Figure 1.3 shows the locations of fluvial features colored by geographic era, alongside a map of aqueous mineral deposit detections.

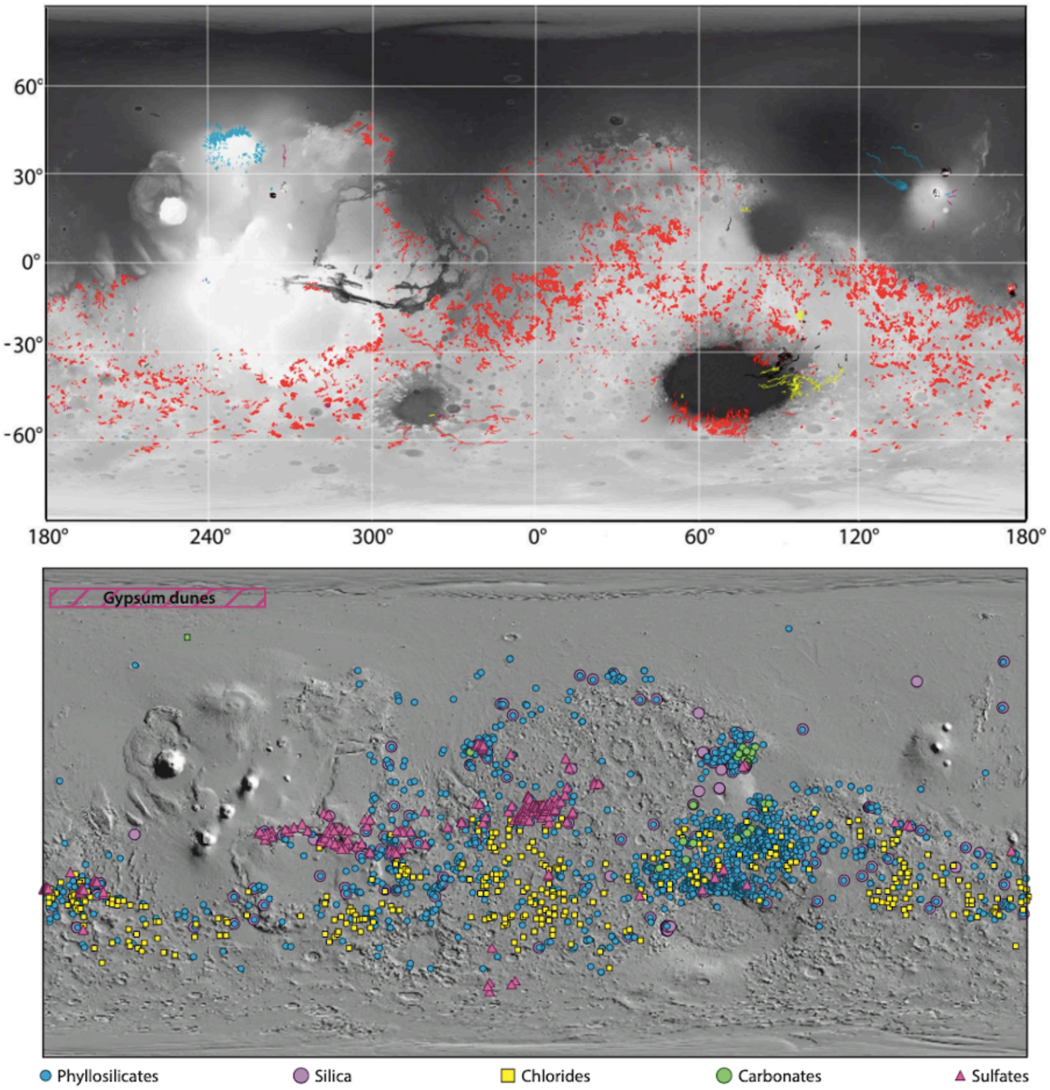

Figure 1.3: Map of fluvial features colored by era (red - Noachian, Noachian-Hesperian in yellow, Hesperian in black, Hesperian-Amazonian in pink, and Amazonian in black) from Alemanno et al. [2018] (top) and a map of mineralogical features from Ehlmann and Edwards [2014]. Both figures use the MOLA topographical map as a background.

Pre-Noachian geological history has been erased due to the Late Heavy Bombardment, but likely was when the global dichotomy formed, which is the ~3 km elevation difference between the ancient heavily cratered southern hemisphere “highlands” and the presumably younger northern hemisphere “lowlands” [Frey et al. 1998]. The Noachian is strongly associated with the presence of stable aqueous environments. The strongest geological evidence is the valley networks, geological formations that resemble terrestrial drainages. Valley networks were first identified in images from Mariner 9 [McCauley et al. 1972] and have since been intensively mapped and studied (e.g. Fassett and Head [2008]). Orbiters have identified globally widespread phyllosilicates, minerals associated with aqueous alteration of basalt that include clays [Poulet et al. 2004]. Some have argued that the sediments and fewer craters in the northern lowlands are evidence of a vast ocean with a shoreline coincident on the dichotomy boundary (e.g., Di Achille and Hynek [2010]), but this hypothesis is controversial and continues to be debated [Dickeson and Davis 2020].

There is a puzzling lack of widespread carbonates that date to the Noachian. Widespread water in contact with atmospheric carbon dioxide should lead to widespread carbonate deposits. Several explanations have been put forth to explain this, such as that flowing water and the associated aqueous alteration was subsurface and not in contact with the atmosphere (e.g. Ehlmann et al. [2011]), that acidic waters suppressed carbonate formation or weathered existing carbonates (e.g. Bullock and Moore [2007]), or that carbonates are spectrally concealed by phyllosillicates and/or buried deeper in the crust (e.g. Wray et al.[2016]).

In the Hesperian, valley network formation rates declined. Instead, episodic and large outflow channels occurred more frequently, representing episodic release of subsurface water or ice [Rodriguez et al. 2015]. More localized deposits of phyllosillicates, sulfates, chlorides, and carbonates are associated with lacustrine environments below sitting lakes [Ehlmann and Edwards 2014]. The presence of sulfate, likely from dissolved volcanic sulfur dioxide in water, is particularly suggestive of the formation of acidic environs [Bibring et al. 2006], supported by the Opportunity rover's finding of "blueberries", spherical hematite concretions [Squyres et al. 2004].

Finally, the Amazonian has a distinct lack of aqueous alteration mineralogy. The recognizable fluvial features are attributed to ice-related flows, such as glaciofluvial valleys (e.g. Fassett et al. [2010]), and can be unrelated to water, such as gullies (e.g. Pilorget and Forget [2016]). Liquid non-briny water is globally unstable at modern Mars, and ice is only stable below the surface as permafrost and interleaved with carbon dioxide ice at the poles (e.g. Bibring et al. [2004]). While recurring slope lineae (RSLs) were recently discovered and hypothesized to be evidence of active water processes in the modern era, the apparent correlation with hydrated salts is likely an instrumental artifact [Vincendon et al. 2019] and the topography isn't consistent with a groundwater source [Chojnacki et al. 2016]. Instead, they may occur due to dry processes such as granular flows (e.g. Dundas [2020]). For further details on Mars geological features organized by era, see Carr and Head [2010].

1.2.3. Search for an ancient habitable climate

The geological record shows that Mars went through a likely shift in climate at the end of the Hesperian around three billion years ago. Many models have been developed to explain how fluvial activity was sustained in the past, as the current atmospheric pressure and temperature cannot support stable surface water. The models initially could broadly be split into "warm and wet", which assumed Mars had a much denser carbon dioxide atmosphere that produced a greenhouse effect and warmed the surface enough to stabilize surface water (e.g. Pollack et al. [1987] and Craddock and Howard [2002]), and "cold and dry", which assumed all aqueous features are groundwater processes that occurred in a continuously cold climate (e.g. Gaidos and Marion [2003]). While cold-dry models had difficulty forming rivers, warm-wet models have been unable to heat the Mars surface with a dense carbon dioxide atmosphere alone [Kasting 1991]. Some warm-wet models have stabilized surface water by assuming significant volatile inventories of hydrogen or methane (e.g. Ramirez et al. [2018]). Hypotheses of episodic warming to sustain a cold but wet Mars have been put forth [Fairén 2010, Kite et al. 2014], as well as snow and ice driven climates [Wordsworth et al. 2015]. Recent models have suggested that snowmelt rather than rainfall could better explain the distribution of valley networks (Figure 1.4). However, no climate model to date completely fits the available geological evidence, and the present geological records does not necessarily require prolonged and/or global water activity [Kite 2019]. If Mars was only episodically habitable, any potential ancient organisms and associated biosignatures would be concentrated in specific lacustrine or hydrothermal microenvironments [Westall et al. 2015].

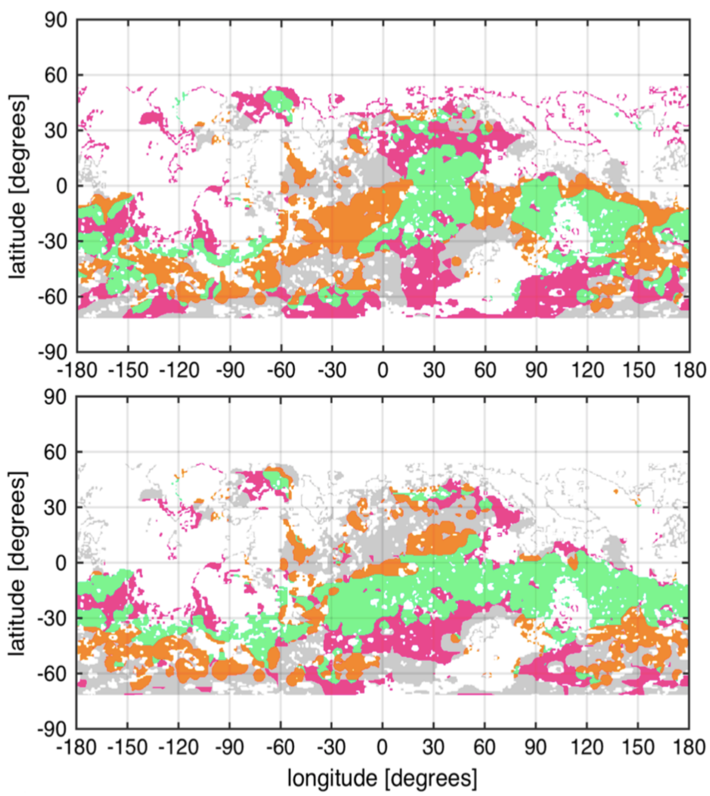

Figure 1.4: Maps of valley networks as predicted by a model for warm-wet (top) and cold-icy (bottom) climate scenarios from Wordsworth et al. [2015]. Green marks where each model matches observed valley network locations, while magenta/orange shows where the model overpredicts/underpredicts the formation of valley networks. While the warm-wet model predicts fewer valley networks than the cold-icy model, neither model completely matches the observations.

Although the warm and wet Mars hypothesis has declined in likelihood, evidence for the requisite thicker atmosphere has increased. Enrichment in heavier isotopes has been observed in Earth-based telescope observations of hydrogen (e.g. Owen et al. [1988]) and in-situ measurements of nitrogen (e.g. McElroy et al. [1976]). Mass-sensitivity in these isotopes imply loss to space, as the mass separation means the gases were removed after reaching an altitude where the isotopes could gravitationally separate. Further evidence for escape-associated fractionation has been found in Martian meteorites [Greenwood et al. 2008] and surface rocks [Mahaffy et al. 2015].

Isotope ratios are not the sole evidence for atmosphere loss. The presence of escaping hydrogen atoms has been observed [Anderson and Hord 1971], and the earliest ionosphere measurements by Mariner 4 were used to constrain a photochemical model that predicted substantial escaping fluxes of oxygen atoms [McElroy 1972]. The solar wind convective electric field was postulated to sweep up or "scavenge" ionospheric constituents [Cloutier et al. 1969], which was later confirmed by observations from the Phobos 2 mission [Lundin et al. 1990].

While isotopic fractionation and modern atmosphere escape processes are clear evidence for loss to space, past carbon dioxide and water could have also been sequestered in the subsurface. However, carbonates are oddly rare on the surface as mentioned previously, and searches for subsurface water are currently limited to detecting near-surface (<1 m) ices [Feldman et al. 2004] and possible radar detections of subglacial lakes [Lauro et al. 2021]. Thus, it is useful to estimate how carbon dioxide and water escaped to space to establish lower limits on the ancient Mars atmosphere density and pressure. This was the primary goal of the Mars Atmosphere Volatile Evolution (MAVEN) mission.

1.2.4. Search for magnetism (or lack thereof)

Before further discussing atmosphere escape, it is important to address the topic of whether Mars has a magnetic field. Older than the search for water at Mars was the search for planetary magnetism. Mariner 4, the first spacecraft to successfully execute a flyby at Mars, was equipped with a magnetometer. At the point of closest approach (~3.9 R_M), no magnetic disturbance occurred, meaning either there was no intrinsic dipole moment from interior sources, or there was and it was four orders of magnitude weaker than Earth's [Smith et al. 1965]. Mariner 4 also did a radio occultation while passing by Mars, allowing a determination of the peak ionospheric density and altitude [Kliore et al. 1965]. These findings guided the development of gasdynamic models that assumed Mars lacked intrinsic magnetism and instead that the pressure balance of the ionosphere stood off the magnetic field at an "ionopause" [Spreiter et al. 1970]. However, the Mars 2 and Mars 3 spacecraft recorded a magnetic disturbance nearby to Mars, which was considered possible evidence of a weak intrinsic field [Dolginov et al 1973]. While this disturbance was shown to be replicable in a gasdynamic model without an intrinsic field [Russell et al. 1984], controversy continued until Mars Global Surveyor (MGS) arrived at Mars.

MGS found no evidence of an intrinsic dipole field. However, MGS did discover strong magnetism bound to the planet's crust in specific regions of the southern hemisphere (Figure 1.5) [Acuña et al. 2001]. These "crustal fields", also called crustal anomalies for their unexpected appearance or remanent fields for having acquired the signature from no longer present magnetic fields, are evidence of a dynamo that expired in the early Noachian before the formation of the Hellas, Utopia, Argyre, and Isidis impact basins [Acuña et al. 1999]. While crater dating [Arkani-Hamed 2004, Lillis et al. 2013, Vervelidou et al. 2017] and analysis of meteorites [Weiss et al. 2008] are in close agreement that the dynamo ceased ~4.1 Gya, higher-resolution analysis of the crustal anomalies has identified a later magnetization signature that suggests the dynamo was present 3.7 Gya [Mittelholz et al. 2020]. The timing of dynamo cessation(s), the role of impactors in activating or deactivating the dynamo, and the field strength remain open questions.

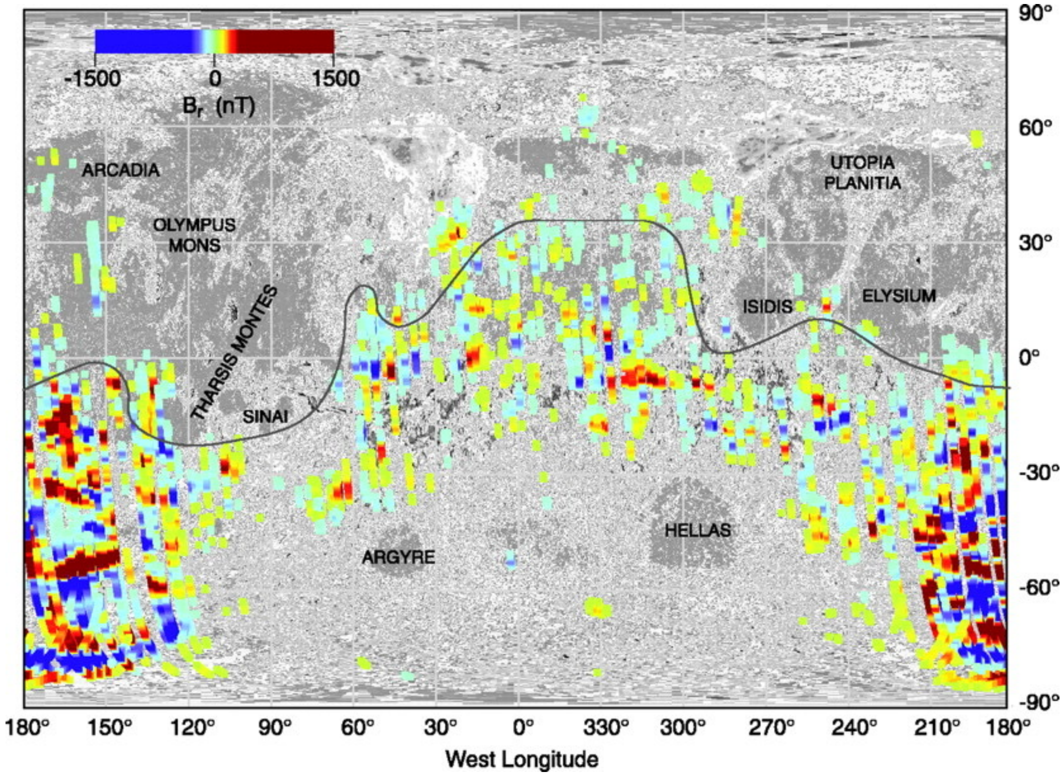

Figure 1.5: Map of the radial component of MGS-observed magnetic field from Acuña et al. [1999].

1.3. Thermosphere, ionosphere, and solar wind coupling at Mars

Whether or not Mars had a habitable climate in the past, substantial atmosphere has been lost to space. This section will describe the structure of the atmosphere, ionosphere, and solar wind interaction of Mars in preparation for a discussion of atmosphere escape.

1.3.1. Atmosphere structure

Our understanding of the structure of the Martian atmosphere has improved markedly since the Viking missions made the first in-situ measurements. The atmosphere is a dynamically-coupled system that can be roughly classified in three regimes: the lower atmosphere (0-50 km), the middle atmosphere (50-100 km), and the upper atmosphere or "thermosphere" (100-200 km). Temperatures decrease from the surface to the lower boundary of the thermosphere, and then increase (Figure 1.6). The high temperatures in the thermosphere are caused by EUV-induced ionospheric processes, specifically by dissociative recombination of the ionospheric constituents at higher altitudes (>120 km) and quenching of metastable atmospheric constituents in the lower altitudes [Fox and Dalgarno 1979]. Meanwhile, gravity waves, thermal tides, and dust storms originate in the lower atmosphere. Water vapor is also trapped in the lower atmosphere in the absence of dust storms and must be converted into hydrogen gas to diffuse upwards [Yung et al. 1988]. The middle atmosphere mediates the lower atmosphere and thermosphere by conveying waves and dust upwards, radiating heat via CO_2 15 μm emission, and redistributing heat globally by winds [Bougher et al. 2017a].

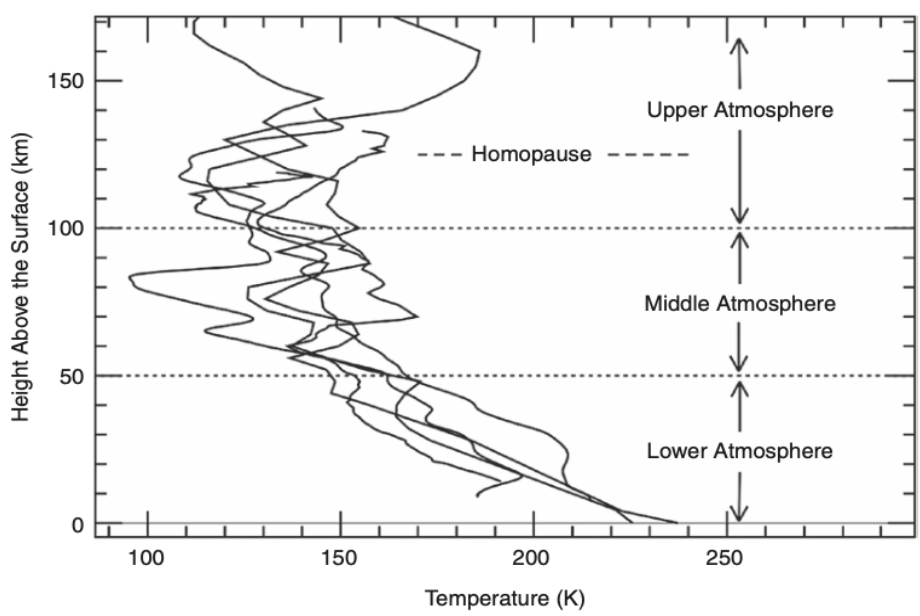

Figure 1.6: An altitude profile of the temperatures inferred from accelerometer data during the descent of the Vikings 1 and 2, Mars Exploration Rovers (MERs) Spirit and Opportunity, Pathfinder, and Phoenix [Smith et al. 2017].

Global circulation models (GCMs) have been developed to describe the processes within the atmosphere, e.g. Mars Thermosphere GCM (MT-GCM) [Bougher et al. 1999] or Mars Global Ionosphere Thermal Model (M-GITM) [Bougher et al. 2015]. Since EUV strongly heats the thermosphere, there is significant seasonal, solar cycle, and flare-sensitive variability. When Mars is at perihelion and/or when the sun is in a solar maximum phase, the thermosphere expands. As Mars travels further from the sun and/or the solar cycle wanes, the thermosphere contracts [Bougher et al. 2017a]. This trend is observed in both the models and data (Figure 1.7). Recent analysis based on MAVEN observations, which has taken place during solar minimum, have found that seasonal variation drives temperature variability of ~70 K [Bougher et al. 2017b] and that an X-class flare drove a ~70 K increase of temperature to ~310 K [Jain et al. 2018].

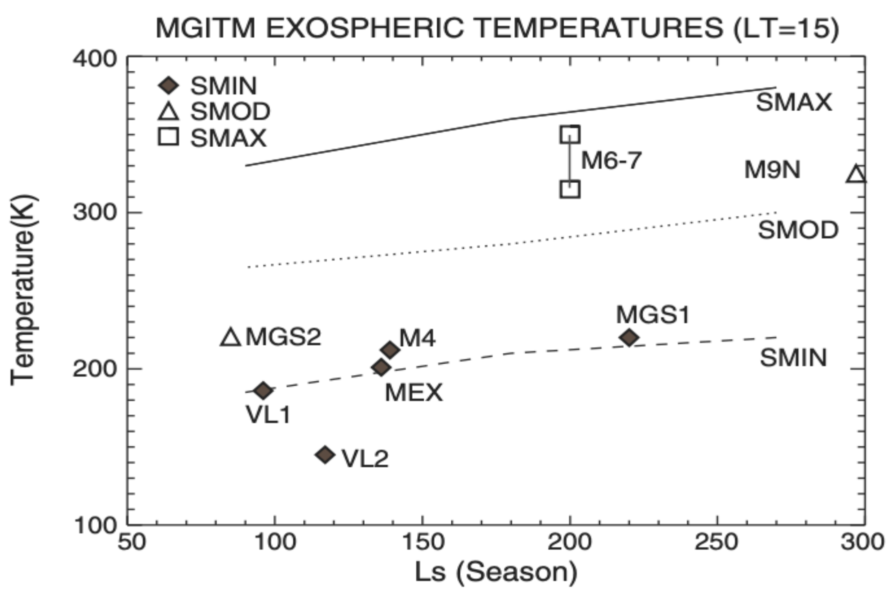

Figure 1.7: Temperatures as a function of season (solar longitude L_s) and solar cycle (SMAX: solar maximum, SMOD: solar moderate, SMIN: solar minimum) [Bougher et al. 2015]. Lines are from M-GITM and markers from pre-MAVEN spacecraft measurements.

Although the upper atmosphere is typically defined as the region between 100 km and 200 km, the choice of upper boundary is actually arbitrary and case-dependent. For atmospheric escape, a frequent choice of upper bound is instead the bottom of the exosphere, or the exobase.

The exosphere is an effectively collisionless region of space mostly consisting of dissociated and/or escaping atmospheric constituents. The exobase is the altitude where an atom can cross the exosphere in one mean free path, or $r_{exobase}$ such that $\int_{r_{exobase}}^{\infty} N(r)\sigma dr \sim 1$ for exosphere density N and scattering cross-section σ. Assuming a fixed scale height H, this expression reduces to the altitude such that $N(r_{exobase})\sigma H = 1$. Since solar activity can cause the thermosphere to contract or expand, the exobase altitude can vary by tens of kilometers. In addition, the use of the exobase as a fixed boundary for escape studies may introduce inaccuracies. Atoms can diffuse from ~30 km below the exobase and supply additional escape, particularly if they scatter preferentially forwards rather than isotropically [Fox and Hac 2009].

1.3.2. Ionosphere

In general, EUV radiation photoionizes and photodissociates the upper atmosphere of Mars. The resulting dayside ionosphere was first measured via radio occultation by Mariner 4. Subsequent missions (Mariners 6, 7, and 9) carried UV spectrometers that observed emissions from carbon monoxide (Cameron bands, Fourth Positive Bands), ionized carbon dioxide (UV doublet, Fox-Duffendack-Barker), atomic oxygen (1304-Å, 1356-Å, and 2972-Å), and atomic hydrogen (Lyman alpha) [Barth et al. 1971]. The carbon monoxide and ionized carbon dioxide emissions were recorded in the upper atmosphere (<220 km), while the atomic oxygen and hydrogen emissions extended far from Mars by 100s of kilometers and multiple Mars radii respectively. These latter emissions are produced by the oxygen and hydrogen coronae, the components of the Martian exosphere. In-situ measurements of the atmosphere and ionosphere were subsequently determined from the Viking landers upon descent [Nier et al. 1976]. Although carbon dioxide was the dominant atmospheric constituent, singly charged diatomic oxygen (O_2^+) was the primary ionospheric constituent due to rapid conversion of CO_2^+ into either CO_2 or O_2^+.

Figure 1.8 shows the vertical structure of the atmosphere and ionosphere as observed by Viking 1 and modeled by Fox and Dalgarno [1979].

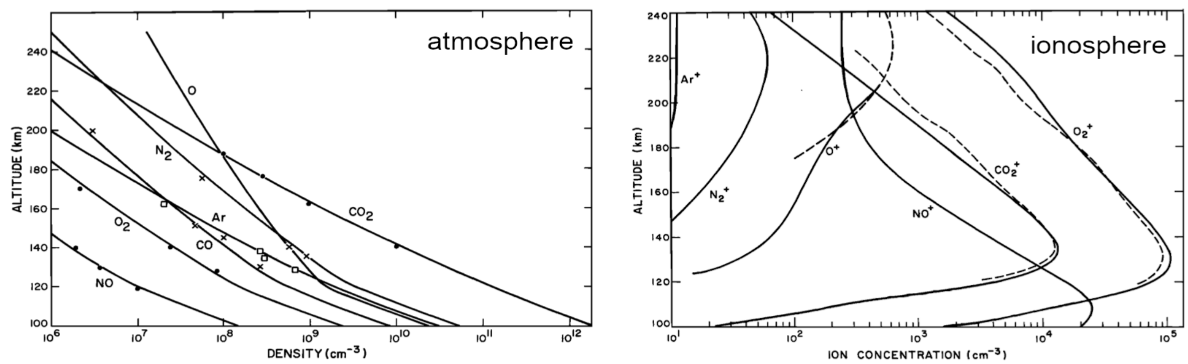

Figure 1.8: Altitude profiles of the neutral and ionized constituents of the Martian atmosphere from Fox and Dalgarno [1979]. Viking 1 data is plotted with markers on the left and dashed lines on the right, while modeled atmospheric and ionospheric densities are plotted as solid lines.

In the absence of EUV irradiance, the nightside of Mars has a patchy ionosphere associated with both plasma transport from the dayside and energetic particles “precipitating”, or traveling into and depositing their energy in the atmosphere. Zhang et al. [1990] showed the peak electron density in Viking observations of the nightside was low or below detection thresholds. While irregular and diffuse radar reflections found by MARSIS were suggested to be associated with vertical regions of the crustal fields [Gurnett et al. 2008], plasma transport from the dayside by horizontal transport via thermal pressure gradients and ion-neutral coupling with winds can also supply nightside ionospheres [Nemec et al. 2010, Adams et al. 2018].

1.3.3. Solar wind interaction with Mars

Since Mars has an ionosphere but lacks an intrinsic global magnetic field, the incoming solar wind flow induces currents in the ionosphere to form an induced magnetosphere. Much like at Venus, solar wind plasma is shocked, decelerated, and deflected around the resulting magnetic fields (see Nagy et al. [2004] for further details). This near Mars plasma environment goes by two main names, the Mars-solar wind interaction region and the induced magnetosphere [Espley

2018]. Figure 1.9 shows a schematic of the region alongside measurements of magnetic fields and electron spectra from a spacecraft passing through the region. The supersonic solar wind approaching a stationary planet forms the bow shock, a collisionless boundary that separates the solar wind from the shocked solar wind. Within the shock is the sheath or magnetosheath, a highly turbulent region that spans roughly a proton gyroradius. This is where mass loading begins to influence the magnetic fields, causing them to drape as substantial newly-ionized stationary exosphere particles are incorporated into the plasma and slow the convective flow [Dubinin et al. 1997, 2017].

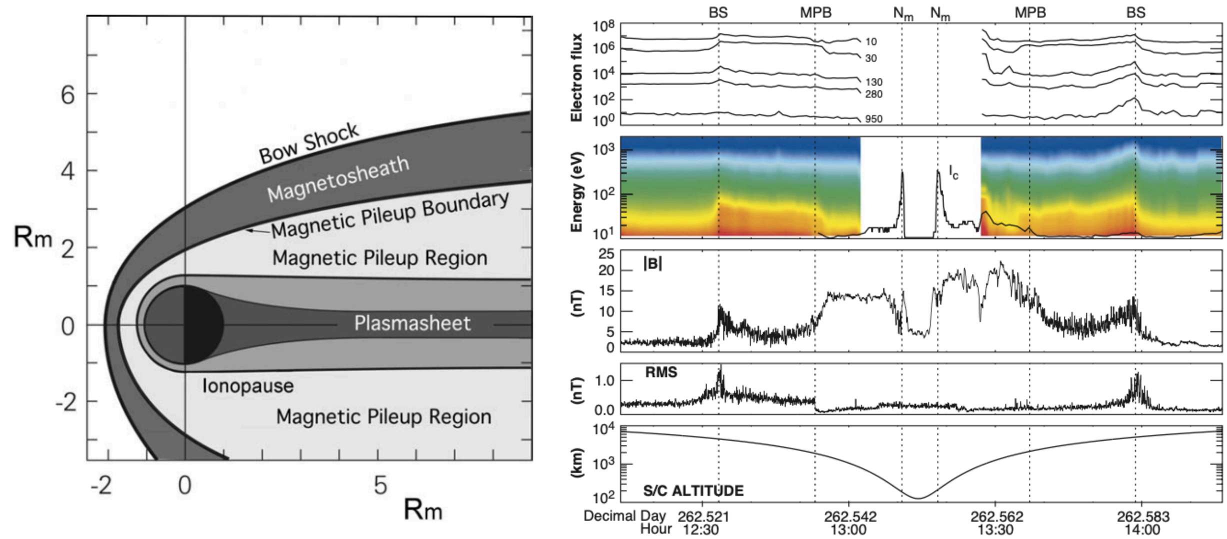

Figure 1.9: Schematic of the Mars-solar wind interaction [Nagy et al. 2004] (left) and plasma data (electron flux, electron spectra, magnetic field magnitude, magnetic field variability, spacecraft altitude) recorded by the MGS spacecraft with vertical bars to indicate the spacecraft crossing the bow shock (BS), magnetic pileup boundary (MPB), and the ionospheric main peak (Nm) [Acuña et al. 1998] (right).

The shocked solar wind density then drops precipitously within the magnetic pileup region, which is significantly less turbulent and dominated by planetary heavy ions. The clear delineation between the magnetosheath and magnetic pileup region is thin and known by many names: in order of decreasing usage, the magnetic pileup boundary (MPB) since the magnetic fields rapidly rise in magnitude as they have “piled up” [Crider et al. 2000, Vignes et al. 2000], the induced magnetosphere boundary (IMB) since it separates the interplanetary and near-Mars plasma environments [Lundin et al. 2004], the protonopause for reduced proton densities [Sauer et al. 1995], the planetopause by analogy to a cometopause [Riedler et al. 1989], and more. Below the magnetic pileup region is the ionosphere. The delineations used to separate these regions are the photoelectron boundary (PEB), which is the altitude below which electron spectra is dominated by photoelectrons with energies of 10s of eV [Mitchell et al. 2001], and the ionopause, a boundary initially described by the pressure balance between the ionosphere and incident solar wind (e.g. Spreiter et al. [1970]). Draped fields stretch behind Mars to form the magnetotail, which can be separated into two tail lobes, Marsward and anti-Marsward, separated by the tail current sheet or plasma sheet [DiBraccio et al. 2018].

There is considerable variability in the boundaries, leading to changing dynamics. The bow shock and MPB are often approximated as a fixed boundary, usually a fitted axisymmetric conic model (e.g. Trotignon et al. [2006]). However, the bow shock can vary from the fitted model by up to half a Mars radius (0.5 R_M) under nominal conditions [Acuña et al. 1998]. Crustal anomalies also change the solar wind interaction, pushing the IMB and bow shock outwards from Mars in regions of strong magnetism [Edberg et al. 2008]. EUV irradiance, solar wind dynamic pressure, and placement of crustal anomalies have also been observed to shift the bow shock [Gruesbeck et al. 2018].

1.3.4. Magnetic topology

When discussing precipitating particle populations as in this thesis, magnetic topology terms are useful. Soon after the discovery of the crustal anomalies, electron spectra above the anomalies were found to have dropouts or “voids” when rotated on the nightside, and would be populated by photoelectrons when rotated on the dayside [Mitchell et al. 2001]. It was inferred that these spectra were measured on “closed field lines”, or magnetic fields that are entirely disconnected from the solar wind and instead connected to Mars on both termini. Flux “spikes” also interleaved these voids, particularly where the magnetic field was strongly directed away from or towards Mars. These spectra were analogized to Earth cusp regions. Krymskii et al. [2002] later suggested these regions could reconnect to produce “open field lines”, with one field line terminus connected to Mars and the other to the solar wind.

Brain et al. [2007] introduced the magnetic topology formalism for MGS data, identifying magnetic field measurements as either closed, open, or draped based on electron pitch angle distributions. In this approach, open and closed field topologies were determined with respect to the atmosphere rather than the Martian crust. Closed fields were identified by either the absence of fluxes or the presumably collisional depletion of both field aligned and anti-aligned electrons, open fields by the absence of field-aligned or anti-aligned electrons, and draped fields by the absence of any pitch angle dependent depletions. The distribution of closed, open, and draped field lines is geographically dependent, with closed fields clustered over the crustal anomalies and open fields distributed elsewhere (Figure 1.10). This approach has since been applied to MAVEN data [Weber et al. 2017] and combined with an electron shape parameter to infer magnetic topology from the presence/absence of photoelectrons [Xu et al. 2014, 2019]. While this is not a strictly accurate definition of open field lines, which require connectivity to the crust, it is useful for describing regions where particles may precipitate and/or escape.

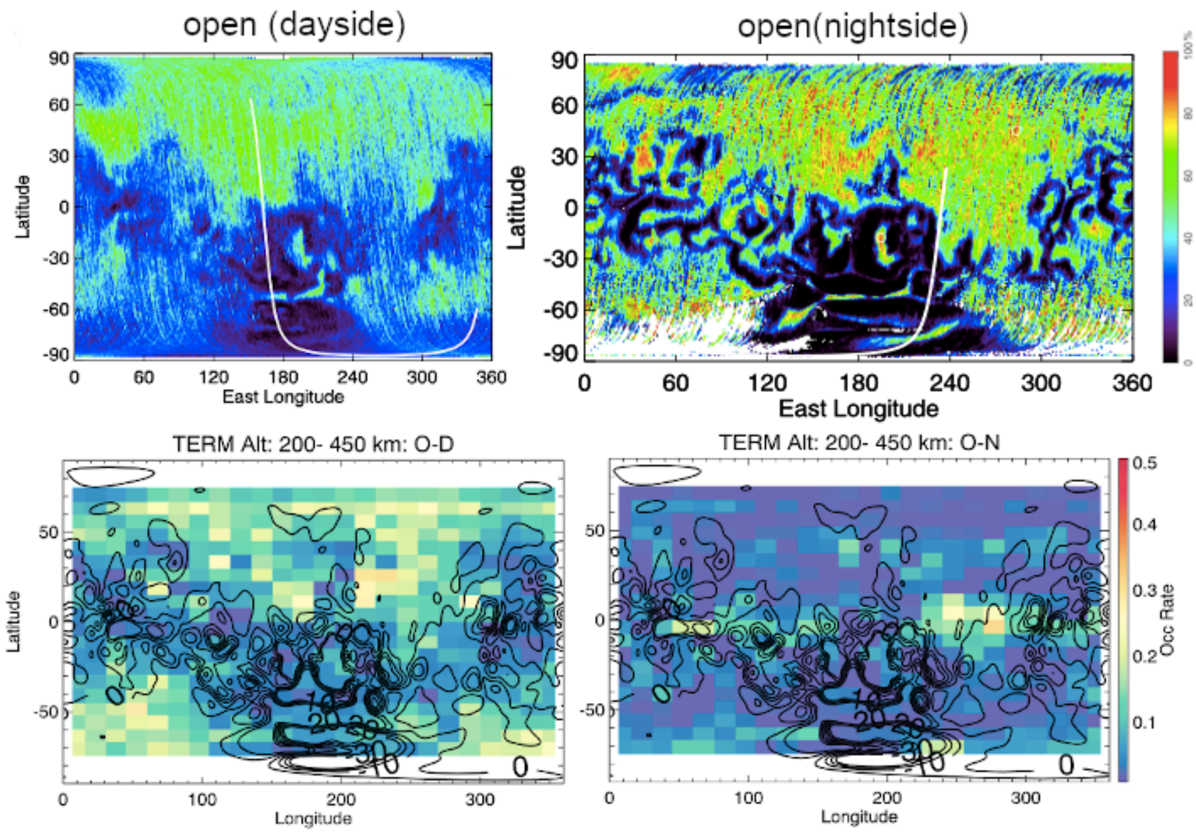

Figure 1.10: The frequency of measuring open field lines at 400 km from MGS [Brain et al. 2007] (top) and between 200-450 km from MAVEN [Xu et al. 2019] (bottom) that connect to the dayside of Mars (left) and the nightside of Mars (right) as a function of geographic latitude and longitude.

1.4. Atmosphere escape

The prior section discussed the neutral and plasma flows at Mars from surface to space, providing a basis for discussing atmosphere escape. Figure 1.11 shows a schematic of the solar drivers at Mars and several escape processes. There are four main channels for escape: thermal escape, which is most effective on hydrogen atoms; photochemical escape, which is effective on O_2^+; ion escape, which scours all ionosphere constituents; and sputtering, an episodic cascade process that preferentially drives escape of oxygen.

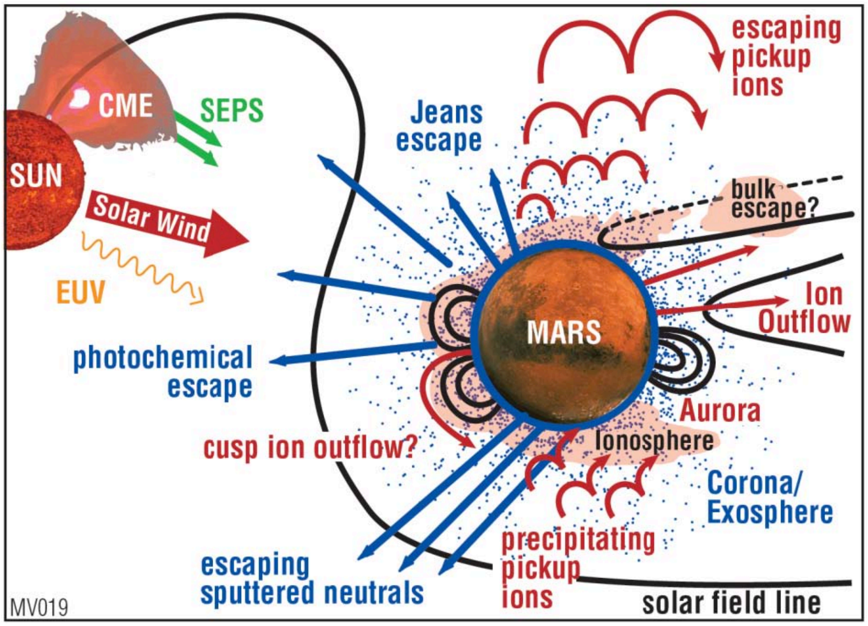

Figure 1.11: A schematic of the energy inputs to Mars (EUV, solar wind, SEPs, CMEs), the neutral escape processes (in blue: Jean's, photochemical, sputtered neutrals, corona/exosphere), and the ion escape processes (in red: escaping pickup ions, precipitating pickup ions, aurora, ion outflow, cusp ion outflow). Credit: CU/LASP.

A neutral atom will leave an atmosphere provided it has a speed above escape velocity, an altitude above the exobase, and a trajectory directed away from the planet. Escape velocity can easily be calculated as $v_{esc} = \sqrt{2GM/R}$, which is ~5 km/s above Mars. This escape velocity is much less than the escape velocity of atoms at Venus or Earth, which is part of the reason why atmosphere escapes from Mars more easily than Venus and Earth. A hydrogen atom, an oxygen atom, an oxygen molecule, and a carbon dioxide molecule have escape energies of ~0.1 eV, 2.1 eV, 4.2 eV, and 5.7 eV respectively.

1.4.1. Thermal escape

Thermal escape, also called Jean's escape, occurs when the thermal energy of an atom meets or exceeds the escape energy. Assuming an atmospheric temperature between 140 K and 350 K per prior spacecraft observations during different phases of the solar cycle [Bougher et al. 2015] and that the temperature can rise by ~70 K during an X-class flare [Jain et al. 2018], the average thermal energy of an atmospheric constituent is roughly 0.01-0.03 eV for a nominal thermosphere and can rise by an additional ~0.01 eV during a solar event. While this thermal energy is far smaller than the requisite escape energies for atomic oxygen or molecular constituents, it is comparable to the escape energy of hydrogen atoms. The total fraction of escaping atoms can be calculated by integrating the Maxwell-Boltzmann distribution above escape velocity (Figure 1.12) and halving the resulting cumulative probability to account for half of the particles traveling downwards instead of upwards. For nominal temperatures 140-350 K, this fraction is 0.01-3% and rises to 0.2-6% for a solar flare.

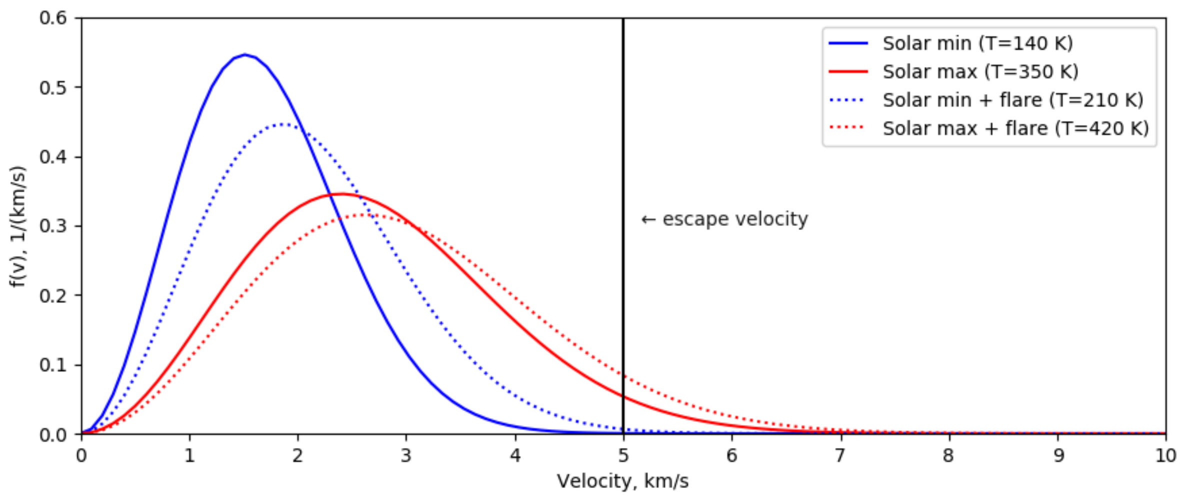

Figure 1.12: The Maxwell-Boltzmann distribution function of atmospheric hydrogen atoms for different atmospheric temperatures, with a black vertical line drawn to show the small fraction of the distribution above escape velocity.

Thermally escaping hydrogen is the source of the extended hydrogen corona [Anderson and Hord 1971]. Measurements of hydrogen abundance can be made via observation of the Lyman alpha emission (e.g. Chaffin et al. [2014]), solar wind ions that have reacted with the hydrogen exosphere to become hydrogen atoms and reconverted into protons close to Mars (e.g. Halekas et al. [2015]), and energized pickup hydrogen (e.g. Rahmati et al. [2017]). Escape rates are subsequently estimated by using a derived coronal temperature. Jakosky et al. [2018] estimated a modern escape rate of ~1-11 x 10^{26} hydrogen atoms per second using these methods, which is equivalent to removing a global layer of water that is 2.6-25 meters thick. This estimate is uncertain due to the significant variability of the hydrogen exosphere. While the corona is usually described as a 1-D spherically symmetric exosphere [Chamberlain 1963], this model underestimates hydrogen densities near to Mars and overestimates them far from Mars [Chaffin et al. 2015]. The corona is also seasonally influenced, increasing in extent when Mars is in southern summer [Halekas 2017]. Dust activity can also drive increases in the escaping hydrogen by a factor of 10 [Chaffin et al. 2021].

1.4.2. Photochemical escape

Photochemical escape is the process in which an exothermic chemical reaction produces a particle that is sufficiently energetic to escape. Dissociative recombination is the main process that drives the escape of oxygen, nitrogen, and carbon atoms [Chassefière and Leblanc 2004]. Ionized constituents (O_2^+, N_2^+, and CO^+) recombine with an electron and then split into constituent atoms. For example, when O_2^+ dissociatively recombines, the resulting oxygen atoms may have energies of 0.4-3.5 eV [Kella et al. 1997]. These nonthermal or "hot" oxygen atoms form the oxygen corona (Figure 1.13). Many studies have modeled the oxygen corona at Mars and estimated the hot oxygen production rates (e.g. Chaufray et al. [2007], Lee et al. [2015]). The corresponding hot oxygen escape rates are predicted to increase with EUV irradiance (e.g. Cravens et al. [2017]). Lillis et al. [2017] used MAVEN observations of electron temperature and O_2^+ densities to estimate hot oxygen escape rates of 1.2-5.5 x 10^{25} atoms per second depending on season and EUV irradiance.

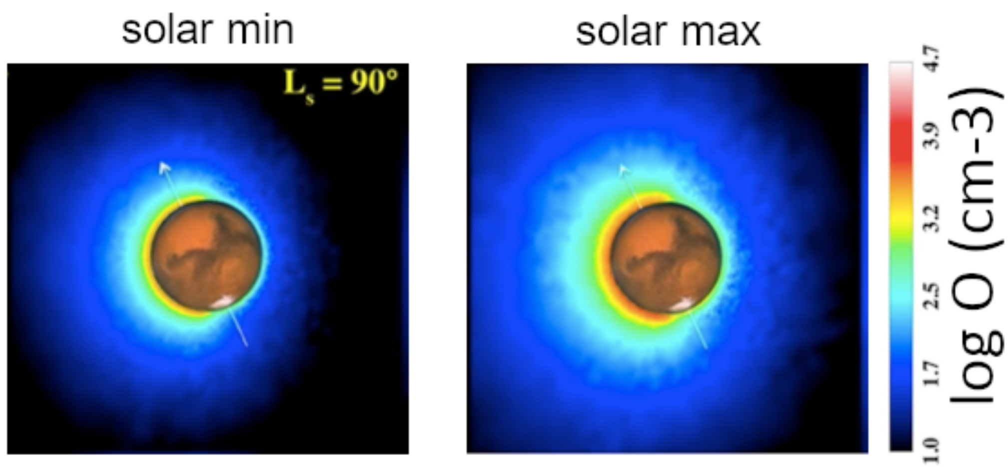

Figure 1.13: Modeled hot oxygen corona densities [Lee et al. 2015].

1.4.3. Ion escape

Ion escape is the broad collection of processes that involve acceleration of ionospheric constituents to escape velocities by electric fields. Ion outflow is the low energy (<1 keV) population of ions that escape down the magnetotail while pickup ions or "plume escape" is the energetic (>1 keV) population that escapes along the direction of the motional electric field. Ion escape can also vary locally and episodically, depending on the source. Given the presence of crustal fields, many studies have investigated the influence of crustal fields on ion outflow. While most agree that the crustal anomalies contain elevated heavy ion fluxes, some argue that crustal anomalies inhibit escape by trapping the fluxes (e.g. Lundin et al. [2011]) or enhance escape by uplifting the ionospheric plasma to higher altitudes (e.g. Dubinin et al. [2020]). Data and models have also predicted potentially significant cusp ion outflow [Poppe et al. 2021]. On the other hand, episodic plasma waves may also be able to drive escape via wave-particle heating [Ergun et al. 2006, Fowler et al. 2020].

Many missions have estimated ion escape rates. The earliest measurements were made by the ion spectrometers aboard Mars 2, 3, and 9, for which an escape rate of ~10^{24} O^+ per second was estimated [Vaisberg and Smirnov 1986], followed by measurements aboard Phobos 2 of “cold” (<100 eV) and “auroral” (~keV) escaping oxygen in the magnetotail to estimate a rate of ~10^{25} O^+ per second [Lundin et al. 1989, 1990]. The Ion Mass Analyzer (IMA) aboard Mars Express also observed ion escape, but at a significantly lower rate of ~10^{23} O^+ per second. [Barabash et al. 2007]. This was revised upwards to ~10^{24} O^+ per second after the software was updated to include low energy ions [Lundin et al. 2008, Ramstad et al. 2015], which agrees with MAVEN-observed ion escape rates [Brain et al. 2015, Dong et al. 2017].

The presumed driving mechanism of ion escape before MAVEN arrived was ion outflow from cold ions leaving the planet in a variety of mechanisms [Dubinin et al. 2011] and auroral-like ions that had been accelerated by the $\boldsymbol{J} \times \boldsymbol{B}$ force in the current sheet behind Mars [Dubinin et al. 1993]. However, pickup ions were predicted to be a significant outflow channel in many models, appearing as a distinctive “plume” along the direction of the convective electric field (e.g. Najib et al. [2011]). Indeed, energetic oxygen ion beams now known to be associated with this flow had been measured by Phobos 2 (e.g. McKenna-Lawlor et al. [1992]). Unfortunately, searches for the pickup ion plume in IMA data were inconclusive since the spacecraft’s orbit and instrument field-of-view hindered the likelihood of a successful observation [Liemohn et al. 2014]. MAVEN observations ultimately confirmed the existence of the plume (Figure 1.14), estimating that it accounted for ~23% of escaping >25 eV O^+ ions [Dong et al. 2015]. Plume escape flux is characteristically invariant with EUV irradiance although the energy of the accelerated particles increases with EUV [Dong et al. 2017], while tailward ion outflow increases with EUV irradiance (e.g. Dubinin et al. [2017]). With the plume included, MAVEN observations were used to estimate heavy ion escape rates of ~10^{24} ions per second [Brain et al. 2015, Dong et al. 2017].

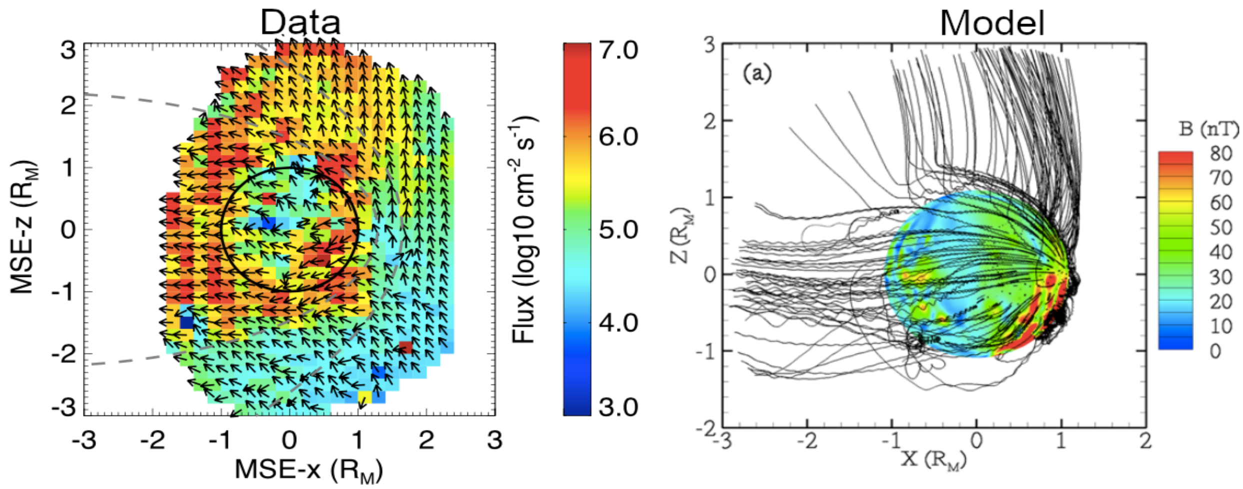

Figure 1.14: Measured O^+ fluxes [Dong et al. 2015] (left) and modeled O^+ trajectories [Fang et al. 2008] in the XZ plane.

While pickup ion escape is the acceleration of heavy ions via the convective electric field away from the planet, the same mechanism can accelerate the ion back towards the planet. The precipitating particle re-enters the atmosphere with significant energy (10 eV - 100 keV) that is distributed as recoils in atmospheric constituents, which is theoretically sufficiently to energize the impacted atoms above escape velocity [Johnson 1990, Luhmann and Kozyra 1991]. This mode of escape, called "sputtering", is very difficult to measure, due to the effective invisibility of recoils relative to the thermal energy. The primary indirect evidence for sputtering loss is argon fractionation, which requires that 40-60% of atmospheric argon was lost to space [Slipski et al. 2016, Jakosky et al. 2017]. MAVEN's observations of precipitating heavy ion fluxes have been used to infer sputtering-induced escape rates that are orders of magnitude below the photochemistry-associated escape rates (~10^{23} O^+ per second) [Leblanc et al. 2015, 2018]. However, MAVEN observations to-date are confined to solar minimum and models have shown that EUV may have a strong control on sputtering. However, many such models were derived from Luhmann et al. [1992], which used a gasdynamic model to estimate precipitating oxygen fluxes (e.g. Leblanc and Johnson [2002]). Recent models that account for mass-loading find significantly suppressed precipitating oxygen fluxes even in solar maximum phases [Chaufray et al. 2007].

1.4.4. Ancient escape

While we have reviewed the modern escape mechanisms, there are two additional channels of escape that are irrelevant to modern escape but relevant to ancient Mars: impactors and hydrodynamic escape. Impactors like meteorites, comets, and asteroids can add and subtract material from planetary atmospheres. Although impactors likely helped initially supply the atmospheres of all inner solar system planets, fast impactors that were more common in the early Noachian might have ejected considerable atmosphere from Mars due to the low mass and radius of the planet [Melosh and Vickery 1989, Brain and Jakosky 1997]. Hydrodynamic escape, also called "blowoff", occurs when EUV heating and the planetary hydrogen inventory is significant enough that the volume of escaping hydrogen exerts drag on heavier atmospheric constituents [Hunten 1973]. It can be considered an extreme case of Jean's escape, as EUV energy is supplied in excess of the thermal energy and instead converted into kinetic energy [Chassefière and Leblanc 2004]. The required conditions are likely common in primordial planetary atmospheres and have been observed at exoplanets [Tian et al. 2005]. Evidence of hydrodynamic escape in the early solar system is currently limited to the fractionation of xenon isotopes at Mars and Earth [Hunten et al. 1987, Pepin 1994].

1.4.5. Current loss to space

Summing over the active escape processes, the current total atmospheric loss of hydrogen and oxygen atoms is roughly 2-3 kg/s [Jakosky et al. 2018]. Dissociative recombination produces the most significant escaping fluxes of oxygen atoms, followed by ion escape and sputtering. This rate is not reflective of all sources of loss, such as photochemical escape of nitrogen and carbon atoms, and thermal deuterium loss, and does not account for episodic influences such as CMEs, gravity waves, and plasma waves. The modern rate can be extrapolated back in time to estimate escape in the young solar system. Observations of main sequence stars early in their lifetime like the ancient sun show they are dimmer in overall luminosity, the famous "faint young sun" problem. Despite this overall reduced luminosity, these stars also have a higher magnetic activity due to a more efficient dynamo driving rapid rotation rates, which produces more intense X-ray and EUV emissions [Güdel 2007]. These modern escape rates were extrapolated backwards given the higher EUV irradiances to estimate that either 0.8 bar of carbon dioxide or a 23 meter global equivalent layer of water have been lost [Jakosky et al. 2018]. When combined with estimates for impact ejection to space and deep subsurface sequestration, ~1.3-3 bars of carbon dioxide are estimated to have been lost from an ancient Mars atmosphere [Jakosky 2019].

1.5. Space weather at Mars

While atmospheric loss rates and projections to ancient times generally incorporate the increased EUV emissions present in the solar system, the early sun also released a faster solar wind and likely had more frequent CMEs. Evidence of more frequent energetic SEP events in the early solar system can be seen as enhanced spallation in meteoric grains dating to the early solar system [Caffee et al. 1987]. Given this relevance, many studies have investigated the atmospheric and ionospheric response of Mars to space weather events. In general, ion escape rates increase by a factor of 10 during CME passages [Futaana et al. 2008, Jakosky et al. 2015] and ~2.5 during SIR passages [Edberg et al. 2010, Nilsson et al. 2011]. Flares can cause significant atmospheric heating [Jain et al. 2018], leading to increases of hydrogen escape by a factor of 5 [Mayyasi et al. 2018] and oxygen escape by 50% [Thiemann et al. 2018].

Unfortunately, observations of thermal and photochemical escape are infrequent and sensitive to noise, making it difficult to determine how much increased escape is due to the flare, CME, or SEPs.

Projecting the role of space weather at early Mars requires estimating atmospheric escape in response to more frequent events. However, disambiguating the influence of each space weather process (flare, CME, SEPs) on in-situ processes is difficult, particularly for more infrequently measured neutral escape processes (e.g. hydrogen and oxygen corona). Models are often useful to predict the response of a system to specific processes, but there is significant variability based on the included physics. For example, for the September 2017 space weather events, a MHD simulation predicted escape that was increased by a factor of 10-20 while a hybrid model for the same event estimated an increase by a factor of 2.5 [Lee et al. 2018]. Current existing models of space weather at Mars do not usually include SEPs and their associated effects. Those that do are often applied to predicted surface dose rates (e.g. Gronoff et al. [2015]) or atmospheric ionization (e.g. Sheel et al. [2012]). However, a simplified 1-D model of protons slowing in a pure monatomic oxygen atmosphere scaled to the total atmospheric density of Mars was used to estimate that SEP protons could increase heating in the Martian atmosphere by ~20% [Leblanc et al. 2002]. It was also shown that SEP protons would be unhindered by all but the strongest crustal fields. SEP electrons have not been investigated by any of these models.

1.6. Thesis roadmap

This thesis intends to disambiguate the role of SEPs in the larger scheme of space weather influences on atmospheric escape, with particular emphasis on how the Mars-solar wind interaction and crustal fields affect SEP transport. The work presented in this thesis is organized into five chapters as follows:

Chapter 2 (Model of SEP transport and energy deposition): Description of the 3-D Monte Carlo test particle and energy degradation simulation that is applied in Chapters 3 and 4.

Chapter 3 (SEP proton ionization in crustal fields): Predictions of how crustal fields influence atmospheric ionization from SEP proton precipitation.

Chapter 4 (SEP electron transport): Predictions of how the solar wind interaction with Mars and the crustal fields influence SEP electron transport and precipitation.

Chapter 5 (Inventory of solar driver energy input): Calculated relative energy input of SEPs compared to EUV and solar wind as recorded by MAVEN observations during the onset of solar minimum.

Chapter 6 (Conclusion): Summary of the work completed in the thesis and a speculative estimate of energy input at ancient Mars.

Chapter 2

Model of SEP transport and energy degradation

A 3-D Monte Carlo test particle model called ASPEN (Atmospheric Scattering of Protons, Electrons, and Neutrals) was developed for the work presented in this thesis. The model was initially developed to count collisions of energetic (10 eV – 5 MeV) protons and hydrogen atoms in the Martian thermosphere and subsequently extended to predict relativistic motion and include electron collisional physics. The simulation applies Monte Carlo methods by randomizing individual particle collision probability to estimate average energy deposition into a planetary atmosphere for a large number of particles, while simultaneously accounting for motion in prescribed 3-D inhomogeneous electromagnetic fields (Figure 2.1).

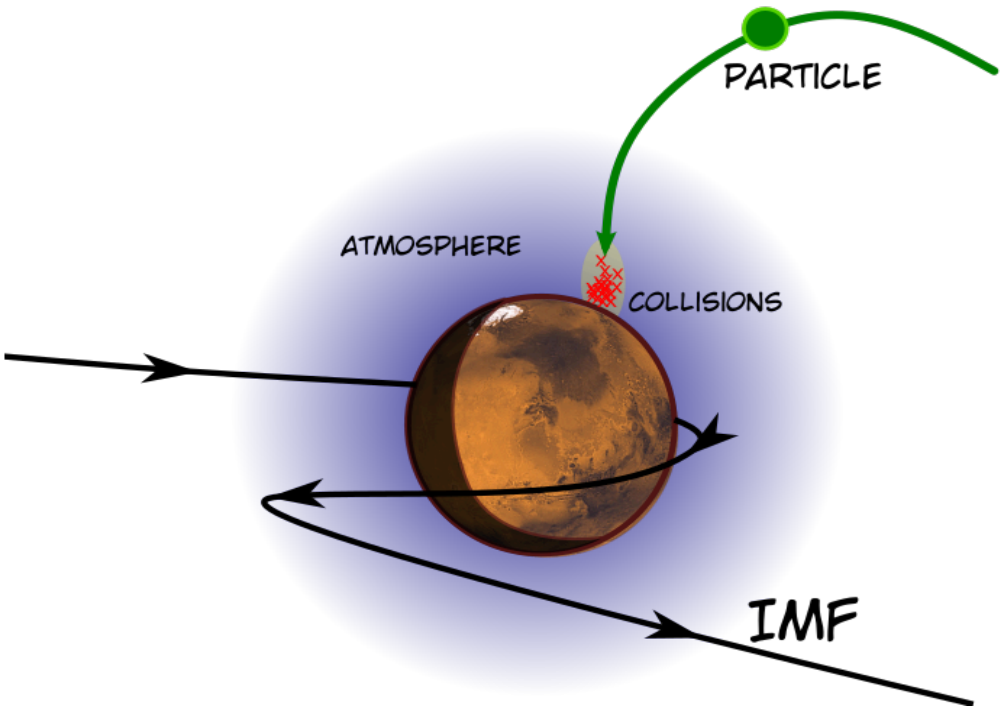

Figure 2.1: Simplified schematic of ASPEN tracing a particle moving in the IMF near Mars and precipitating into the atmosphere, colliding and imparting energy to the atmosphere.

This chapter is based on sections of two papers published in the Journal of Geophysical Research - Space Physics [Jolitz et al. 2017, 2021]. Due to the increasing capabilities of the model, these sections were combined and updated to describe the current state of ASPEN. First the chapter will contextualize the need for ASPEN's development with a discussion of prior existing particle energy degradation and plasma interaction models, and explain why the test particle and collision-by-collision approaches were chosen. Then an overview of ASPEN will be provided, with subsections describing solving Lorentz force equations for each particle and the collision-by-collision energy degradation method, followed by a description of all possible simulation inputs. Finally, prior model validation and current model applications unrelated to SEPs will be mentioned.

2.1. Background

This section will review current approaches used in modeling energy degradation and plasmas. The drawbacks and advantages of each approach are discussed, and provide rationale for the development of a new simulation.

2.1.1. Prior energy degradation models

Model type	Advantages	Disadvantages
Continuous slowing down approximation (CSDA)	Easy to calculate, can be parameterized using results of other approaches.	Assumes continuous energy loss, difficulty in modeling inelastic collisions, does not estimate energy partitioning into processes
Kinetic Boltzmann equations	Most accurate, accounts for energy partitioning into processes, predicts distribution functions of both projectiles and targets.	Equations often require a simplified geometry or magnetic field configuration
Collision-by-collision	Accounts for energy partitioning into processes, can be easily combined with a test particle algorithm	Computationally intensive.

Table 2.1: Table comparing different energy degradation approaches

Many models have been developed to study energy degradation of energetic particles in planetary atmospheres. The approaches can be broadly categorized as stopping power approximations, kinetic Boltzmann equation solvers, or collision-by-collision Monte Carlo models (Table 2.1). Stopping power approximations, also called the continuous slowing-down approximation (CSDA), assume energy is gradually lost in proportion to the atmospheric density. While the CSDA is easily estimated, it can mishandle inelastic processes that cause discrete energy loss. The accuracy of the CSDA depends on the estimated loss function, which can include corrections for multiple collisional processes (e.g. Porter and Green [1975]) and backscattering (e.g. Kallio and Barabash [2000]). Alternatively for high energy particles, collisions are sufficiently frequent that the energy loss may be approximated as continuous loss [Sheel et al. 2012].

Kinetic Boltzmann equations (also called “multistream” or “transport” equations) have the advantage of describing the energy deposition and transport of energetic particles in a self-consistent manner. Unlike CSDA, the collisional conversion of protons to hydrogen atoms and vice versa can be easily described by a set of coupled Boltzmann equations. Such models include the Trans* model series, initially developed for Earth [Lummerzheim and Lilensten 1994, Lilensten and Blelly 2002] and since adapted to many other planets (e.g. Aeroplanets, Gronoff et al. [2012]), which solve the differential equations iteratively over altitude for predefined boundary conditions [Galand et al. 1997]. Alternatively, a stochastic direct simulation Monte Carlo method can be used to solve the equations [Shematovich et al. 1994, 2011]. Unfortunately, the equations assume a 1-D plane parallel atmosphere and absent or simplified magnetic field configurations.

In collision-by-collision Monte Carlo simulations, random numbers are used to estimate the collision probability of atoms and decrement the energy per collision for a given individual particle. The process is repeated until the particle is considered “thermalized” or below an energy threshold, and then repeated for a large number of particles. This is the most memory-intensive simulation type, since a particle may undergo thousands of collisions before thermalizing. However, collision-by-collision simulations are also the most amenable to studies of beam-spreading (e.g. Davidson [1965]), differential energy input into various collision processes (e.g. Kallio and Barabash [2001]), and magnetic field influence (e.g. Lillis et al. [2008]). Since this thesis primarily intends to investigate how the complex configuration of the Mars-solar wind interaction affects SEP precipitation, this was the approach chosen.

Studies of high energy particles sometimes use Geant4, a package which includes several modules to describe hadronic interactions, pair production, particle showers, and more [Agostinelli et al. 2003]. This package is integrated into Planetocosmics [Desorgher et al. 2006], which has been applied to several studies estimating surface dose rates and ionization [Dartnell et al. 2007, Gronoff et al. 2015]). However, Geant4 is not usually applied in aeronomical studies of particles with energies below 1 MeV since Geant4 outputs do not distinguish between collisional processes. For example, atmospheric ionization rates may be estimated by taking the output altitude profile of energy deposition and dividing by an average pair production energy of 35 eV (e.g. Gronoff et al. [2015]). In addition, Geant4 applies the CSDA to solve for multiple elastic collisions. Because of these issues, we deliberately chose to not use Geant4.

2.1.2. Prior plasma models

As with collisional energy degradation models, there are many models of plasma interaction. In the analysis of plasma at Mars, there are four primary kinds of simulations: magnetohydrodynamic (MHD), hybrid, particle-in-cell (PIC), and test particle.

MHD models are derived from gasdynamic models, which were developed in the 1960s to solve conservation of mass, momentum, and energy equations for a solar wind flow into a fixed “ionopause” boundary [Spreiter 1966]. Although gasdynamic models could replicate the bow shock and magnetosheath of Mars, they neglected dissipative processes such as magnetic induction and mass loading [Russell et al. 1984]. Increasing computational capacity in the 1990s drove the development of MHD models that could capture these effects [Tanaka 1993]. MHD models approximated plasmas as a self-neutralizing fluid and solve continuity, momentum, magnetic induction, and energy equations to obtain plasma parameters. Many MHD models exist and have been applied to the Mars system [Ma et al. 2004, Harnett and Winglee 2003, Terada et al. 2009, Najib et al. 2011]. They differ from each other in a variety of ways, ranging from the solver used to approach the system of equations, whether each ion species is approximated by the same or individual momentum and energy equations, and how many terms of the magnetohydrodynamic equations are included.

While mostly effective at predicting the local plasma environment at Mars, it is important to mention that MHD models will not describe wave activity or finite gyroradius effects. These effects are captured in hybrid models, so-named because they model ions as macroparticles and electrons as a massless charge-neutralizing fluid. Many hybrid models have been developed for the Mars system to describe kinetic effects of solar wind protons and ionospheric oxygen [Brecht and Ledvina 2006, Kallio et al. 2006, Bößwetter et al. 2007, Modolo et al. 2016]. Hybrid models have continued to increase in complexity, such as incorporating two charge-neutralizing fluids to represent ionospheric and solar wind electrons and finite ionospheric conductivity [Modolo et al. 2016] and including magnetic diffusion [Jarvinen et al. 2018]. Hybrid models have the advantage of self-consistency and describing proton kinetics across the shock. However, they are highly computationally intensive, causing them to have lower resolution and/or limited domains compared to MHD models. PIC models go a step further than hybrid simulation by self-consistently solving for the motion of all energetic particles, and are accordingly known as "fully" kinetic simulations. However, they can only be applied in simplified magnetic field configurations due to the computational complexity (e.g. magnetic cusps in Poppe et al. [2021]).

MHD, fluid, and PIC simulations self-consistently account for the influence of charged particles on the ambient magnetic and electric fields. However, a charged particle population sometimes does not require self-consistent modeling because it isn't sufficiently dense to alter ambient electromagnetic fields. This is true for SEPs. Even at the peak of the 2003 Halloween event, the lowest energy channels of ACE/SWEPAM measured fluxes of ~6 x 10^5 ions cm^{-2} s^{-1} (47-66 keV) and ~3 x 10^5 electrons cm^{-2} s^{-1} (45-62 keV) [Malandraki et al. 2005], giving an effective plasma density of ~0.001 cm^{-3}. Although this calculation inaccurately implies a fluidic description of SEPs, it shows that the effective plasma density of SEPs is three orders of magnitude below nominal solar wind densities (~3-10 cm^{-3}). As the density of ambient plasma only increases closer to Mars due to mass loading, self-consistent modeling descriptions should never be required for SEPs.

When self-consistent modeling is unnecessary, a test particle model is ideal. Test particle models describe plasmas as collections of individual particles moving in a prescribed magnetic field by the Lorentz force. Test particle models have been used before in predicting SEP transport at Mars (e.g. Luhmann et al. [2007], McKenna-Lawlor et al. [2012], Kallio et al. [2012]). For the prescribed magnetic fields used in ASPEN, magnetic and electric fields from a multifluid MHD (MF-MHD) simulation are used (further details in Section 2.3).

2.2. ASPEN overview

Each particle is single-stepped in prescribed electric and magnetic fields until the calculated likelihood of collision with atmospheric constituents along its path exceeds a random number. When that occurs, the consequences of the collision are determined (e.g. energy imparted to the atmosphere) and the particle begins moving again. The process repeats until the particle energy falls below a given energy threshold or the particle exits the simulation boundaries. The simulation boundaries are assigned based on the application. For tracing test particles in the overall Mars-solar wind interaction, the domain is limited by the range over which the prescribed MHD fields are defined and accurate. Modeling collisions calls for a simulation domain that is focused on the atmosphere, so it is appropriate to choose a radially-defined domain with an upper altitude limit above the exobase and a lower altitude limit below the thermalization altitude. In addition, an energy threshold is useful to avoid excessive computational burden incurred by simulating very low energy particles that impart inconsequential energy solely via elastic collisions at low altitudes. This can be either fixed at an arbitrary cutoff (10 eV in Chapter 3) or set to the energy where the likelihood of an inelastic collision is less than 1%, which varies depending on the projectile.

Many useful quantities can be inferred from ASPEN. The simulated population's energy and location upon exiting the simulation domain can be used to estimate parameters like the fraction of particles that are backscattered or magnetically deflected. When modeling collisions, the projectile name, collision location, species impacted, process occurred, energy deposited, and secondary energy (if produced) can all be recorded. When the simulation is complete, the collision logs can be combined and normalized by the total number of simulated particles to estimate energy deposition or collision rates. Subsets of the logs can be used to estimate more specific quantities, such as the ionization rate of carbon dioxide or Lyman alpha emission profiles from only hydrogen atom impact. Since ASPEN is a Monte Carlo simulation, increasing the number of particles simulated improves model predictions.

The model has four key assumptions. First, neutral atmospheric molecules are stationary relative to each simulated particle. Since the thermal energy of atmospheric molecules is ~0.01 eV and the maximum possible energy of a hot oxygen atom is on the order of eVs, the simulation is halted before interactions become significant. Second, simulated charged particles never interact with other charged particles. The simulated SEPs are already low in density, making collisions rare. The energy loss of fast particles in an ambient plasma can be estimated from the formula in Dalgarno et al. [1963], $dE/ds = n_e (1.95 \times 10^{-12}\ eV\ cm^2)/E$ for a particle of energy E

and ambient electron density n_e. Assuming the peak ambient electron density is ~10^5 cm^{-3}, the energy loss is ~2 meV/km for a 10 eV particle. Third, electromagnetic fields and atmospheric densities do not temporally vary over the lifetime of a simulated particle. Even in the most intensive Monte Carlo simulations run for Chapter 4, the average particle lifetime from initialization in the deep solar wind to precipitation or escape back to the solar wind was ~1 second, with a maximum of ~50 seconds.

The next subsections will describe the approach to solve for the motion of test particles, followed by a detailed discussion of collision detection and handling.

2.2.1. Particle motion

Each test particle has a three-dimensional trajectory and location. They move according to the nonrelativistic Lorentz force equation for a particle of charge q and mass m with position $\boldsymbol{s}$ and velocity $\boldsymbol{v}$:

$$m\frac{d\mathbf{v}}{dt} = q\big(\mathbf{v} \times \mathbf{B}(\mathbf{s}) + \mathbf{E}(\mathbf{s})\big) \qquad (2.1)$$

If a particle is or converts to a neutral atom, this equation reduces to zero and the atom will move ballistically. While a nonrelativistic approach is appropriate for the protons studied in Chapter 3, since the relativistic factor $(\gamma - 1)$ for 20 keV to 5 MeV protons is 10^{-5} - 10^{-3}, it breaks down for the electrons studied in Chapter 4, which have a relativistic factor $(\gamma - 1)$ between 0.5 - 10 for the same energy range. When this is the case, the Lorentz force equations need to be adjusted for a relativistic application:

$$\gamma = \frac{1}{\sqrt{1-(\mathrm{v}/c)^2}}, \qquad (2.2)$$

$$\mathrm{U} = \frac{1}{2}\mathrm{mv}^2 \rightarrow (\gamma - 1)\mathrm{mc}^2, \qquad (2.3)$$

$$|\mathbf{v}| = \sqrt{\frac{2\mathrm{U}}{\mathrm{m}}} \rightarrow \mathrm{c}\sqrt{1 - \left(\frac{1}{1+\frac{\mathrm{U}}{\mathrm{mc}^2}}\right)^2}, \tag{2.4}$$

$$\mathbf{F} = \mathrm{q}\big(\mathbf{E} + \mathbf{v} \times \mathbf{B}(\mathbf{s})\big) \rightarrow \mathrm{q}\gamma^{-1}\left(\mathbf{v} \times \mathbf{B} + \mathbf{E} + (\mathbf{v} \cdot \mathbf{E})\ \frac{\mathbf{v}}{\mathrm{c}^2}\right) \tag{2.5}$$

Alternatively, if a particle is assumed to have a sufficiently tight gyroradius and drifts are negligible, it can be assumed to follow a magnetic field line. In such a situation, the Lorentz force equation can be replaced with a differential equation that describes motion parallel or antiparallel to the magnetic field:

$$\frac{d\boldsymbol{s}}{dl} = \pm\frac{\boldsymbol{B}(\boldsymbol{s})}{|\boldsymbol{B}|} \tag{2.6}$$

Many methods can be used to solve the aforementioned differential equations. By default, ASPEN uses a Fourth Order Runge-Kutta method (RK4) to estimate the change in velocity ($d\boldsymbol{v}$) and position (*ds*) after elapsed time (*dt*). While RK4 is often sufficient to solve these equations, truncation error is cumulative and can increase for an excessive number of steps. The influence of truncation error can be estimated by calculating the change in particle energy in the absence of electric fields and collisions, since magnetic fields do no work. For cases when RK4 is insufficient, the Boris algorithm has been included in the simulation. Although the Boris algorithm is not a symplectic integrator, it can conserve energy due to conserving phase space volume in a manner similar to a symplectic integrator [Qin et al. 2013]. The Boris algorithm is a form of leapfrog algorithm, which evaluates the position and velocity at different time steps (usually half a time step apart). A relativistic version of the Boris algorithm from Ripperda et al. [2018] was implemented.

The time step *dt* is defined as $dl/|\boldsymbol{v}|$ where $\boldsymbol{v}$ is the particle's velocity and *dl* is a spatial step length. The step length *dl* is variable depending on the application. For example, a fixed step length of 1 km was used in Chapter 3 since the resolution of the energy deposition altitude profiles was 1 km. Because particles were released at the same altitude, a longer fixed step length caused artifacts such as energy deposition increases spaced a step length apart. On the other hand, this step length was far too short and computationally intensive for the study in Chapter 4. It was more appropriate for this application to use a step length that could parameterize the electron's gyration around the field line, such as 5% of the gyroradius. Unfortunately this length scale choice can be problematic in low magnetic field regions such as near the current sheet, where the magnitude of the magnetic field can be as low as ~0.01 nT and lead to a gyroradius prediction of tens of thousands of kilometers. In this region, the gradient scale of the magnetic fields is a better length scale for parameterizing particle motion. ASPEN chooses a varying step length that is the minimum of 5% of the local gyroradius, 10% of the gradient scale of the magnetic fields ($|\mathbf{B}|/|\nabla\mathbf{B}|$), and a predefined maximum step length (1,000 km). Figure 2.2 shows example traces using RK4 with a fixed step length and the varying step length along with one that used the Boris algorithm with the varying step length. As expected, the RK4 with a fixed step length incurred the most error with an energy increase of ~1.5% over the simulation

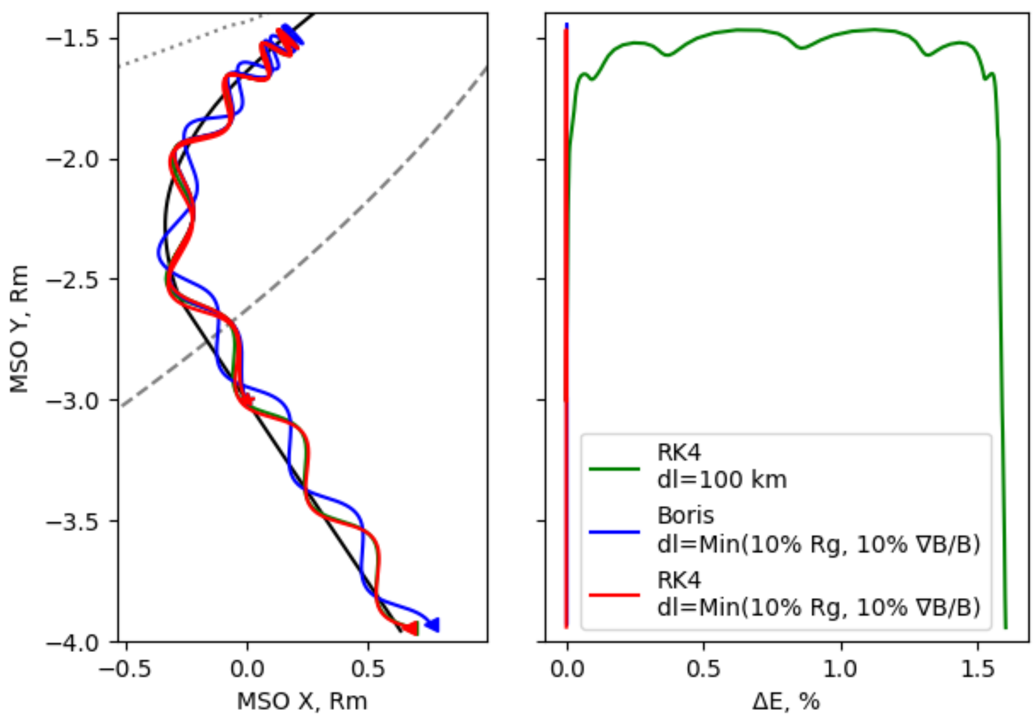

Figure 2.2: Traces of a 100 keV electron with a pitch angle of 35 degrees traveling towards Mars from **s** = (0, -3 R_M, 0) in the XY plane alongside the relative increase in energy as a function of Y position. The bow shock (dashed) and the MPB (dotted) are in gray, and the magnetic field line traced from the starting position is in black.

2.2.2 Particle collisions

As each particle is singly stepped, the collisional probability is simultaneously estimated. While particle motion is deterministic, particle collisions with the atmosphere are stochastic. The probability of a projectile colliding with a stationary target is random. However, a particle is more likely to collide if it travels in a denser medium or has a higher interaction cross-section area with a target. When applied to a particle beam of intensity *I*, this relation is known as Beer's Law:

$$dI = -n\sigma I dl \tag{2.7}$$

where *n* is the density of scattering targets, *σ* is the cross-sectional area presented by each scattering target, and *dl* is the distance over which a beam attenuates. Following an approach for electron-neutral collisions from Lillis et al. [2008], we solved Beer's Law for intensity and set the collision probability equal to the ratio of attenuated beam intensity to the initial beam intensity. For a particle traveling distance *l* and encountering *N* atmospheric species with spatially varying densities, the scattering probability:

$$P(l,U) = \exp\left[-\sum_{i}^{N}\int_{0}^{l}\sigma_i(U(l'))n_i(l')dl'\right] \tag{2.8}$$

where $\sigma_i(U(l'))$ is the cross-section presented to a proton with energy $U(l')$, and $n_i(l')$ is the number density of the ith atmospheric neutral species encountered by the proton after traveling distance l' between 0 and l. By choosing a random probability for the left hand side of the equation, the equation can determine the distance *l* a particle travels before colliding, which is effectively a weighted random number.

Because atmospheric densities and cross-sections for each species may vary along a particle's path (i.e. along a curving path in magnetic field), this equation cannot be directly inverted to find distance *l* for a random collision probability *P*. Instead ASPEN implicitly solves for distance *l* between collisions by selecting a random number between 0 and 1 and incrementally moving the particle by a step length until the calculated probability of scatter exceeds the random probability on the left hand side. Per the prior section discussion, the step length can be fixed or variable. If the step length is variable and used to model collisions, the local mean free path $1/\sum_i n_i\sigma_i$ can also be used to constrain the step length. For example, a simulation that includes both collisions and test particle tracing can choose a variable step length as the shortest distance between 10% of the local mean free path, 5% of the local gyroradius, 10% of the gradient scale of the magnetic field, and a predefined maximum step length.

Sometimes the fixed step length or local mean free path is insufficient in estimating the distance before colliding. If the step length is too long, the particle will possibly overstep multiple collisions and penetrate deeper in the atmosphere than it physically should have, which can lead to energy deposition at unrealistically low altitudes. For this reason, ASPEN uses an adaptive step length. If the cumulative collision likelihood increases too rapidly (e.g. over 20% in a single step), ASPEN reduces the step length by half and tries the step again. Figure 2.3 shows a comparison of effective collision probability distributions and energy deposition altitude profiles determined using multiple fixed step lengths and the adaptive step length assuming an initial step length of 1 km. If no adaptive step is used, the cumulative probability distribution becomes biased and is no longer uniformly random, which leads to particles improperly colliding and depositing their energy at lower altitudes.

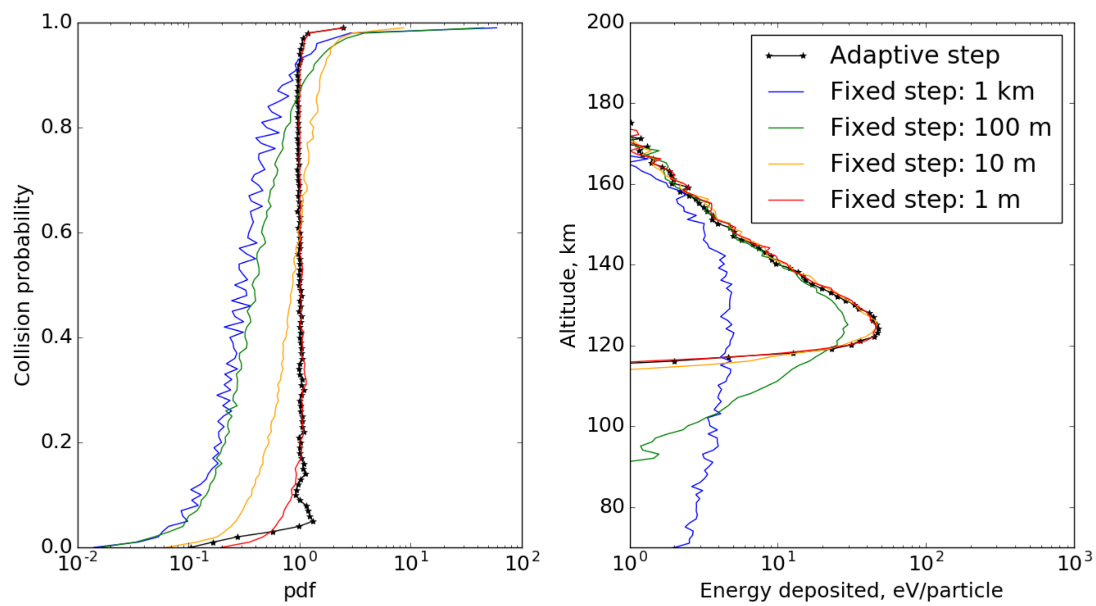

Figure 2.3: The probability distribution function of effective collision likelihoods and energy deposition altitude profile for multiple fixed step lengths and the adaptive algorithm.

When a collision occurs, the individual collision probability with each atmospheric species is determined and used to construct a probability distribution function. The species impacted is determined by comparing a new random number to the probability distribution, which is weighted in favor of the species with the highest likelihood to have been impacted.

Provided the name of the impacting particle and the target atom, the relative cross-sections that describe the collisional processes are retrieved. These relative cross-sections are determined from a compiled set of cross-sections for each included collisional process as a function of energy, which are then normalized to predict the relative likelihood of each process as a function of energy. These relative cross-sections are compiled from many sources. Chapter 3 applied process cross-sections from Kallio & Barabash [2001] and Basu et al. [1987]. Subsequent studies using ASPEN have included more cross-sections, such as electron attachment and detachment from Nakai et al. [1987]. The process cross-sections are summed to estimate the total cross-section used in the scattering probability calculation. Figure 2.4 shows the current cross-sections in-use. For further details on the source of these cross-sections, see Appendix A.

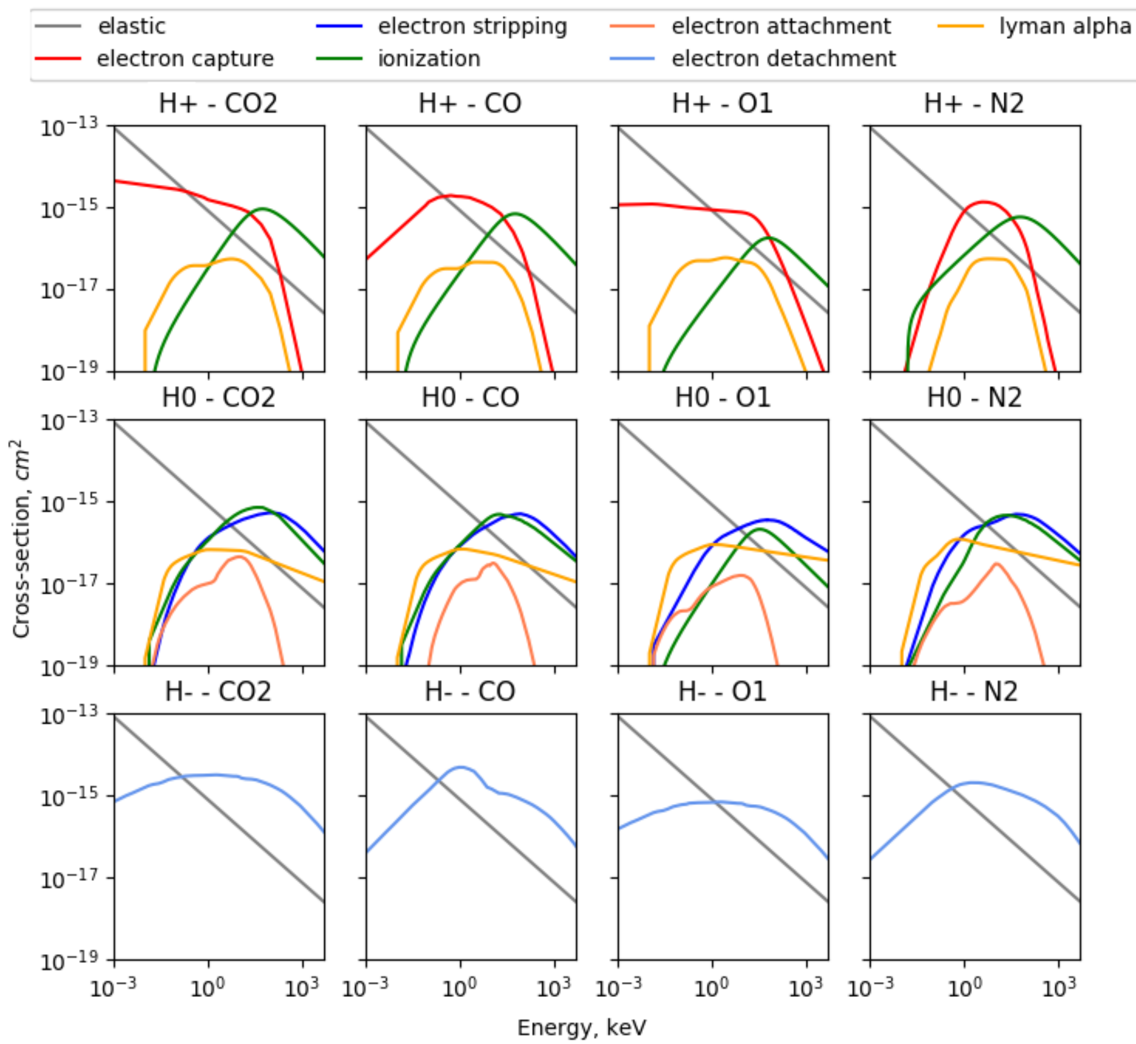

Figure 2.4: Compilation of current cross-sections used in ASPEN.

The simulation can describe six categories of collision. For projectile incident on a target atom A:

- *Elastic collisions* ((H, H^+, H^-, e^-) + A → (H, H^+, H^-, e^-) + A): The projectile strikes the target and scatters in a manner that conserves momentum and energy per classical theory.
- *Ionization* ((H, H^+, H^-, e^-) + A → (H, H^+, H^-, e^-) + A^+ + e^-): The removal of an electron from a target atom.

- *Target excitation* ((H, H^+, H^-, e^-) + A → (H, H^+, H^-, e^-) + A^*): A particle excites a band in a target species. This can co-occur with ionization (e.g. UVD emission from ionized carbon dioxide).
- *Electron capture* (H^+ + A → H + A^+ or H + A → H^- + A^+): A proton or hydrogen atom gains an electron from a target species and becoming a fast hydrogen atom or hydrogen anion, respectively. Does not occur for electrons. Sometimes called charge exchange or electron attachment.
- *Electron stripping* (H + A → H^+ + A + e^- or H^- + A → H + A + e^-): A hydrogen atom or hydrogen anion losing an electron after impacting a target species, becoming a proton or hydrogen atom, respectively. For a hydrogen atom, this can be considered ionization of the projectile. Does not occur for electrons. Sometimes also called charge exchange.
- *Projectile excitation* ((H or H^+) + A → H^* + A): A hydrogen atom is excited upon impact on a target species. Alternatively, a proton charge-exchanges to become a hydrogen atom and is subsequently excited in the same interaction. This is a source of Lyman alpha emission ("proton aurora") as well as H-alpha and H-beta emission. Does not occur for electrons.

Each of these processes can cause the projectile to lose energy and scatter. Although energy lost in elastic collisions is sometimes ignored since it is small for sufficiently low energies (e.g. Kallio and Barabash [2001]), ASPEN tracks the energy loss for use in estimating heating rates. Elastic scattering is predicted using the distribution presented in Kallio and Barabash [2001] (based on data from Noel and Prölss [1993]) and used to estimate the energy loss via the conservation of energy and momentum equations for a two-body collision.

Energy loss in inelastic processes is often discrete and can depend on the interaction between projectile and target atom or molecule. For electron capture, the energy defect is fixed and can be calculated by subtracting the ionization energy of a target species from the ionization energy of hydrogen. The energy defect can be zero for a resonant process (e.g. H), low for a near-resonant process (e.g. 0.018 eV for O), or high for a non-resonant process (e.g. ~2 eV for N_2). In an excitation, the energy lost is the threshold excitation energy of the impacted neutral.

For processes that eject an electron such as electron stripping and ionization, the energy lost is the sum of the ejected (secondary) energy and the ionization threshold to remove the electron from the projectile (stripping) or target (ionization). The ejected secondary electron energy depends on projectile energy. There are two approaches to predict secondary electron energies. In Basu et al. [1993] and Kallio & Barabash [2001], ionizations and electron stripping collisions produce a secondary electron with a fixed energy depending on the primary energy (e.g. a 10 keV proton impacting N_2 in a charge-stripping collision produces a 6.4 eV electron). The fixed energy approach uses an approximate formula to predict secondary electron energy [Basu et al. 1993]. Alternatively, secondary electron production can be modeled using differential cross-sections as in electron precipitation codes, e.g. Lillis et al. [2009], allowing for the production of a range of secondary energies for a given projectile energy using random numbers. The random energy approach uses proton-impact ionization double differential cross-sections with CO_2, O_2, O and N_2 from Rudd et al [1985]. Unfortunately, there are no double differential cross-sections for electron production in electron stripping collisions. ASPEN uses a fixed secondary approach for electron stripping collisions and supports both fixed and double differential secondary production for ionization collisions. The approaches will be compared in Chapter 3.

Following a collision, the particle's velocity is recalculated to account for lost energy and a new scattering direction before resuming tracing. The particle identity can also change, as the collision can change the state of the proton to a neutral hydrogen atom (charge exchange) and back (electron stripping). If the particle becomes a neutral hydrogen atom, the particle travels in a straight line unaffected by electromagnetic fields.

2.3. Model inputs

ASPEN may use many different data sources to describe the ambient magnetic fields and atmospheric densities. Fixed values can also be supplied for debugging purposes. Densities are required for modeling collisions, but optional for test particle tracing. Likewise, magnetic fields are required for test particle modeling, but optional for modeling collisions. If both are used, they should correspond to the same solar wind condition and orientation of Mars. Electric fields may also be included, although they are not expected to significantly influence results due to the high energy of the simulated particles.

In this thesis, 1-D altitude-varying density profiles from MT-GCM (Mars Thermosphere Global Circulation Model) are used. While M-GITM, which is 3-D, is integrated into the simulation and is also available, MT-GCM density profiles are simpler to analyze and are available for multiple solar conditions (Figure 2.5).

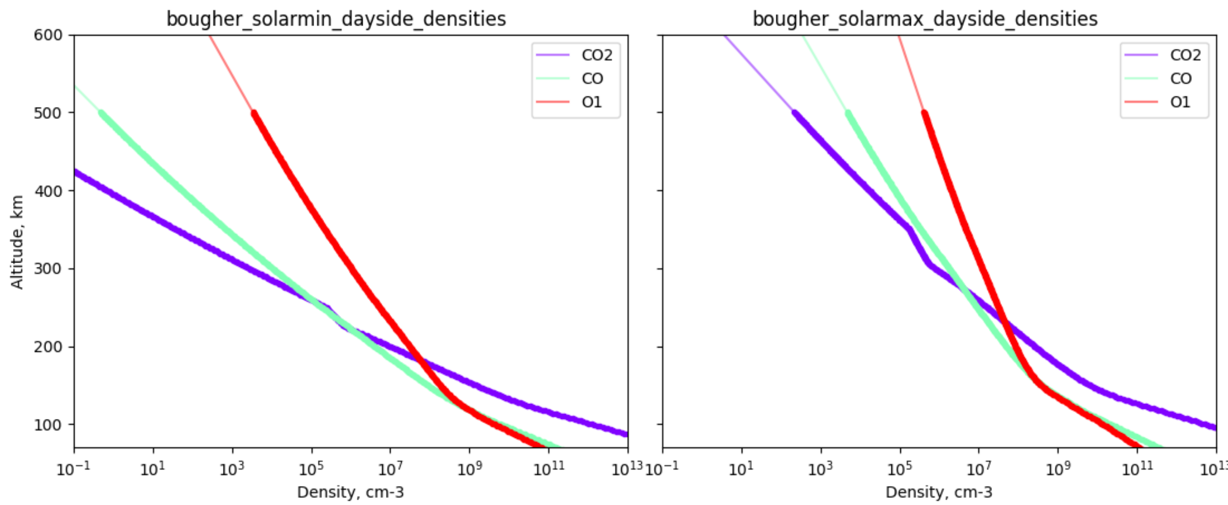

Figure 2.5: Altitude profiles of densities from MT-GCM for the dayside of Mars during solar minimum (left) and maximum (right).

The prescribed magnetic and electric fields are generated by the MF-MHD model described in Najib et al. [2011] and Dong et al. [2014]. The MF-MHD model is an evolution of an earlier single-fluid MHD (also called MS-MHD for "Multiple ion Species") [Ma et al. 2004]. Instead of approximating all ions with a single momentum and energy equation while retaining a continuity equation for each ion species, a multifluid approach solves continuity, momentum, and energy equations for each ion species. Like MS-MHD, MF-MHD uses the BATS-R-US (Block Adaptive-Tree Solar wind Roe-type Upwind Scheme) code to solve the MHD equations on a 3-D spherical grid. MF-MHD also includes the crustal fields from Cain et al. [2003]. In Dong et al. [2014], the model was coupled with a 3-D MT-GCM to include the influence of seasons and solar cycle from the neutral atmosphere on the Mars plasma environment. Figure 2.6 shows an example of the magnetic fields produced by MF-MHD.

Outputs from the MF-MHD model are determined under solar minimum and autumnal equinox conditions. While SEP events are often associated with disturbed solar wind conditions, all described modeling studies of precipitation assume nominal solar wind conditions. This makes the predictions applicable to a subset of energetic particle events where energetic particles are not accompanied by disturbed solar wind conditions and gives a necessary baseline for further comparison. The interplanetary magnetic field is assumed to be a “Parker spiral”, with a magnitude of 3 nT and cone angle of 56°. Crustal fields are assumed to be located on the dayside at noon, with the strongest arcades facing the sun.

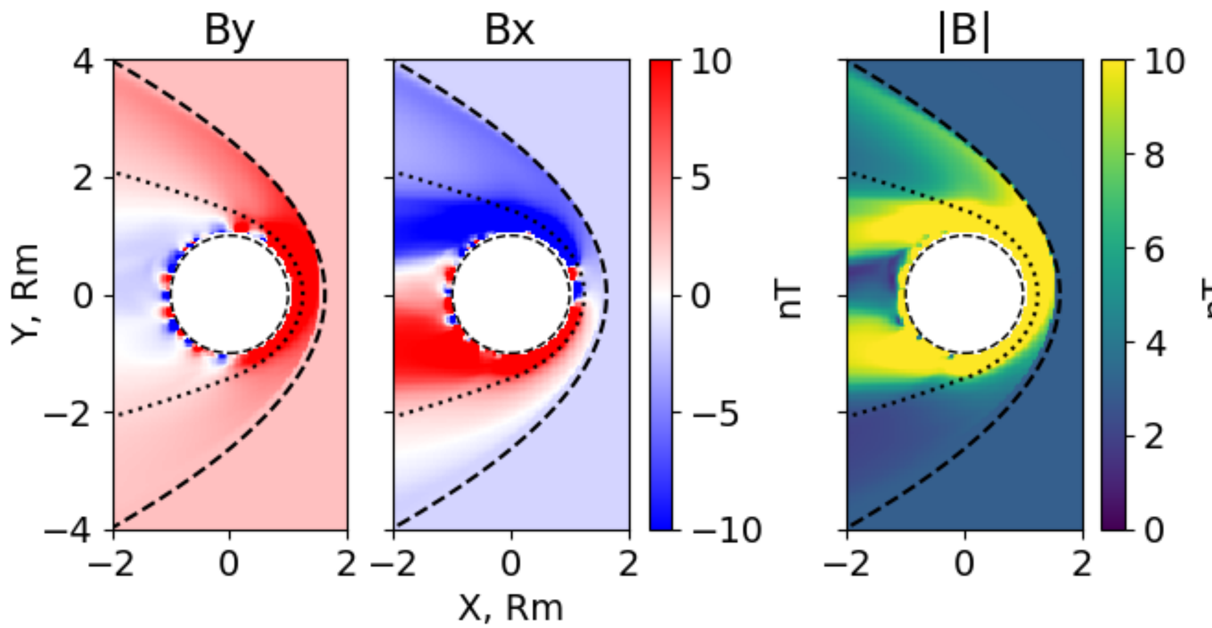

Figure 2.6: Magnetic fields in the equatorial (Z = 0) plane as predicted by MF-MHD for an away sector “Parker spiral” IMF (By > 0) with crustal fields aligned towards the sun.

2.4. Inter-model validation

Because each procedure in the simulation code was written de novo, ASPEN was systematically tested to ensure the model provides reasonable results. The test particle module was initially qualified by simulating a charged particle in a uniform magnetic field and verifying that the gyroradius stayed fixed over many time steps. Subsequent collisionless studies repeatedly checked and confirmed that the model conserved energy in the absence of electric fields.

The collisional physics module is more difficult to verify. Variability in cross-sections, secondary energy distributions, and scattering angle approximations can lead to different results for the same problem. Still, three inter-model comparisons were done to sufficiently validate the code. In this section, we will describe comparisons of ASPEN predictions to prior model studies for stopping altitude, energy partitioning, and neutral heating rates. Electromagnetic fields were disabled for each comparison.

2.4.1. Stopping altitude comparison

Particles deposit more energy at lower altitudes because of increasing atmospheric densities. The maximum energy deposited is limited by the projectile's energy, causing particles to be thermalized or "stopped" at a specific altitude as a function of energy. ASPEN-predicted stopping altitudes were determined by calculating the average altitude of particles that fall below the model energy threshold (10 eV). For comparison, CSDA stopping altitudes were calculated based on Henriksen [1979]. Assuming an atmosphere in hydrostatic equilibrium, the hydrostatic pressure is balanced with an opposing pressure from atmospheric collisions, $P(z) = P_0 e^{-z/H} = R(E)g$ for stopping altitude z, stopping range $R(E)$, gravitational constant g, scale height H, and surface pressure P_0. This equation is solved for stopping altitude assuming an isothermal carbon dioxide atmosphere with a scale height of 11.1 km, applying stopping ranges in carbon dioxide from proton stopping range tables provided by the National Institute of Standards and Technology [Berger et al. 2005].

Figure 2.7 shows stopping altitudes from ASPEN and the simplified CSDA. The CSDA predicts higher stopping altitudes than ASPEN for protons with energies less than 2 MeV and electrons with energies less than 20 keV. Above those energy thresholds, the CSDA predicts deeper penetration into the atmosphere than ASPEN. This discrepancy is partially explained by differing atmospheric densities, as the hydrostatic atmosphere assumed for the CSDA has higher densities than MT-GCM prediction used in ASPEN. Particles will stop at higher altitudes in a denser atmosphere. However, there is an energy threshold where ASPEN predicts that particles stop at higher altitudes than the CSDA predicts. This is likely because the simplified CSDA does not account for backscatter and the model does. Without a backscattering term, the CSDA will predict lower stopping altitudes.

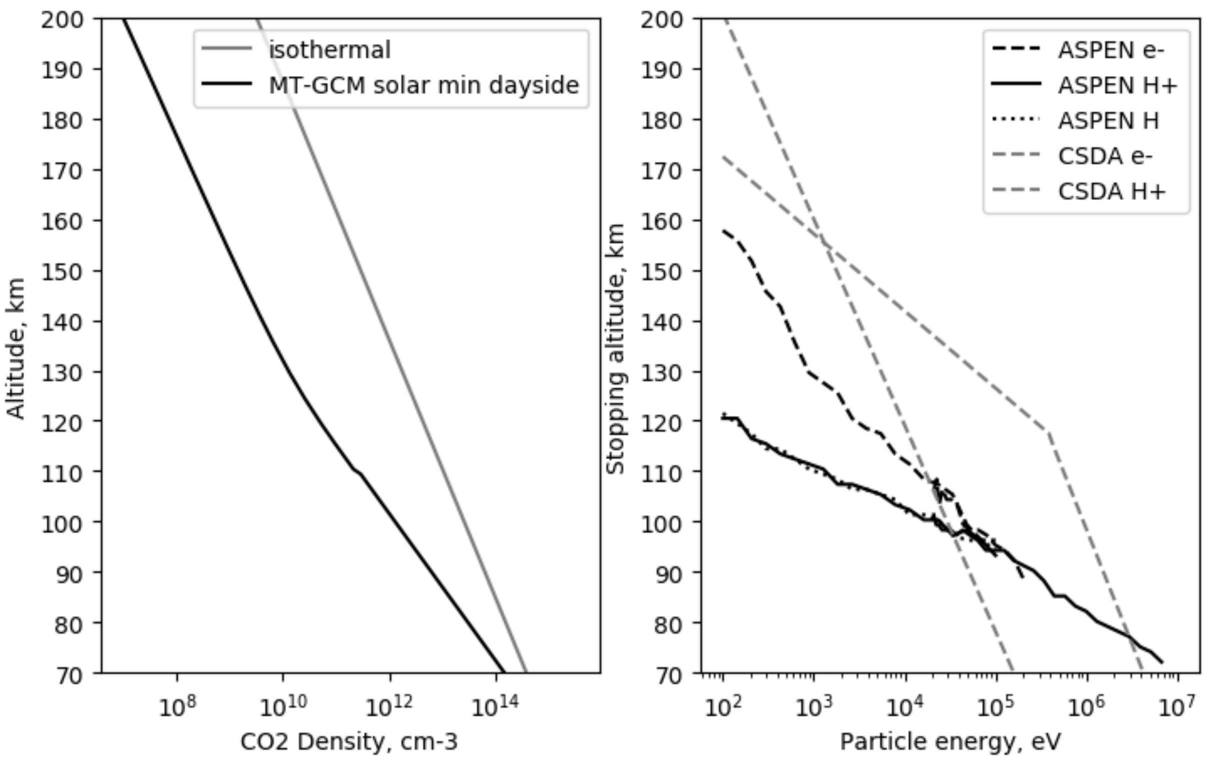

Figure 2.7: Atmospheric carbon dioxide densities (left) and stopping altitudes (right) as predicted from ASPEN using an MT-GCM profile and the CSDA using an isothermal hydrostatic atmosphere for electrons, protons, and hydrogen atoms.

2.4.2. Collisional physics comparison

The partitioning of energy deposition was compared to reported results from two different models of light ion energy deposition in the Martian atmosphere: the Stopping and Range of Ions in Matter model (hereafter called "SRIM") [Leblanc et al., 2002] and a model of fast neutral hydrogen atoms (hereafter called "K&B") [Kallio and Barabash, 2001]. These predictions were previously compared in Leblanc et al. [2002] for a test case of incident 800 eV neutral hydrogen atoms. SRIM predicted 16% of the energy was deposited into neutral heating, compared to 14% in K&B. ASPEN predicts 13% of energy is deposited into heating, in close agreement with the prior two results. ASPEN also found 32% of the atoms were backscattered, which settles between SRIM's prediction of 10% and K&B's estimate of 58%. We exclusively compared ASPEN and K&B predictions to validate energy deposition by ionization and excitation because SRIM does not distinguish inelastic processes. ASPEN predicted 26% of energy is deposited into ionization, agreeing with the 27% estimated from K&B. However, the energy deposited into excitation processes differs, as ASPEN predicted only 6% excitation unlike the 30% in K&B. This was likely because ASPEN lacked cross-sections for Lyman-alpha emission at the time these comparisons were made in Jolitz et al. [2017].

2.4.3. Ionization rate comparison

In Leblanc et al. [2002], SRIM was used to estimate neutral heating due to SEPs. The heating rate was estimated by multiplying atmospheric densities in a thick slab by both SEP proton fluxes entering the exobase and energy deposited by protons in each slab. Using an atomic-equivalent atmosphere model, they approximated all atmospheric atoms as monatomic oxygen and determined the equivalent atmospheric density. Proton energy deposition was then determined using SRIM predictions of proton energy deposition in a column of monatomic oxygen.

Despite how ASPEN's operating range is limited to below 5 MeV due to lacking nuclear processes, extrapolating our non-relativistic cross-sections to 100 MeV enables ASPEN to estimate a rate that can be compared to SRIM. Using the same SEP proton fluxes at fourteen energies between 1 keV and 1 MeV used in Leblanc et al. [2002], we calculated and compared heating rates using both MT-GCM solar minimum dayside densities (plotted in red) and the same atomic-equivalent atmosphere densities used in Leblanc et al. [2002] (plotted in blue) (Fig. 2.8).

We also show heating rates using atomic-equivalent atmosphere densities integrated over the operating range of ASPEN (plotted in green).

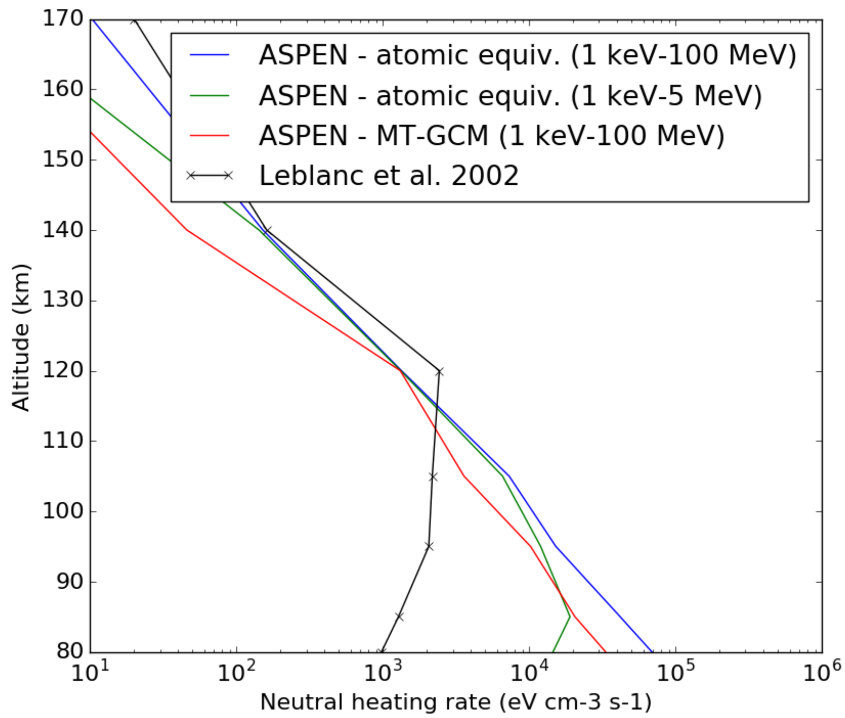

Figure 2.8: Comparison of neutral heating rates predicted by ASPEN and the SRIM results from Leblanc et al. [2002].

ASPEN predicts up to two orders of magnitude more heating below 115 km and as low as two orders of magnitude less heating above 115 km. The missing relativistic processes cannot account for this, as we see the same trend for heating rates calculated using ASPEN operating range energies above 85 km. The effect is caused by particles in ASPEN depositing energy at lower altitudes than SRIM does. While Leblanc et al. [2002] predicts a heating peak at 120 km caused by particles with energy between 0.5 and 10 keV, neither ASPEN prediction shows a peak. At 120 km, ASPEN predicts 20-500 keV proton fluxes deposit as much energy as 10 keV proton fluxes. These discrepancies can be owed to differences in cross-sections, as our result is consistent with our cross-section database. For example, using the ratio of the elastic cross-section to the total cross-section, the approximate probability of a 5 MeV proton elastically colliding with O is 4%. Since 5 MeV particles can have over twenty thousand collisions before thermalizing, up to a thousand collisions can be elastic and heat the atmosphere. That is roughly the same number of elastic collisions that a 2 keV proton would have, as 2 keV protons can have 1,500 collisions and a 70% chance of elastically scattering. However, the energy imparted by an elastic collision is proportional to the particle's incident energy. Thus, protons should impart energy to heating in amounts proportional to their energy, causing higher energy protons to heat the atmosphere more than low energy protons and preventing the existence of a visible heating peak between 80 and 170 km.

We can also compare the fraction of energy imparted by heating to all altitudes between 80 and 170 km to the total energy imparted by the SEPs with energies between 1 keV and 100 MeV. ASPEN predicts 22% of the SEP energy flux is imparted to heating for MT-GCM densities. Using the atomic-equivalent atmosphere increases this heating efficiency to 31%, which is consistent with the heating efficiency of atomic oxygen. However, SRIM predicts only 2% of the input SEP energy is imparted to heating in this altitude range despite how SRIM predicts a heating efficiency of 16%. Because the energy can't be imparted to other collisional processes, SRIM either underestimates heating above 80 km or predicts more heating energy is imparted below 80 km.

2.5. Non-SEP applications

Since the model was first published in 2017, the ASPEN simulation has been applied to other topics not covered by this thesis. Here we will make a brief summary of two applications, a comparison of proton aurora emission rates and hydrogen precipitation.

ASPEN was applied in a model challenge that compared predicted Lyman alpha emission due to hydrogen precipitation, which is also called "proton aurora". Figure 2.9 shows the preliminary comparison from Hughes [2021]. For the most part, ASPEN was found to be in close agreement with predictions made using the model from Kallio and Barabash [2001], which is also a 3-D Monte Carlo model. ASPEN-predicted emission exceeded the emission predicted by both 1-D kinetic Boltzmann equation solvers, Aeroplanets and the model by Shematovich et al. [2011]. All models predicted an emission peak at a lower altitude than the data. Although this difference was mitigated by background subtraction, a 5-10 km discrepancy remained. This suggests that some aspect of collisional physics is unaccounted for across all models. The cross-sections for Lyman alpha emission are not known for energies below 1 keV in carbon dioxide. If the cross-section for Lyman alpha emission was higher than what the models assume at lower energies, the altitude of emission would be closer to the measured peak emission altitude.

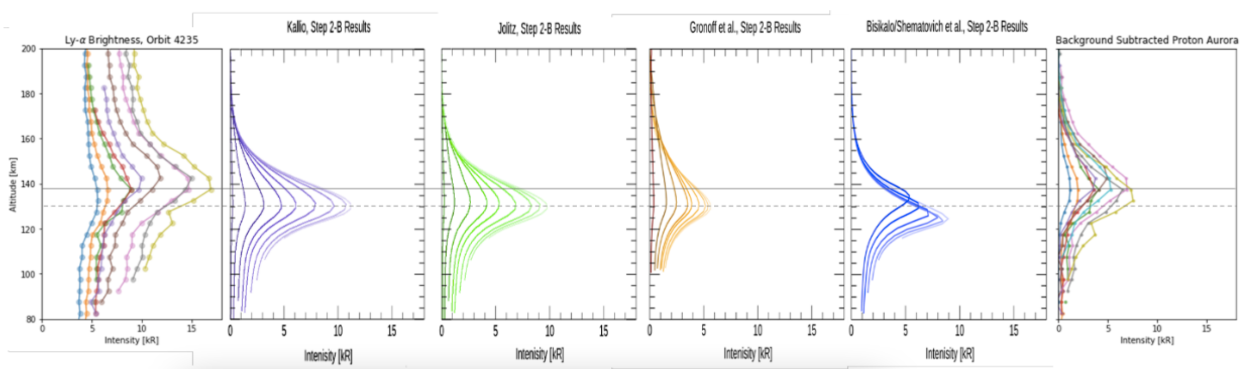

Figure 2.9: Comparison of Lyman alpha emission rates from Hughes [2021]: from left to right, observations by MAVEN IUVS, model predictions from Kallio and Barbash [2001], ASPEN predictions, model predictions from Aeroplanets, model predictions from Shematovich et al. [2011], and background-subtracted data.

ASPEN has also been applied to predict the spectra of hydrogen atoms that charge exchange to become protons in the upper atmosphere. These “penetrating” or “ghost” protons can be measured by SWIA at atmospheric altitudes (~200 km) [Halekas et al. 2015]. In order to study this population, we can estimate the precipitating hydrogen from the solar wind ion spectra, since ~3% solar wind protons charge exchange with the hydrogen corona to become hydrogen. Then the spectra can be combined with ASPEN predictions of precipitation to determine the energy spectra associated with reconverting protons. Figure 2.10 shows the ASPEN-predicted total energy flux of protons produced in the upper atmosphere using the SWIA solar wind spectra recorded at spacecraft apoapse (2015 March 4 13:55) alongside the SWIA observed fluxes on the inbound and outbound passes on orbit 827. While this shows approximate agreement, there is ongoing work to validate ASPEN predictions with SWIA observations as a function of viewing geometry.

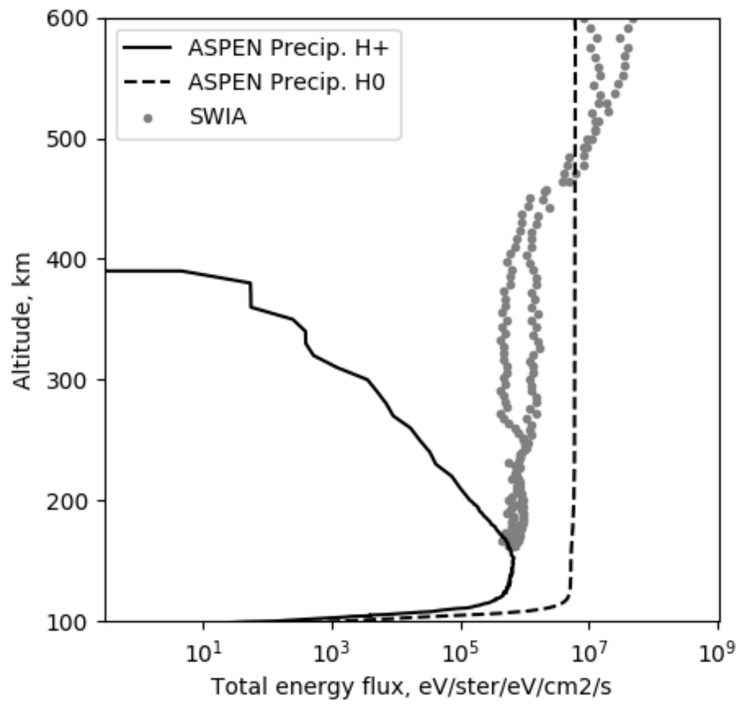

Figure 2.10: Total energy flux of ions as measured by SWIA and predicted by ASPEN, assuming ~3% of solar wind protons convert to hydrogen atoms in the corona.

2.6. Conclusions

In this chapter, the context and implementation of a 3-D Monte Carlo test particle simulation was discussed. In ASPEN, the Lorentz force equation for charged particles is iteratively solved at the same time as the collision probability. When a collision occurs as determined by a compilation of cross-sections for multiple processes, the energy loss is calculated and logged. Step lengths can be fixed or locally determined as the minimum of magnetic and/or collisional scale lengths. In addition, adaptive step length for collisional modeling is essential for preventing modeled particles reaching unphysically low altitudes and undercounting collisions. The simulation continues to trace the particle until it exits the simulation boundaries or falls below an energy threshold. Depending on the application, the model may be run in a collisionless test particle mode or collisional in the absence of magnetic fields.

ASPEN was extensively tested and validated for multiple applications. The test particle module was validated by confirming energy conservation in the absence of electric fields. ASPEN was compared to prior collisional model predictions of stopping altitude, energy partitioning into different processes, and heating rate. An apparent discrepancy in stopping altitudes with a simplified CSDA is explained by different atmospheric densities and the lack of backscattering in the CSDA. The energy partitioning compared favorably for ionization and heating to two prior simulations, although the excitation energy deposition estimate was different. This was likely due to the absence of Lyman-alpha emission cross-sections. Finally, ASPEN predicted significantly greater heating than the model presented in Leblanc et al. [2002] at lower altitudes.

ASPEN has already been involved in non-SEP modeling projects, such as proton aurora modeling and predicting hydrogen precipitation. Preliminary results from the proton aurora model challenge [Hughes 2021] show that ASPEN compares favorably with other 3-D Monte Carlo models and predicts higher altitudes and magnitudes of emission than models based on solving kinetic Boltzmann equations. However, ASPEN, like all other models, falls short of predicting the peak emission altitude. This may be due to an underestimate of the proton and hydrogen emission cross-sections in carbon dioxide, as they are not constrained below 1 keV.

We have also described some preliminary results from modeling “ghost” protons measured by MAVEN at low altitudes. The ASPEN model has demonstrated broad applicability and could be a community-modeling tool.

Chapter 3

SEP proton energy deposition in crustal fields

Sections of this chapter were originally published as “A Monte Carlo model of crustal field influences on solar energetic particle precipitation into the Martian atmosphere” [Jolitz et al. 2017]. While the detailed description of the ASPEN model from that paper was adapted in Chapter 2, the material in this chapter focuses on the science predictions from the model.

3.1. Introduction

SEPs that precipitate into planetary atmospheres can have a substantial effect on ionospheric and neutral chemistry. In the terrestrial atmosphere, precipitating SEPs are known to cause heating, ionospheric outflow and increased atmospheric ionization [Moore et al. 1999, Usoskin et al. 2009]. This in turn leads to enhanced electrical conductivity in the atmosphere, changes in lower atmosphere electrochemistry such as increased ozone concentrations via hydroxyl ion formation, and formation of aerosol particles between altitudes of 10 and 25 km [Kokorowski et al. 2006, Damiani et al. 2010, Mironova and Usoskin 2014]. However, all these effects are typically confined to the poles, as Earth's strong global magnetic field shields equatorial latitudes from energetic particles [Mironova et al. 2015].

Mars, on the other hand, lacks a strong intrinsic magnetic field. Charged particles can precipitate into the atmosphere if they are accelerated past the compressed magnetic fields of the magnetosheath and bow shock formed by solar wind plasma draping over the dayside ionosphere [Acuña et al. 2001]. Unlike solar wind particles, SEPs are mostly unaffected by this barrier. Phobos 2 measurements showed energetic particle fluxes recorded during a SEP event crossed the region without substantial change [McKenna-Lawlor et al. 1998]. Subsequent modeling found the barrier does not attenuate SEP protons with energies greater than 50 keV [Leblanc et al. 2002].

There are two main obstacles to SEP entry into the atmosphere. The first is physical obstruction by the planet or "shadowing", which most strongly affects extremely energetic (> 1 MeV) SEPs that are not significantly influenced by magnetic fields. Measurements from Mars Odyssey found that a combination of planetary shadowing, anisotropy of SEPs, and detector field of view caused orbital modulations of 20-200 MeV SEPs [Luhmann et al. 2007]. The second obstacle is the localized crustal magnetic anomalies in the Southern hemisphere that present strong magnetic fields capable of reflecting incident SEPs [Acuña et al. 2001]. Prior modeling studies on crustal anomaly influences on SEP fluxes suggest the strongest field anomalies can attenuate SEP fluxes by over 50% at altitudes of 200 km [Leblanc et al. 2002].

Compared to Earth, information on the atmospheric effects caused by SEP precipitation is relatively limited. Up until the MAVEN spacecraft's arrival at Mars, evidence of SEP precipitation was inferred from indirect observations during SEP events. SEP fluxes were determined by using background count rates in plasma analyzers as proxies for 20-100 MeV protons [Delory et al. 2012, Futaana et al. 2008]. Radar ground reflections observed by the MARSIS instrument on Mars Express disappeared during SEP events, suggesting that SEP precipitation increased ionization [Espley et al. 2007, Morgan et al. 2008]. The Electron Reflectometer (ER) on Mars Global Surveyor measured increased upward fluxes of superthermal electrons linked to SEP events [Lillis et al. 2012]. However, further analysis of radio occultation data during periods of high SEP activity only found small increases of electron density below altitudes of 100 km in four out of six SEP events and no increase in electron densities between altitudes of 100 and 200 km in all six events [Ulusen et al. 2012]. SEP events were linked to ionization and electron production but the exact mechanism remained unknown.

In 2014, MAVEN arrived at Mars carrying a suite of instruments designed to study the upper atmosphere and plasma environment, including a detector called Solar Energetic Particle, or SEP, to directly monitor SEPs [Larson et al. 2015]. The SEP instrument has been used to further characterize the near-Mars energetic particle environment. Measurements of anisotropic high-energy (>200 keV) SEP flux attenuation have confirmed Mars Odyssey observations of planetary shadowing. SEP has also observed complex low-energy shadowing governed by local magnetic field geometry [Lillis et al. 2016]. The SEP instrument has also made measurements of SEP electrons and ions during solar flare and coronal mass ejection events [Lee et al. 2017]. Coincident measurements of SEPs and atmospheric emission have led to the discovery of SEP electron-linked diffuse aurora [Schneider et al. 2015].

SEP events are frequently coincident with changes in solar X-ray and extreme ultraviolet fluxes. Modeling studies can decouple these changes and isolate the causation of atmospheric effects like electron production and aurora.

SEP precipitation has been previously modeled using approximations. Leblanc et al. [2002] used a 1-D stopping-and-range-of-ions-in-matter (SRIM) model to calculate the total heating by SEPs in the atmosphere between altitudes of 80 and 170 km. Their model predicted SEP heating rates that were less than a tenth of heating rates due to solar ultraviolet fluxes, meaning SEP precipitation only increased atmospheric heating by ~30%. Sheel et al. [2012] used a stopping approximation that assumed all energy is deposited at a fixed altitude for a specific SEP energy. Once they predicted the total energy deposited for each trace species in the atmosphere, they determined ion densities by assuming an ion-electron pair is produced for every 35 eV deposited. They predicted that electron densities could reach 3,000 cm^{-3} at 80 km during a SEP event that was a hundred times weaker than the total flux measured during the 29 September 1989 SEP event, which would be sufficient to cause the MARSIS radar reflection disappearance. These approaches are mutually exclusive, as Sheel et al. [2012] assumes SEP energy deposition is solely imparted to ionization, and Leblanc et al. [2002] assumes SEP energy deposition is either imparted to heating or electronic excitation.

SEP transport to the surface has also been modeled to predict the surface radiation environment during an event. Leblanc et al. [2002] estimates that only protons with energies greater than 83 MeV can make it to the surface. Because only extremely energetic particles can reach the surface, surface flux models need to account for nuclear processes [Gaisser, 1990]. Planetocosmics and HZETRN (High-charge (Z) and Energy TRaNsport) are two such models [Desorgher et al. 2005, Norman et al., 2013, Gronoff et al. 2011]. Both models are in close agreement, predicting ionization rates of ~1,000-2,000 cm^{-3} s^{-1} below 60 km during the 29 September 1989 SEP event [Gronoff et al. 2015].

Existing models of SEP energy deposition do not partition the deposited energy into heating, excitation, ionization, and charge transfer on a collision-by-collision basis like the model presented in Kallio & Barabash [2001]. Others do not consider possible effects caused by proton gyromotion in crustal magnetic anomalies. In this chapter, ASPEN is applied to track transport and energy deposition of SEP protons in the Martian atmosphere. I will primarily discuss transport processes as a function of SEP proton energy, focusing on influences by crustal fields. Then I will use the ASPEN model results to predict ionization altitude profiles, maps and secondary electron spectra during a specific SEP event.

3.2. Approach

To study atmospheric effects due to precipitating SEPs near crustal field anomalies, protons with energies up to 5 MeV are simulated and allowed to scatter between the altitudes of 70 km and 500 km. ASPEN particles either "magnetically reflect" without depositing any energy, deposit their entire energy and "thermalize", or deposit a fraction of their energy before turning away and "backscattering". Only particles with energies exceeding 5 MeV may reach the lower boundary of the simulation before depositing all their energy.

When magnetic fields were included, the simulation used a RK4 method to solve the nonrelativistic Lorentz force equations. This study focused on SEPs with energies below 5 MeV since they were most likely to be affected by crustal magnetic fields. The energy threshold in ASPEN was set to 10 eV to minimize computational overhead. Given the relative cross-section of elastic collisions as a function of energy, a 10 eV proton has a 99.989% chance of imparting its energy to heat and can be assumed to thermalize with minimal impacts on simulation results. The cross-sections used in this study can be found in Appendix A. Note that this study did not account for projectile excitation, electron attachment, and electron detachment. In addition, this study used target excitation cross-sections from Basu et al. [1987], which were later removed since they were determined by rescaling electron cross-sections and were not based on any measured proton or hydrogen impact cross-section. This does not have a significant influence on the results reported in this study, as excitation was orders of magnitude rarer than the other collisional processes.

Secondary electron production models are also investigated in this chapter. There are two approaches to predict secondary electron energies. The fixed energy approach is the secondary electron energy formula that was applied in Basu et al. [1993], which is based on fitted secondary electron production data by approximating the average secondary energy as $\sqrt{IEd}/A$ where E is the proton energy, I is the ionization threshold, d is the electron-to-proton mass ratio (~1/1836), and A is a parameter set to 0.91 to best fit the data. This approximation is only supposed to be used at energies below 150 keV, as secondary electron production reduces by a factor of E^{-2}. The stripping secondary electron energy is estimated similarly as $Ed + b$ where E is the primary energy, d is the electron-to-proton mass ratio, and b is the mean energy in the hydrogen rest frame (~1 eV). The random energy approach instead uses proton-impact ionization double differential cross sections with CO_2, O_2, O, and N_2 from Rudd [1988] to estimate the secondary electron energy using a random number. This differential cross-section was also adapted for hydrogen-impact ionization due to the lack of existing data.

Figure 3.1 shows a comparison of these approaches for estimating the average ionization secondary electron energy produced in collisions with CO_2. Double differential cross-sections can be estimated and normalized by the total cross-section to determine the likelihood of emission of each secondary energy as a function of primary energy. The average secondary energy from the random model was estimated by selecting the electron energies where the production probability is ~50% (plotted in red). When compared to the fixed model (in black), the average secondary energy from double differential cross-sections agrees with the fixed model below ~100 keV, in agreement with Basu et al. [1993]. Above that energy, the average produced secondary energy peaks at ~10 eV, and then decreases.

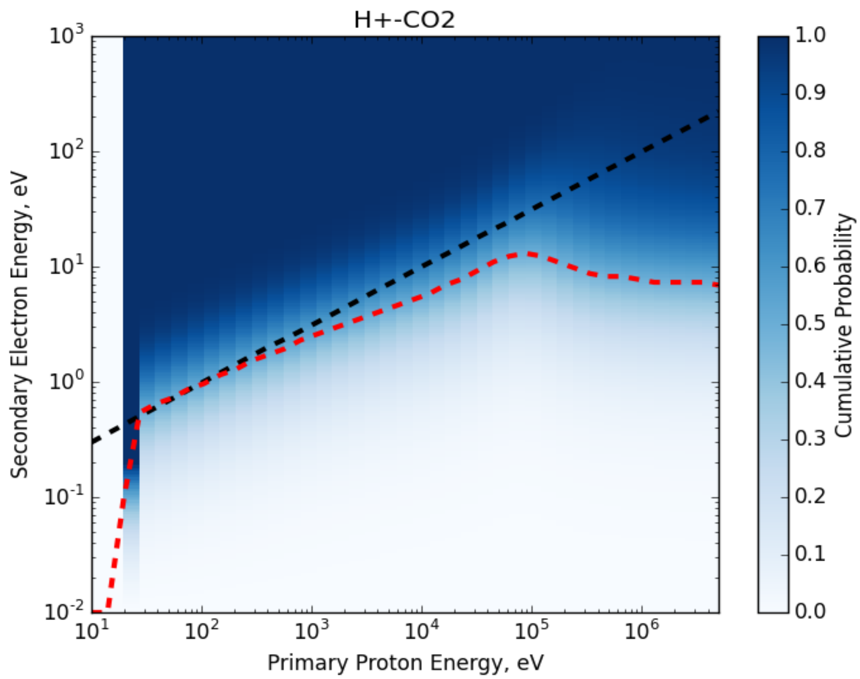

Figure 3.1: Cumulative probability of emission of a secondary electron energy as a function of energy is plotted in the blue gradient. The average secondary energy from double differential cross-sections is marked as the red dashed line, while the fixed model secondary electron energy is marked as the black dashed line.

This chapter assumes a 1-D altitude profile from MT-GCM for dayside Mars during solar minimum for the four most common species, CO_2, O, N_2, and CO [Bougher et al. 1999, Bougher et al. 2006]. For test particle tracing, MF-MHD magnetic and electric fields were determined for solar minimum conditions. While the MF-MHD simulation domain was set to a nonuniform spherical grid structure with a radial resolution varying from 5 km near the inner boundary to 1000 km near the outer boundary, particles were only traced below an altitude of 600 km.

In this study, large numbers of particles with the same energy were simulated to study energy-dependent backscattering and energy deposition. Then a representative event spectrum was interpolated to determine the flux of each simulated energy channel, and the energy-dependent frequency of ionizations was integrated to estimate an event-specific ionization rate. This chapter focuses on SEP-induced atmospheric ionization either in the absence of strong magnetic fields or nearby a specific crustal magnetic anomaly, including altitude profiles, geographical maps, and secondary electron spectra. Simulations are also run for both fixed and random secondary electron energy models.

In the next two sections, ASPEN results are computed for multiple simulation runs. In all runs, a thousand protons with energies between 2 keV and 5 MeV are released from an altitude of 500 km traveling directly towards the dayside atmosphere of Mars. In the "crustal field anomaly" run, particles are released over a crustal anomaly located at 50° S and 182° E. In the "absent magnetic fields" run, particles are released from the same location while magnetic fields are set to 0 nT. In each of these runs, the secondary production model can be toggled to using the "fixed" or "random" models.

3.3. Energy-dependent proton transport and energy deposition

In this section, I study proton transport and energy deposition as a function of proton energy. First, I review backscattering for ten representative 10 keV protons. Next, rates of backscattering and thermalization as a function of energy, the presence of a crustal field, and secondary model are calculated and discussed. Predictions are also made of backscattered spectra and average energy imparted by backscattered versus thermalized protons. Finally, altitude profiles of energy deposition as a function of altitude and proton energy are shown and described for the presence and absence of magnetic fields..

3.3.1. Backscattering: Case study

Not all protons that precipitate into an atmosphere are absorbed. Backscattering can attenuate and distribute the energy-depositing particle population. There are two causes of proton backscatter: atmospheric collisions and magnetic reflection. Atmospheric collisions stochastically turn particles back upwards and away from the lower atmosphere. They are the only source of backscatter in the absence of magnetic fields. Magnetic reflection turns away protons in the upper atmosphere before they can deposit any energy. Atmospheric reflection and magnetic reflection can also act in tandem, allowing protons to deposit some energy in the atmosphere before being magnetically reflected.

Backscatter mechanisms are observable in traces of protons depositing energy (Fig. 3.2). Fig. 3.2a shows the paths of ten identical 10 keV protons depositing energy in the absence of magnetic fields. Differences between the paths are caused by stochastic scattering events predicted by ASPEN. Six protons thermalize, losing all energy in the lower atmosphere. Four protons atmospherically scatter, losing substantial energy before reflecting with 10-50% of their initial energy. Atmospheric scattering is characterized by particles escaping with less than half of their initial energy. Fig. 3.2b shows the paths of ten 10 keV protons depositing energy into the atmosphere at a crustal anomaly located at 177° E and 7° S. Six protons magnetically reflect, taking the Lorentz path (the path of the same proton moving in without atmosphere, plotted in black) and escaping with 100% of their original energy. One proton atmospherically scatters exactly as in the previous case, escaping with less than 50% of its initial energy. Three protons have a different escape mechanism that is a combination of atmospheric scattering and magnetic reflection. Each scatters from 265 km, the altitude of closest approach in the Lorentz path (hereafter called the “magnetic reflection altitude”), and escapes with over 50% of their initial energy. Increased scattering at the magnetic reflection altitude is caused by particles moving parallel to the surface at this altitude, encountering the same neutral density for tens of kilometers which rapidly increasing the collision likelihood. The traces show that this mechanism distributes energy deposition over a greater area. Two of the three traces show protons that become neutral hydrogen near the magnetic reflection altitude, causing them to travel in straight lines from the magnetic reflection altitude down to 240-250 km over 5-10° E from the launch location. These particles deposited energy along these paths before they were charge-stripped, becoming again susceptible to magnetic fields, and then escaped.

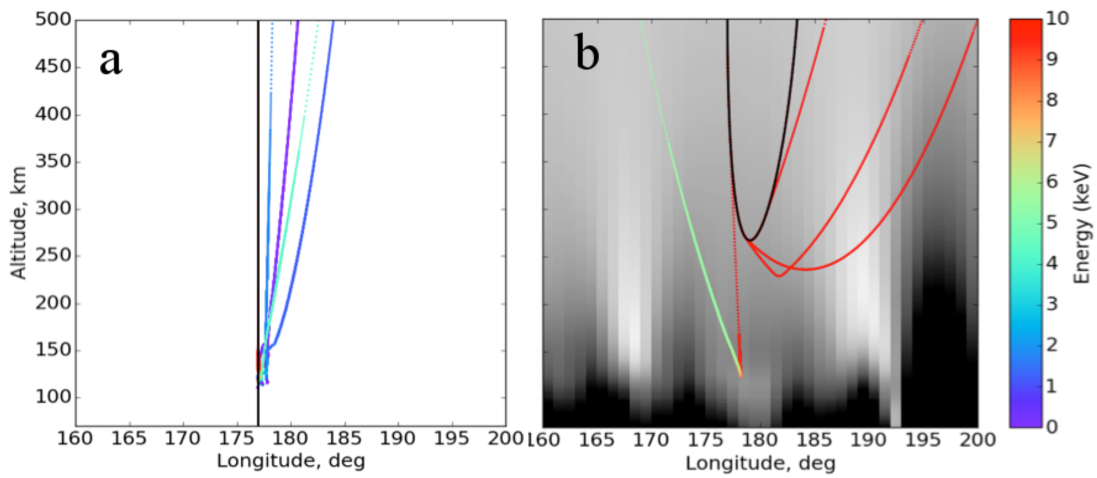

Figure 3.2: Traces of eleven 10 keV protons simulated in ASPEN entering at 177°E and 7°S injected directly (α = 0°) in a (a) purely collisional atmosphere with no magnetic fields and a (b) collisional atmosphere with magnetic and electric fields from MF-MHD. A noncollisional Lorentz path is plotted in black in both plots. Contours of the total magnetic field in the right figure are plotted in gray between 0 and 150 nT. Since the 10 traces are very similar, only ones that significantly scatter can be distinguished.

3.3.2. Energy-dependence of backscatter and thermalization

Protons with energies less than 5 MeV either thermalize or reflect, whether via magnetic forces or by atmospheric scattering. Atmospheric backscattering requires the occurrence of a non-forward scattering event, which is favored at different proton energies. Likewise, the likelihood of magnetic reflection depends on proton energy. Protons with lower energy are more susceptible to deflection by magnetic fields, meaning low-energy protons reflect higher in the atmosphere than high-energy protons. Magnetic reflection is likely also dependent on the magnetic topology of the region, but that is beyond the scope of this chapter.

The energy dependence of backscattering is shown for absent magnetic fields in Fig. 3.3. All protons deposit energy in this case. In both the random and fixed secondary models, up to 75% of protons with energies below 80 keV deposit their entire energy in the atmosphere. However, for the random secondary model, the chance of thermalizing a 1 MeV proton is only 50% and protons with energies over 1.6 MeV are more likely to backscatter than to impart all their energy to the atmosphere. This threshold energy is higher for the fixed secondary model (~6 MeV). This is likely because the higher energy secondaries produced in the fixed secondary model cause the proton to lose more energy in ionizations, leading to fewer collisions and accordingly fewer chances to backscatter than predicted by the random secondary model at the same energy.

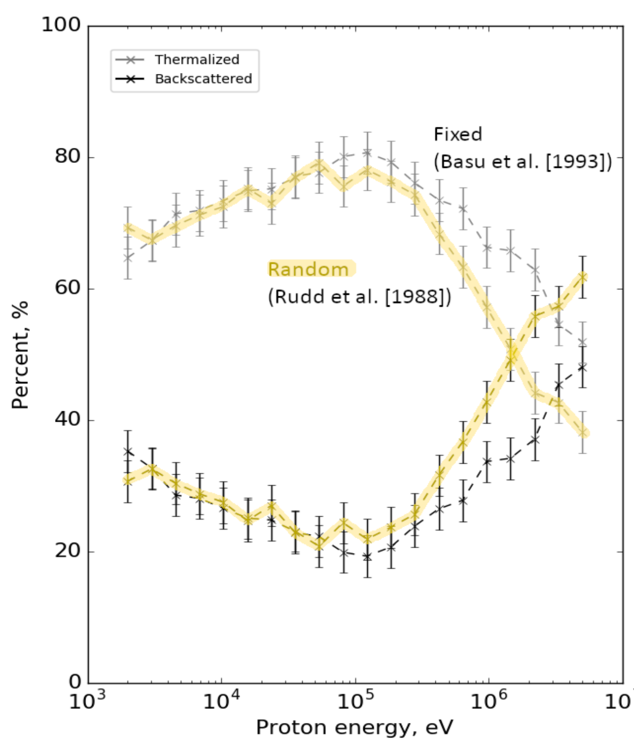

Figure 3.3: Likelihood of a proton either thermalizing (gray) or backscattering (black). The random secondary model is highlighted while the fixed secondary model is not.

The greater likelihood of higher-energy protons backscattering may seem counter-intuitive. Due to the lack of angular cross-section data for inelastic processes, a key model assumption is that particles only change trajectory in elastic collisions. Elastic collisions only occur frequently for protons with energies below 500 eV. However, particles with energies over 1 MeV have over ten thousand collisions before thermalizing. Even a 5% chance of an elastic collision would cause over five hundred elastic collisions, causing the overall likelihood of backscattering to increase for higher energies.

The energy dependence of backscattering in the presence of crustal fields is shown in Fig. 3.4, with an added category for magnetic reflection without any collisions. In the crustal field anomaly case for both secondary models, protons with energy less than 400 keV are either magnetically reflected or backscattered. Over 95% of protons with energies below 10 keV magnetically reflect without depositing any energy. The dominant proton backscattering process for energies below 119 keV is magnetic reflection without energy deposition. The dominant process becomes atmospheric scattering for protons with energies between 119 keV and 800 keV. There are more backscattered 120-800 keV protons nearby a crustal anomaly than in the absence of magnetic fields. Most protons with these energies impart energy to the atmosphere before being magnetically reflected, like the three traces presented in section 3.3.1.

The choice of secondary model does not strongly influence the reflection of protons with energies below 400 keV, suggesting that the crustal fields influence scattering below a given energy threshold that overlaps SEP energies. However, the partitioning of protons into thermalized or backscattered above 400 keV begins converging to the same values as estimated in the absent fields case for each secondary model. In the random secondary model the fraction of protons that thermalize never exceeds 50%, whereas in the fixed secondary model more protons are thermalized between 400 keV and 5 MeV.

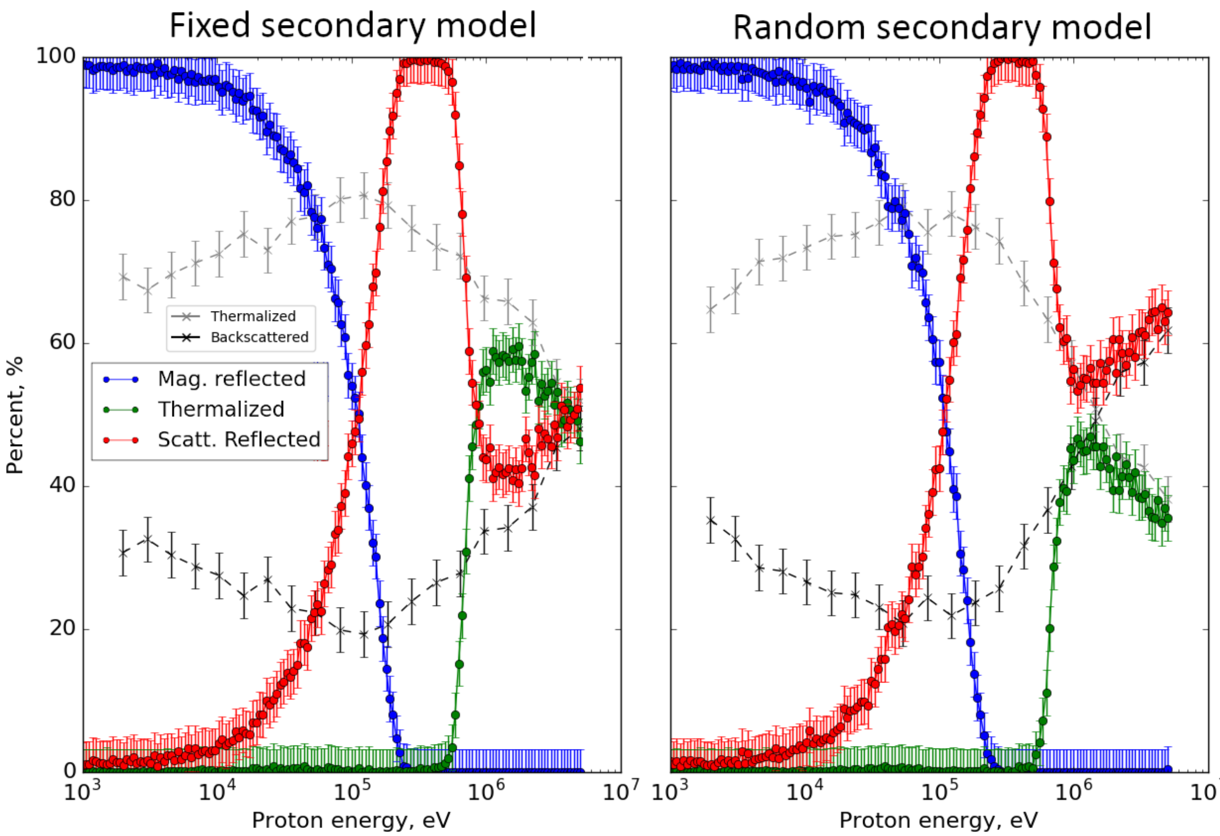

Figure 3.4: Likelihood of a proton either magnetically reflecting (blue), thermalizing (geen), or atmospherically backscattering (red) for the fixed secondary model (left) and random secondary model (right). The thermalize/backscatter fraction of particles in the absence of fields is also plotted to show how the fractions converge to the absent-field case at high energies.

Regardless of secondary model, protons with energies above 1 MeV in the representative crustal field are not as likely to atmospheric backscatter as protons with energies between 100 keV and 1 MeV. This influences the anticipated observed backscattered fluxes. Since ASPEN logs the energy of backscattering and magnetically reflected fluxes as well as whether the backscattered particle is a proton or hydrogen atom, it is possible to estimate the backscattered spectra. The predicted backscattered model fluxes were convolved with a representative spectra observed by MAVEN SEP during the March 2015 SEP event in Figure 3.5. In the absent crustal fields, the backscattered fluxes were predicted to be an order of magnitude below the incident fluxes. In addition, there are higher backscattered fluxes of <30 keV hydrogen atoms than <30 keV protons. This trend reverses above 30 keV and ASPEN predicts that more protons would backscatter than hydrogen atoms. However, the presence of crustal fields changes the reflected fluxes. In the example crustal field studied, most of the incident protons with energies below ~400 keV will reflect, which causes the reflected spectra to be comparable to the incident spectra. There is also an escaping hydrogen flux component, but it is two orders of magnitude less than the incident flux. Interestingly, the reflected hydrogen flux component is similar in magnitude in both cases.

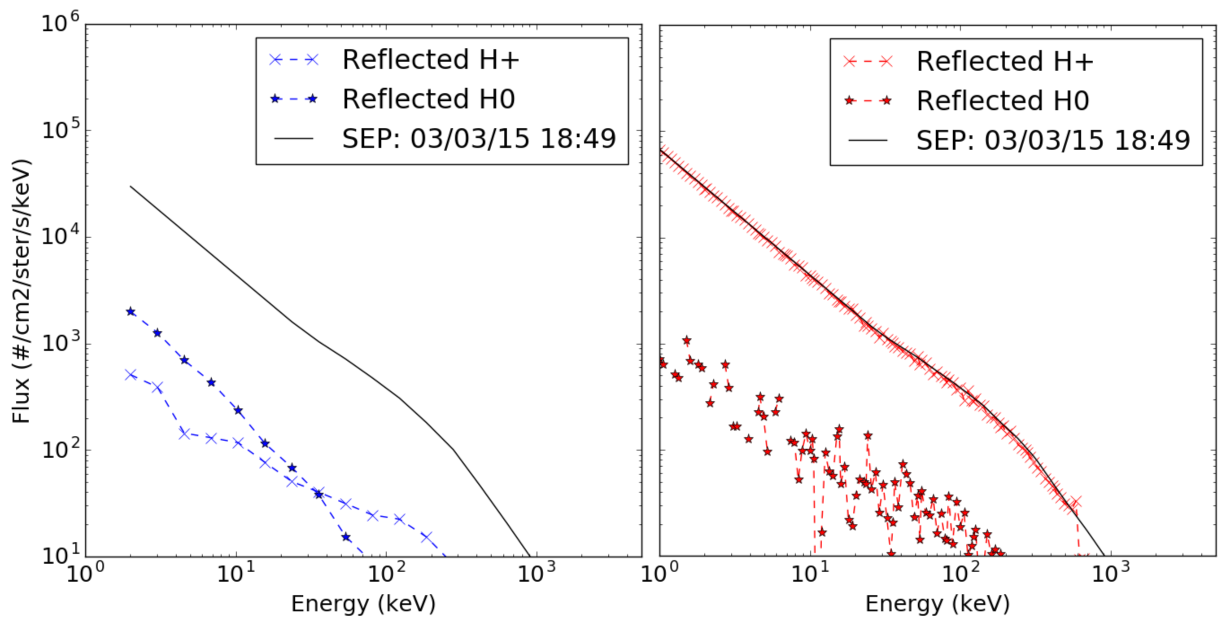

Figure 3.5: Predictions of reflected proton and hydrogen atom flux in the absence of crustal fields (left) and in the representative crustal field (right).

The total energy deposited can be separated into deposition by thermalized protons and deposition by reflected protons. Figure 3.6 shows the fraction of deposited energy that is supplied by thermalized versus reflected protons. Note that the average fraction of energy deposited decreases with energy, corresponding to increased backscatter above 400 keV.

Backscattered protons supply 10-20% of the energy deposition in the absence of magnetic fields regardless of energy. In the crustal fields, since protons below 200 keV are mostly magnetically reflected, there isn't significant energy deposition via reflection or thermalization. This will be further discussed in the next subsection. However, above 400 keV, the relative energy deposition in crustal fields approaches absent field energy deposition, depending on the secondary model used.

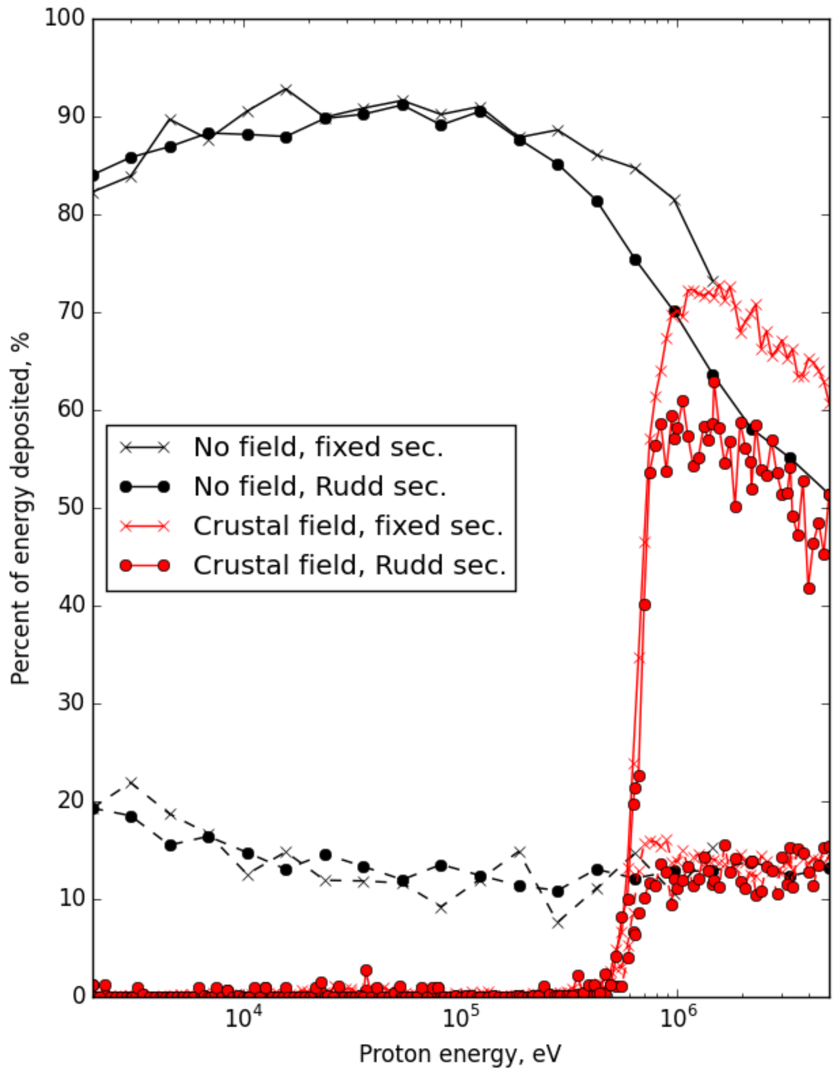

Figure 3.6: Relative energy deposition by backscattered protons (dashed) versus thermalized protons (solid) in crustal fields (red) and in the absence of fields (black) using the random secondary model (circles) or the fixed secondary model (x).

3.3.3. Energy-dependence of altitude-varying energy deposition

In this subsection, total energy deposition is aggregated regardless of mechanism, both overall and as a function of altitude, to study energy absorption as a function of proton energy and magnetic fields. In the absence of magnetic fields, protons with energies below 454 keV deposit 80-91% of their energy in the atmosphere. Energy deposition by protons with energies above 454 keV steadily declines, as 963 keV protons deposit 70% and 5 MeV protons deposit only 51% of their energy. The lowered energy deposition corresponds with increased elastic scattering.

Nearby a crustal field anomaly, protons with energies below 454 keV only deposit as much as 1% of their energy. Opposite to the absent fields case, energy deposited by protons with energies above 454 keV dramatically increases with primary energy. 1.5 MeV protons deposit approximately 60% of their energy. Percent energy deposition slowly decreases for protons with energies above 2.3 MeV, with 5 MeV protons depositing 51% of their energy. In net, protons with energies below 1 MeV deposit nearly no energy in the vicinity of a crustal anomaly, while protons with energies above 1 MeV deposit as much energy near a crustal anomaly as they would in the absence of magnetic fields.

Regardless of the presence of magnetic fields, the net energy deposition aggregated by altitude between 70 and 300 km is inversely proportional to the altitude, smoothly increasing as altitude decreases (Fig. 3.7). Higher energy protons deposit more energy at lower altitudes.

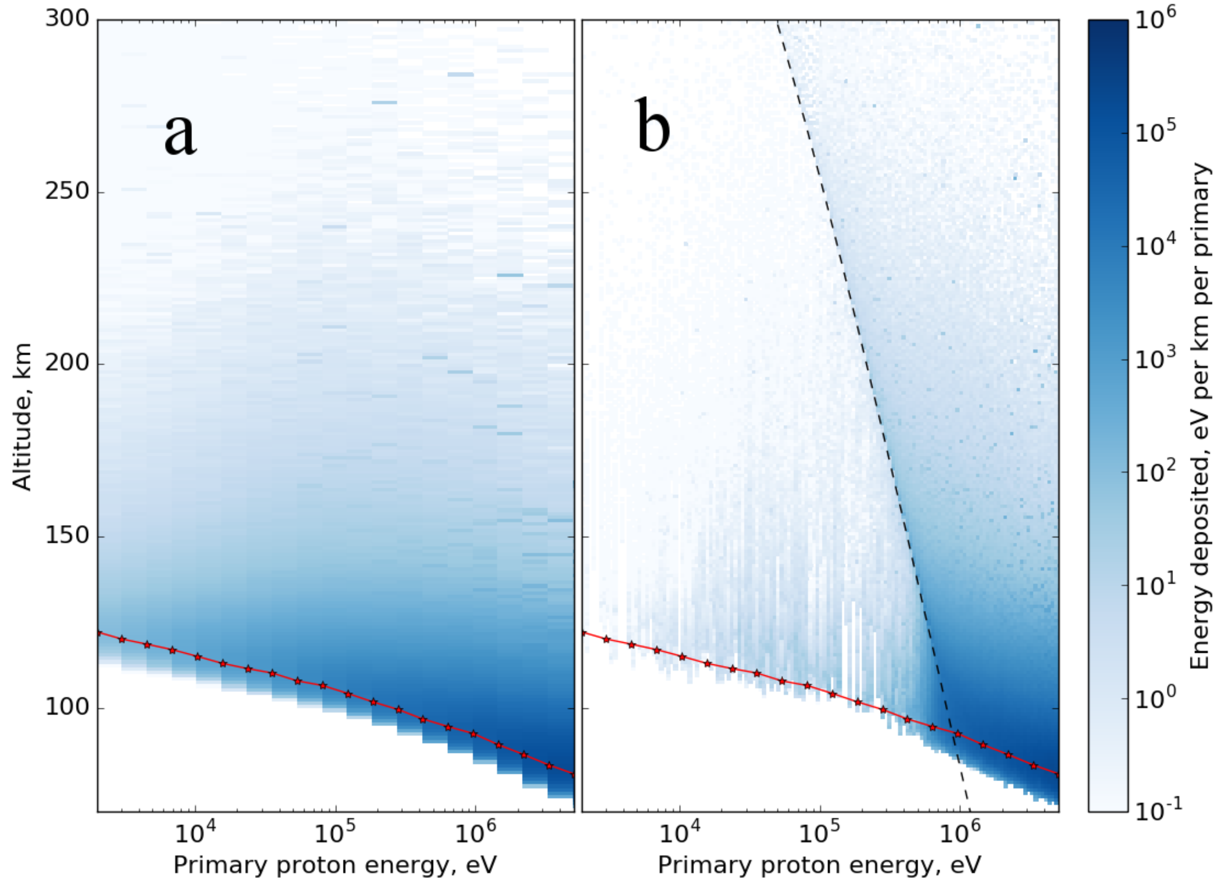

Figure 3.7: Energy deposited per primary by protons with energies between 2 keV and 5 MeV injected in a (a) purely collisional atmosphere with no magnetic fields and a (b) collisional atmosphere with magnetic and electric fields from MF-MHD. The altitude of magnetic reflection is plotted in black, and the stopping altitude in a purely collisional atmosphere is plotted in red.

Protons deposit 99.94% of their energy below 150 km in the absence of fields (Fig. 3.7a). The average maximum deposited energy above 150 km is 1.7 eV per km. Occasionally energies over 50 eV per km are deposited above 150 km, seen as speckles in Fig.83.7a. These seemingly anomalous large energy depositions at higher altitudes are caused by elastic collisions. Although elastic collisions are infrequent for particles with energies greater than 500 eV, the energy lost in a single elastic collision is proportional to the proton's initial energy at the time of scatter.

The energy deposition distribution by protons near a crustal field anomaly shows overall much less energy deposition compared to the absent fields case (Fig. 3.7b). The most notable feature of Fig. 3.7b is that protons with energies between 50 keV and 800 keV deposit energy in two regions: in a narrow altitude range around the proton stopping altitudes in the absence of magnetic fields (plotted in red), and at the magnetic reflection altitude (plotted in black). More energy is deposited at the magnetic reflection altitude than between the stopping altitude and magnetic reflection altitude. This is because the particle is traveling laterally, so the path length in that altitude bin is higher, increasing the energy deposited. When the altitude of magnetic reflection falls below 110 km (for 700 keV), the energy deposition profile is similar to the absent fields case except with a slightly higher altitude of maximum energy deposition. For example, 1.5 MeV protons deposit the maximum amount of energy at 87 km near a crustal field anomaly compared to 85 km in the absence of magnetic fields.

Energy deposition in the lower atmosphere by protons with low energies (< 500 keV) is much less in crustal fields than in the absence of magnetic fields. These protons must be both elastically scattered and charge stripped at the magnetic reflection altitude in order to deposit energy below 150 km. Protons with energies below 100 keV deposit ~1 eV per km below 150 km, compared to 190 eV per km in the absence of magnetic fields.

3.4. Predictions for the 2003 Halloween SEP event

Using the datasets generated in the previous section, ASPEN can determine rates of ionization near a crustal anomaly and in the absence of magnetic fields. For the flux *F(E)* and collision rate *R(E, a)* at altitude *a* for SEP protons with energy *E*, the process rate during a SEP event is:

$$I(a) = \int_{Ei}^{Ef} F(E)R(E,a)\,dE \qquad (3.1)$$

Following the method for determining rates in Leblanc et al. [2002] by using fourteen energies between 1 keV and 100 MeV, the lower energy bound is set to 1 keV. The upper energy bound is set to 5 MeV, since that is the highest energy ASPEN can simulate. This upper limit means that results will be valid above 70 km. Fluxes from the peak SEP spectrum measured by the Electrons, Protons and Alpha Monitor (EPAM) on the ACE spacecraft on 29 October 2003 at 5:59 are used to estimate ionization rates (Fig. 3.8) [Chiu et al. 1998]. This event is colloquially known as the “Halloween storms” and has been previously used to estimate SEP effects at Mars [Lillis et al. 2012].

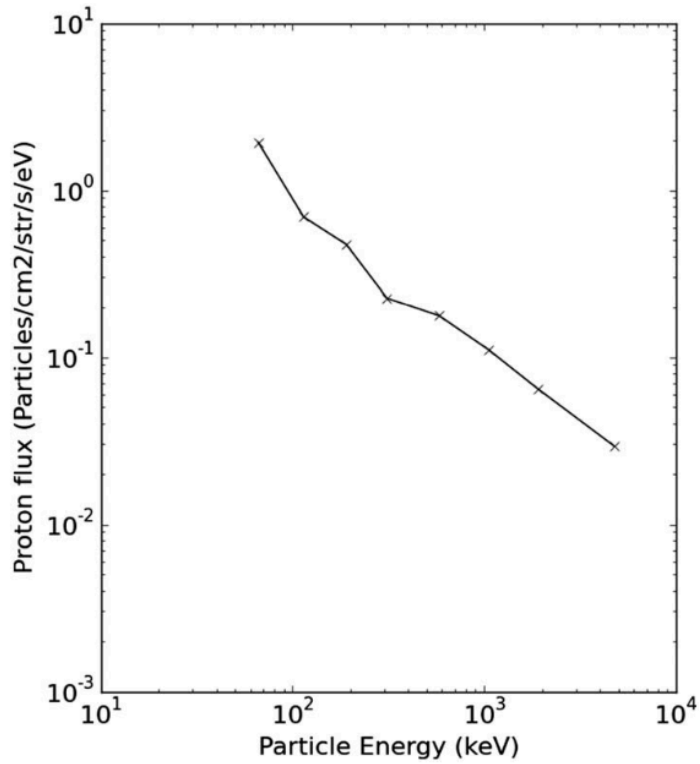

Figure 3.8: Spectrum of peak spectrum during the 28 October 2003 SEP event as measured by ACE Electron, Proton, and Alpha Monitor.

3.4.1. Crustal field influences

Predicted ionization rates near a crustal field anomaly and in the absence of magnetic fields during the EPAM event are shown in Fig. 3.9. In the absence of magnetic fields (black line), the peak ionization above 70 km is 14,853 cm^{-3} s^{-1} at 83 km. There is a slight increase in ionization between 105 and 132 km that peaks at ~2,000 cm^{-3} s^{-1} at 115 km, which is caused by the slightly higher fluxes of 100-300 keV particles measured by EPAM. Total ionization nearby a crustal field anomaly (red line) is 68.3% of ionization in the absence of magnetic fields. Such a decrease is expected, as crustal fields attenuate SEP penetration below 500 keV. Peak ionization is 12,552 cm^{-3} s^{-1} at 83 km, which is a ~15% reduction compared to the absent fields case. There is no comparable ionization bump at 115 km nearby the crustal anomaly.

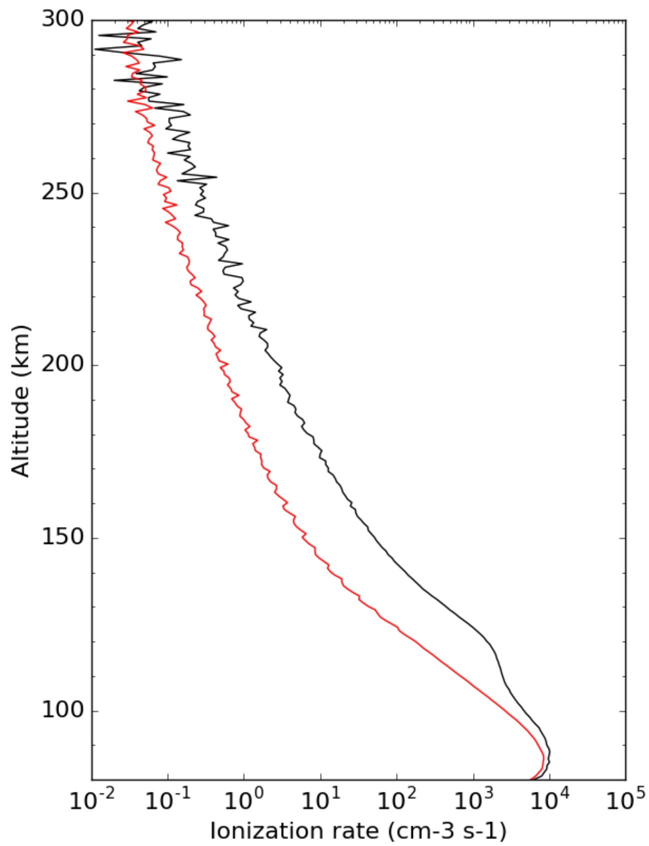

Figure 3.9: Altitude profiles of ionization rate during the 28 October 2003 SEP event using a population of protons injected at 50°S and 182°E on the dayside over unmagnetized crust (black) and a crustal anomaly (red).

We determined volume rates of ionization in the vicinity of proton injection location (Fig. 3.10). In the absence of magnetic fields, the maximum ionization rate is 697 cm^{-3} s^{-1} per °N per °E, located at the same geographic location protons were injected at (marked with a star, Fig. 3.10a). Ionization is overall radially symmetric across the region, spreading in 5° in each direction.

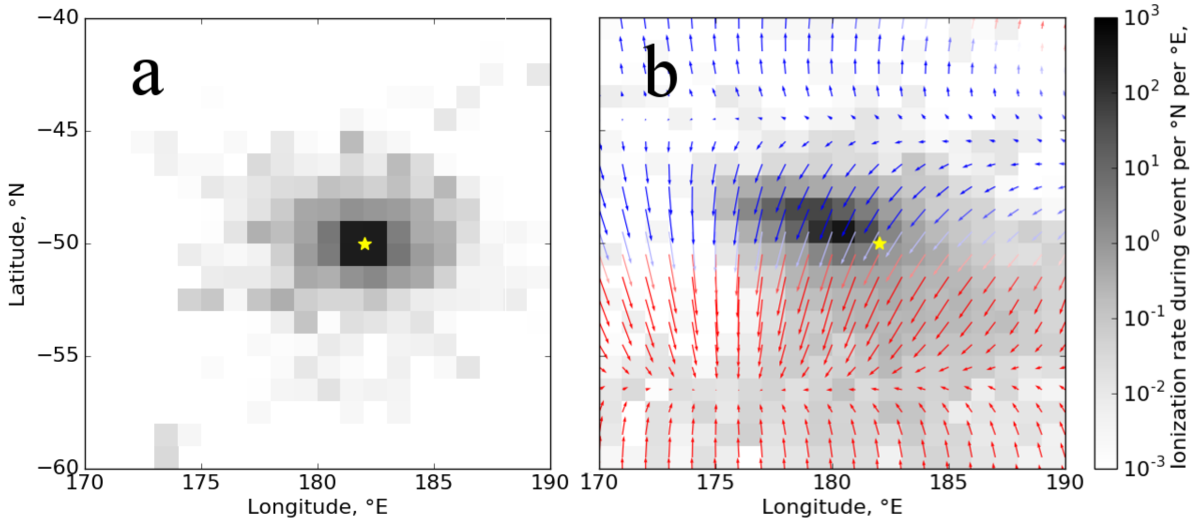

Figure 3.10: Map of SEP-induced ionization volume rate for SEPs directed at the anomaly located at 50°S and 182°E if magnetic fields in the simulation are toggled (a) off or (b) on. The star marks where protons are injected. The contours mark horizontal magnetic fields at an altitude of 400 km where the color indicates the radial component of the magnetic field where red is +40 nT and blue is 40 nT.

Ionization volume rates near a crustal anomaly are not symmetric at all (Fig. 11b). Volume rates are plotted below contours representing horizontal magnetic fields, colored according to the radial component (blue is below -40 nT and red is above 40 nT). The maximum ionization rate is 481 cm^{-3} s^{-1} per °N per °E at 50° S 180° E, approximately 2° E from where protons were injected. Ionization over 50 cm^{-3} s^{-1} per °N per °E spreads northwest of the injection location and ionization below 50 cm^{-3} s^{-1} per °N per °E largely occurs southeast. The northwest ionization follows the Lorentz trajectory of energetic particles.

3.4.2. Secondary electron production

ASPEN can log the energy of any produced secondaries from ionization and charge stripping. Secondary energies are aggregated to predict the spectrum of secondary electrons at each altitude. Similar to the calculation of ionization rate, each spectrum per altitude is integrated over the EPAM fluxes to predict an altitude profile of secondary electron production during an event.

We compared ionization and secondary production from the random and fixed secondary electron models. Both approaches produce near-identical ionization rates down to an altitude of 95 km. Below an altitude of 95 km, the fixed secondary model predicts 28% less ionization than the random secondary model. The discrepancy is because the fixed secondary model extrapolation predicts substantially higher secondary energies for > 1 MeV protons than the Rudd secondary energy method, causing protons to lose energy quicker and ionize less frequently. Since the Rudd secondary energy approach is based on an empirically verified double-differential cross-section expression, we consider it more realistic than the fixed secondary energy approach. We will continue to use this approach in the future.

Altitude profiles of secondary electron spectra were determined in the absence of magnetic fields using fixed (Fig. 3.11a) and random secondary model (Fig. 3.11b). The fixed secondary model predicts that most secondaries have energies between 10 eV and 200 eV. The random secondary model predicts production of many more secondary electrons with energies distributed between 0.01 eV and 100 eV. The models have different implication for SEP-produced upward electron fluxes. The production rate of 110 eV electrons at 150 km is 13 electrons cm^{-3} s^{-1} keV^{-1} in the fixed energy model and 4 electrons cm^{-3} s^{-1} keV^{-1} in the random energy model.

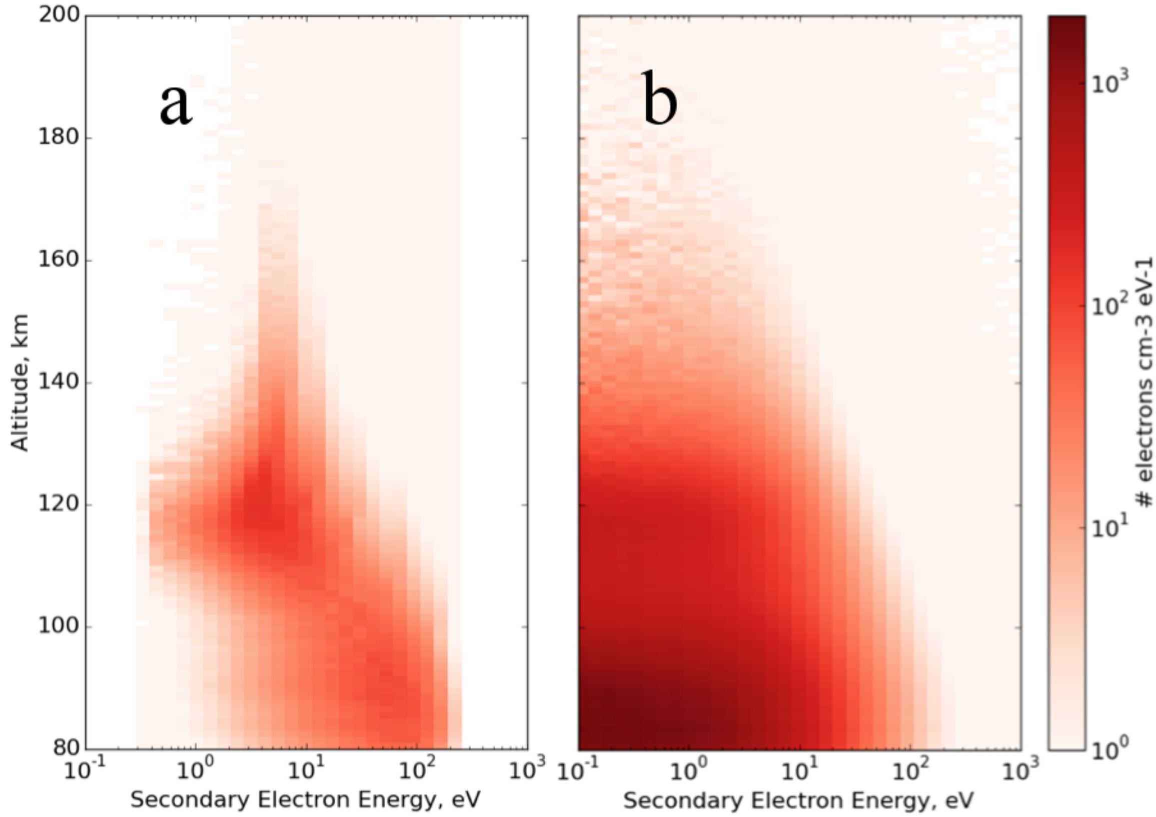

Figure 3.11: Spectrum of electrons produced by SEP proton-impact ionization over unmagnetized crust using a (a) fixed secondary electron energy model and a (b) random secondary electron energy model.

3.4. Conclusions

We used ASPEN to study the effects of a specific anomaly located at 50°S and 182°E on atmospheric ionization. Early results suggest that SEP protons deposit a substantial amount of energy in the atmosphere above the crustal field anomalies. However, proximity to crustal fields can reduce overall atmospheric ionization by ~30%. Atmospheric ionization near a crustal anomaly spreads over a wider geographic area than atmospheric ionization in the absence of magnetic fields. The distribution of atmospheric ionization occurs along an axis corresponding to the Lorentz trajectories of SEP protons.

We also compared ASPEN secondary electron production predictions in negligible magnetic fields using two different methodologies: randomly selecting a secondary energy using the double differential cross section or using a formula to calculate a fixed secondary energy as a function of primary energy. Overall ionization predicted by both methods is similar above an altitude of 95 km. We determined production rates of superthermal electrons (~110 eV) from proton-impact ionization at the limiting altitude where electrons preferentially thermalize instead of backscattering (150 km) [Lillis et al. 2012]. Electron production rates predicted using the random secondary energy model are half that from using the fixed secondary energy model. These electron populations can be modeled using electron transport codes to see if they explain the increased upward electron fluxes observed by MGS.

We demonstrated that SEP protons cause substantially less ionization if they are incident on a specific location near a crustal field anomaly. Future work will include an investigation of how crustal anomalies influence ionization from SEP protons precipitating globally. Precipitating low-energy SEPs (~10 keV) can be magnetically reflected from between 18 and 50% of the atmospheric area presented by the dayside southern hemisphere if the crustal fields are on the dayside. We intend to determine and incorporate the SEP flux dependence on solar zenith angle to study SEP ionization over crustal anomaly regions, which eventually will be expanded into global maps. The progression of atmospheric ionization during a SEP event can also be tracked using data from the SEP instrument on MAVEN, allowing for estimates of time dependent and total ionization and heating during an event.

Chapter 4

SEP electron transport

The majority of this chapter was originally published as "Test Particle Model Predictions of SEP Electron Transport and Precipitation at Mars" [Jolitz et al. 2021]. Sections of the paper detailing the modifications made to ASPEN were integrated into Chapter 2, while the material in this chapter focuses on the results.

4.1. Introduction

SEP precipitation at Mars has been connected to enhanced electron densities and both discrete and diffuse aurora [Espley et al. 2007, Morgan et al. 2006, Němec et al. 2014, Schneider et al. 2015, Schneider et al. 2018, Harada et al. 2018]. However, energetic electrons and ions can be released concurrently, making it difficult to identify if electrons, ions, or both cause these effects. Understanding how and where SEPs precipitate can assist in determining causation. The transport of SEP protons in the Mars magnetosphere and associated energy deposition has been extensively modeled [Luhmann et al. 2007, McKenna-Lawlor et al. 2012, Kallio et al. 2012, Leblanc et al. 2002, Lingam et al., 2018]. However, there is presently no modeling study on the transport of SEP electrons.

Planetary magnetic fields direct where SEPs can precipitate. For example, at Earth an intrinsic dipole magnetic field channels SEP precipitation towards the poles and shields equatorial latitudes (e.g., Mironova et al. [2015]). On the other hand, SEPs at unmagnetized bodies are directed according to the interaction between the solar wind and the object. When solar wind plasma decelerates upon reaching a planetary obstacle, the embedded interplanetary magnetic field (IMF) is compressed and "drapes" over the ionosphere (see Nagy et al. [2004] and references therein). The resulting magnetic field configuration is variable and affected by many factors, e.g., IMF configuration and disturbed conditions in the solar wind. Mars also has strongly magnetized regions in the Southern hemisphere called crustal fields or anomalies that can modify global magnetic field topology [Acuña et al. 1999, Krymskii et al. 2002].

Though there are presently no studies on SEP electrons at Mars, there are several studies on SEP protons at Mars. Findings from those studies can help contextualize predictions of SEP electron transport. We will discuss some of these studies, which will cover both spacecraft data analysis and simulation predictions.

Prior research on SEP protons at Mars has suggested that all but the lowest energy particles are uninhibited by the induced magnetosphere. Luhmann et al. [2007] described oscillations of 20-200 MeV SEP fluxes observed by Mars Odyssey in near-Mars orbit. However, they determined these observations were caused by a physical obstruction or "shadowing" by the planet, rather than the influence of the Mars-solar wind magnetic interaction. The SLED instrument aboard Phobos-2 measured SEP proton flux dropouts within the shock [Afonin et al. 1989]. Simulations suggested that the region where dropouts occur is a "magnetic" or "solar wind flow" shadow behind Mars along the direction of the IMF [McKenna-Lawlor et al. 2012, Kallio et al. 2012]. This region is generated by the deflection of SEP protons initially flowing along the IMF direction. While the planet is the only obstacle to higher energy SEP protons (e.g., MeVs), the Mars-solar wind interaction magnetic fields can displace lower energy SEPs (e.g., tens of keVs). Recent data analysis from MAVEN has suggested further causes for SEP proton shadowing such as rapid changes to the IMF direction [Lillis et al. 2016]. Other modeling efforts have suggested only strongly magnetized anomalies can attenuate precipitating SEP proton fluxes and associated ionization [Leblanc et al. 2002, Jolitz et al. 2017].

Although the Mars induced magnetosphere has a minor influence on SEP protons, we expect to see its significant influence on SEP electrons. The smaller mass of an electron results in a gyroradius more likely to be comparable to the length scale of variations in the local magnetic field. If the magnetic field does not substantially vary over the gyration of the particle, the particle will tightly circle the local magnetic field. This particle can be considered to be "adiabatic" since it satisfies the first adiabatic invariant, which is the conservation of magnetic moment. Guiding center path theory, which assumes particle motion can be decoupled into gyration and guiding center motion, can then be used to predict the behavior of these particles. The magnetic moment is conserved while the guiding center can drift across field lines independent of gyration. However, if the gyroradius is comparable or larger than the scale of variations in the magnetic field, the particle will experience excursions in the local magnetic field as it orbits. If a particle has a large enough gyroradius, the particle can move into an area with a different magnetic field before it can complete a gyration. This can cause a particle to veer from one field line and begin to circle another without necessarily conserving magnetic moment.

Resulting nonadiabatic drifts and pitch angle scattering can affect where and how the particles precipitate into a planetary atmosphere.

SEP protons are nonadiabatic in the Mars-solar wind interaction region. With gyroradii of between ~2–20 Mars radii for 20 keV to 2 MeV protons in a 3 nT IMF, they are often displaced along their orbit before they complete a gyration around the IMF. The induced magnetic fields act to perturb SEP protons within a single gyration. This is why most prior SEP protons in the past were modeled using test particle approaches that solve the Lorentz force equation [McKenna-Lawlor et al. 2012, Leblanc et al. 2002, Jolitz et al. 2017].

SEP electrons like SEP protons span the same energy range (tens of keVs to hundreds of MeVs) but they are three orders of magnitude less massive than SEP protons. They will have an overall smaller gyroradius. However, it is unclear if SEP electrons are adiabatic in the Mars-solar wind interaction.

In this paper, we find that nonadiabatic transport significantly influences SEP electron precipitation. We will first describe how ASPEN was applied to simulate relativistic electrons incident from the solar wind onto the disturbed IMF in the near-Mars environment. We will show test particle traces that demonstrate the influence of drifts and nonadiabatic transport. We will then discuss how to sample appropriate initial conditions for energetic electrons from the solar wind, including energy, pitch angle, and locations, particularly within the bow shock. We perform a validation within the model of these assumptions for position and pitch angle distributions. Finally, we apply these approximations to predict where electrons precipitate into the Martian atmosphere. We present a qualitative analysis of the results within the model, which we then use to estimate energetic electron fluxes in the Mars-solar wind system. Ultimately we show that energetic electron precipitation is favored into cusps, but also exceeds estimates made from a simplified guiding center path approximation without drift terms.

4.2. Approach

For studying extremely energetic electron motion in the near Mars magnetic fields, relativistic effects were included in the ASPEN model along with field line tracing for a coupled analysis of magnetic topology. The simulation domain was also extended to include the bow shock, magnetic pileup, and magnetotail regions of the Mars induced magnetosphere. As in the prior chapter, this study also used results from the MF-MHD model. The results are recorded on a spatially-varying grid to capture near-Mars features as well as the overall structure of the Mars-solar wind interaction region. Since the coordinate system used in ASPEN is defined on the same grid as the prescribed magnetic fields, all results are presented in MSO (Mars Solar Orbital) coordinates, where X points from the center of Mars towards the sun, Y opposes the direction of Mars' orbital velocity, and Z completes the right-handed coordinate system. The MF-MHD results are defined on a grid that spans $-24\ R_M < X < 10\ R_M$ and $-16\ R_M < Y, Z < 16\ R_M$.

The outputs from the MF-MHD model are solved under solar minimum and autumnal equinox conditions, with a "Parker spiral" interplanetary magnetic field configuration with a magnitude of 3 nT and cone angle of 56°. Crustal fields are assumed to be located on the dayside at noon, with the strongest arcades facing the sun. Mars is rotated such that the subsolar longitude is 180° and the strongest crustal fields are oriented on the dayside. This will be the coordinate system of all results presented in this paper.

The step length in ASPEN was variably determined (the minimum of 5% of the local gyroradius, 10% of the gradient scale, and a predefined maximum step length of 1,000 km). While the choice of step length can affect the accuracy of the RK4 differential equation solver, we determined this choice was sufficient by comparing simulated particles using half the dynamically calculated value and found no substantial difference. Also, when electric fields were ignored, the energy of simulated particles was conserved within an appropriately small margin (below 0.01%). Finally, to ensure that the choice of step algorithm didn't cause artifacts, the simulation was reran using a Boris algorithm instead of RK4 and found to produce similar results.

This study is focused on the motion of electrons before they reach the atmosphere and begin colliding with the constituents. However, there will be some collisions far from the planet due to the oxygen and hydrogen coronae. It is possible to estimate the likelihood of a collision of a 10 keV to 1 MeV electron by calculating the collision probability. Using the formulas for oxygen and hydrogen corona densities from Diéval et al. [2012] and electron impact cross-sections collected in Lillis et al. [2009], the likelihood of a 10 keV electron colliding as it travels radially into the planet is 0.005% in the hydrogen corona and 0.001% in the oxygen corona (Figure 4.1). Since higher energy electrons have a smaller collisional cross-section and thus even less likelihood of colliding in the corona, this is sufficiently low to ignore the corona. Likewise, this indicates that it would be unlikely for solar energetic electrons to meaningfully increase mass-loading in the corona and change the draping of the induced magnetosphere.

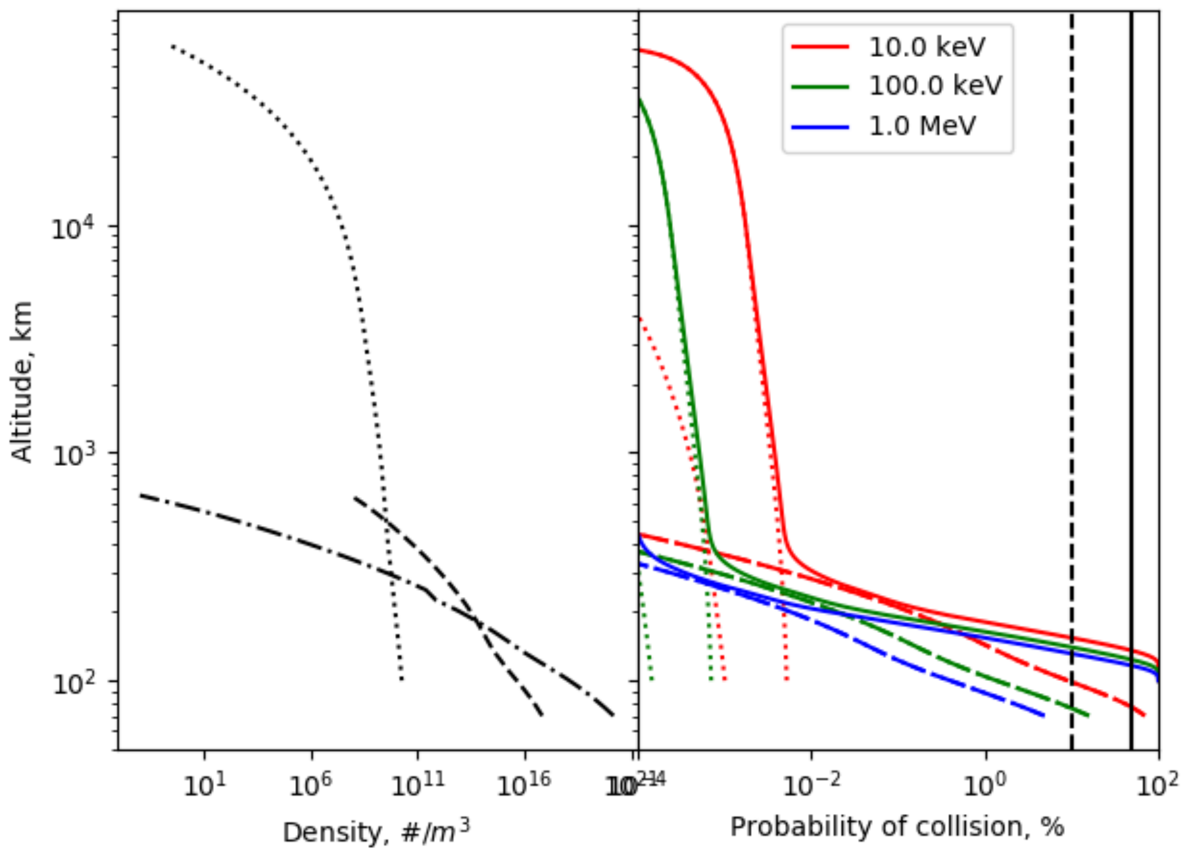

Figure 4.1: Densities of the hydrogen corona (dotted), hot oxygen corona (dashed), and atmospheric oxygen (dash-dotted) (left) alongside the calculated probability of collision for a 10 keV, 100 keV, and 1 MeV electron. Vertical lines mark where the collision probability is 10% (dashed) and 50% (solid).

ASPEN stops tracing electrons at a lower simulation boundary of 200 km. We decided against setting the simulation boundary approximately to the exobase, or the altitude where the mean free path is equivalent to the atmospheric scale height. Electrons of different energies have different mean free paths. Implementing an exobase simulation boundary requires different lower altitude boundaries for different simulated electron energies, interfering with side-by-side results comparison.

4.3. Nonadiabatic particle motion

Before applying the model to predict energetic electron precipitation on a wide scale, it is worth discussing and showing nonadiabatic transport mechanisms as they occur in the near-Mars system.

For a particle with gyroradius R_g in a field line of scale length L, the curvature parameter $\kappa = \sqrt{L/R_g}$ indicates if the motion is adiabatic [Büchner and Zelenyi et al. 1989]. The field line scale length may be defined as the radius of curvature R_c if nonadiabaticity is solely from the field line curving. It can also be defined as the gradient scale length $|\boldsymbol{B}|/|\nabla \boldsymbol{B}|$, which will capture nonadiabaticity from any spatial variation in the vector field. Unless otherwise specified, the gradient scale length is used to calculate the curvature parameter.

If a particle's gyroradius is much smaller than the scale length of magnetic field variations ($\kappa \gg 1$), the particle's magnetic moment is conserved and motion is adiabatic. When the gyroradius is comparable to the magnetic field scale length ($\kappa \rightarrow 1$), motion becomes stochastic due to nonlinear resonances occurring between the gyromotion and guiding center bounce motion, scattering the pitch angle without accelerating the particle [Murakami et al. 1990]. The behavior can be described as akin to a centrifugal force in the particle's frame [Delcourt et al. 1994]. If the gyroradius is longer than the scale length of variations ($\kappa < 1$), a particle's motion can be stochastic or meandering, e.g. Speiser orbits. Meandering motion commonly occurs in the sharp magnetic field reversal in a magnetotail [Chen and Palmadesso 1986]. Downstream of Mars, energetic electron motion is adiabatic unless at the quasiparallel shock field reversal ($\kappa \rightarrow 1$) or at the magnetotail field reversal ($\kappa < 1$). For the magnetic fields from MF-MHD, a 1 keV electron in the equatorial plane will move nonadiabatically in the quasiparallel shock field reversal ($\kappa \sim 10$) and in the current sheet ($\kappa \sim 0.5$). Higher energy electrons will have lower curvature κ, increasing the influence of nonadiabatic changes. Figure 4.2 shows the curvature parameter calculated for 200 keV electrons, which is very low in the current sheet, some crustal fields on the nightside, and between the quasiparallel shock and MPB.

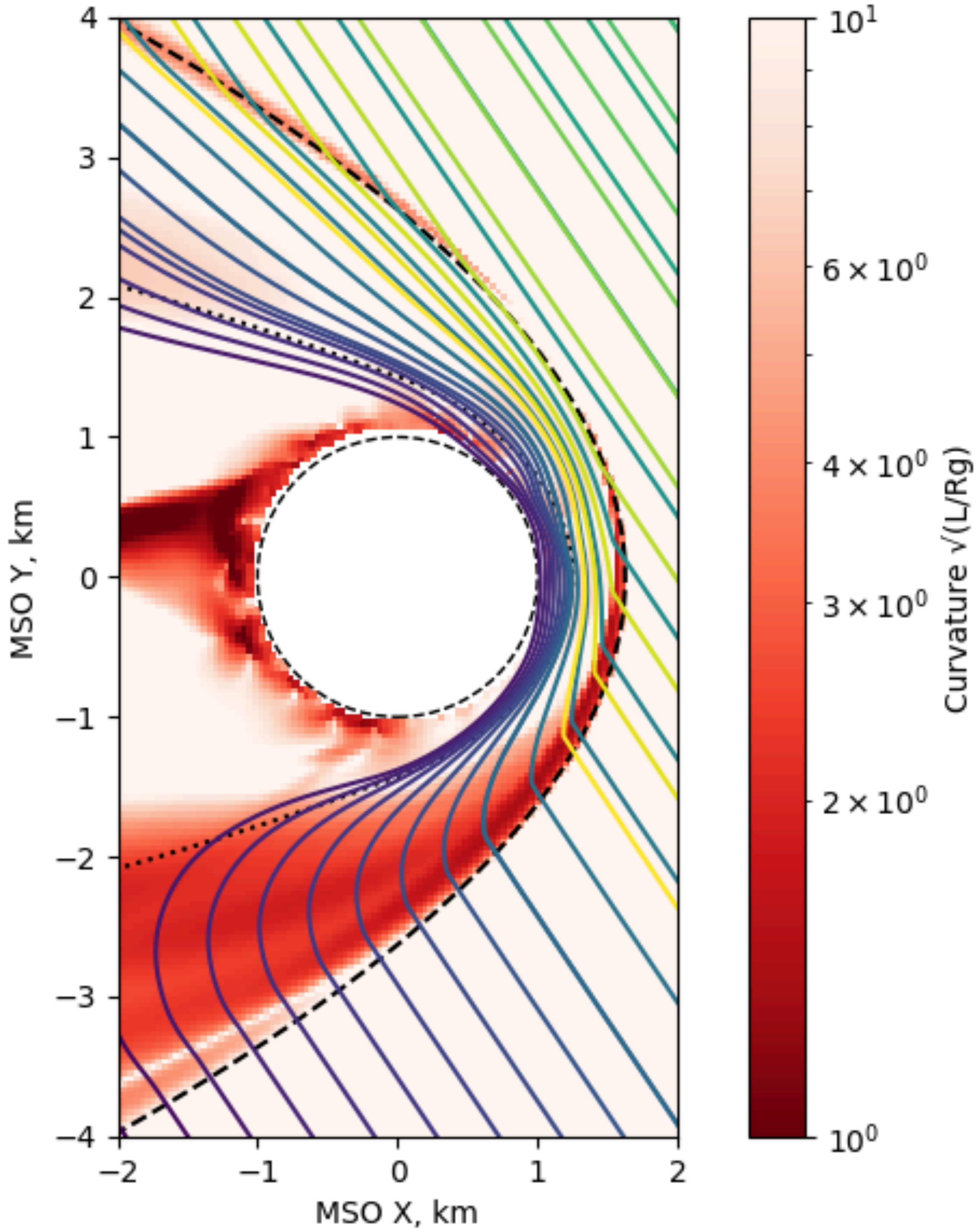

Figure 4.2: Map of the curvature parameter for 200 keV electrons moving in equatorial magnetic fields. Field line traces are overlaid for reference.

We can examine traces of particles to see this behavior directly in the Mars system. Figure 4.3 shows traces of 1 keV, 10 keV, 100 keV, and 1 MeV electrons alongside their initial magnetic field line. All particles are incident on the quasiparallel flank of the magnetotail with a pitch angle of 35°. The electric fields have been set to 0 μV/km to highlight magnetic field influences.

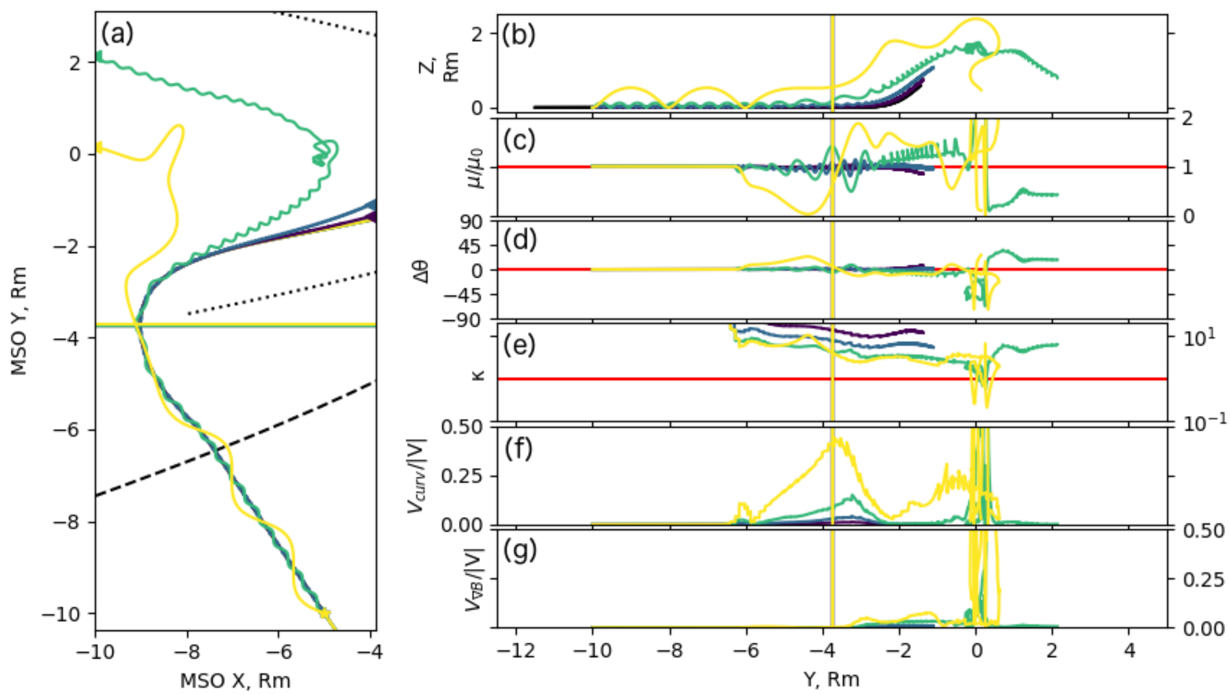

Figure 4.3: Representative traces of 1 keV (purple), 10 keV (blue), 100 keV (green), and 1 MeV (yellow) electrons in the XY-plane (a) and in the YZ-plane (b) alongside the normalized magnetic moment (c), difference between the adiabatically calculated pitch angle and the model pitch angle (d), curvature parameter (e), curvature drift velocity (f), and gradient drift velocity (g). Solid lines for each particle are drawn at the quasiparallel shock field reversal. The red horizontal line marks where magnetic moment is conserved (c), where calculated pitch angle matches the modeled pitch angle (d), and where the curvature parameter is one (e). The magnetic field line connected to the initial particle location is plotted in black. Dashed and dotted black lines mark the bow shock and magnetic pileup boundary conic section fits from Trotignon et al. [2006].

The magnetic moment is constant until each electron crosses the quasiparallel shock field reversal. The curvature parameter then plummets, the magnetic moment oscillates, and the model pitch angle deviates from the adiabatically calculated pitch angle. This is consistent with pitch angle scattering from nonlinear resonances at the point where the magnetic field bends back towards Mars. As the magnetic moment changes, electron pitch angle can deviate from adiabatic theory depending on the electron's initial energy. In this case, the adiabatically predicted pitch angle is approximately the same as the modeled pitch angle for the 1 keV electron, while the 10 keV – 1 MeV electrons can vary up to 26° from the adiabatically predicted pitch angle in the quasiparallel shock field reversal and up to 67° in the current sheet. This will lead to departures from adiabatic predictions after crossing the quasiparallel side of the bow shock.

The particles also begin to separate from each other in space, with higher energy particles traveling further from the magnetic field line in the +Z direction. This is consistent with a gradient or curvature drift, as those drifts are proportional to energy. Gradient and curvature drifts are expected to push particles both perpendicular to the IMF and the direction of the curvature vector. To confirm this, we can calculate the curvature and gradient drift velocities based on terms in the guiding center path approximation:

$$v_{\nabla B} = \frac{\mu}{\gamma q |\boldsymbol{B}|^2} \left| \boldsymbol{B} \times \nabla |\boldsymbol{B}| \right| \tag{4.1}$$

$$v_c = \frac{m u_{\parallel}^2}{\gamma q |\boldsymbol{B}|^2} \left| \boldsymbol{B} \times (\boldsymbol{B} \cdot \nabla) \boldsymbol{B} \right| \tag{4.2}$$

The drift velocities can be normalized with respect to the magnitude of each particle's velocity to compare them on the same axis. Figure 4.3 shows the drift velocities increase upon crossing the quasiparallel shock, where curvature drift increases more than gradient drift, therefore, curvature drift is responsible for particle displacement.

4.4. Modeling energetic electrons: Initial distributions

The goal of this work is to predict where SEP electrons precipitate at Mars. That will require proper selection of three initial conditions: energy, pitch angle, and position. We will use a Monte Carlo approach of randomly selecting these values from predetermined distributions, and then simulating particles down to altitudes of 200 km.

SEP electrons span a wide range of energies. The flux distribution has been found to best fit a power law $F \propto \alpha E^{-\kappa}$ for different ranges of energy [McGuire and von Rosenvinge 1984]. In this study, we will focus on 10-200 keV electrons. This energy range includes the predicted source population of observed aurorae (50-200 keV electrons) [Gérard et al. 2017, Haider and Masoom 2019] and is an energy range that MAVEN SEP is actively measuring at Mars [Larson et al. 2015], which allows for later cross-study comparison. For now, we will sample energies from a power law distribution with κ set to -0.6, as recommended for 10-200 keV electrons in McGuire and von Rosenvinge [1984].

SEP electrons can be isotropic or field-aligned depending on the influence of scattering mechanisms and resonances as they traverse the solar system. Interplanetary energetic electrons are affected by a combination of scattering by magnetic fluctuations and focusing by the radially declining IMF. Depending on the magnetic connectivity of an energetic particle source to Mars, the energetic electrons can be "diffusive" and isotropized by scattering, or be "scatter-free" and have directionality [Lin 1974, Allum et al. 1970, Dresing et al. 2014]. According to Allum et al. [1970], initially field-aligned electrons will become isotropic within an hour of the onset of an event. Likewise, Lin [1974] estimated that ~80% of electron events recorded at 1 AU are diffusive. We conclude that isotropic electron pitch angle distributions are representative of the majority of SEP events for most of the time, and will use an isotropic pitch angle distribution to describe all electrons that are initially in the solar wind.

The most challenging initial distribution to construct is initial SEP electron positions. SEP electrons are sourced outside of the Mars-solar wind interaction region. Ideally we would sample all electrons outside the bow shock and trace each through the induced magnetosphere. However, the magnetic fields connecting the solar wind to the nightside of an unmagnetized planet can stretch ~50-100 planet radii from the planet, based on observations at Venus [Dubinin and Fraenz 2015]. An MHD run over this domain and test particles subsequently simulated would be unacceptably computationally intensive.

Instead, we will start electrons from a constrained grid consisting of four emitter planes surrounding Mars that are perpendicular to the IMF (Figure 4.4). Since all electrons that reach the near-Mars system initially travel along the IMF within a gyroradius and the IMF is in a Parker spiral configuration with no z-component, we can assume every incident electron has traveled parallel to the XY plane. The problem of simulating incident electrons can be reduced to initializing them on emitter planes perpendicular to the IMF direction, which are XZ planes and YZ planes for a Parker spiral IMF. We select two XZ planes outside of the flanks of Mars and two YZ planes, one in front of the nose of Mars' bow shock and one behind Mars in the magnetotail. Spatial distributions of energetic particles are ordered by ambient magnetic fields. Since the IMF is assumed to be uniform and constant relative to Mars for this paper, we can sample initial locations from a uniform distribution on the three planes outside the bow shock. This does not work for the fourth plane, which intersects inhomogeneous magnetic fields.

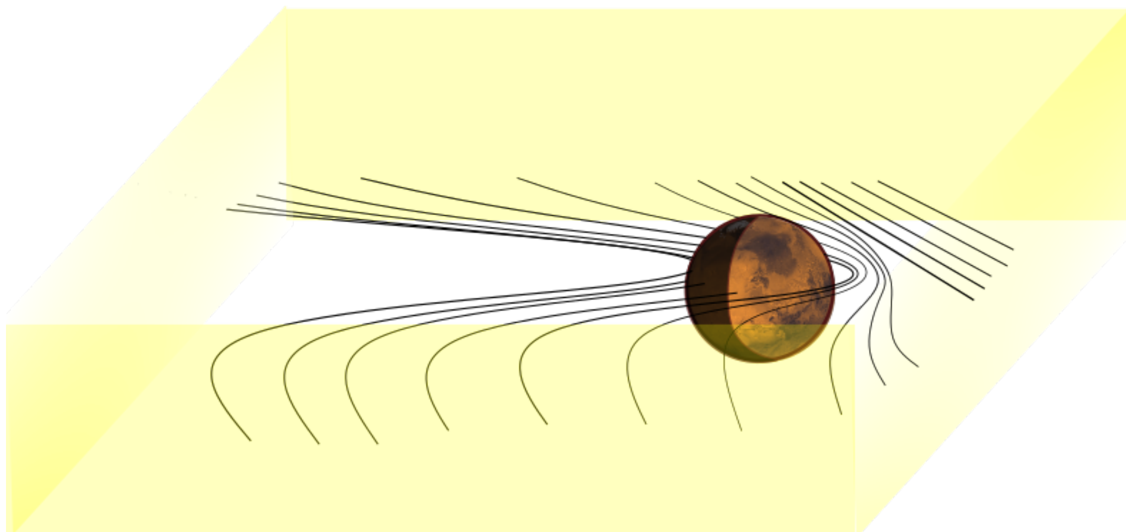

Figure 4.4: The simulated model box with field lines plotted to guide the eye. Note that the fieldlines are parallel to the IMF in the two flank planes and the plane ahead of the bow shock, but the field lines will be bowed behind Mars.

We can approximate the spatial particle distribution in the fourth plane by sampling a distribution in the Y-Z plane weighted by magnetic flux. Since magnetic flux is conserved in the solar wind and the magnetotail far from Mars by Alfven's theorem, the volume of a parcel of plasma in the solar wind should expand or contract in the magnetotail depending on the local magnetic flux. More particles are simulated from higher magnetic flux regions and less from lower magnetic flux regions. The distribution can be modified to further exclude particles that are predicted by adiabatic theory to have reflected before reaching a point in the magnetotail. This is equivalent to restricting precipitation to only particles in the "loss cone". We multiply the magnetic flux by the fraction of particles that will enter the loss cone and not be reflected before reaching that spot in the magnetotail. To do this, we calculate the loss cone angle $sin\ \theta_c = \sqrt{|\boldsymbol{B}|/|\boldsymbol{B}_{SW}|}$ for local magnetic field $\boldsymbol{B}$ and solar wind magnetic field $\boldsymbol{B}_{SW}$, and then calculate the relative fraction of velocity space below the loss cone angle where *F(θ)* is the pitch angle distribution function:

$$T = \frac{\int_0^{\theta_c} F(\theta)d\theta}{\int_0^{\pi/2} F(\theta)d\theta} \tag{4.3}$$

This factor will reduce the number of particles simulated in the magnetotail lobes.

We can modify the pitch angles sampled in the fourth plane according to the loss cone. After sampling a given pitch angle distribution up to the loss cone angle cutoff to get pitch angle θ_{SW} outside the bow shock, we calculate the pitch angle θ_{MT} in the magnetotail assuming the magnetic moment was held constant:

$$(\sin\theta_{MT})^2/|B_{MT}| = (\sin\theta_{SW})^2\,/|B_{sw}| \tag{4.4}$$

Before proceeding with a global precipitation simulation, we want to confirm these approximations are sufficient. Curvature drifts and pitch angle scattering across the quasiparallel shock field reversal may disrupt the approximations made for the fourth plane. We can quantify these effects by comparing the proposed spatial and pitch angle distributions to distributions determined by applying the test particle on particles crossing the quasiparallel shock field reversal. Though it is computationally infeasible to simulate all particles that cross the bow shock and enter the magnetotail, it is feasible to simulate a subset.

We begin tracing electrons from the edge of the simulation domain outside the quasiparallel shock, an XZ-plane defined over -23 R_M < X < 0 R_M and |Z| < 1 R_M at Y = -12.5 R_M. Electrons with energies of 10 keV and 200 keV were simulated to investigate energy-dependent behavior at the extremes of the simulation energy distribution. We trace the electrons until they either cross a YZ-plane at a predefined distance from Mars in the magnetotail or exit the simulation domain. We choose a distance of 8 R_M to ensure distance from any crustal field influences. We can then compare the modeled distribution with the previously discussed distribution that is weighted by magnetic flux and the loss cone.

We also trace magnetic field lines from the same initial plane to the stopping YZ-plane. The resulting distribution will mostly coincide with a distribution weighted by only magnetic flux. There will be a lack of traced field lines near the current sheet since those magnetic field lines extend to the deep magnetotail and outside the simulation domain, causing the distribution to appear compressed and "fall off" near the center of the magnetotail. The location of the fall off is the limit to which the distributions can be compared.

Figure 4.5a shows where field lines cross the YZ-plane at X = -8 R_M. The traced field lines cluster near the center of the Mars-directed magnetotail lobe. This is expected for the higher magnetic flux. There is an absence of traced field lines within 0.5 R_M of the Mars-sun line due to the restricted simulation domain, setting the limit where modeled spatial distributions can be compared.

Figure 4.5a also shows where simulated electrons enter the magnetotail plane. While some simulated electrons cross the quasiparallel shock again due to backscattering (Y < -4 R_M) or pitch angle scattering following crossing the current sheet (Y > 0 R_M), the majority cluster inside the lobe of the magnetotail directed towards Mars.

Our goal is to confirm our proposed spatial distribution is sufficient for electrons traveling toward Mars in the magnetotail. To that end, we select the electrons and field lines that cross the magnetotail within a box bounded by Y ∈ [-4 R_M, 1 R_M] and Z ∈ [-1 R_M, 1 R_M]. We then generate locations within the box that are sampled from the previously discussed distributions. One set of locations is sampled by magnetic flux alone, representing a numerical prediction of field line spatial distribution that can be directly compared to the spatial distribution of traced field lines. The other set of locations is a numerical prediction of adiabatic electron spatial distribution, sampled by both magnetic flux and fraction of particles within the loss cone, and can be compared to simulated electrons. The sampled distributions represent the proposed distributions.

Figure 4.5b compares the spatial distribution of traced field lines, simulated electrons, sampled field lines, and sampled adiabatic electrons. The majority of traced field lines and simulated electrons cluster at Y = -2 R_M. This clustering is caused by the simulation domain restriction. The proposed field line distribution has the same shape as the modeled field line distribution below the fall off at Y = -1 R_M. The simulated different energy populations have similar distributions. The simulated electron distribution is broader than the traced field line distribution and peaks at the same region. This behavior is also observed in the proposed electron distribution compared to the proposed field line distribution. These suggest that drift is not substantially influential on the particles entering the deep magnetotail, and that the proposed spatial distribution will be acceptable.

We can also confirm the choice of pitch angle distribution by selecting all electrons in the sample box and calculating the difference between an electron's pitch angle in the model and the pitch angle predicted by adiabatic theory. Figure 4.5c shows most modeled electrons have pitch angles consistent with adiabatic theory. The accuracy of adiabatic theory is dependent on energy, as 80% of modeled 10 keV electrons and 65% of modeled 200 keV electrons in the bow shock have a pitch angle that is within 15° of the adiabatically-predicted pitch angle. However, up to 15% of the modeled electrons that reach the magnetotail are outside the loss cone, indicating a population of electrons that enter nonadiabatically.

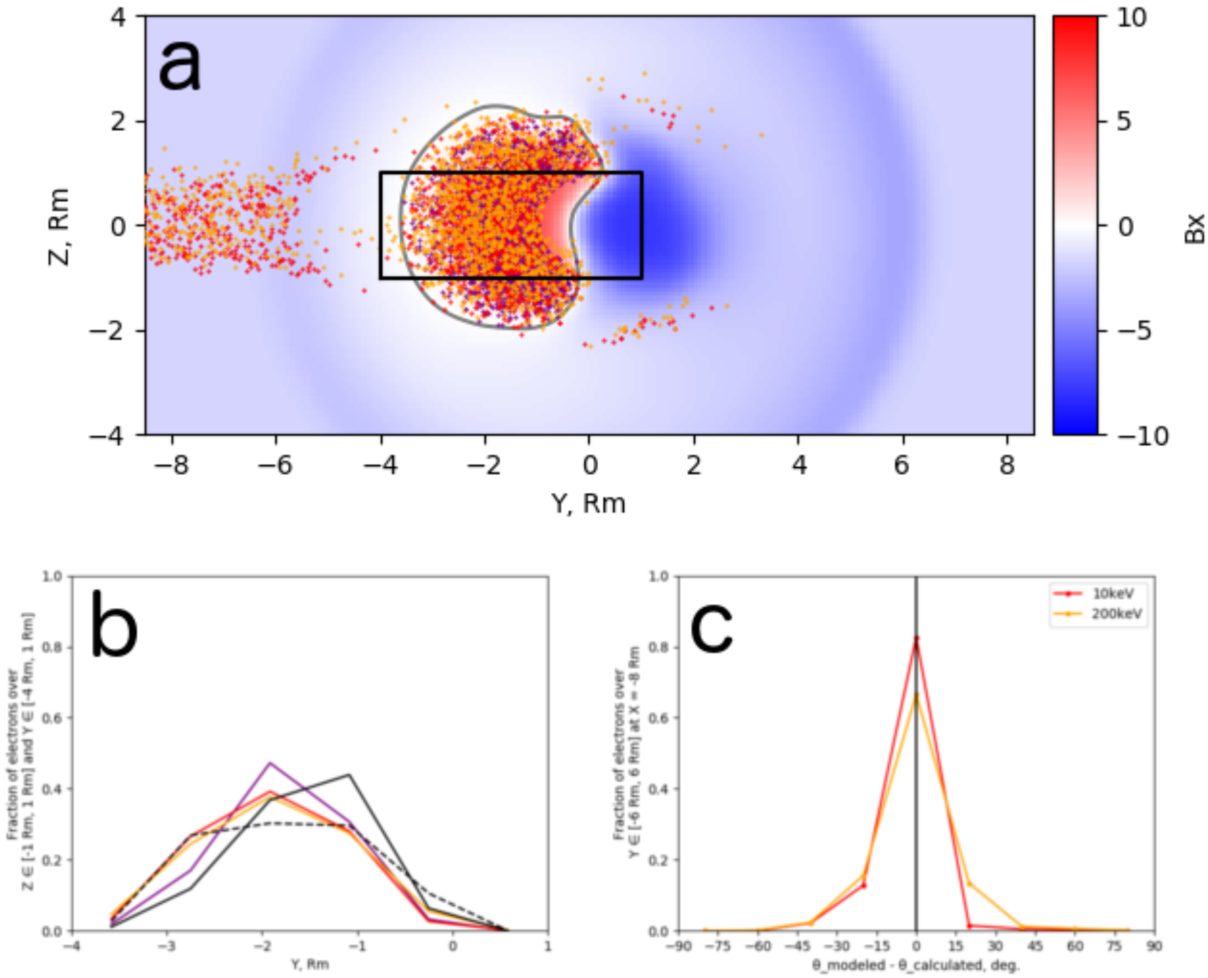

Figure 4.5: (a) Locations where traced magnetic field lines (in purple), simulated 10 keV electrons (in red), and simulated 200 keV electrons (in orange) cross a YZ-plane downstream of Mars at X = -8 R_M, plotted over the X-component of the magnetic field in the plane with a contour where Bx = 0 nT (in gray) and a line demarcating the sample box (in black). (b) Fraction of simulated 10 keV electrons (red), simulated 200 keV electrons (orange), traced field lines (purple), numerically predicted field lines (solid black), and numerically-predicted electrons (dashed black) in the sample box as a function of Y coordinate. (c) Fraction of simulated 10 keV electrons (red) and 200 keV electrons (orange) in the sample box as a function of deviation from adiabatic pitch angle (black line plotted where $\theta_{model} = \theta_{adiabatic}$).

We can bound the influence of nonadiabatic electrons by comparing simulations of energetic electrons from the magnetotail. For 100,000 electrons from a plane at X = -8.5 R_M (Y ∈ [-8.5 R_M, 8.5 R_M] and Z ∈ [-6 R_M, 6 R_M]), 1% of electrons weighted only by magnetic flux conservation reach 200 km compared to 0.6% using the adiabatic approximation and magnetic flux conservation. If 85% of electrons reach the magnetotail adiabatically and 15% are nonadiabatic, then 0.75% of electrons would be expected to precipitate, which is a negligible increase from the adiabatic assumption case. This suggests the proposed initial distributions will be sufficient approximations for electrons incident on the magnetotail.

4.5. Modeling energetic electrons: Global precipitation

We will start electrons inside a box defined by the boundaries of $-8.1\ R_M < X < 3.2\ R_M$ and $|Y| < 10\ R_M$. Electrons are released from four emitter planes surrounding Mars. Locations of electrons on the magnetotail plane are weighted in accordance to the previously discussed distributions.

It is important to point out that simulating electrons within a box can impose an unphysical geometry if not normalized properly. The number of electrons from each plane is proportional to the area of the plane and cosine of the direction of the particle flow relative to the emitter plane normal vector. This ensures that the simulation is properly weighted. For a simulation of 323,937 total electrons, 100,000 are simulated from a plane at $X = -8\ R_M$ spanning a range of $Y \in [-4\ R_M, 8.5\ R_M]$ and $Z \in [-2\ R_M, 2\ R_M]$, 73,605 are simulated from two planes at $Y = \pm\ 8.5\ R_M$ that span a range of $X \in [-8\ R_M, 3\ R_M]$ and $Z \in [-1\ R_M, 1\ R_M]$, and 76,727 are simulated from a plane at $X = 3\ R_M$ that spans a range of $Y \in [-8.5\ R_M, 8.5\ R_M]$ and $Z \in [-1\ R_M, 1\ R_M]$. The limited range of the plane at $X = -8\ R_M$ allows for simulating only electrons that will be inbound to Mars, increasing the accuracy of the results.

4.5.1. Predicted properties of precipitating electrons

Only a fraction of simulated particles reach an altitude of 200 km (0.7%, N = 2,267), with most coming from the magnetotail plane (95%, N = 2,146) (Figure 4.6).

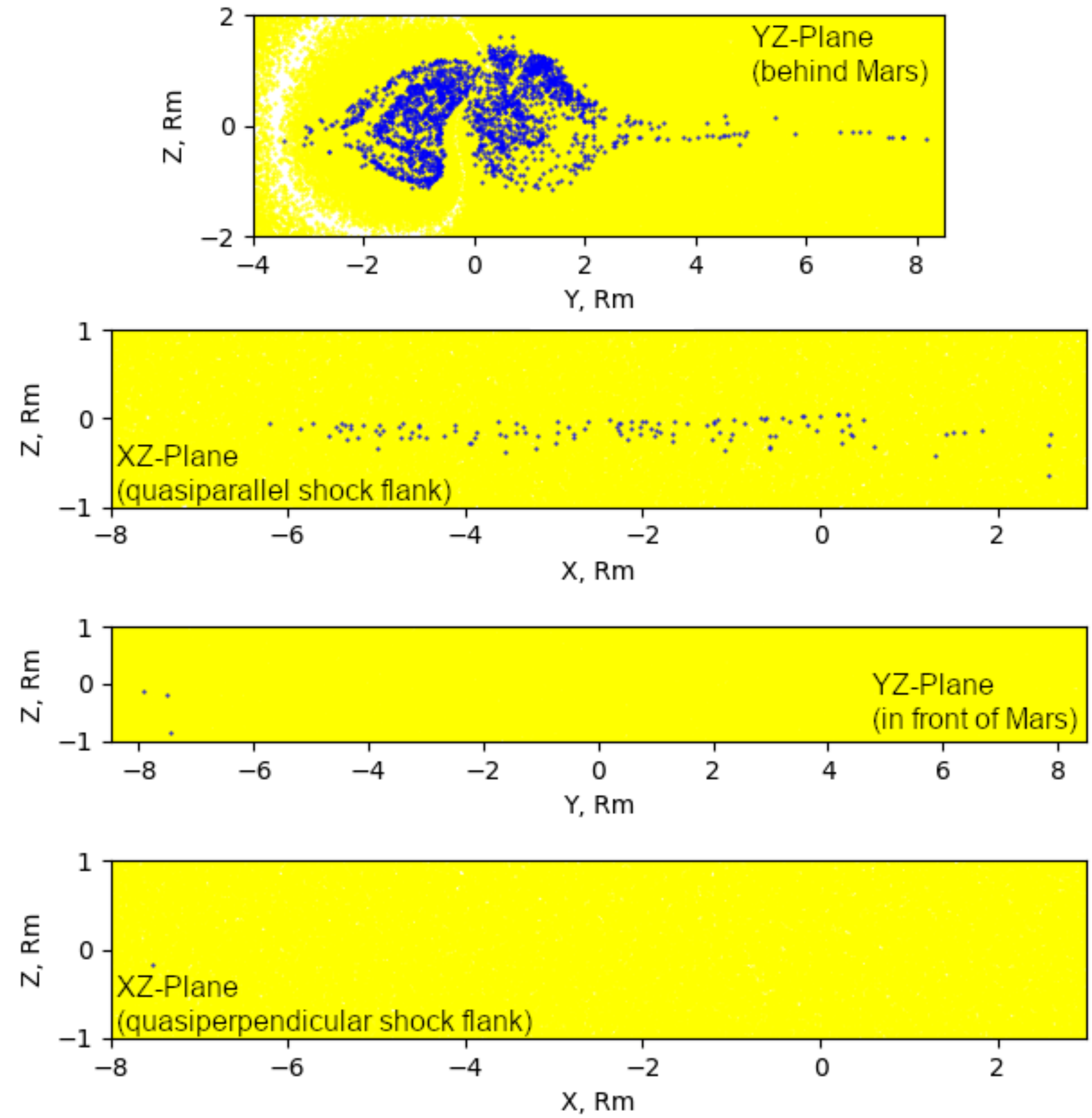

Figure 4.6: Initial locations of simulated particles that did not precipitate (yellow) and those that did precipitate (blue).

Figure 4.7a shows where these electrons precipitate. About 1.5x more electrons precipitate on the nightside (N = 1,341) of Mars than the dayside (N = 926). The electrons are not distributed evenly over the atmosphere and cluster at specific locations. Mapping the electrons over the spherical components of the magnetic field at the stopping altitude shows that electrons favor precipitating in low magnetization areas where $B\varphi \sim 0$ nT. These locations coincide with cusps in the crustal field arcades and where magnetic field lines deeply drape into the ionosphere.

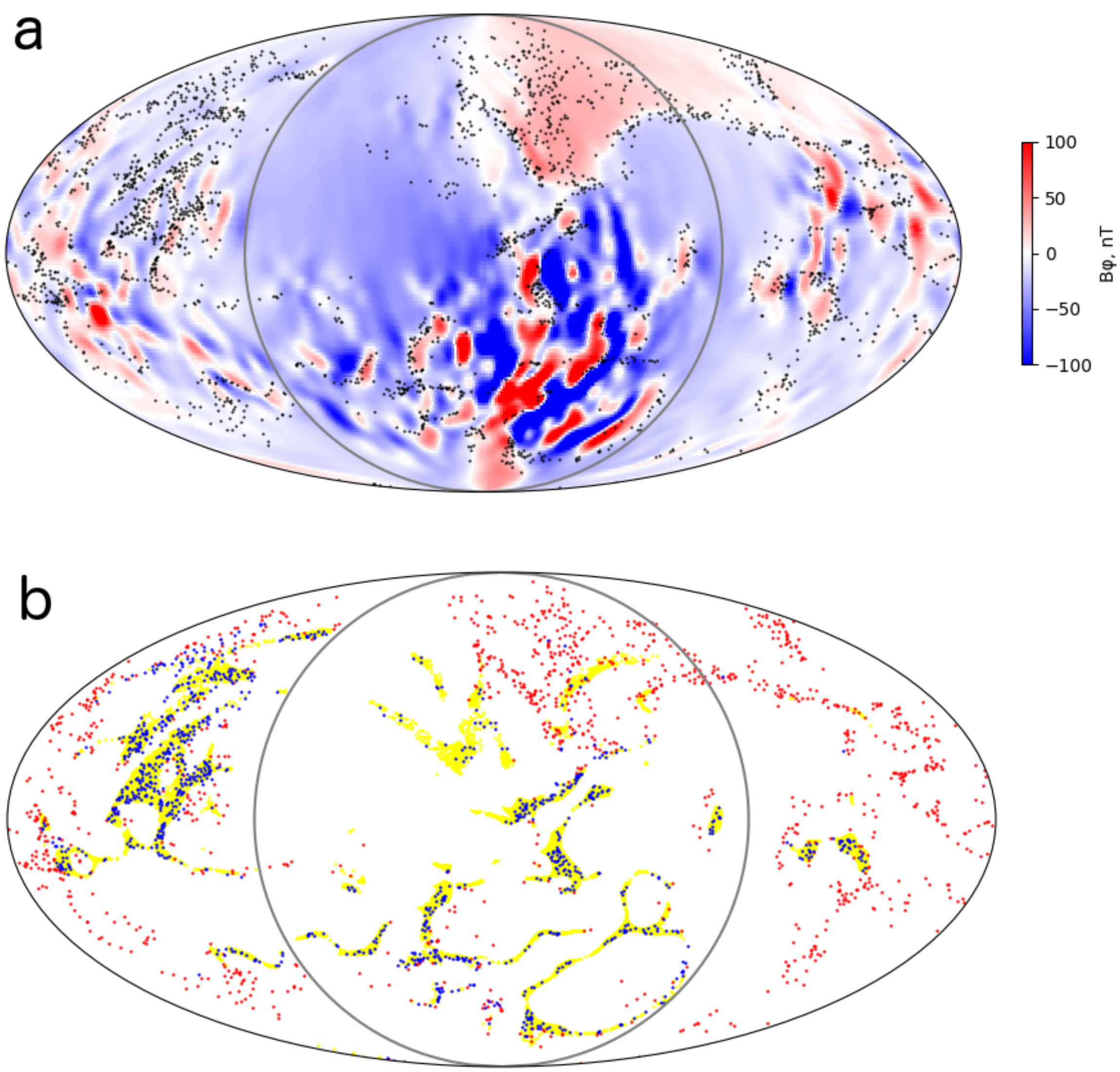

Figure 4.7: (a) Locations where SEP electrons precipitate at 200 km altitude over a Mollweide projection of the $B\varphi$ component of the magnetic field. (b) Locations where SEP electrons precipitate at 200 km colored by number of times the particle magnetically mirrors (blue if never, red if once or more) and locations where field lines connect to the solar wind (in yellow). The day-night terminator line is plotted in gray. The subsolar point is located at the center of the plot.

We map the field lines from the lower simulation boundary altitude of 200 km and identify where they connect to the solar wind. We will describe these regions as “open field lines”, as particles are expected to precipitate into these areas under the adiabatic approximation

[Brain et al. 2007, Xu et al. 2014, Weber et al. 2017]. It is important to caveat that this is not a strictly accurate definition of an open field line. Technically a field line can only be called “open” if it connects the IMF to the Martian crust. However, for the purposes of determining where electrons enter the atmosphere, a draped field line that intersects the atmosphere is as effective as an open field line, and we will call them both “open” for the sake of brevity.

Figure 4.7b shows that the simulated energetic electrons preferentially precipitate into open field lines. Like how the majority of simulated precipitating electrons originated from the magnetotail, the majority of open field lines were traced back into the deep magnetotail rather than the dayside or flanks. Approximately 55% (N = 1,243) of electrons that precipitate at an altitude of 200 km will precipitate within 100 km of the traced open field lines. That leaves 45% (N = 1,023) that entered far from the open field lines (>100 km), suggesting they drifted onto closed field lines.

We can indirectly investigate the role of drift by counting the number of times an electron “magnetic mirrors” by reaching a pitch angle of 90°. According to a simplified guiding center path approximation without drift terms, all electrons that magnetically mirror once would be turned away from Mars and cannot precipitate. However, electrons can drift by crossing the highly curved current sheet and appear to reach a pitch angle of 90°, entering Speiser-like orbits near the magnetotail. Gradient drifts can also transport electrons initially trapped on draped field lines onto open or closed field lines. Figure 4.8 shows representations of such orbits. While this analysis will not capture every possible drift, as curvature drift across a boundary like the bow shock wouldn’t be counted in this analysis, this is an indicator of the extent to which a simplified guiding center path approximation without drift terms breaks down.

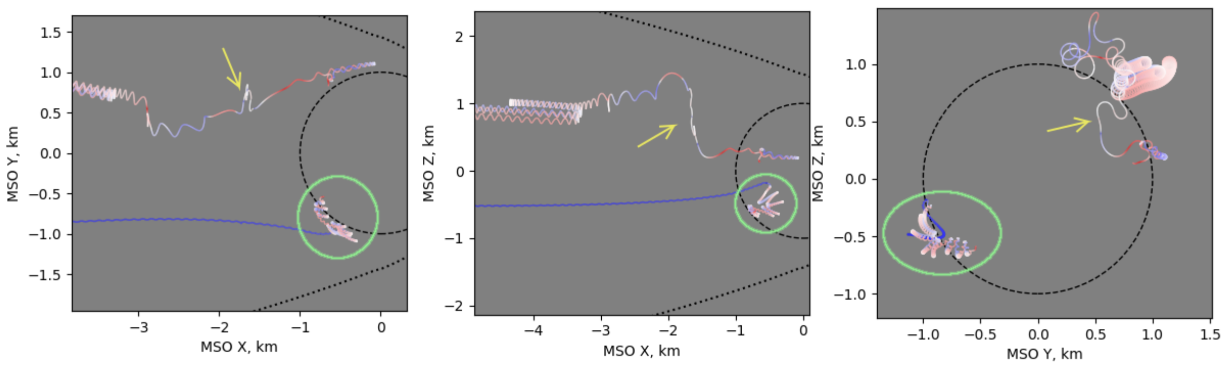

Figure 4.8: Two example traces of electrons that reach 200 km colored by pitch angle where blue is 0°, red is 180°, and white is 90° in the XY-plane (left), XZ-plane (middle), and YZ-plane (right). The region of a representative trace showing the see-saw bounce motion influenced by gradient drift is circled in green, while yellow arrows point to serpentine Speiser-like meandering in another representative trace. An outline of Mars and the magnetic pileup boundary is marked in black dashed lines.

Just over half of all simulated electrons (54.3%, N = 175,470) and under half of electrons that reach 200 km (47.5%, N = 1,077) will exit the simulation without magnetically mirroring. Of the ones that magnetically mirror, there are more simulated electrons that mirror only once (28.4%, N = 91,848) than multiple times (17.5%, N = 56,619). However this trend is reversed for electrons that reach 200 km, with less than half mirroring more than once (43.7%, N = 991) and a small fraction mirroring only once (8.8%, N = 199). This implies that drifts increase precipitation. Electrons drift at the point they magnetically mirror repeatedly onto field lines connected to the ionosphere. We also find that, of the electrons that ended up in proximity to open field lines when they reached 200 km, not all of them began on open field lines. About 13% of electrons precipitating on or adjacent to open field lines (N = 166) were recorded to have magnetically mirrored at least once, suggesting some electrons drift onto open field lines.

A cursory glance at the precipitation as a function of energy shows that more electrons with higher energy precipitate than electrons with lower energy. 0.6% of simulated 10-20 keV electrons precipitate compared to 1% of simulated 110-200 keV electrons. This is expected, as gradient drift motion is energy dependent.

Drift can be facilitated by both adiabatic and nonadiabatic mechanisms. In order to identify the role of nonadiabatic mechanisms, we repeated the analysis we did earlier on electrons entering the magnetotail for precipitating electrons. We calculated the pitch angle of each precipitated electron assuming the magnetic moment was conserved, and compared it to the pitch angle of the modeled electron. Only 24% had a pitch angle that roughly matches the calculated pitch angle (within 10°). By comparison, 38.2% of the electrons have pitch angles that differ by over 10 degrees, and 37.8% of the simulated electrons would have not reached Mars if they had conserved magnetic moment. This shows that over two-thirds of the simulated electrons were influenced by nonadiabatic transport mechanisms.

4.5.2. Calculating precipitating flux

So far we have used a test particle simulation to establish a qualitative picture of energetic electron behavior. We will now quantify energetic electron precipitation.

First we convert the test particle results into units of flux. This is done by summing over all test particles in an area after scaling each by the ratio of an assumed incident flux to the effective simulated flux. For the previously described simulation run, if the integrated instantaneous flux of 10-200 keV electrons during an event is 0.01 electrons cm^{-2} s^{-1}, the ASPEN model predicts a flux of 3.2×10^{-4} electrons cm^{-2} s^{-1} at an altitude of 200 km. The flux is depleted, which is expected from the qualitative behavior described in the prior section.

Instantaneous number fluxes of energetic particles vary by many orders of magnitude during an event. Instead of arbitrarily picking a time to estimate flux, we will report precipitating flux as a fraction of incident flux, F/F_{in}. This number directly describes precipitation, as fluxes are predicted to be enhanced if $F/F_{in} > 1$ and depleted if $F/F_{in} < 1$, and can be combined with any instantaneous flux observed during an event to estimate an instantaneous precipitating flux.

For example, ASPEN predicts that fluxes of 10-200 keV electrons are depleted to 3.2% of the incident flux (F/F_{in} = 0.032) at an altitude of 200 km.

The precipitating fraction of incident flux is dependent on our choice of electron spectra. Figure 4.9 shows predicted incident and precipitating differential energy fluxes for an assumed integrated instantaneous flux of 0.01 electrons cm^{-2} s^{-1}, and the fraction of incident differential flux. The earlier qualitative finding that more electrons with higher energy reach 200 km than lower energy electrons is supported. The fraction of precipitating differential flux is proportional to E^{υ} where $\upsilon = 0.2$ for electron energy E in range 10-200 keV. This implies that all energies would contribute equivalent precipitating flux if a power law of $E^{-\kappa}$ where $\kappa = 0.2$ described an incident spectrum. Similarly, the precipitating flux will be dominated by lower energy electrons for energetic electron spectra "softer" than this (e.g., $E^{-\kappa}$ where $\kappa < 0.2$). Energetic electron spectra generally follow a power law on the order of $\kappa \sim 0.6$ to 2 that steepens to $\kappa \sim 2.4$ to 4.3 above 200 keV [McGuire and von Rosenvinge 1984]. Thus the majority of precipitating energy flux into the Martian atmosphere should come from the lowest SEP electron energies.

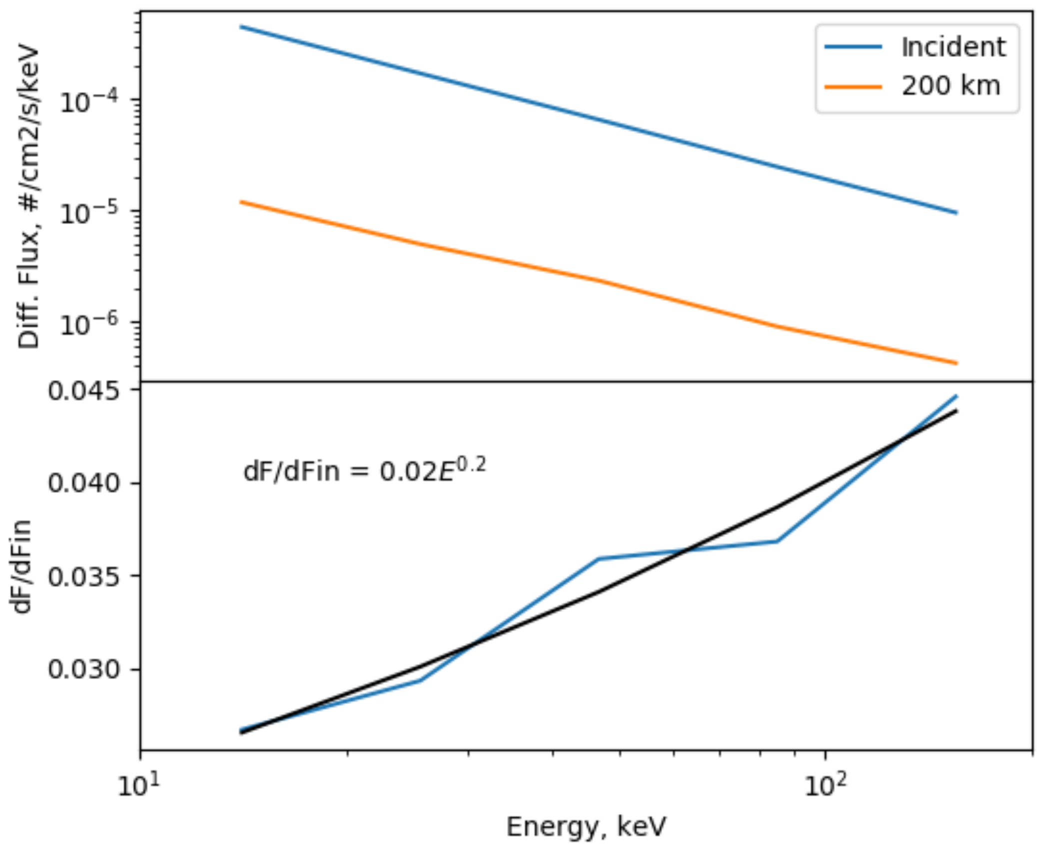

Figure 4.9: Differential energy fluxes of incident and predicted precipitated electrons for a hypothetical energetic electron event (top) and relative fraction of flux that precipitates (bottom).

ASPEN-predicted flux depletion can be compared to an estimate of flux depletion from guiding center path theory in the absence of drift. If electrons are unaffected by drifts this guiding center approximation predicts they will only precipitate on open magnetic field lines if they are in the loss cone. The flux at 200 km is proportional to the product of the fraction of open field lines over the surface and the fraction of flux that can enter the loss cone on those open field lines. We can trace 100,000 random field lines from the lower simulation boundary at an altitude of 200 km. Out of that number, 9% are open field lines. We can then calculate the depletion:

$$F/F_{in} = \left(\sum_i^{N_{open}} f_{lc,i}\right)/N = \left(\sum_i^{N_{open}} 1 - \cos\theta_{lc}\right)/N \quad (4.5)$$

F/F_{in} is 0.5%. Global precipitation is over six times higher than what would be predicted by a simplified guiding center path approximation without drift terms.

The model can also predict fluxes as a function of MSO latitude and longitude at an altitude of 200 km (Figure 4.10). The flux is globally depleted. Energetic electron fluxes are least attenuated at cusps and the post-midnight zone of the nightside. The cusps around the strongest crustal fields at latitudes below 60° S can receive up to 22.5% of incident flux and the post-midnight zone (LT 2:30-4:30) between latitudes of 0° - 30° N can receive up to 27% of incident flux.

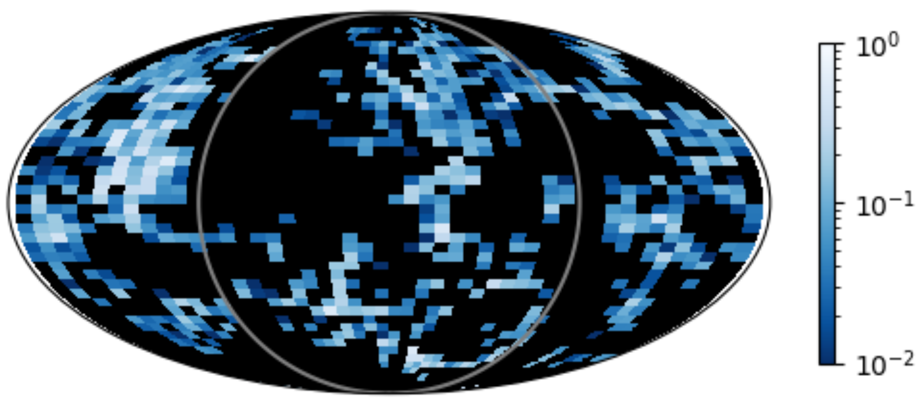

Figure 4.10: Fraction of incident flux that precipitates at 200 km altitude as a function of MSO latitude and longitude. Black pixels are plotted where zero electrons are recorded reaching 200 km altitude in the simulation.

Fluxes can also be predicted as a function of altitude and local time (Figure 4.11). At midday, dawn, and dusk, fluxes are approximately the same at altitudes above 2,000 km. In contrast, energetic electron fluxes at night are depleted by up to a factor of 2 above an altitude of 2,000 km. The fluxes are structured at lower altitudes, with local enhancements and depletions below 2,000 km. The pre-midnight and post-midnight profiles are different below 3,000 km because the structure of the crustal anomalies is not symmetric across the distant current sheet plane. Geographical variability in crustal fields will cause discrepancies between pre- and post-midnight fluxes. In addition, the interaction between crustal fields and IMF twists and offsets the location of the magnetotail current sheet [DiBraccio et al. 2018]. In the MF-MHD results, the current sheet in the equatorial plane is pushed towards the pre-midnight plane close to Mars and fewer open field lines connect to the pre-midnight sector. This supports that the interaction between crustal fields and the draped IMF leads to different fluxes in the post- and pre-midnight sectors. Enhancements below 2,000 km are likely linked to electrons diverting and mirroring over closed field lines, as they occur above regions where depletions occur. The pre-midnight altitude profile shows this most clearly with depleted fluxes at 950 km and 650 km alternating with enhanced fluxes at 1,050 km and 450 km. All altitude profiles except for the one during midday are attenuated to below a tenth of incidence at 200 km.

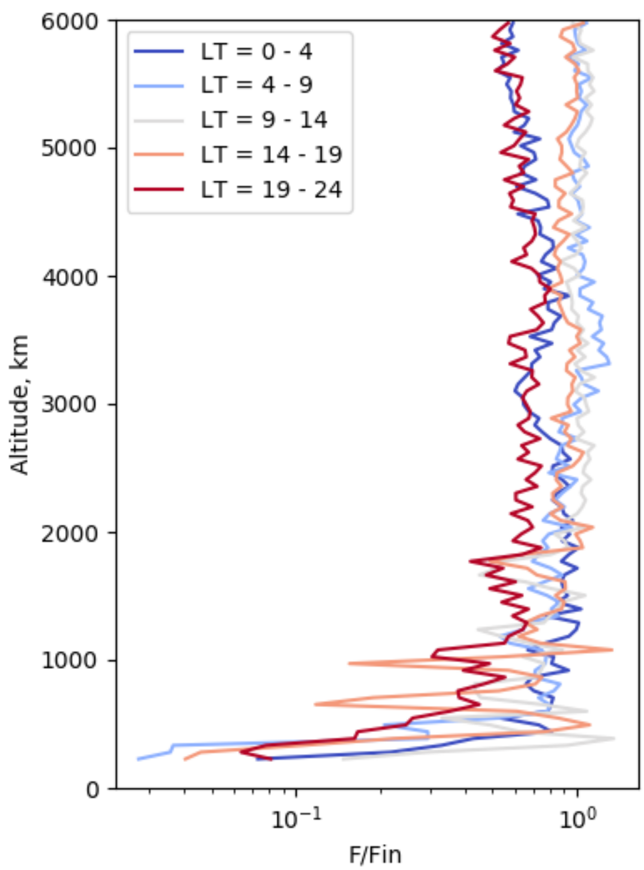

Figure 4.11: Fraction of incident flux as a function of altitude for different local time ranges: post-midnight (LT 0-4), dawn (LT 4-9), midday (LT 9-14), dusk (LT 14-19), and pre-midnight (LT 19-24).

Finally, the model can quantify the influence the bow shock has on energetic electron fluxes. Figure 4.12a shows energetic electron fluxes in the equatorial plane. Depleted fluxes are found between the bow shock and the pileup boundary in the magnetotail. The fraction of flux in this region is ~20-40% of the incident. This is expected, as particles should follow field lines diverging out of the equatorial plane as they drape around Mars. Fluxes are also somewhat depleted in the region immediately behind Mars. This is also visible in Figure 4.12b, which shows energetic electron fluxes in the meridian plane. The depletions at lower altitudes are visible in Figure 4.12b and coincide with crustal field regions. Unfortunately, these equatorial and meridian flux maps are low resolution and susceptible to test particle discretization artifacts. In particular, the alternating bands of high and low fluxes outside the bow shock in Figure 4.12a are caused by binning test particles with gyroradii less than the bin size. Multiple gyrations from the same simulated particle cause multiple counts in the same bin, leading to bands along the IMF direction. The bands reduce in intensity as the number of simulated particles is increased, and disappear when the average gyroradius exceeds the bin size.

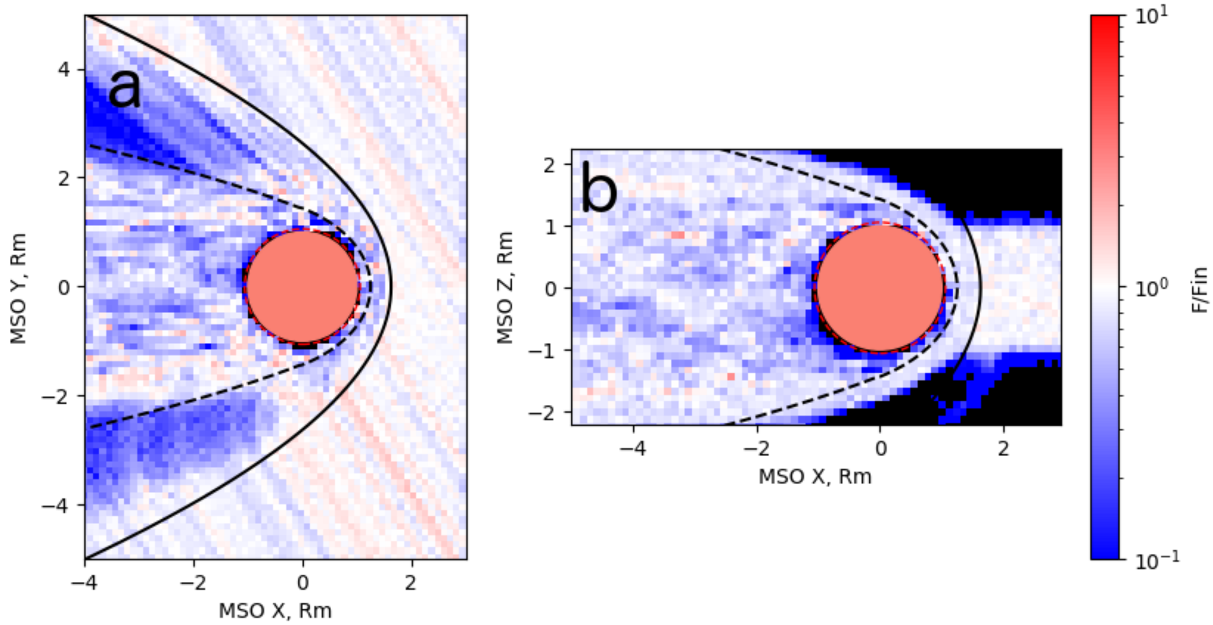

Figure 4.12: Fluxes of 10-200 keV electrons in the (a) equatorial (Z = 0) plane and (b) in the meridian (Y = 0) plane. Areas where no electrons were counted are marked in black. Solid and dashed black lines mark the bow shock and magnetic pileup boundary conic section fits from Trotignon et al. [2006].

4.6. Modeling energetic electrons for different IMF configurations

During a SEP event, the IMF may vary considerably. While the full time-dependent response to the changing IMF conditions that can accompany a SEP event is out-of-scope for this study, the precipitation response to a toward-sector IMF ($B_y < 0$) was modeled to look for changes in precipitation. In addition, higher energy electrons (0.2-2 MeV) were simulated using the power law distribution with κ set to -2.4 as recommended in McGuire and von Rosenvinge [1984]. Finally, to assess the role of crustal fields in either obstructing or increasing SEP precipitation, the simulation was run using MF-MHD fields that were calculated without crustal fields.

Table 4.1 shows simulation results for different IMF configurations and the relative fraction of flux that precipitates. The IMF configuration did not strongly influence the relative fraction of flux, as slightly higher precipitation was predicted for the away sector IMF than for the toward sector IMF. On the other hand, the energy of precipitating particles significantly increased the flux. The precipitating fraction of 0.2-2 MeV electrons was a factor of 1.75-2 times higher than the precipitating fraction of 10-200 keV electrons. This supports the conclusions of curvature and gradient drifts increasing precipitation, as these drifts increase in magnitude for higher energy particles. Finally, removing crustal fields from the model seems to reduce precipitation, as the precipitating flux with crustal fields is higher by a factor of 1.4.

MF-MHD parameters (IMF orientation, presence of crustal fields)	ASPEN parameters (Simulated electron energies)	Percent of simulated particles that precipitate (Number precipitated)	Relative fraction of flux
Away ($B_y > 0$), with crustal fields	10-200 keV	0.7% (N=2,267)	0.032
Toward ($B_y < 0$), with crustal fields	10-200 keV	0.6% (N=1,916)	0.026
Away ($B_y > 0$), with crustal fields	0.2 - 2 MeV	1.3% (N=4,230)	0.056
Toward ($B_y < 0$), with crustal fields	0.2 - 2 MeV	1.2% (N=3,317)	0.054
Away ($B_y > 0$), no crustal fields	0.2 - 2 MeV	0.8% (N=1,767)	0.039

Table 4.1: The fraction (and number) of simulated particles that precipitate and fraction of precipitating flux for different permutations of MF-MHD and ASPEN parameters.

Figure 4.13 shows the predicted precipitation maps for a subset of these model runs. The higher energy fluxes have a much broader area of precipitation on the nightside of Mars and in the northern hemisphere. Reversing the IMF shifts the distribution, which is expected since a different IMF interaction with the crustal fields should change the magnetic topology in weaker magnetic field regions. Finally, the absent crustal fields case shows that if there were no crustal fields, precipitation would be limited to the nightside. This is expected since the magnetic fields drape deeper into the ionosphere in the absence of crustal fields, so the particles traveling along field lines will precipitate on the nightside before the field line crosses the terminator.

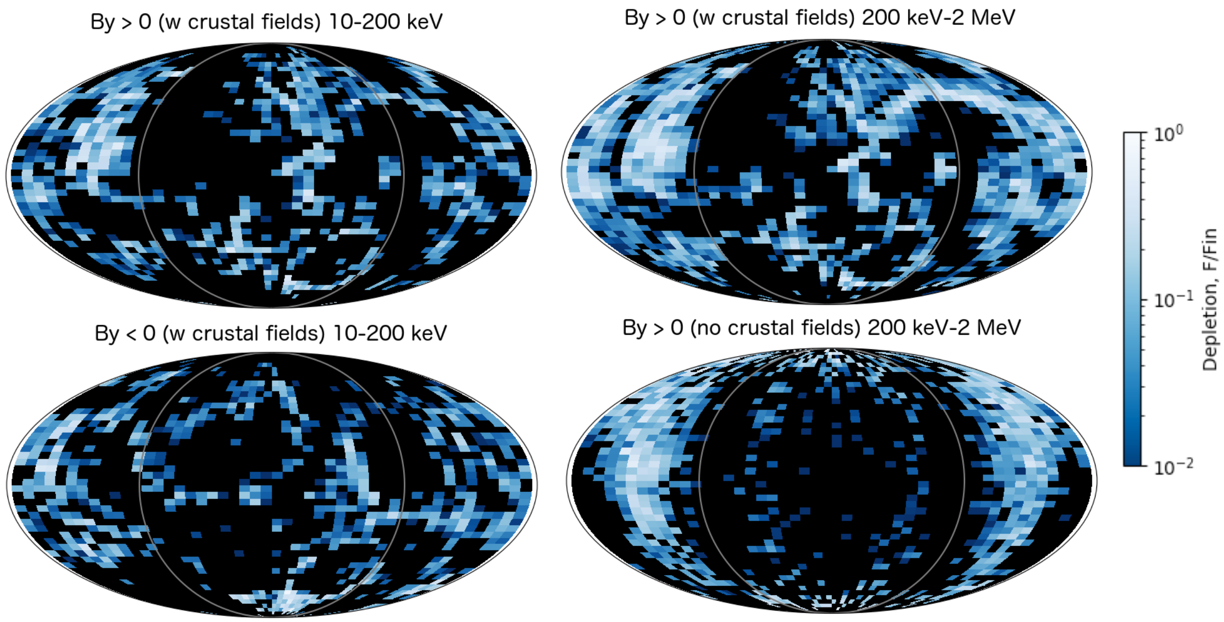

Figure 4.13: Maps of precipitating flux depletions for four cases: 10-200 keV electrons in an away sector IMF with crustal fields (top left), 0.2-2 MeV electrons in an away sector IMF with crustal fields (top right), 10-200 keV electrons in a toward sector IMF with crustal fields (bottom left), and 0.2-2 MeV electrons in an away sector IMF without crustal fields (bottom right).

4.7. Discussion

We have made predictions of electron precipitation under nominal IMF conditions. These conditions are relevant to a subset of energetic particle events where there is no accompanying solar wind disturbance, such as when Mars is magnetically connected to a moving shock front ahead of a coronal mass ejection during the early phase. Three such events were observed by the Mars Atmospheric and Volatile EvolutioN (MAVEN) spacecraft at Mars out of a survey of twenty-one events during the declining phase of solar cycle 24 from December 2014 to May 2016 [Lee et al. 2017].

It is more common that the arrival of energetic particles at Mars coincides with disturbed solar wind conditions. The increased solar wind density and interplanetary magnetic field from corotating interaction regions (CIRs) and coronal mass ejections (CMEs) can compress the Martian induced magnetosphere, pushing plasma boundaries towards Mars and increasing ion escape [Dubinin et al. 2009, Opgenoorth et al. 2013, Dong et al. 2015]. MAVEN observations have shown that the interface between draped and closed field lines are likewise compressed, and models predict that reconnection will increase the proportion of open field lines [Xu et al. 2018, Luhmann et al. 2017]. Knowing this, we can expect that the extent of cusps will increase during disturbed conditions and the total precipitating flux into cusps along open field lines will increase as well. However, it is unclear how the nonadiabatic precipitation mechanisms will be affected, if at all, by disturbed solar wind conditions. The increased overall magnetization of the induced magnetosphere and tail lobes could make drifts more significant and facilitate precipitation. Alternatively, the induced magnetization could have the effect of shortening the effective gyroradius of electrons in the magnetotail, reducing the proportion of particles that are able to precipitate after several current sheet crossings. The significance of these mechanisms has yet to be determined and is an important topic for future studies.

We have also fixed two key properties of SEP populations for this study, spectrum hardness and anisotropy. These parameters can vary from event to event. To assess the choice of spectrum hardness, we have estimated precipitating flux fraction as a function of energy, E^{ν} where $\nu \sim 0.2$. While this implies harder spectra should have overall higher precipitation, the majority of observed energetic electron spectra is “softer” and described by $E^{-\kappa}$ for $\kappa \sim 0.6$ to 2. Low energy SEP electrons will carry the bulk of SEP electron energy deposited.

There is also the matter of SEP anisotropy. While continuously anisotropic electron events are not common, SEPs can be anisotropic during the early hours of many events. We can expect that field-aligned SEP electrons will be more likely to precipitate into cusps. Field-aligned electrons will also be more strongly affected by curvature drifts at the quasiparallel shock, due to how curvature drift is proportional to parallel velocity, making the depletion regions starker.

Since field-aligned SEPs are likely to arrive before CME ejecta or a CIR pressure pulse, the presented model predictions under nominal IMF conditions are likely to hold.

The focus of this study is on 10-200 keV electrons precipitating into the Martian atmosphere. We'd be remiss to not discuss applicability to one of the more significant findings related to this particle population: diffuse aurora. An extended diffuse emission over the northern hemisphere was observed during a strong SEP electron event in December 2014. Modeling has suggested the emission is caused by ~60-200 keV electrons [Schneider et al. 2015, Gérard et al. 2017, Haider and Masoom 2019]. Our simulations suggest electrons of these energies would preferentially precipitate discretely along open field lines, rather than precipitating diffusely. As the spectra reported during the event is softer than the spectra simulated in the presented model (~E-2.2), the tendency to precipitate into cusps should be intensified. However, the model predictions are made for a non-disturbed magnetic environment and with the crustal fields fixed on the dayside. Lee et al. [2017] describes the event in detail. At the onset of the highest SEP electron fluxes, the IMF reverses from antisunward to sunward followed by a CME flank impacting Mars. It is possible that IMF reversal reconfigured the magnetic field topology on the nightside and the pressure pulse increased the extent of the resulting cusps, leading to broader geographical precipitation than what would be predicted for nominal conditions.

4.8. Conclusions

We have described and implemented a test particle simulation that predicts energetic electron precipitation in the Mars-solar wind interaction. Unlike for SEP protons, we have found the magnetic field configuration of Mars influences where energetic electrons can precipitate. However, energetic electrons can exhibit drift motion such as curvature drift across the quasiparallel shock and gradient drift over the ionosphere. The former leads to depletions within the bow shock, while the latter leads to precipitation onto closed magnetic field lines. We have also shown that there is a minor contribution of electrons that reach the magnetotail nonadiabatically, which can slightly increase predicted precipitation by a factor of 1.25.

Our model predicts that, for a “typical” isotropic energetic electron spectra incident on Mars when the crustal fields are oriented on the dayside during an away-sector IMF, ~3% of the incident flux reaches the atmosphere. We have also estimated the fraction of precipitating differential flux varies as a function of energy, $\sim E^{\upsilon}$ for $\upsilon = 0.2$. These estimates can be combined with any observed energetic electron flux to estimate precipitating flux into the atmosphere, which can in turn be used to quantify energy input by SEPs. We have shown the predicted fraction of flux that precipitates exceeds estimates made using a simplified guiding center path approximation by over six times. This is linked to gradient and curvature drifts, and nonadiabatic mechanisms like meandering motion across the magnetotail current sheet. Approximately 55% of precipitation occurs in the vicinity of open field lines, while the remaining 45% occurs on closed fields.

We have mapped where energetic electron fluxes precipitate into the atmosphere. Energetic electron fluxes are particularly depleted over draped fields, while precipitation is favored into cusps and regions of the nightside connected to open field lines. While our map is limited in applicability due to the assumed conditions of an away-sector IMF and dayside-oriented crustal fields, the result shows that energetic electron precipitation is non-uniform and globally patchy. Since the locations of open field lines are partially controlled by crustal field orientation and IMF configuration [Ulusen et al. 2016], we can predict that the pattern of precipitation will shift upon varying these conditions. This is a recommended topic for further study.

Finally, we have contextualized the model and applicability to SEP events. We have described how precipitation would likely be impacted by disturbed solar wind conditions that accompany many SEP events. We also investigated the model assumptions of isotropic SEPs for a specific electron spectrum. Given the influence of curvature drifts and how precipitation is favored into open field lines, we suggest a higher fraction of anisotropic SEP electrons would likely precipitate. We present a formula for fraction of precipitating differential flux that can also be combined with different SEP spectra to estimate precipitating flux for varying spectra hardness. We have also discussed how geographically diffuse aurora has been linked to precipitation of 10-200 keV electrons, while the simulation has predicted that the same electrons would precipitate in a structured manner over the nightside.

Taking this study further would entail applying the model to specific events, particularly during disturbed solar wind periods. While we predict precipitation should increase due to increased access to the atmosphere along open field lines, additional models would be able to show how nonadiabatic transport would be influenced by the passage of CME ejecta or CIRs. The results would further bound the input of energetic electrons into the atmosphere of Mars, which is relevant to quantifying the energy input of extreme space weather.

There are also avenues for data-model comparison. We can compare predictions of where SEPs precipitate to locations of observed electron-induced aurora at Mars, which can help uncover the processes that lead to aurora. There is also a SEP monitor aboard MAVEN that is currently recording energetic electron fluxes. Because MAVEN's orbit is elliptical, the SEP monitor would be able to record depletions as a function of altitude during events. It is possible to modify the model approach to improve resolution and compare directly to MAVEN SEP observed fluxes.

Chapter 5

Inventory of energy input

This chapter will be submitted to the Journal of Geophysical Review as "Energy input of EUV, solar wind, and SEPs at Mars: MAVEN observations during solar minimum" following submission of this thesis.

5.1. Introduction

Solar energy inputs drive atmospheric, ionospheric, and induced magnetospheric processes at unmagnetized planets like Mars. Solar extreme ultraviolet (EUV) radiation ionizes the upper atmosphere, generating an ionosphere. Without an intrinsic magnetic field, the incoming solar wind flow induces currents in the ionosphere to form an induced magnetosphere. Solar wind plasma is then shocked, decelerated, and deflected around the resulting magnetic fields (see Nagy et al. [2004] and references therein). However, the solar wind can directly impart energy to the atmosphere, both as ions that have been converted into energetic neutral atoms (ENAs) that impact the dayside and electrons precipitating into magnetically connected regions of the upper atmosphere, which are known as "open field lines" [Brain et al. 2007]. In addition, extreme solar activity such as coronal mass ejections (CMEs) can direct extremely energetic particles called solar energetic particles (SEPs) towards Mars, which may episodically deposit substantial energy to the upper atmosphere.

Many prior studies have separately quantified the energy received from EUV, solar wind, and SEPs. Solar energy flux in the EUV is the dominant energy source, heating the Martian atmosphere and producing the majority of the Martian ionosphere via direct photoionization and photodissociation and secondary impact by resulting photoelectrons (for further details, see Bougher et al. [2017] and references therein). Variation in received EUV irradiance leads to observable dayside atmospheric and ionospheric responses, and can be caused by Mars' seasonal variation (e.g. tilt, varying heliocentric distance between 1.38-1.67 AU) and solar variation (e.g. solar rotation, solar cycle). Precipitating particles can be an additional, but usually minor, energy source relative to EUV on the dayside of Mars. Analysis of Mars Global Surveyor data shows that solar wind and/or magnetosheath electrons impart between 0.1-2.0% of the incident EUV energy flux to magnetically connected regions of the dayside [Xu et al. 2014]. Due to a dearth of observations of energy deposited by ENAs and SEPs in the Martian atmosphere, models have been used to predict atmospheric energy deposition by these particles on the dayside. These modeling efforts have predicted that EUV energy deposition in the atmosphere exceeds the energy deposited from precipitating ENAs by two orders of magnitude and from precipitating SEPs by one order of magnitude [Kallio and Barabash 2001, Leblanc et al. 2002].

On the other hand, precipitating particles may be more significant on the nightside of Mars. Radar investigations have found that the nightside ionosphere is transient. The presence of ionospheres in weakly-magnetized regions is controlled by proximity to the terminator, implying cross-terminator transport of ions and photoelectrons from the dayside, while ionospheres in magnetized regions depend on connectivity to the solar wind, implying electron precipitation [Němec et al. 2010, 2011; Girazian et al. 2017]. Several models have estimated substantial ionization on the nightside from precipitation of different electron populations from the solar wind, plasma sheet, and magnetotail [Fox et al. 1993, Haider et al. 2002, Fillingim et al. 2007, Lillis et al. 2009, Niu et al. 2021].

Modeling has also estimated that SEP protons could increase the ionization substantially, as predicted ion production associated with the peak SEP spectra during the 2003 Halloween CME event exceeded average nightside electron precipitation ion sources by up to three orders of magnitude [Lillis et al. 2012]. SEP protons are also more likely than solar wind electrons to access areas that are not magnetically connected to the solar wind [Leblanc et al. 2002, Jolitz et al. 2017], although there is evidence for shadowing of SEP ions antisunwards of Mars along the interplanetary magnetic field and solar wind flow directions [Luhmann et al. 2007, McKenna-Lawlor et al. 2012]. This doesn't necessarily hold for SEP electrons, as modeling suggests that SEP electron precipitation and associated ionization would be more closely confined to magnetic cusps [Jolitz et al. 2021]. Radar sounding has supported the finding of elevated ionization during SEP events [Němec et al. 2014, Morgan et al. 2014, Harada et al. 2018]. However, these ionization enhancements may instead be associated with simultaneously occurring high dynamic pressure pulses, which compress the ionosphere and increase magnetic connectivity, leading to increased non-SEP electron precipitation [Diéval et al. 2014].

Given the prevalence of studies describing solar energy inputs under disparate solar conditions and seasons, it is beneficial to have an overarching study that directly compares the energy input of each solar driver received by Mars over time. SEPs in particular have previously been studied on an event-by-event basis at Mars, and prior ionization estimates have been made using near-Earth proxies rather than Mars-based observations. Coincident measurements of each solar driver at Mars offer a birds-eye view of the total energy input received by Mars, allowing clear and direct comparisons of solar drivers at the same season and solar activity. The Mars Atmosphere Volatile Evolution (MAVEN) spacecraft has four instruments that observe EUV, solar wind, and SEPs simultaneously at Mars. The spacecraft's precessing elliptical orbit allows the instruments to semi-frequently sample incident fluxes before they are perturbed by the near-Mars plasma environment.

Since MAVEN has orbited Mars for over three Mars years during the declining phase of solar cycle 24 (SC 24) and onset of solar cycle 25 (SC 25), the instruments have measured both seasonal and solar cycle variability of each solar input. Seasons modulate all solar energy inputs, as EUV irradiance, SEP flux, and solar wind density decreases with increased heliocentric distance, although SEP flux attenuation over distance is more variable and event-dependent [Smart and Shea 2003]. In addition, solar wind and EUV energy fluxes are correlated with the solar cycle [Lean 1997, Le Chat 2012]. The correlation between the solar cycle and SEP energy fluxes is less certain. While CMEs are more frequent at solar maximum and can generate significant SEP fluxes, SEP fluxes can also be released by corotating interaction regions (CIRs), which are more common during solar minimum [Reames 2021, Richardson 2004].

In this chapter, we compute and compare energy fluxes of EUV, SEPs, and solar wind observed by MAVEN at Mars. We review the relevant MAVEN instruments and data processing for each solar driver. We describe the approach taken to process fluxes observed by the SEP instrument, especially identifying and filtering observations containing oxygen contamination. We then estimate the net energy input at Mars, mitigating inter-event variation by calculating average energy flux during multimonth periods when MAVEN has access to the undisturbed solar wind for consecutive orbits. We also estimate the net energy flux that reaches Mars, which varies across the solar drivers. We then discuss the impacts of seasonal and solar cycle variation, noting the onset of solar minimum and how it differs for each solar driver. We finally contextualize our observations with prior study discussions on previous solar cycle intensities and estimates of young sun energy fluxes.

Due to the spacecraft's precessing elliptical orbit, MAVEN does not always have consistent daily access to the solar wind. There can be long periods of time where the spacecraft does not encounter the solar wind, corresponding to when the spacecraft is located on the dayside during periapsis. We used fits from Trotignon et al. [2006] to estimate times when the spacecraft is likely located outside of the bow shock and retrieve the corresponding observations between 2014 December 1 and 2020 October 14. We then split the resulting dataset into periods of consecutive daily solar wind coverage. There are thirteen such periods and the duration of each ranges from 61 days to 137 days. Calculating average energy fluxes during these times is equivalent to integrating fluxes for 2-5 Carrington rotations, mitigating the influence of solar rotation on results.

5.2. Data

The datasets used in this thesis come from four instruments aboard MAVEN. The EUV monitor (EUV) records irradiance in three wavelength bands, which is used to constrain the Flare Irradiance Spectral Model (FISM) and provide a Level 3 data product of spectral irradiance between 0 and 194 nm with 1 nm resolution and a cadence of 1 minute [Eparvier et al. 2015, Thiemann et al. 2017]. We applied the accompanying quality flag that demarcates when the sun is fully in the field-of-view to select only high quality data. Spectral irradiance was then integrated over the range of EUV wavelengths (10-120 nm) and converted into units of energy flux (eV/cm^2/s).

The Solar Wind Ion Analyzer (SWIA) records differential energy fluxes of 25 eV - 25 keV ions, which covers the range of solar wind proton energies. SWIA is a toroidal electrostatic analyzer mounted on the side of the spacecraft so it can sample the solar wind when the spacecraft is outside the shock (see more details in Halekas et al. [2015a]). The instrument's Level 2 data product consists of energy fluxes as a function of energy and two internal sensor angles, deflection angle and hemispheric angle. We use the coarse data product, which has a cadence of 4 seconds and resolution of 48 energy bins. While SWIA records a higher-resolution "fine" data product that is intended to observe solar wind fluxes specifically, solar disturbances can sometimes introduce interplanetary shocks to the Mars system that trigger SWIA to record flux in only the "coarse" data product. We average the energy fluxes over all internal sensor angles to determine a single energy flux at a given time. Since SWIA is an electrostatic analyzer, the instrument has a constant background energy flux from extremely energetic particles like galactic cosmic rays (GCRs) and SEPs penetrating the instrument housing and leaving false counts. SWIA can also occasionally observe ionized oxygen "picked up" and accelerated by the solar wind at energies between 2-10 keV [Rahmati et al. 2017]. However, the energy flux of the solar wind beam is four orders of magnitude higher than the GCR/SEP background and three orders of magnitude greater than pickup oxygen fluxes, so there is no need to correct the data for these sources.

The Solar Wind Electron Analyzer (SWEA) records energy fluxes of 3-4600 eV electrons. Like SWIA, it is also a hemispheric electrostatic analyzer with a 4 second cadence, sweeping over two internal view angles (see more details in Mitchell et al. [2016]). We use the

Level 2 energy spectra data product that is already averaged over the view angles, which has a resolution of 64 energy bins. GCRs and SEPs also contribute to background counts in SWEA, but are generally negligible compared to solar wind electron fluxes. On the other hand, spacecraft charging can significantly affect the measured fluxes [Lavraud and Larson, 2016]. We correct the spectra for the shift in energy and increase in fluxes when the spacecraft is charged to between +3 to +10 V in sunlight, using the spacecraft potential calculated from the discontinuity in the low-energy SWEA spectra from Mitchell et al. [2016].

The Solar Energetic Particle (SEP) instrument records fluxes of 20 keV - 7 MeV ions and 20-200 keV electrons. The instrument is a pair of double-ended solid state telescopes (SSTs) that are mounted on opposite sides of the spacecraft, which leads to observations in four orthogonal look directions. The observed fluxes in each look direction are recorded in the Level 2 data product and labeled according to the sensor number, “1” or “2”, and how the detector is oriented with respect to the spacecraft, “F” for forward or “R” for reverse (see more details in Larson et al. [2015]). Each sensor has an attenuator, which activates when the sun is in a fraction of the field-of-view or when the SEP fluxes exceed a threshold (>20 kHz). The SEP instrument response when attenuators close is complex and not yet determined, so we exclude data from when one SST or both have closed attenuators. Fluxes from this instrument require in-depth correction in a process that will be described in the next section.

Once all datasets are corrected for contamination and measurement error, we integrate each spectra, over energy for particles and wavelength for photons, to calculate the energy flux of each solar driver. The number flux of each particle solar input is similarly determined. However, a final processing step is required. While these fluxes are calculated during times when the spacecraft encounters the solar wind per the Trotignon et al. [2006] empirical formula for the bow shock location, the bow shock is not a static boundary and can diverge from this formula, particularly during space weather events [Gruesbeck et al. 2018, Kajdić et al. 2021]. If the bow shock is located further from Mars than the empirical formula suggests, we sample the sheath in addition to the solar wind. Since we are quantifying solar inputs before they are processed by the Mars plasma environment, we need to exclude this data. In particular, sampling the sheath is recognizable in SWIA and SWEA data as rapid 10 to 100 fold increases in fluxes as the plasma is heated and energized. Observations in the sheath present as significant outliers. For each presumed solar wind pass, we identify outliers by calculating the logarithm of the number fluxes and excluding observations that exceed the average by at least one standard deviation. This approach, called standard scoring or z-scoring, was evaluated and confirmed to successfully remove sheath contamination from SWEA and SWIA data.

5.3. MAVEN SEP data contamination: Sources and mitigation

The Level-2 data product from the SEP instrument consists of electron and ion spectra for each SEP look direction. The datasets have slightly different energy bins owing to differences in energy response characteristics of the detectors within each SST (e.g. dead layer thickness), and slightly different time bins since SEP 1 and SEP 2 are commanded separately. In addition, low fluxes associated with minor events or the background are noisy in the instrument's native 1-32 second accumulation windows. Before identifying contamination or computing the average SEP flux, a rolling window is applied to the fluxes observed in each energy channel such that a minimum number of counts are recorded in a variable time window. If less than five counts are recorded in a given SEP observation, counts are summed across multiple observations until at least five counts are recorded and the resulting flux is calculated over the rolling window duration. The fluxes of each energy channel are subsequently interpolated over a common time axis and the resulting spectrum is interpolated over a common energy axis. Figure 5.1 shows this approach applied to an hour of ion fluxes recorded by SEP 1 in the forward look direction for three cases: background fluxes in the absence of SEP events on 2020 March 20, mild fluxes associated with a weak CME on 2020 October 9, and high fluxes associated with a sequence of CMEs on 2015 March 3. These cases demonstrate that this procedure does not alter measured fluxes when counts are above the count limit during strong SEP events, reduces noise in weaker SEP events, and allows a determination of the background in the instrument due to non-SEP sources. While the variable rolling window can obscure changes in fluxes that occur within the variable time windows, the overall trends are preserved if the variable time windows do not exceed the duration over which SEP fluxes evolve. The duration of the variable time windows were longest while recording non-SEP background, which was several minutes for energies below 100 keV and 10s of minutes for energies above 100 keV. These rolling window durations are shorter than the time it takes for SEP fluxes to evolve (hours to days) and our studied time periods (tens of days), so we deemed the reduced resolution an acceptable tradeoff.

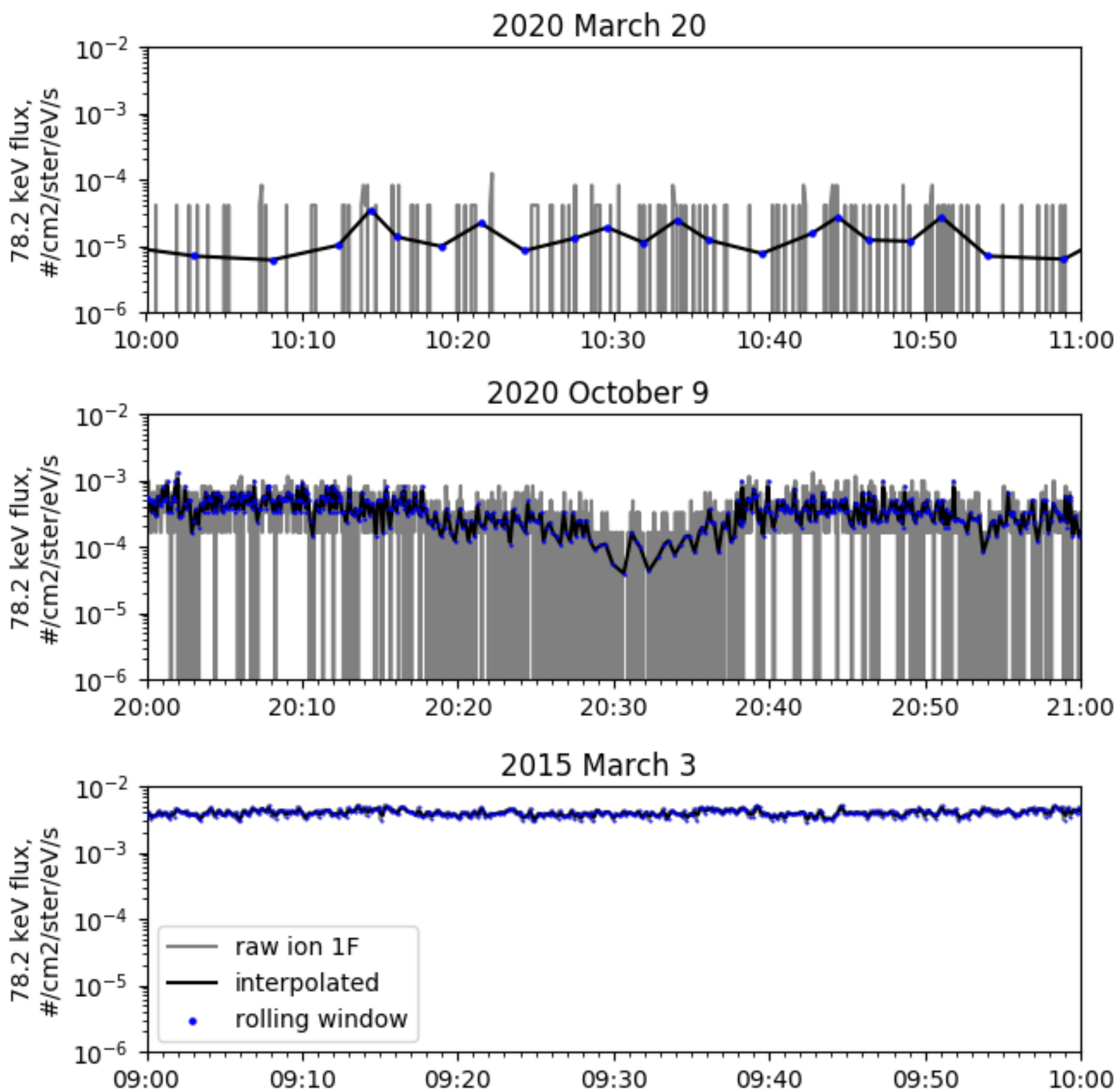

Figure 5.1: Fluxes of 78.2 keV ions measured by SEP 1 in the forward look direction in the absence of SEP events (top), during a weak CME (middle) and a strong CME (bottom). Raw data is shown in gray, the flux determined with the variable rolling window is in blue, and the interpolated flux over the common time axis is plotted in black.

Data from the SEP instrument is susceptible to contamination by both photocurrent and energized oxygen ions. Both the SEP ion and electron detectors can measure errant counts in the lower energy channels when the detector is pointed at the sunlit surface of Mars [Rahmati et al. 2020]. This "Mars shine" can be easily filtered out by ignoring data taken when over 10% of the detector's field-of-view is obstructed by Mars. Sporadic X-ray sources can also lead to errant counts. However, no filter was deemed necessary since flare-related X-rays are transient, lasting for seconds to minutes, and extrasolar X-rays like those from Scorpius X-1 are recorded in energy channels excluded from the Level 2 data product [Rahmati et al. 2020].

The SEP instrument can measure high fluxes of energetic oxygen ions, which can exceed actual SEP energy fluxes by several orders of magnitude. The oxygen ions have energies of 10s to 100s of keVs and appear as bursts superimposed on any existing SEP flux. Oxygen contamination can be observed in each SEP detector and sometimes multiple detectors simultaneously as shown in Figure 5.2. The dominant source of contamination is ionized oxygen from the corona that is "picked up" and accelerated by the solar wind convective electric field [Rahmati et al. 2015]. Pickup oxygen preferentially enters the forward-looking detectors SEP 1F and SEP 2F since these detectors are often oriented along the solar wind direction. Spacecraft maneuvers can reorient the reverse-looking detectors SEP 1R and SEP 2R to similarly observe pickup ions. In addition, ionospheric oxygen can be accelerated from the magnetosheath to cause bursty fluxes in the reverse-looking detectors. While oxygen contamination is often observed in only one forward-looking detector and/or one reverse-looking detector, occasionally it is detected in both at once. During one such event, proton cyclotron waves with periodicity of 10-20 seconds were recorded while both SEP 1F and SEP 2F simultaneously observed pulses of oxygen, which suggests that wave activity might affect the ionized oxygen.

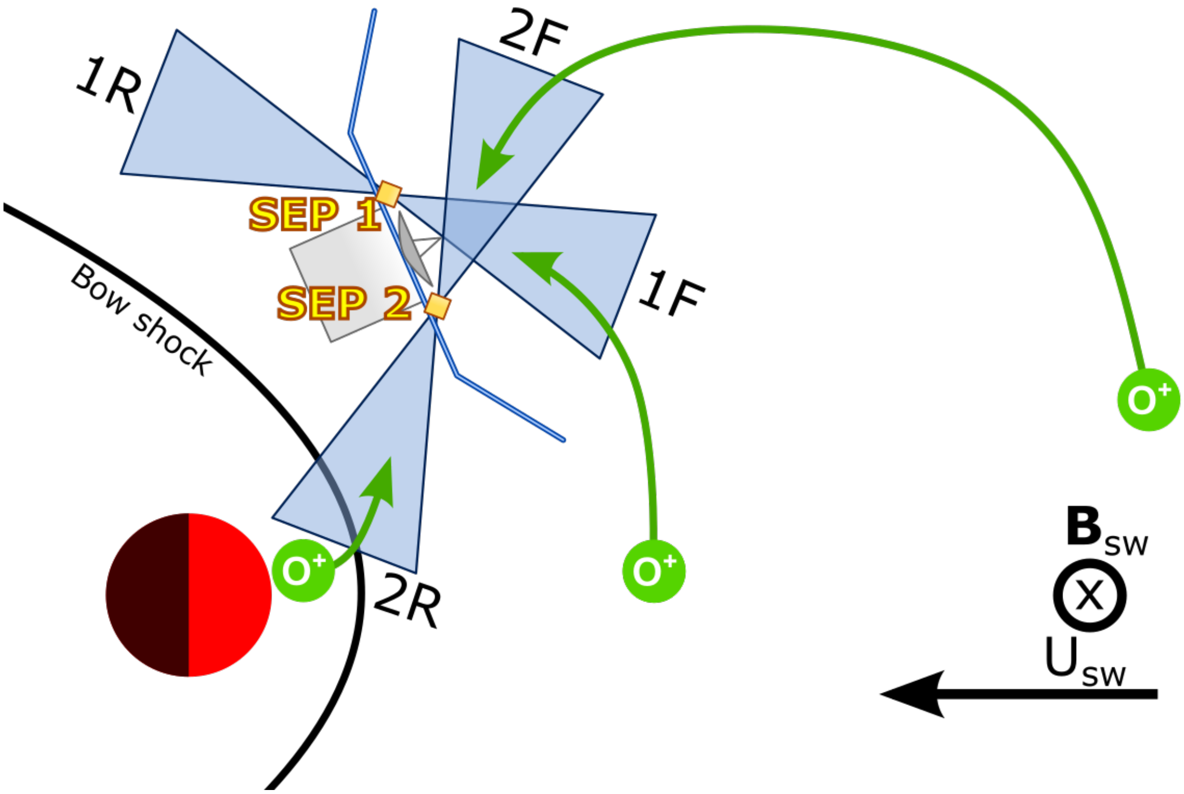

Figure 5.2: A schematic of oxygen ion contamination as observed by the SEP instrument while MAVEN is in the solar wind outside of the induced magnetosphere of Mars. Oxygen ions are produced within the bow shock and in the extended corona, which are picked up by the convective electric field and accelerated into the SEP fields of view.

Initially, we attempted to identify and exclude oxygen ions based on the theorized source and acceleration mechanism. First we calculated the maximum energy an oxygen ion can have when accelerated by the solar wind convective electric field, intending to ignore fluxes below the theoretical maximum. However, fluxes of oxygen ions were observed with energies above this maximum. It is possible that other mechanisms such as plasma waves are additionally accelerating pickup oxygen. We then attempted to exclude measurements at times when the observing geometry favored pickup oxygen, calculating the angle between the electric field and the SEP detector pointing direction and excluding observations when that angle was within the detector aperture viewing angle. Unfortunately, as oxygen ions can take several minutes to complete a single gyromotion, the varying magnetic field and solar wind velocity can cause this plane to oscillate, introducing too much variability in the filter. In addition, this approach cannot be used to identify accelerated ionospheric oxygen in the reverse look directions due to the lack of concurrent measurements of magnetic fields within the bow shock.

Instead, we developed an empirical approach to detect and remove oxygen contamination. The filter-and-average algorithm can identify oxygen contamination by comparing low energy fluxes observed in each SEP detector and flagging times when one or more SEP detectors have orders of magnitude higher fluxes compared to each other. The filtered-and-averaged SEP data product is then determined by excluding flagged observations and averaging the rest.

We begin by calculating the difference between the logarithm of the flux F recorded by two detectors D_1 and D_2 in a given energy bin E:

$$d(E) = \left|\log\big(F(E, D_1)\big) - \log\big(F(E, D_2)\big)\right| \quad (5.1)$$

Theoretically, for an isotropic SEP population, the flux difference $d(E)$ for each possible pair of look directions should be approximately 0. When oxygen is detected in one of the detectors and not the other, ion fluxes below 100 keV will differ by several orders of magnitude. This means we can exclude observations if the flux difference at low energies is above a fixed threshold. In order to estimate a reasonable threshold, we note that flux difference can be nonzero for other reasons. SEP fluxes can be anisotropic, particularly during the onset of a SEP event [Li and Lee 2019]. The flux difference can also be high due to statistical fluctuations when sampling low number fluxes.

We want to avoid filtering realistic SEP anisotropy and fluctuations. When SEPs are anisotropic or fluctuating, the flux difference should be approximately the same in all energy bins. We estimate the variability as the minimum of flux difference at two other energies, a "middle" energy bin at the center of the SEP instrument sampled energy range E_{mid} (~97 keV) and a "high" energy bin that is the maximum common energy bin E_{high} (~1.3 MeV). Using the minimum of flux differences calculated for two energies ensures the calculated variability is not as susceptible to dropouts or "shadowing", since high energy SEPs can be physically obstructed and mid-range energy SEPs can be reduced by changes in magnetic and viewing geometry.

We define the adjusted flux difference as the flux difference in lowest common energy bin E_{low} (~22 keV) subtracted by the flux variability over other energy channels:

$$d_{adjusted} = d(E_{low}) - \min\left(d(E_{mid}), d\left(E_{high}\right)\right) \tag{5.2}$$

We now calculate the average flux over two look directions. If the adjusted flux difference is below a threshold value a, the total flux as the average of the two look directions, otherwise we use the minimum of the two fluxes:

$$F(D) = \begin{cases} \frac{1}{2}\left(F(D_1) + F(D_2)\right) & if\ d_{adjusted} < a \\ \min\left(F(D_1), F(D_2)\right) & if\ d_{adjusted} > a \end{cases} \tag{5.3}$$

We calculate the average forward look direction flux SEP F from SEP 1F and SEP 2F in this manner. We determined that a threshold value of 0.2 was the best choice to filter out oxygen in the forward look directions, which is equivalent to stating that the low-energy SEP fluxes cannot exceed each other by more than a factor of 1.5. However, this layer of filtering will not remove oxygen fluxes measured simultaneously in SEP 1F and SEP 2F. We repeat the calculation for SEP 1R and SEP 2R to find the average reverse look direction flux SEP R, and finally repeat the calculation using the filtered fluxes SEP F and SEP R to determine the total average SEP flux. This final comparison removes simultaneously measured oxygen fluxes. When averaging SEP F and SEP R, we found that a threshold value of 2 was sufficient to account for anisotropy along the sunward-antisunward axis. Finally, with the oxygen contamination mostly suppressed, breakthrough contamination is rare enough to be mitigated with standard-scoring to remove outliers on each orbit.

This approach is limited to removing oxygen contamination in the solar wind. If there are dropouts in the lowest common energy bin, the filtering will significantly underestimate the flux. Shadowing of low energy SEPs does not usually occur in the solar wind and is generally associated with magnetic conditions within the magnetosheath [Lillis et al. 2016]. However, we can observe shadowing of low- and mid-energy SEPs in the solar wind if a significantly strong shock or CME reaches the Mars system. This likely occurs because magnetic fields associated with a shock passage can be comparable in scale to a SEP ion gyroradius. To prevent these measurements from aliasing the filtered flux, we do not apply oxygen filtering to orbits where SEP fluxes rapidly rise in accordance with an energetic storm particle enhancement during a shock passage.

Figure 5.3 presents an example of the filter-and-average method. First we show the measured fluxes of 25.7 keV ions for two solar wind passes on 2014 December 5 on the top panel. The baseline ion flux is ~1-2 x 10-4 particles/ster/eV/cm2/s. Oxygen contamination is visible as rapid surges of flux above this value that are either sporadic, as viewed by SEP 1R and SEP 2R, or prolonged, as viewed by SEP 1F and SEP 2F. The adjusted flux difference is calculated per Equation (2) and plotted in the middle panel for the forward-looking detectors (SEP 1F and SEP 2F) and the reverse-looking detectors (SEP 1R and SEP 2R). The calculated flux difference is frequently above the threshold value of 0.2, which is denoted by the horizontal dashed black line. The filtered-and-averaged forward fluxes and reverse fluxes of 25.7 keV ions are accordingly calculated using Equation (3) and shown in the top panel in red and blue respectively. The most substantial oxygen contamination is suppressed by this step, although there are several spikes during both orbits. The adjusted flux difference for filtered-and-averaged forward and reverse spectra is calculated and shown in the middle panel alongside the threshold value of 2, which is demarcated as a horizontal solid black line. Though the raised threshold is important to prevent underestimation of anisotropic events, this example event is isotropic and so this filtering step is less effective.

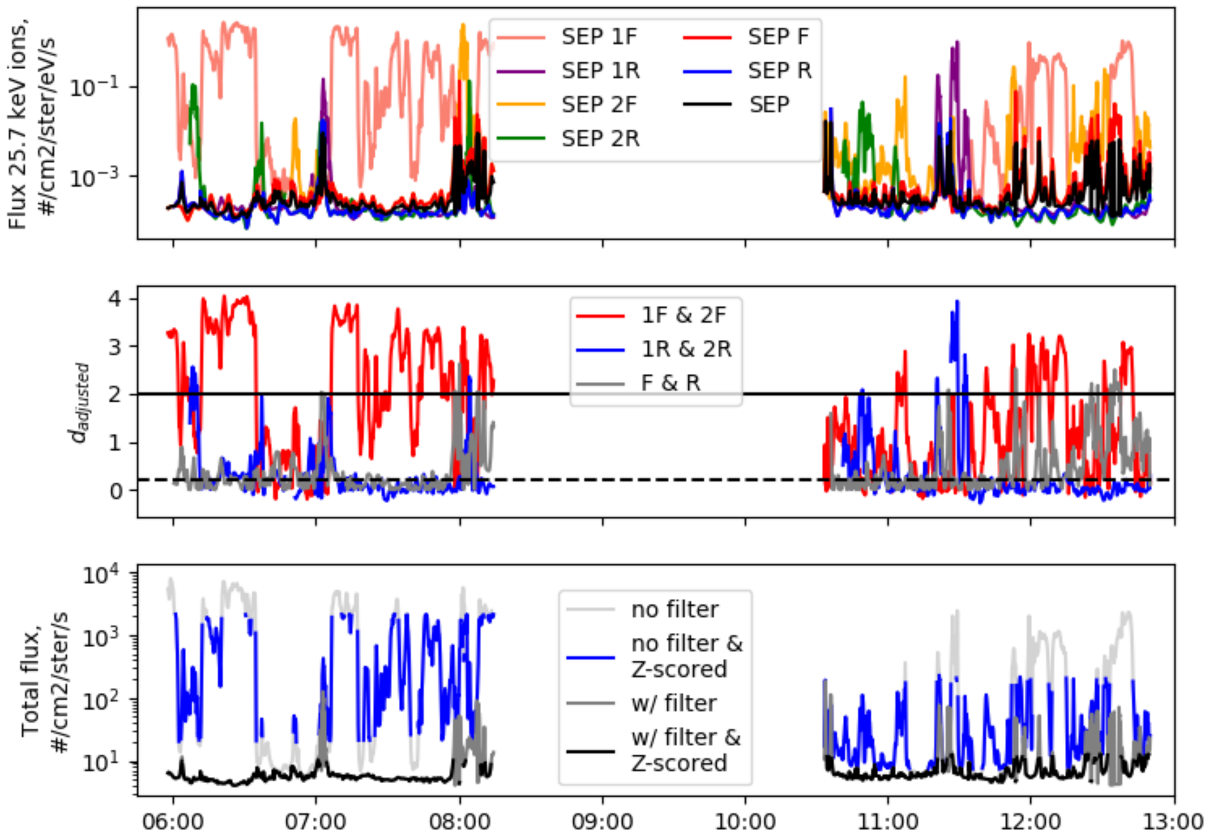

Figure 5.3: Fluxes of 25.7 keV ions recorded during two solar wind passes on 2014 December 6 (top), the adjusted flux difference estimated between three pairs of measurements (middle), and the total SEP flux integrated over all SEP energies that is determined with and without oxygen filtering and Z-scoring (bottom).

The final filtered and averaged flux of 25.7 keV ions is shown in black in the top panel of Figure 5.3. Though the oxygen contamination is suppressed compared to the original data, it occasionally breaks through the filtering. Coincident contamination in all look directions occurs between 7:00 and 7:06 UTC, violating our assumption that pristine fluxes are recorded in at least one look direction, and spikes are visible in the final SEP flux product at times when SEP 1F and SEP 2F are comparable between 11:15 and 12:45 UTC. However, contamination in the filtered dataset is substantially reduced compared to the contamination in the original dataset. This allows us to use z-scoring to remove outliers via the same process that sheath data was excluded from SWIA and SWEA data. The bottom panel of Figure 5.3 shows the total SEP ion flux, integrated over all SEP energies, determined without filtering oxygen (light gray), without filtering oxygen and using z-scoring to eliminate outliers (blue), with filtering oxygen (dark gray), and with filtering oxygen and using z-scoring to eliminate outliers (black). Not filtering oxygen leads to overestimated total flux by several orders of magnitude, and attempting to exclude outliers via standard scoring in the unfiltered SEP data does not improve the data due to frequent oxygen contamination. However, filtering oxygen reduces the contamination substantially. Breakthrough contamination is subsequently cleaned up by standard scoring.

Compared to SEP ion data, SEP electron data requires minimal filtering after removing photocurrent-contaminated data. We exclude the first four energy bins of the SEP electron data, since they show an unphysical roll-off in fluxes between 22-28 keV that is caused by energy losses in the dead layer of the detector and extrapolate over these energy bins to correct the data [Larson et al. 2015]. While this is effective when the instrument measures substantial fluxes, statistical fluctuations during observations of low fluxes can cause errant extrapolation. We mitigate this by selecting orbits where the average total flux during a solar wind pass is below a threshold (~10^4 particles/ster/cm2/s) and instead calculating the average spectral slope during a solar wind pass and using that to extrapolate fluxes for each observation during the solar wind pass.

There is an additional source of contamination in SEP observations that we do not correct for. During extremely energetic events, there can be cross-talk in the ion and electron detectors. Extremely energetic electrons can leave counts in the ion detector, and vice versa. This type of contamination is infrequent and only occurs during particularly energetic events. As we already ignore data when the instrument attenuators are closed due to saturation from excessive counts, situations where cross-talk occurs have been further reduced. Since there is currently no tool to disambiguate or remove cross-talk, we will only mention if an analyzed period of SEP data is susceptible.

Unlike the other energy inputs analyzed in this study, SEP events are transient, making it important to quantify what MAVEN SEP observes in the absence of SEP events. We approximate this background as the lowest observed energy flux during each solar wind coverage period. This is an adequate assumption provided that each coverage period has a duration of no active SEP producing events and/or no distinguishable SEP fluxes above the background, and that the background does not substantially change over the solar wind coverage period. The former condition holds for all studied time periods with the exception of 2014 December 1 to 2015 March 15. This outlier is caused by the continuously elevated electron fluxes from at least 14 catalogued sequential flares and CMEs [Lee et al. 2017]. Except for this outlier, the background energy fluxes in the SEP instrument were determined to be 1-1.6 x 10^6 eV/cm^2/s for electrons and 4.3-8 x 10^6 eV/cm^2/s for ions.

We determined there are two sources of background fluxes in SEP data, X-rays and GCRs. Figure 5.4 shows the background spectra for five representative times between 2015 and 2020. The ion and electron background spectra are very similar in shape and magnitude below 200 keV, so much so that the electron spectra were multiplied by a factor of 10 to distinguish the datasets. The similarity across ion and electron spectra implies a photon source, since the "low-energy" background source is neither affected by the magnet that prevents low energy electrons from entering the ion detector nor the foil that prevents low energy ions from entering the electron detector. The low-energy source dominates the background of the electron data, as electron data is restricted to below 200 keV in the Level-2 data product due to significant ion contamination of higher energies. Figure 5.4 also shows that the low-energy source does not vary with time, as the total energy flux calculated from the electron background shows no discernible trend. Given SEP's prior demonstrated sensitivity to X-rays, these background fluxes are likely due to an ambient source of X-rays [Rahmati et al. 2020]. As for the "high-energy" background source, Figure 5.4 shows that the ion background fluxes measured above 200 keV and the total calculated energy flux increase between 2015 and 2019. This trend is consistent with increasing GCR contamination as SC 24 wanes, since GCR flux in the solar system will be elevated at solar minimum due to the weakening heliospheric magnetic field [Jokipii et al. 1977, Heber et al. 2009, Delory et al. 2012].

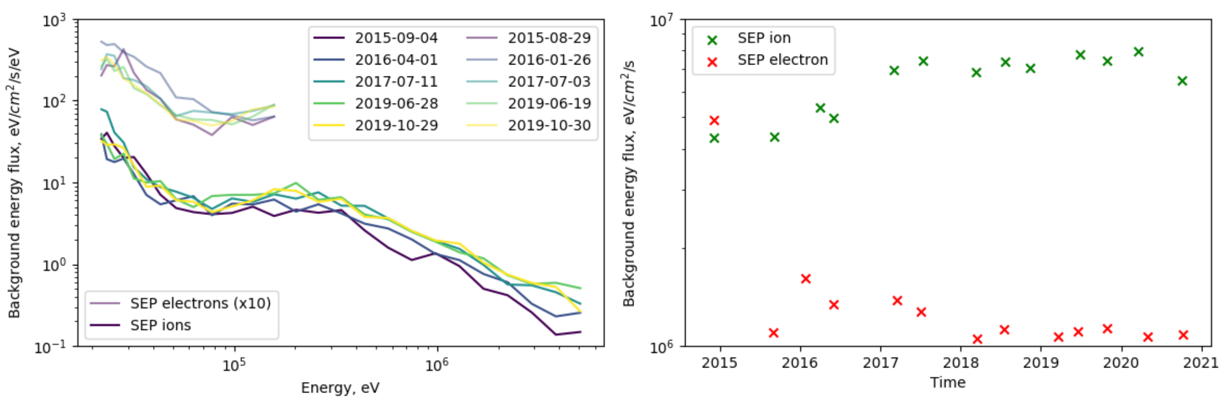

Figure 5.4: Background electron and ion spectra (left) and energy fluxes (right) observed by SEP between 2015 and 2020.

5.4. Energy input by solar drivers as measured by MAVEN

The energy flux of each solar driver measured by MAVEN instruments between December 2014 and November 2020 is shown in Figure 5.5. As expected, EUV energy input consistently exceeds the energy input from solar wind ions and electrons, and the time-averaged energy input by solar wind exceeds the time-averaged energy input by SEPs. During the studied times over the MAVEN mission, the time-averaged energy fluxes received by Mars in units of 10^9 eV/cm^2/s are 650-1,390 for EUV, 40-110 for solar wind ions, 6-35 for solar wind electrons, 0.01-2.7 for SEP ions, and 0-0.4 for SEP electrons. Time-averaged EUV energy flux consistently exceeded solar wind ion energy flux by a factor of ~10-20 and solar wind electron energy flux by a factor of ~40-140. Similarly, time-averaged solar wind ion fluxes consistently exceeded time-averaged SEP energy fluxes by one or more orders of magnitude.

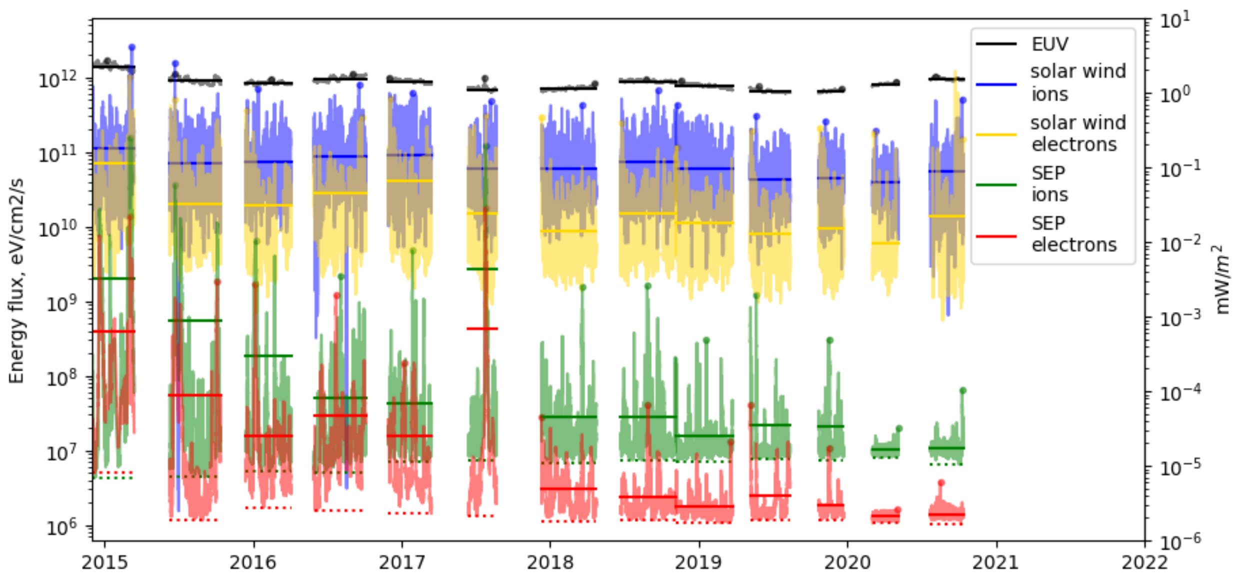

Figure 5.5: EUV, solar wind, and SEP energy fluxes for thirteen periods of time during the MAVEN mission between December 2014 and November 2020. The semitransparent lines are the total energy fluxes over time in each instrument's native cadence, the horizontal bars are the average energy flux calculated over the marked range of time, the circles are the peak energy fluxes recorded for each period, and the dotted lines are the background SEP energy fluxes.

Solar inputs can also be described by the peak energy flux recorded. While the average flux indicates the overall energy that Mars absorbs, one solar input might briefly exceed another and drive further ion production or heating. MAVEN observations show that peak solar wind ion and electron energy flux occasionally reach or exceed the average EUV. The highest recorded solar wind ion energy fluxes in this study are 2.2-2.5 x 10^{12} eV/cm^2/s on 2015 March 8 between 20:55 and 21:25 UTC, coinciding with the arrival of a CME shock [Lee et al. 2017, Dong et al. 2015]. The measured solar wind ion energy fluxes exceed the EUV energy flux by a factor of 1.3 for the entire duration that MAVEN sampled the solar wind on orbit 850. Since MAVEN doesn't have continuous solar wind sampling coverage, the elevated fluxes might have been sustained for as long as three hours. Similarly, the highest recorded solar wind electron fluxes are 0.7-2.4 x 10^{12} eV/cm^2/s on 2015 March 3 between 18:29 and 19:57 UTC, which coincides with an earlier CME shock arrival. These energy fluxes exceed both the average and concurrent instantaneous EUV energy fluxes of 1.4 and 1.6 x 10^{12} eV/cm^2/s, respectively.

In the subsequent years surveyed by this study, solar wind electron energy flux did not approach or exceed EUV energy flux again, and solar wind ions exceeded average EUV energy input only one more time. On 2015 June 22 between 21:30 and 22:40 UTC, solar wind ion energy fluxes were measured between 0.8-1.6 x 10^{12} eV/cm^2/s, coinciding with another CME shock arrival [Lee et al. 2017]. This energy flux is a factor of 0.8-1.6 of the time-averaged EUV energy flux over the surrounding period (2015 June 10 to October 14), but a factor of 0.7-1.4 of the simultaneously measured EUV energy fluxes, which are elevated due to concurrent flare activity.

SEPs are usually described as an extremely energetic solar input. However, the instantaneous SEP energy fluxes in this study never exceed time-averaged or instantaneous EUV energy fluxes. Occasionally instantaneous SEP energy fluxes can be comparable to or exceed the time-averaged solar wind energy fluxes for a given period. The highest measured SEP ion energy fluxes in this study were 0.6-1.6 x 10^{11} eV/cm^2/s on 2015 March 3 between 18:45 and 19:57 UTC, which exceeded the time-averaged solar wind ion and electron energy fluxes by a factor of 1.4 for the surrounding period (2014 December 1 to 2015 March 15). Despite this, the simultaneously measured instantaneous solar wind ion and electron energy fluxes were nearly 10 times higher than the SEP ion energy fluxes. This is likely because a passing CME shock caused elevated SEP fluxes via energetic storm particle enhancement, but also significantly increased ambient solar wind ion energy fluxes.

There is an instance in our analysis when SEP energy fluxes exceeded solar wind energy fluxes for a period of time. A sequence of CMEs and interacting shocks led to elevated SEP fluxes recorded by MAVEN from 2017 July 24 to 2017 August 1[Luhmann et al. 2018]. This was a similar type of event to the much-studied 2017 September 10-17 event, as both generated such high SEP fluxes that the MAVEN SEP attenuators closed to protect the instrument [Lee et al. 2018]. The maximum SEP energy flux would have likely arrived at Mars while the attenuators were closed between July 24 21:06 and July 25 22:37 UTC, and was likely higher than our calculated peak of 1.2 x 10^{11} eV/cm^2/s at 2017 July 25 22:47 UTC. At this time, our estimated SEP energy flux exceeded the solar wind energy flux, both ion and electron, by a factor of 3. While the SEP ion energy fluxes rapidly decreased to below the concurrently measured solar wind ion energy fluxes over the subsequent hour, the SEP ion energy fluxes were up to 2.5 times the solar wind electron energy fluxes between July 26 22:45 and July 27 16:10 UTC. Unfortunately, the calculated SEP ion energy flux is suspect due to the presence of crosstalk between July 24 and July 28: extremely energetic electrons from the solar event left counts in the ion instrument, particularly at MeV energies. This event will require more analysis to disambiguate the overestimation due to crosstalk and underestimation due to the attenuators closing during measurement of the highest fluxes.

These energy flux estimates upstream of Mars are useful to guide a discussion of relevant energy input to the atmosphere. In general, dayside atmospheric processes are driven by EUV photons while nightside processes are driven by particle precipitation and cross-terminator transport from the dayside. Can these dominant drivers be temporarily displaced? Despite how solar wind energy fluxes exceeded EUV energy fluxes during significant CMEs in March 2015 and July 2017, they would be insufficient to displace EUV as the primary driver. Models predict that only ~3% of solar wind ions will convert into ENAs that can directly precipitate into the dayside atmosphere of Mars during solar minimum [Kallio et al. 1997]. Direct precipitation is even more infrequent, with analysis of Mars Express observations finding proton precipitation occurs 3.2% of the time to deposit 0.2% of the solar wind energy flux [Diéval et al. 2013]. In the case of solar wind electrons, they can only precipitate along magnetic field lines that connect the atmosphere to the solar wind, which make up ~5% of magnetic field lines at atmospheric altitudes (170-250 km) [Weber et al. 2019]. Since they can only impart 40% of their energy flux due to magnetic reflection [Xu et al. 2014], we estimate less than 2% of the incident solar wind flux will precipitate. Since all solar wind fluxes are reduced by two orders of magnitude before they can influence the atmosphere, solar wind energy fluxes would have to be over a hundred times greater than EUV energy flux before they could impart equal energy to the dayside atmosphere.

Could a strong enough SEP event displace EUV as the dominant energy source on the dayside? Although SEP energy fluxes are consistently lower than EUV energy input in this study, MAVEN observations have been limited to a particularly weak solar cycle with few extreme solar events. Unlike solar wind particles, SEP ions are overall unhindered by Mars' induced magnetosphere and are only attenuated by the strongest crustal anomalies [Leblanc et al. 2002, Jolitz et al. 2017]. Accounting for the inhibition of solar wind particles as they enter the Mars plasma environment, energy flux from SEPs are the closest to EUV in terms of actual energy input to Mars during high-activity times. However, the peak energy input is still a tenth of energy input from EUV, which is in agreement with model predictions of energy deposition by SEP ions and EUV for a representative gradual SEP event [Leblanc et al. 2002]. The total SEP ion energy flux would have to exceed 10^{12} eV/cm2/s to possibly be comparable to EUV.

Relative influences on the nightside are more difficult to estimate due to cross-terminator transport. Determining the fraction of EUV energy flux converted into photoelectrons and conveyed into the nightside would require calculating photoionization rates and knowing what fraction of magnetic field lines connect the dayside to the nightside. Since this would require incorporating atmospheric density variability, which is an added complexity beyond the scope of this study, we neglect cross-terminator transport and only consider particle precipitation sources. This is an adequate approximation for magnetized zones of the nightside [Němec et al. 2011]. Assuming 40% of the energy flux of solar wind electrons reach the atmosphere without magnetically reflecting and given that 20% of magnetic field lines on the nightside connect the solar wind and the atmosphere [Weber et al. 2017], we can approximate that ~8% of the total energy flux from solar wind electrons is absorbed on the nightside of Mars.

Under this approximation, SEP ion energy input is comparable to actual solar wind electron nightside energy input during both weak and strong CME events for days. There were four time periods where SEP energy fluxes exceeded nightside solar wind energy input by a factor of 10 for one or more orbits: 2015 March 7-9, 2015 June 23, 2016 January 7-10, and 2017

July 24-29. Two of these time periods are associated with the strong SEP activity from sequential CMEs (March 2015 and July 2017). Usually these elevated fluxes are only recorded for hours. The most persistent elevation of SEP ion energy fluxes over solar wind nightside energy input was recorded in 2014 December 19-26, peaking at a factor of 6-7 greater on 2014 December 21. Interestingly, this coincided with observations of elevated ion densities and diffuse aurora on the nightside [Girazian et al. 2017, Schneider et al. 2015]. Otherwise, SEP fluxes associated with weaker events are occasionally comparable to solar wind electron nightside energy input, but tend to decay within hours.

We have made predictions of the relative importance of solar drivers in the dayside and nightside atmosphere. However, we do not account for how each solar driver will deposit energy differently. More energetic particles like SEPs will impart energy deeper in the atmosphere than solar wind electrons, and each solar driver has a different partitioning of deposited energy into ionization, heating, and other processes. Ultimately this would require simulating the energy loss of SEPs and solar wind particles and calculating photoionization and heating rates by EUV in different atmospheric profiles that reflect seasonality and day-night asymmetry, which is beyond the scope of this study.

5.5. Variability of solar drivers: Seasonal and solar cycle trends

Overall, the MAVEN-recorded energy flux of each solar driver at Mars has decreased as the solar cycle has waned (Figure 5.6). Both solar wind and EUV energy fluxes have periodic oscillations corresponding to varying Mars-sun distance, while SEP energy fluxes appear unaffected by seasonal trends. This is expected since EUV intensity and solar wind density both decrease as a function of heliospheric distance, while SEP fluxes depend more on the acceleration process and an observer's magnetic connectivity to the source [Shea and Smart 2003].

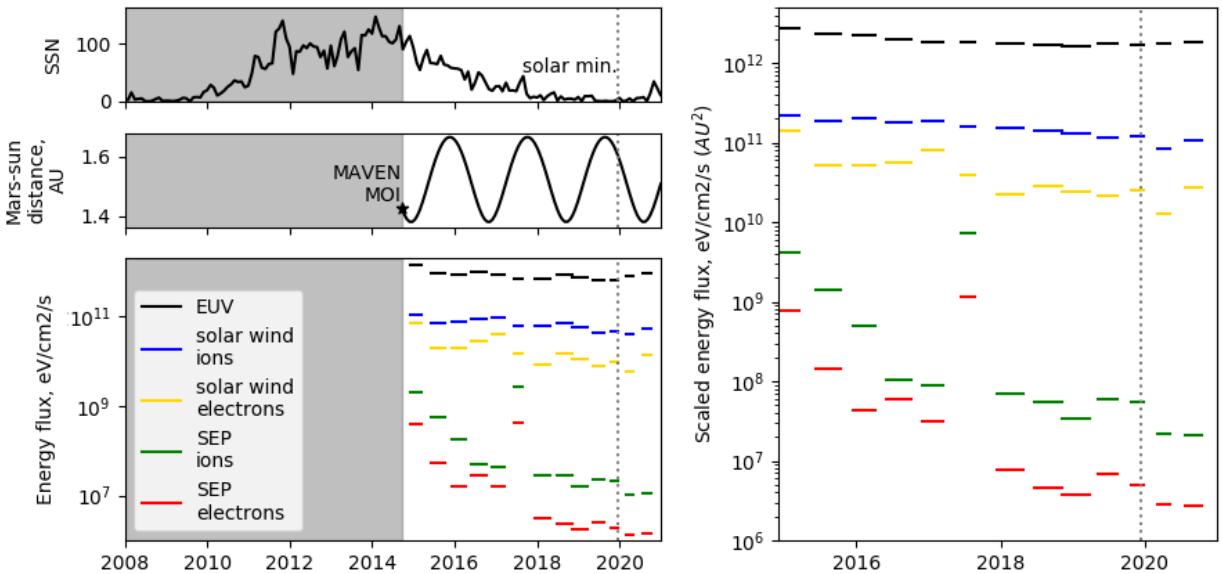

Figure 5.6: The monthly smoothed sunspot number (SSN) of solar cycle 24, Mars-sun distance during the MAVEN mission until January 2021, and the time-averaged energy fluxes of each solar driver on the left, and energy fluxes scaled for Mars-sun distance on the right. The gray dotted line marks solar minimum according to WDC-SILSO. Monthly SSN is from SILSO data [Royal Observatory of Belgium, Brussels].

Seasonal variation can obscure changes in energy input related to the declining solar cycle. Decoupling the seasonal dependence is an uncomplicated exercise for EUV and solar wind fluxes, as irradiance and solar wind density decreases are inversely proportional to the square of the heliocentric distance. However, the relationship between SEP energy flux and heliocentric distance is more complex. Unfortunately, there is no recent consensus strategy to decouple SEP intensity from heliocentric distance. The decrease of SEP intensity with radial distance has been studied with analytical expressions, models, and datasets. In the most basic approximation, solving the radial Fokker-Planck equation for energetic particle transport in the solar wind reduces the problem to diffusion when convection and adiabatic energy loss is excluded [Parker 1965]. This predicts a radial dependence of peak intensity $I \propto R^{-3}$ and fluence $F \propto R^{-2}$ for heliocentric distance *R* [Hamilton 1988, Vainio 2007]. These analytical predictions were codified as functional form recommendations for extrapolating fluxes and fluences measured at 1 AU to distances closer and further than the Earth in the heliosphere [Feynman and Gabriel 1988]. In particular, fluence at 1 AU was to be extrapolated using a functional form ranging from R^{-3} to R^{-2}. However, while these predictions compared favorably to impulsive events with magnetic connectivity between observers, they did not capture interplanetary shock acceleration that led to gradual events [Hamilton 1977, Smart and Shea 2003]. Recent studies have examined SEP transport in the inner solar system and found that the passage of interplanetary shock structures can make the power law radial dependence steeper or softer than the pure diffusion model [Lario et al. 2013]. Models have demonstrated further variability in the radial dependence due to, among others, magnetic focusing, pitch angle scattering, and interplanetary shock phenomena (e.g. Lario et al. [2007], Verkhoglyadova et al. [2012]). In general, radial dependence of SEPs varies based on a multiplicity of event-specific factors ranging from $R^{-0.88}$ to $R^{-5.3}$. Unfortunately, there is a lack of observational studies on the radial diffusion of SEPs as they reach Mars. Since we are averaging fluxes over multi-month time periods that may include tens of events, we approximated the SEP radial dependence as R^{-2}. Accordingly, all energy fluxes are multiplied by the square of the Mars-sun distance at the time of measurement.

Figure 5.6 shows the seasonally-decoupled energy input. The oscillations in solar wind ion and EUV energy fluxes disappear, showing a steady decline over the solar cycle. The variability in SEP energy fluxes is overall unaffected, reflecting the episodic behavior of the source processes, and appears to decrease with the declining solar cycle. However, we estimated the highest time-averaged energy fluxes between 2017 June 13 and 2017 August 22, a period late in the declining phase of SC 24. The elevated time-averaged fluxes are owed to the 2017 July space weather events described earlier. Both 2017 July and September events were unusual for generating high SEP fluxes near the trailing end of an already weak solar cycle. Two hypotheses have been offered for these types of events. Both events were caused by CMEs that erupted from pseudostreamer sites that developed late in the solar cycle, and though pseudostreamer-associated CMEs are typically slow, a sequence of CMEs from a pseudostreamer site may be particularly conducive to extreme particle acceleration [Luhmann et al. 2018, Li et al. 2012]. Alternatively, successive CMEs may have simply increased the seed population enough and produced multiple shocks, priming conditions for high energy fluxes [Kahler and Vourlidas 2014, Liu et al. 2019]. Regardless, the causation of this outlier requires further investigation.

While solar wind ion energy fluxes smoothly decline with the declining solar cycle, solar wind electron energy fluxes show unaccounted for oscillations. The elevated time-averaged energy flux during the earliest time window was likely related to SEP activity, which might have caused real elevated fluxes from the passing shocks and/or penetrating counts in the instrument housing. The other elevated time-averaged energy fluxes occur when Mars is near or at periapse. Since spacecraft charging is largely caused by solar UV-induced ejection of photoelectrons from the spacecraft when MAVEN is in the solar wind, this apparent seasonal relation might imply that spacecraft charging is not completely corrected. Over the mission, the average spacecraft potential in the solar wind has steadily declined from +7 V to +5 V, as expected from the declining solar activity. The mode of the spacecraft potential has oscillated seasonally, charging up to +8-9 V during periapse times. While we correct electron spectra for spacecraft charging, underestimated spacecraft potentials can cause solar wind electron fluxes to be overestimated.

Solar activity and seasonal variation can interact to cause Mars-specific trends. For example, while the lowest EUV irradiances in solar minimum were measured in late 2018, the lowest EUV irradiances at Mars were recorded later. At Mars, the lowest EUV irradiances (~1 mW/m^2) were measured between July and December 2019, with the nadir when Mars was at aphelion in late August 2019.

On the other hand, the nadir of energetic particle fluxes was less affected by seasonal attenuation and more by heliospheric conditions. According to SILSO, the end of SC 24 was determined to have occurred in 2019 December. Unlike EUV fluxes, the lowest time-averaged energetic particle fluxes were recorded months after solar minimum. During the time period that included solar minimum (2019 October 23 to 2019 December 23), there were seven minor SEP events, three of which occurred in December 2019, and the time-averaged solar wind energy fluxes were 45 x 10^9 $eV/cm^2/s$ for ions and 7.4 x 10^9 $eV/cm^2/s$ for electrons. In contrast, the post-solar minimum time period (2020 March 3 to 2020 May 6) lacked SEP activity and the time-average solar wind energy fluxes were at their lowest, 39 x 10^9 $eV/cm^2/s$ for ions and 5.8 x 10^9 $eV/cm^2/s$ for electrons. Figure 5.7 shows the solar wind energy flux, velocity, density, and pressure alongside the SEP energy flux for both the solar minimum period and the post-solar minimum period.

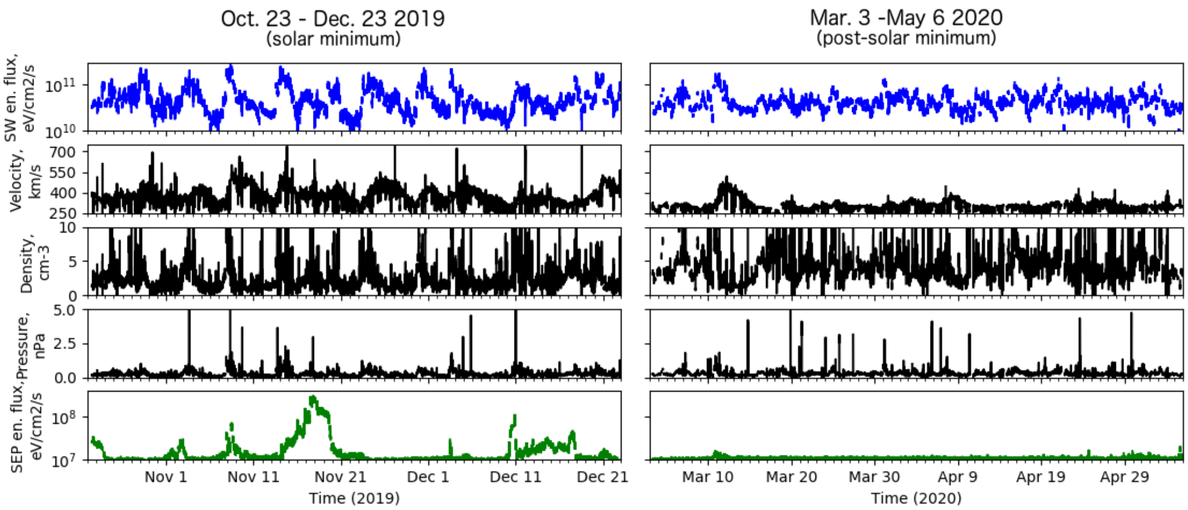

Figure 5.7: Solar wind ion energy flux, velocity, density, and pressure and SEP energy flux recorded between 2019 October 23 and December 23 (left) and between 2020 March 3 and May 6.

Delayed minimum fluxes are likely related to the predominance of high-speed solar wind streams during solar minimum, which can interact with slow solar wind to form stream-interaction regions (SIRs), which can also be called coronal interaction regions (CIRs) if they recur on multiple solar rotations [Schwenn 2007, Richardson 2004]. The resulting shock formation can cause SEP events, which can recur for several solar rotations [Lee et al. 2010]. The SEP events observed during the SC 24 minimum time period at Mars coincide with fast solar wind speeds, leading us to infer they are SIR or CIR related. If this is the case, there may be times during the rise of SC 25 when solar wind energy fluxes are even lower, as high-speed solar wind streams will be fewer. Le Chat [2012] found that the lowest solar wind energy fluxes measured by the WIND and Ulysses spacecraft occurred three years after the solar minimums that followed SC 22 and SC 23.

5.6. Contextualizing MAVEN observations: Present, past, and ancient Mars

Part of MAVEN's goal is to understand how the Martian atmosphere responds to solar drivers, and project back in time. However, MAVEN's observations have been mostly confined to SC 24, the weakest solar cycle in fifty years. While SC 25 is just beginning, current predictions expect similar behavior to SC 24: a "mini solar maximum" and low sunspot activity [Bisoi et al. 2019]. It is therefore important to place our energy flux calculations in context, and compare with parameters from recent solar cycles and the early solar system.

MAVEN arrived at Mars in October 2014, six months after the maximum phase of SC 24. This solar cycle has been characterized by overall reduced sunspot activity, few events that generate sufficiently energetic fluxes to produce ground-level enhancements, and an extended solar minimum [Gopalswamy et al. 2020]. We can contextualize our calculated energy fluxes with the corresponding smoothed sunspot number (SSN), averaged over the same periods as the energy fluxes (Figure 5.8). The majority of our observation periods see fewer than ten sunspots per day, corresponding to the extended solar minimum, while the rest correspond to the declining phase of SC 24. Figure 5.8 shows a positive correlation between SSN and energy flux for each solar driver: EUV, solar wind, and SEPs. This sensitivity to solar activity via the proxy of SSN is expected and well-known for EUV energy fluxes [Lean 1997]. Unlike the other solar drivers, seasonal variation in EUV is comparable to the solar cycle variation. In the case of the solar wind, a weak correlation between SSN and solar wind ion energy fluxes has been observed before [Le Chat 2012]. Still, we note that solar wind ion and electron energy fluxes vary similarly, suggesting the presence of additional factors that specifically control solar wind energy fluxes.

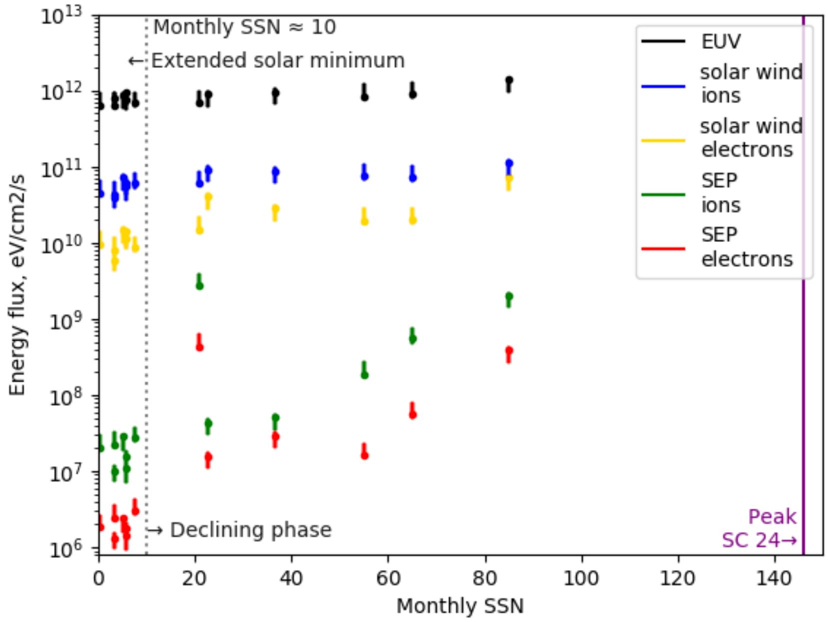

Figure 5.8: Energy fluxes of EUV, solar wind, and SEPs as a function of monthly SSN. The dots are the time-averaged energy fluxes while the bars mark the range of time-averaged energy fluxes scaled between periapse and apoapse. The dotted line marks the rough separation between "extended solar minimum" time periods with monthly SSN < 10 and "declining phase" time periods with monthly SSN > 10. The purple line marks the peak monthly SSN in SC 24, which was measured months before MAVEN arrived.

Unlike solar wind and EUV energy flux, SSN is not usually compared to total time-averaged SEP energy flux observed at a location in the solar system. SEP fluxes are usually studied in the context of the source event, such as a flare, SIR, or CME. Each source leads to different behavior from the resulting SEPs. SIR-associated energetic particles are frequently soft in spectra, short-lived, and can be recurrent over solar rotations [Richardson, 2018]. CME-associated particles have event-dependent spectral characteristics and arrive over the course of days. Flares can be associated with "impulsive" energetic particle events that last hours, co-occur with CMEs and lead to particularly extreme energy fluxes, and can also possibly generate no observable SEPs whatsoever [Reames 2013, Klein et al. 2011]. After the particles are accelerated, intervening space weather structures like interplanetary shocks and magnetic clouds can disperse, energize, or otherwise alter an energetic particle population. Each SEP source has different occurrence rates over a solar cycle. CME and flare occurrence rates are correlated with solar proxies like SSN and solar decimetric flux, occurring most frequently during solar maximum phases [Cremades and St. Cyr 2007, Webb and Howard 1994]. In contrast, SIRs can be distinguished in the absence of CMEs and flares, and are observed most frequently during solar minimum [Richardson 2004].

By time-averaging the SEP energy fluxes regardless of event type, we have convolved the source occurrence rates and spectral features of each event. Despite this, time-averaged SEP energy fluxes received by Mars appear to be correlated with SSN. The correlation can be explained by different events occurring in different phases of the solar cycle. MAVEN observed the lowest SEP energy fluxes during extended solar minimum, while the highest SEP energy fluxes were measured during the declining phase. Several CMEs of varying strength were recorded during the declining phase, while SIRs were most common in solar minimum. Although SIRs were present and producing energetic particles during solar minimum, their overall softer spectra reduced their total energy input to below the energy fluxes measured during the more CME-rich declining phase.

SEP energy fluxes measured during the declining phase show substantial variability. However, fluxes departing from a correlation by orders of magnitude are not unusual for CME sources. Peak SEP fluxes are known to show positive but noisy correlations with other parameters, particularly flare soft X-ray flux, CME velocity, and if one or multiple CMEs occurred up to 24 hours before [Klein and Dalla 2017, Gopalswamy et al. 2004]. CME occurrence rates can also vary from cycle to cycle, possibly impacting the variation as well.

Finally, our measurements of SEPs from a CME or flare associated event requires Mars to be magnetically connected to the acceleration source.

Despite these expected sources of variation, the July 2017 event presents as a significant outlier. This event requires specific care to analyze, as it was energetic enough to produce a ground-level enhancement (GLE) measured by MSL/RAD [Dumbovic et al. 2018]. GLE events are recognized as the most energetic type of SEP event. They may occur at any phase of the solar cycle, although they are rarer during solar minimum. While they show a stronger correlation to CME speed and flare fluence than non-GLE events, a fast CME with a bright enough flare is not a necessary and sufficient condition for the occurrence of a GLE [Desai and Giacalone 2016, Nitta et al. 2012].

How do these observations compare to previous solar cycles? Prior studies have shown that interplanetary plasma parameters during SC 24 have all been reduced compared to previous solar cycles [McComas et al. 2013, Gopalswamy et al. 2020]. Solar wind energy fluxes recorded in 2009-2013 were 40% lower than energy fluxes recorded in 1974-1994. Although CME occurrence rates were higher in SC 24 than SC 23, the occurrence rate of “fast and wide” CMEs (speed ≥900 km/s and width $\geq 60^0$) that are strongly associated with SEP events was nearly half that of in SC 23 [Lamy et al. 2019, Gopalswamy et al. 2020]. Only two GLE events at Earth were recorded in SC 24 compared to sixteen in SC 23. Mewaldt et al. [2015] estimated that the fluence of >10 MeV protons partway (~5.8 years) into SC 24 was a factor of 4.4 less than the fluence of SC 23 at the same phase. While the mechanism of GLEs remains elusive, decreased heliospheric parameters like IMF magnitude and solar wind density may have contributed to fewer GLEs in this solar cycle [Vainio et al. 2017, Mewaldt et al. 2015]. Since these conditions are likely to persist into the next solar cycle [Bisoi et al. 2019, Gopalswamy et al. 2020], we may see similar frequent CMEs but few GLEs through MAVEN's continuing mission.

We may also compare our results to estimates of plasma conditions of the early solar system. It is assumed that the ancient sun behaved similarly to other main sequence stars early in their lifetime: dimmer in overall luminosity but higher magnetic activity due to a more efficient dynamo driving rapid rotation rates, which enhance X-ray and EUV emissions, stellar mass loss as solar wind, and flare activity [Güdel 2007]. In addition, spallation in meteoric grains have been used to infer that high energetic proton fluence events were more frequent in the early solar system when the sun was in an even more magnetically active pre-main sequence phase [Caffee et al. 1987]. The resulting influence on the development of planetary atmospheres has been the subject of many studies [e.g. Kulikov et al. 2007, Lundin et al. 2007, Lammer et al. 2012]. Mars specifically has been examined as a case study of a planet that lost a dipole magnetic field due to cessation of the dynamo and developed an induced magnetosphere. Many studies have specifically examined Martian atmospheric evolution (e.g. Bößwetter et al. [2010]) and ion escape (e.g. Ramstad et al. [2017]) in the presence of elevated emissions and absent intrinsic magnetic field.

While modern space weather events are likely far weaker than those that occurred during the early solar system, it has been suggested that elevated particle fluxes during events can give a glimpse of the "average" conditions from a young sun. We can investigate that by comparing our time-averaged and maximum energy fluxes to estimates of solar drivers for a young sun.

Figure 5.9 shows EUV, solar wind, and SEP energy fluxes alongside prior study estimates as a function of the sun's age and solar EUV irradiance. All energy fluxes and irradiances are normalized to a heliocentric distance of 1 AU to mitigate seasonal variation.

While we considered normalizing to a Mars-typical orbit radius, normalizing to 1 AU allows us to compare with results directly from most previous studies that estimate young sun conditions at 1 AU. In order to determine the Mars-received energy flux, the normalized value only needs to be divided by the square of the seasonal-dependent heliocentric distance. Since there are no specific estimates of ancient energy fluxes for solar wind and SEP electrons, these datasets were excluded. The observations from this study are the dots clustered at the sun's current age (~4.6 Gyr) and within the lower range of irradiances (2-5 mW/m^2). The gray line in the left panel shows the estimated EUV (10-120 nm) energy flux calculated using fits from Ribas et al. [2005], which were determined from spectral irradiances of solar-type stars at different ages. On the right panel, EUV irradiance from Ribas et al. [2005] is marked as a reference for two solar ages, 0.7 Gyr and 2 Gyr. This expression was also used to calculate a corresponding EUV irradiance for each energy flux determined from a prior study given the provided solar age

The blue line shows the estimated solar wind energy flux calculated using a parameterization for solar wind velocity and density as a function of solar age derived in Grießmeier et al. [2004] based on stellar mass loss rates from Wood et al. [2002]. This expression has been used in several studies (e.g. Lundin et al. [2007], Bößwetter et al. [2010], Lammer et al. [2012]), so we use the parameters given in the most recent study. Interestingly, this expression appears to predict that solar wind energy flux exceeds EUV energy flux before the sun reached an age of 1.3 Gyr. We also calculated and included energy fluxes based on solar wind parameters from more recent studies that have modeled the solar wind at the young sun via magnetohydrodynamic (MHD) codes. We specifically use solar wind densities and velocities for the high coronal base density cases from Sterenborg et al. [2011] for the sun at an age of ~1 Gyr, and include both solutions for slow and fast solar wind from Airapetian and Usmanov [2016] at a solar age of 0.7 Gyr. We note that the slow and fast solar wind energy fluxes from Airapetian and Usmanov [2016] are close to the Lammer et al. [2012] parameterization, while the Sterenborg et al. [2011] prediction is lower by a factor of 5.

Finally, the figure also shows an estimate of ancient SEP ion fluxes from Lingam et al. [2018], which multiplied the fluence of a representative SEP event by an event occurrence rate based on superflare occurrence rates in G-type stars.

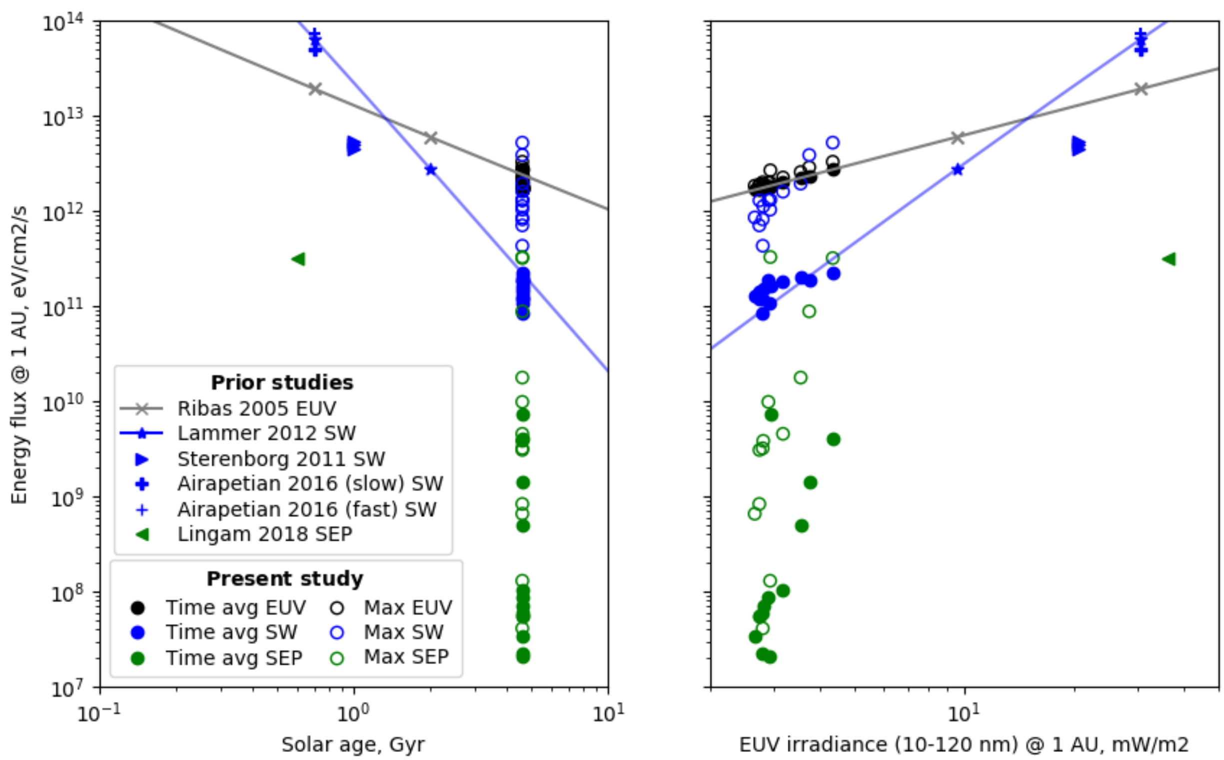

Figure 5.9: Energy fluxes of EUV, solar wind ions, and SEP ions as a function of solar age (left) and solar EUV irradiance (right). Present study data is scaled to a heliocentric distance of 1 AU and are marked with circles (empty for time-averaged energy fluxes and filled for peak energy fluxes). Estimates of young sun energy fluxes were all determined for a heliocentric distance of 1 AU and are marked in different symbols as described in the legend (see text for further details).

As expected, all estimated energy fluxes from the young sun exceed the time-averaged energy fluxes measured during a low-activity phase of a weak solar cycle. Peak EUV energy fluxes do not approach predicted historical levels. The ancient (~0.7 Gyr) solar wind energy fluxes from Lammer et al. [2012] and Airapetian and Usmanov [2016] exceed our time-averaged energy fluxes by ~200-300x and peak energy fluxes by >10x. On the other hand, the ancient (~1 Gyr) solar wind energy fluxes from Sterenborg et al. [2011] are in the range of two peak MAVEN-observed energy fluxes. These solar wind energy fluxes of 3.9-5.2 x 10^{12} eV/cm^2/s were associated with the passage of CMEs in March and June 2015, while Sterenborg et al. [2011] predicted that ancient solar wind energy fluxes were between 4.5-5.3 x 10^{12} eV/cm^2/s. Likewise, the estimated ancient SEP energy flux from Lingam et al. [2018] of ~3.11 x 10^{11} eV/cm^2/s has been twice exceeded by the peak SEP energy fluxes measured in March 2015 and July 2017. While these periods aren't necessarily accompanied by magnetic conditions indicative of the young solar system, there are times when the energetic particle load may have been similar to ancient solar conditions and worth studying.

5.7. Discussion

We have used MAVEN measurements of EUV, solar wind, and SEPs to calculate the energy input of each solar driver on the Mars system. Data was taken when the MAVEN spacecraft resided in the solar wind and was subsequently filtered to remove early spacecraft incursions into the Mars induced magnetosphere. Both time-averaged and maximum energy fluxes are determined for durations spanning 61 to 137 days (2-5 Carrington rotations). This approach has reduced the influence of solar rotation and simplified event-to-event variability in SEP events, allowing a clearer determination of the energy input during episodic space weather.

The observations confirm EUV is the dominant solar driver by total energy flux, followed by solar wind ions, solar wind electrons, SEP ions, and SEP electrons. However, there were rare and brief times during MAVEN's mission where this ranking of energy input was disrupted. During shock passages from the March 2015 and the June 2015 CMEs, the energy input by solar wind ions and/or electrons exceeded the energy input by EUV for 1-4 hour-long periods. While

SEP energy input never approached EUV energy fluxes, the SEP energy fluxes once exceeded solar wind ion energy input for nearly a day in July 2017. However, this result is suspect due to confounding factors of overestimation from cross-talk in the ion detector and underestimation from ruling out observations when the SEP attenuators close.

We have also made estimates of net energy input into the dayside and nightside of Mars. In general, precipitating particle energy fluxes must reach ~10^{12} eV/cm^2/s to be comparable to the energy input from EUV, a condition that is not met by any solar driver during the studied time period. We also predict that SEPs may impart as much or more energy flux than solar wind electrons on the nightside during periods of strong and weak CME activity. However, as pointed out in the text, this prediction makes several assumptions and is only intended as a first approximation. We have assumed that a fixed fraction of each energetic particle population precipitates based on prior studies. While we have assumed that 3% of solar wind ions are converted to ENAs per the estimated conversion rate during solar minimum from Kallio et al. [1997], seasonal and solar cycle changes in the corona influence this conversion rate [Chaffin et al. 2014]. Increases of conversion rate when Mars is at perihelion have already been observed as increased fluxes of ENA-reconverted protons in the upper atmosphere, and significantly increased detection of ENA-associated "proton" aurora during Southern summer [Halekas et al. 2017, Hughes et al. 2019]. We also estimated the fraction of precipitating electrons from the probabilities of open field line occurrence at low altitude, which were derived from MAVEN observations taken between 10 October 2014 and 24 March 2017 for the nightside, and between 1 December 2014 and 26 April 2018 for the dayside [Weber et al. 2017, 2019]. These observations correspond to the declining phase of SC 24. Modeling studies have shown that the draping patterns of the IMF will differ for solar maximum versus solar minimum [Liemohn et al

2017]. In addition, CMEs and magnetic clouds can cause compression of the induced magnetosphere, increasing the global magnetic connectivity to the solar wind [Crider et al. 2005, Xu et al. 2018]. This could mean that the energy input of the SEPs might not exceed the increased precipitating electron fluxes during particularly compressive events.

Our analysis has also assumed that all solar drivers outside of the Mars system are spectrally unchanged when they enter the atmosphere. This is true by definition for EUV photons and has been demonstrated for precipitating ENAs from solar wind ions [Halekas et al. 2015b]. SEPs are also presumed to be spectrally unaffected since they can't be trapped on induced magnetosphere field lines and no relevant wave activity has been recorded, although localized shadowing of SEPs of different energies has been reported [Lillis et al. 2016]. Unlike the other solar drivers, solar wind electrons are susceptible to a variety of acceleration and deceleration processes, ranging from cross-shock potential acceleration, wave-particle interactions, and field-aligned currents [Schwartz et al. 2019, Shane et al. 2019, Xu et al. 2020]. Reconnection can also redistribute solar wind electrons to previously-inaccessible closed field lines connected to the Mars atmosphere [Brain et al. 2006]. These factors could lead to precipitating energy fluxes that are higher than those expected by the pristine solar wind energy fluxes.

Finally, each solar driver has different stopping and relative cross-sections. Higher energy SEPs penetrate deeper into an atmosphere than solar wind ENAs and electrons. Despite how SEPs have a higher likelihood of ionizing constituents than those particles, SEPs with energies above 20 keV in an average solar minimum atmosphere deposit nearly all energy below an altitude of 120 km, where the escape probability of O atoms is much lower than ~1% [Jolitz et al. 2017, Fox and Hać 2009]. These particles are more likely to thermalize due to more frequent collisions with the neutral atmosphere. Indeed, radar sounding observations have shown that SEP events enhance ionization only below 100 km on the dayside, although other observations have found more extensive ionization on the nightside [Ulusen et al. 2012, Withers et al. 2012, Němec et al. 2014].

With these caveats in mind, we can establish an intuition for the role of each solar driver in the context of MAVEN's primary goal: estimating atmospheric loss to space. EUV photons and precipitating energetic particles initiate atmospheric loss by ionizing, dissociating, and heating atmospheric constituents. The resulting basin of ions and heated atoms is subsequently processed by a variety of energization mechanisms, such as dissociative recombination, sputtering, and wave heating [Jakosky et al. 2018, Ergun et al. 2016]. However, these energization processes are only accessible to ions formed in the upper atmosphere, since they will not be immediately thermalized by collisions with the neutral atmosphere. Therefore, although SEPs can be more effective than solar wind and EUV at ionizing the atmosphere, the low altitude of produced ions may make SEP events incapable of raising escape rates in this manner.

It is important to mention that increased ion escape can occur at the same time as elevated SEPs but not be caused by those SEPs. Many studies have estimated significant increases in escaping ion fluxes during significant SEP events [Jakosky et al. 2015, Futaana et al. 2008]. These elevated escape rates are related to the passage of a magnetic structure like a CME or SIR, and not the associated SEPs.

On the other hand, SEPs can drive heating and chemistry in the lower atmosphere. While there are no existing studies on these effects at Mars, there have been many studies at Earth. Due to Earth's magnetosphere, solar energetic protons preferentially precipitate into and influence the polar atmosphere. In these places, SEP proton impact ionization produces odd nitrogen and odd hydrogen, leading to observed ozone depletion, elevated nitric oxides, and perturbed chlorine chemistry [Jackman et al. 2005, Krivolutsky et al. 2008, von Clarmann et al. 2005]. It has even been suggested that elevated SEPs from a young sun warmed the ancient terrestrial atmosphere by formation of nitrous oxide and drove precipitation of nitrogen-rich organic molecules onto the surface [Airapetian et al. 2016]. While there is no current known influence of SEPs on Martian lower atmosphere chemistry, nitric oxide and ozone can be observed at Mars [Clancy et al. 2016, Stevens et al. 2019]. In addition, the recent discovery of lofted HCl up to 30 km during dust storms may suggest a greater role of chlorine chemistry in the Martian atmosphere [Korablev et al. 2021]. Unlike Earth, the near-entirety of Mars is exposed to SEP fluxes during events, so effects may be global and not restricted to the poles.

Our estimates of energy input are determined over the declining phase of SC 24 and the onset of SC 25. We showed the energy input of solar drivers at Mars are modulated by solar activity and distance from the sun to varying extents. Seasonal modulations of EUV are comparable to solar cycle modulation, while all energetic particle fluxes are more strongly driven by solar cycle modulation. In order to mitigate seasonal variation to clarify the role of the solar cycle, we scaled all energy inputs by a function of the heliocentric distance. The scaled EUV and solar wind ion energy fluxes were found to smoothly decline with the monthly SSN. However, oscillations were still present in solar wind electron energy fluxes, likely due to a combination of penetrating particle fluxes and error in the spacecraft charging correction. Using the distance-scaled energy fluxes, we showed that the absolute minimum of energy input received by Mars does not necessarily correspond with solar minimum. In particular, the lowest EUV energy fluxes occurred when Mars was aphelion in August 2019 and the particle energy fluxes were measured three months after the end of SC 24 (December 2019). This observation serves as a reminder that total energy input by EUV, solar wind, and SEPs at Mars are not absolutely "minimum" at solar minimum.

We have also contextualized our observations with the overall behavior of SC 24 as a very weak solar cycle. While time-averaging the SEP energy flux convolved energetic particles regardless of source, we observed a delineation between "low" monthly SSN (< 10) with lower SIR-associated SEP fluxes, and "high" SSN (> 10) with higher and more variable CME-associated SEP fluxes. We have brought up recent studies that have characterized SC 24 as particularly poor at producing GLEs and strong CMEs. Since predictions of the upcoming solar cycle are leaning towards similar heliospheric conditions, we have commented that we will likely see events similar to what MAVEN's seen before [Bisoi et al. 2019]. However, MAVEN will be positioned to observe energetic particle events during a rising and maximum phase of a solar cycle. While all energy fluxes are certain to increase, the relative behavior of each solar driver may differ. There also will be differences in how each solar driver is processed by the atmosphere. In particular, the atmosphere is expected to expand and increase in density in response to higher EUV irradiance, which will lead to ionization and heating at higher altitudes. In the future, this study could be extended to observe relative energy fluxes and estimate the energy input to the Mars atmosphere during the rising and maximum phases of solar cycle 25.

Finally, we have compared our results to prior studies that have estimated energy outputs from a young sun. Despite the weak solar cycle, MAVEN has observed peak fluxes of solar wind and SEPs that are in the neighborhood of predictions of steady-state ancient solar wind from Sterenborg et al. [2011] and SEPs from Lingam et al. [2018]. Based on our comparison, the March 2015 and September 2017 CME events could be useful to study as a proxy for young sun solar wind and SEPs at Mars, particularly during the event peaks. Unfortunately, the other ancient solar wind energy fluxes predicted by Lammer et al. [2012] and Airapetian and Usmanov [2016] were multiple orders of magnitude above any peak energy fluxes MAVEN observed.

We also showed a comparison of energy fluxes as a function of EUV irradiance. While this was done as a means to compactly compare the energy fluxes of prior studies, the figure appears to show a positive linear correlation between the logarithm of irradiance and the logarithm of each particle energy flux. The R^2 values of the correlation are ~0.5-0.6 for each type of energetic particle. This trend could be suggestive of a possible connection between these quantities. It would not be altogether unexpected, as soft X-ray fluxes have been found to be correlated with SEP fluxes [Gopalswamy et al. 2004]. If this were the case, SEP ion energy fluxes from a young sun could be much higher than those estimated in prior studies. However, we are extremely cautious with such speculation given the lack of a clear connecting mechanism and the known significant variability in correlations between soft X-ray fluxes and SEP intensities [Pande et al. 2018].

We have restricted this study to times when MAVEN observed “pristine” fluxes upstream of Mars. This limitation allowed direct and coincident comparison of energy inputs before they could be influenced by the induced magnetosphere. However, this meant neglecting high SEP activity periods such as the 2017 September event, which was the largest SEP and flare event observed by MAVEN and Mars Express in both mission lifetimes as of October 2021 [Lee et al. 2017]. A future version of this study could extend the survey to include observations from within the induced magnetosphere. While solar wind and magnetosheath electrons would be indistinguishable, solar wind ion proxies could be used to infer solar wind ion energy fluxes. However, this would require improvement on our approach to mitigate SEP instrument contamination. Both SEP ion and electron fluxes can be shadowed or depleted at low altitudes

[Lillis et al. 2016, Jolitz et al. 2021]. We would need to identify and remove these events so that the estimated total flux is not underestimated. Identifying shadowing events is also necessary to extend the oxygen filter to measurements at all altitudes, as our algorithm can misidentify real SEP fluxes as oxygen because depleted fluxes are present in another look direction. In addition, we have had to remove data recorded when attenuators close and caveat our analysis due to instrumental cross-talk. These situations are both due to a complex response of the detectors to extremely energetic fluxes. Since these events are of interest for human spaceflight and understanding early solar system conditions, it will be critical to flag and deconvolve the Level-2 spectra at these times. Following this correction, it would be worthwhile to extend this study to the rising and maximum phases of solar cycle 25 as they are observed by MAVEN.

Chapter 6

Conclusion

This thesis primarily focused on understanding the energy input of SEPs at Mars. Each study has investigated a component of this topic. Chapter 2 described a model of SEP transport and energy degradation. This model was applied in Chapter 3 to study how crustal fields affect ionization by SEP protons and in Chapter 4 to study how the Mars-solar wind interaction affected the precipitation of SEP electrons. Then Chapter 5 took a step back to estimate the total incident energy flux of SEPs relative to EUV and solar wind for six years of MAVEN observations, discussing the actual energy flux that would be absorbed, the role of season and solar cycle, and how MAVEN measurements compared to existing energetic flux predictions for the young sun.

6.1. Main contributions

I developed, implemented, and improved a 3-D Monte Carlo test particle model called ASPEN to simulate SEP transport and energy degradation. Initially built for solely modeling protons and hydrogen atoms in crustal fields below 600 km, the simulation has since been expanded to include electron collisional physics as well as tracing over an extended model domain that can stretch up to 15 Mars radii from Mars. ASPEN solves for individual particle collision likelihood while simultaneously tracing gyromotion via solving Lorentz force equations. The simulation has been rigorously compared with continuous slowing down approximations and other collision-by-collision models. All test particle predictions in the absence of collisions and electric fields have been shown to sufficiently conserve energy. Ongoing applications to investigations of proton aurora and hydrogen precipitation have reinforced ASPEN as a promising and sufficiently accurate model at Mars

The first task for ASPEN was to predict how crustal fields could influence the energy deposition of SEP protons. Following on a prior modeling study that had suggested the crustal fields could shield regions of the atmosphere [Leblanc et al. 2002], ASPEN was used to predict backscattering, energy deposition, and ionization in a representative crustal field region (50° S 182° E) and in the absence of fields. The primary ASPEN-derived findings for this study are as follows:

- Crustal fields can suppress ionization from incident SEP protons.
- Protons with energies up to 1 MeV may be magnetically reflected or backscattered, but protons with higher energies may deposit energy as if there were no magnetic fields present.
- The choice of either an approximate formula or double differential cross-sections to estimate the energy of produced secondary electrons influences energy deposition rates.

Next, ASPEN was applied to study the transport of energetic (>10 keV) electrons. While global aurora had been observed during SEP events (e.g. Schneider et al. [2015]), it remains unknown whether this aurora was due to SEP ions or electrons. Prior models indicated SEP ions would have widespread access to precipitate into the atmosphere of Mars [McKenna-Lawlor et al. 2012, Kallio et al. 2012] with the exception of the strongest crustal fields as previously discussed. However, no such modeling study had ever been performed for SEP electrons. ASPEN provided the first-ever model predictions of SEP electron transport through the near Mars magnetic fields and into the atmosphere. The primary findings from this study are as follows:

- For "nominal" solar wind conditions ($|\mathbf{B}_{sw}| = 3$, $B_y > 0$) and the strongest crustal fields oriented sunwards, the model predicted that only ~3.2% of the incident electron flux entered the atmosphere.
- Precipitation is patchy, occurring along open field lines into cusps and closed field lines via drift and nonadiabatic transport mechanisms.
- Varying the IMF orientation does not significantly change the relative flux that precipitates but does shift precipitation to other locations.
- Increasing the energy of the SEP electrons to 0.2-2 MeV increases the precipitating flux by a factor of 1.5 and broadens the patches of precipitation

Finally, I set aside ASPEN for a spacecraft data-centric overview study of the relative energy input of EUV, solar wind, and SEPs at Mars. While it is well-known that EUV is the dominant driver of ion supply and heating on the dayside of Mars, this investigation provides a baseline of the relative energy fluxes presented by each solar driver. Six years of observations from MAVEN during the rather weak solar cycle 24 were compiled to compute peak and average energy fluxes of EUV, solar wind ions and electrons, and SEP ions and electrons over multiple Carrington rotations. While ASPEN was not used in this study, the findings from the two prior studies were used to help guide a discussion of estimated energy deposition in the atmosphere. The primary findings from this study are as follows:

- On average, EUV energy flux exceeded solar wind ion energy flux by a factor of ~10-20 and solar wind electron energy flux by a factor of ~40-140, while solar wind ion fluxes exceeded SEP energy fluxes by at least order of magnitude
- Despite how incident solar wind energy fluxes can occasionally and briefly be comparable to EUV, the precipitating flux never exceeds EUV and would have to be $\sim 10^{12}$ $eV/cm^2/s$ or above to displace EUV as a primary source of ions and heating.
- SEPs may impart as much or more energy flux than solar wind electrons on the nightside during periods of strong and weak CME activity, but unfortunately the relative low altitude of any SEP-produced heating and ionization compared to solar wind electrons may make SEPs incapable of significantly affecting ion escape.
- The declining solar cycle was associated with overall decreased EUV, solar wind, and SEP energy fluxes, although seasonal oscillations more strongly influenced EUV than the charged particle fluxes, and the nadir of energetic particle fluxes followed months after the official end of solar minimum.
- Although MAVEN-observed average fluxes are much lower than the fluxes predicted for a young sun, the peak fluxes from the March 2015 and September 2017 events are comparable to some estimates, suggesting that the response of Mars during the instantaneous peaks of these events may be an analogue to the steady-state response of Mars three billion years ago.

6.2. Implications for ancient Mars

Although the work in this thesis has made many findings that are descriptive of how SEPs deposit energy at modern Mars, the overall question of whether solar storms were impactful to early Mars evolution remains. The tools and datasets developed during this research can be applied to make an estimate. In this subsection, I will use the MAVEN-observed time-averaged spectra and ASPEN to predict ion production rates above the exobase as a function of solar cycle. Next, I apply the apparent correlation between EUV and energetic particle fluxes to estimate total EUV, solar wind, and SEP energy fluxes at ancient Mars. After constructing an appropriate spectral shape for the ancient energetic particle fluxes, ASPEN was applied in the same way as for the MAVEN-observed spectra except using atmospheric densities representative of ancient Mars from Zhang et al. [1993]. Ultimately, I find that even if SEP energy fluxes are a factor of ten greater than the EUV energy flux, the ion production from SEPs is still an order of magnitude below that of EUV and solar wind electrons. If SEPs significantly influence atmospheres, it is only at altitudes below the exobase.

First, I use the time-averaged MAVEN observations calculated in Chapter 5. Average spectra in each instrument's original cadence were estimated using the same sampling criterion. All spectra were scaled to approximately decouple the seasonal variation and then normalized for a typical autumn equinox distance from the sun (~1.47 AU). The data was then binned into irradiance categories for solar minimum (1-1.47 mW/m^2), solar moderate (1.47-2.3 mW/m^2), and solar maximum (2.3-3.4 mW/m^2). While MAVEN has not observed a true solar maximum, the high EUV fluxes in the early mission and normalized to equinox provides a data point in the solar maximum category.

ASPEN was then used to calculate energy-dependent ion production for each spacecraft instrument's native energy resolution. To simplify the problem and increase energy resolution, ASPEN modeled 100,000 particles directly incident on Mars in the absence of magnetic fields. Three cases per solar driver were run to predict precipitation in MT-GCM densities that describe the atmosphere during solar minimum, moderate, and maximum. These energy deposition profiles were then combined with the solar driver spectra based on the binned irradiance category to predict ion production profiles for each spectra. Since ASPEN is focused on precipitating particles, another method was necessary to estimate ion production rates via photoionization. Using cross-sections from Heubner et al. [2015] and equations from Schunk and Nagy [2003], EUV-produced ionization rates as a function of altitude were estimated for each MT-GCM atmosphere and observed EUV spectra.

Each precipitating particle spectra was multiplied by a fixed percent to approximate the overall fraction of flux that precipitates: 3% of solar wind ions that convert into precipitating solar wind hydrogen [Kallio et al. 1997], 5% of solar wind electrons precipitating into cusps (average of dayside and nightside precipitation fractions from Weber et al. [2017, 2019]), 3% of SEP electrons (Chapter 4), and 100% of SEP ions [Leblanc et al. 2002]. In addition, dayside-only precipitating fluxes like solar wind hydrogen and EUV were reduced by 50%. The ion production rates *P(r)* were then integrated over the spherical volume that spanned from the exobase radius $r_{exobase}$ to space to determine the global ion supply *S* as a function of total EUV irradiance I_{EUV}:

$$S(I_{EUV}) = \int_{r_{exobase}(I_{EUV})}^{\infty} P(r, I_{EUV}) 4\pi r^2 dr \tag{6.1}$$

The exobase altitude was calculated for each simulation using the escaping atom cross-section from Fox and Hac [2009] (~3 x 10^{-15} cm^2) and the prescribed density profile.

Finally, the correlation between EUV and energetic particle fluxes was used to predict total energy fluxes of each solar driver. An approximate ancient Mars irradiance of 7.8 mW/m^2

was determined by multiplying the lowest MAVEN-observed EUV irradiance scaled to equinox by a factor of six to approximate the irradiance of Mars about 3.5 billion years ago [Ribas et al. 2005]. Fitting a line to each MAVEN-observed dataset as a function of EUV, the corresponding ancient total energy fluxes of each solar driver were 0.7 mW/m^2 (solar wind ions), 3.3 mW/m^2 (solar wind electrons), 72 mW/m^2 (SEP ions), and 24 mW/m^2 (SEP electrons). Although this correlation predicts total energy flux, it does not describe the shape of the spectrum. Thus we used the spectral shape for the highest time-averaged energy flux to construct an applicable spectra. Each spectra was then combined with an ASPEN run for a hypothetical ancient Mars atmosphere [Zhang et al. 1993] under the same previously described conditions.

Figure 6.1 shows the results of this analysis. The left panel shows the total energy fluxes as a function of EUV irradiance. The SEP energy fluxes appear to be extremely high, exceeding EUV by over an order of magnitude. The right panel shows the global ion supply. These estimated production rates are likely an upper limit, since this analysis ignored mitigating factors such as oblique incidence, strong crustal field shielding of SEP ions, and subsequent ion chemistry. The ion escape rate calculated using Equation 3 from Ramstad et al. [2018] is shown for context. The escape rate is an order of magnitude less than the photoionization supply, which is expected since only a fraction of produced ions will have energies sufficient to escape. Overall ion production from all solar drivers increases with EUV, which causes increasing precipitating fluxes and an expanded atmosphere. However, the ion supply from photoionization still dominates in the ancient Mars case, exceeding SEP-produced ionization above the exobase by a factor of 20.

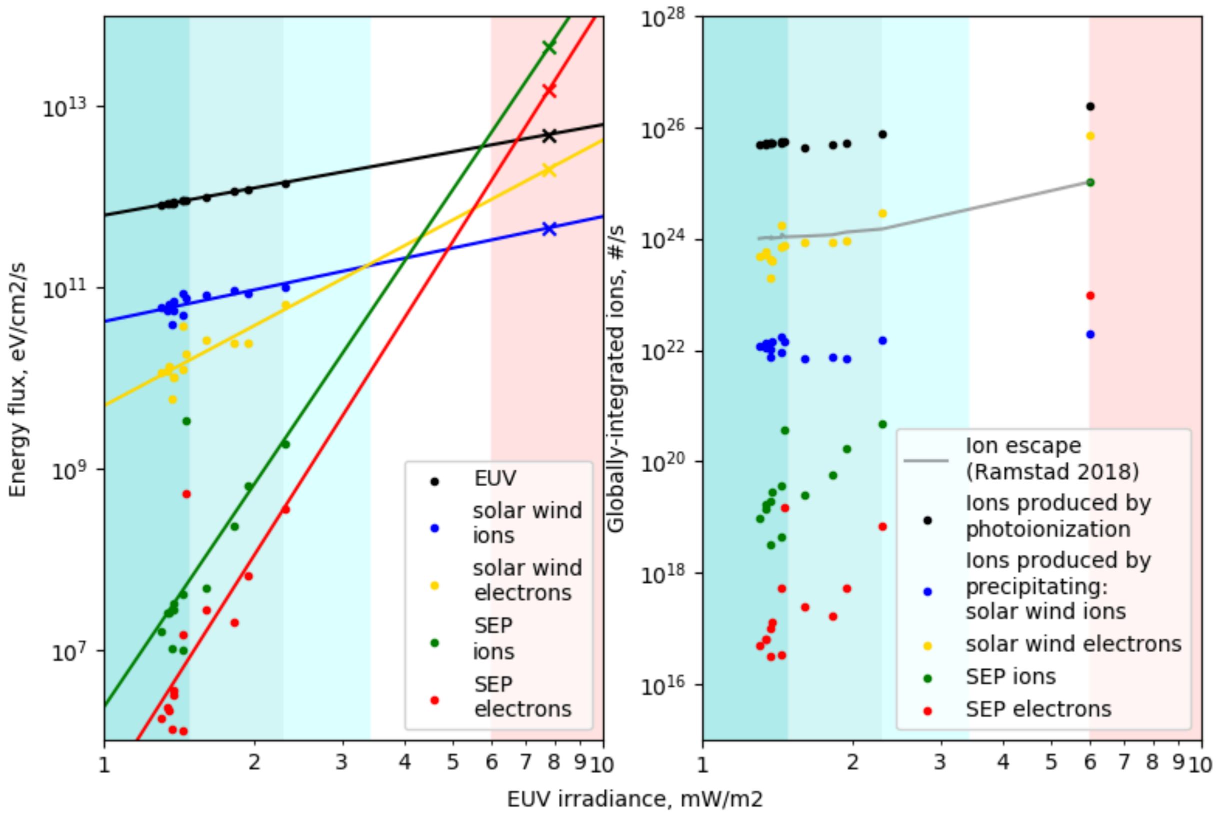

Figure 6.1: Energy flux of solar drivers (left) and globally-integrated ion production rates (right) as a function of EUV irradiance. Ion escape rates calculated based on Ramstad et al. [2018] are shown for comparison.

This back-of-the-envelope analysis suggests that SEPs may not have added meaningful ion supply at ancient Mars to drive escape. However, it does not rule out SEP influences on the mid-to-lower atmosphere. It has been suggested that high fluxes of SEPs drove nitrogen fixation in the terrestrial paleoatmosphere [Airapetian et al. 2016]. Although this specific process is unlikely to have occurred at Mars given the low abundance of nitrogen today, SEP-driven ion chemistry hasn't been studied at Mars and may be relevant to atmospheric processes at modern and ancient Mars.

Bibliography

Acuña, M. H., et al. (1998), Magnetic field and plasma observations at Mars: Initial results of the Mars Global Surveyor Mission, Science, 279(5357), 1676– 1680, doi:10.1126/science.279.5357.1676.

Acuña, M. H., et al. (1999), Global distribution of crustal magnetization discovered by the Mars Global Surveyor MAG/ER Experiment, Science, 284(5415), 790– 793, doi:10.1126/science.284.5415.790.

Acuña, M. H., et al. (2001), Magnetic field of Mars: Summary of results from the aerobraking and mapping orbits, J. Geophys. Res., 106(E10), 23,403– 23,417, doi:10.1029/2000JE001404.

Adams, D., Xu, S., Mitchell, D. L., Lillis, R. L., Fillingim, M., Andersson, L., Fowler, C., Connerney, J. E. P., Espley, J., & Mazelle, C. (2018). Using magnetic topology to probe the sources of Mars' nightside ionosphere. Geophysical Research Letters, 45, 12,190– 12,197. https://doi.org/10.1029/2018GL080629

Afonin, V., et al. (1989), Energetic ions in the close environment of mars and particle shadowing by the planet, Nature, 341(6243), 616–618.

Agostinelli, S., & Geant4 Collaboration (2003). Geant4—A simulation toolkit. Nuclear Instruments and Methods in Physics Research A, 506, 250– 303.

Airapetian, V. S., & Usmanov, A. V. (2016). Reconstructing the solar wind from its early history to the current epoch. The Astrophysical Journal Letters, 817, L24. https://doi.org/10.3847/2041-8205/817/2/L24

Airapetian, V. S., Glocer, A., Gronoff, G., Hébrard, E., & Danchi, W. (2016). Prebiotic chemistry and atmospheric warming of early Earth by an active young Sun. Nature Geoscience, 9(6), 452–455. https://doi.org/10.1038/ngeo2719

Alemanno, G., Orofino, V., & Mancarella, F. (2018). Global map of Martian fluvial systems: Age and total eroded volume estimations. Earth and Space Science, 5(10), 560– 577. https://doi.org/10.1029/2018EA000362

Allum, F. R., Palmeira, R. A. R., Rao, U. R., McCracken, K. G., Harries, J. R., and I. Palmer (1970), The degree of anisotropy of cosmic ray electrons of solar origin, Solar Phys. 17, 241-268.

Anderson, D. E., Jr., and C. W. Hord (1971), Mariner 6 and 7 ultraviolet spectrometer experiment: Analysis of hydrogen Lyman-alpha data, J. Geophys. Res., 76, 6666– 6673, doi:10.1029/JA076i028p06666.

Arkani-Hamed, J. (2004), Timing of the Martian core dynamo, J. Geophys. Res., 109, E03006, doi:10.1029/2003JE002195.

Avakyan, S. V., R. N. Il'in, V. M. Lavrov, and G. N. Ogurtsiv (1998), Collision Processes and Excitation of UV Emission From Planetary Atmospheric Gases: A Handbook of Cross Sections, Gordon and Breach, Amsterdam.

Barabash, S., A. Fedorov, R. R. Lundin, and J.-A. Sauvaud (2007), Martian atmospheric erosion rates, Science, 315, 501– 503, doi:10.1126/science.1134358.

Barnett CF, Ray JA, Ricci E, Wilkers MI, editors. 1977. Atomic data for controlled fusion research. Report no. ORNL-5296. Oak Ridge, TN: Oak Ridge National Laboratory.

Barth, C. A., C. W. Hord, J. B. Pearce, K. K. Kelly, G. P. Anderson, and A. I. Stewart (1971), Mariner 6 and 7 ultraviolet spectrometer experiment: Upper atmosphere data, J. Geophys. Res., 76, 2213– 2227, doi:10.1029/JA076i010p02213.

Basu B., J. R. Jasperse, R. M. Robinson, R. R. Vondrak, and D.S. Evans (1987), Linear transport theory of auroral proton precipitation: A comparison with observations, J. Geophys. Res., 92, 5920-5932.

Basu, B., J. R. Jasperse, D. J. Strickland, and R. E. Daniell Jr. (1993), Transport-theoretic model for the electron-proton-hydrogen atom aurora. 1: Theory, J. Geophys. Res., 98, 21517, doi:10.1029/93JA01646.

Berger, M. J., J. S. Coursey, M. A. Zucker, and J. Chang (2005), ESTAR, PSTAR, and ASTAR: Computer Programs for Calculating Stopping-Power and Range Tables for Electrons, Protons, and Helium Ions (version 1.2.3), http://physics.nist.gov/star, Natl. Instit. of Stand. and Technol., Gaithersburg, Md.

Bibring, J.-P., et al. (2004), Perennial water ice identified in the south polar cap of Mars, Nature, 428, 627– 630, doi:10.1038/nature02461.

Bibring, J. P., et al. (2006), Global mineralogical and aqueous Mars history derived from OMEGA/Mars Express data, Science, 312, 400– 404.

Biemann, K., et al. (1976), Search for organic and volatile inorganic compounds in two surface samples from the Chryse Planitia region of Mars, Science, 194, 72– 76, doi:10.1126/science.194.4260.72.

Birely, J. H. (1974), Formation of N2+B2Su+ and N2C3PiU in collisions of H+ and H with N2, Phys. Rev. A, 10, 550.

Birely, J.H., and R.J. McNeal (1972), Lymanalpha emission cross sections for collisions of 1-25 heV H+ and H with CO, CO2, CH4, and NH3, J. Chem. Phys., 56(5):2189-2194.

Bisoi, S.K., Janardhan, P., Ananthakrishnan, S.: 2020, Another mini solar maximum in the offing: a prediction for the amplitude of solar Cycle 25. J. Geophys. Res. 125(7), e2019JA027508. doi:10.1029/2019JA027508

Bößwetter, A., H. Lammer, Y. Kulikov, U. Motschmann, and S. Simon (2010), Non-thermal water loss of the early Mars: 3D multi-ion hybrid simulations, Planet. Space Sci., 58(14-15), 2031.

Bößwetter, A., et al. (2007), Comparison of plasma data from ASPERA-3/Mars-Express with a 3-D hybrid simulation, *Ann. Geophys.*, 25, 1851– 1864.

Bougher, S. W., Engel, S., Roble, R. G., & Foster, B. (1999). Comparative terrestrial planet thermospheres: 2. Solar cycle variation of global structure and winds at equinox. Journal of Geophysical Research, 104(E7), 16,591– 16,611. https://doi.org/10.1029/1998JE001019

Bougher, S. W., J. M. Bell, J. R. Murphy, M. A. Lopez-Valverde, and P. G. Withers (2006), Polar warming in the Mars thermosphere: Seasonal variations owing to changing insolation and dust distributions, Geophys. Res. Lett., 33, L02203, doi:10.1029/2005GL024059.

Bougher, S. W., Pawlowski, D., Bell, J. M., Nelli, S., McDunn, T., Murphy, J. R., et al. (2015). Mars Global Ionosphere-Thermosphere Model: Solar cycle, seasonal, and diurnal variations of the Mars upper atmosphere. Journal of Geophysical Research: Planets, 120, 311– 342. https://doi.org/10.1002/2014JE004715

Bougher, S. W., Brain, D. A., Fox, J. L., Francisco, G.-G., Simon-Wedlund, C., & Withers, P. G. (2017a). Upper neutral atmosphere and ionosphere. In R. Haberle, R. Clancy, F. Forget, M. Smith, & R. Zurek (Eds.), The atmosphere and climate of Mars, Cambridge Planetary Science (pp. 433–463). Cambridge: Cambridge University Press. https://doi.org/10.1017/9781139060172.014

Bougher, S. W., et al. (2017b), The structure and variability of Mars dayside thermosphere from MAVEN NGIMS and IUVS measurements: Seasonal and solar activity trends in scale heights and temperatures, J. Geophys. Res. Space Physics, 122, 1296–1313, doi:10.1002/2016JA023454.

Brain, D.A., and B.M. Jakosky (1997), Loss of Martian atmosphere by impacts since the formation of the Martian geologic record, Lunar Planet Sci. XXVIII.

Brain, D. A., Halekas, J. S., Peticolas, L. M., Lin, R. P., Luhmann, J. G., Mitchell, D. L., et al. (2006). On the origin of aurorae on Mars. Geophysical Research Letters, 33, L01201. https://doi.org/10.1029/2005GL024782

Brain, D., Lillis, R., Mitchell, D., Halekas, J., & Lin, R. (2007). Electron pitch angle distributions as indicators of magnetic field topology near Mars. Journal of Geophysical Research, 112, A09201. https://doi.org/10.1029/2007JA012435

Brain, D. A., et al. (2015), The spatial distribution of planetary ion fluxes near Mars observed by MAVEN, Geophys. Res. Lett., 42, 9142– 9148, doi:10.1002/2015GL065293.

Brain, D. A., Weber, T., Xu, S., Mitchell, D. L., Lillis, R. J., Halekas, J. S., et al. (2020). Variations in nightside magnetic field topology at Mars. Geophysical Research Letters, 47, e2020GL088921. https://doi.org/10.1029/2020GL088921

Brecht, S., and S.A. Ledvina (2006), The solar wind interaction with the Martian ionosphere/atmosphere. Space Sci. Rev. 126, 15-38, doi: 10.1007/s11214-006-9084-z.

Büchner, J., and L. M. Zelenyi (1989), Regular and chaotic charged particle motion in magnetotaillike field reversals: 1. Basic theory of trapped motion, J. Geophys. Res., 94 (A9), 11,821-11,842.

Bullock, M. A., and J. M. Moore (2007), Atmospheric conditions on early Mars and the missing layered carbonates, Geophys. Res. Lett., 34, L19201, doi:10.1029/2007GL030688.

Caffee M. W., Hohenberg C. M., Swindle T. D., and Goswami J. N. (1987). Evidence in meteorites for an active early Sun. The Astrophysical Journal 313: L31– L35.

Cain, J. C., B. B. Ferguson, and D. Mozzoni (2003), An n = 90 internal potential function of the Martian crustal magnetic field, J. Geophys. Res., 108(E2), 5008, doi:10.1029/2000JE001487.

Carr, M. H., & Head, J. W. (2010). Geologic history of Mars. Earth and Planetary Science Letters, 294, 185– 203. https://doi.org/10.1016/j.epsl.2009.06.042

Chaffin, M. S., J.-Y. Chaufray, I. Stewart, F. Montmessin, N. M. Schneider, and J.-L. Bertaux (2014), Unexpected variability of Martian hydrogen escape, Geophys. Res. Lett., 41, 314– 320, doi:10.1002/2013GL058578.

Chaffin, M. S., et al. (2015), Three-dimensional structure in the Mars H corona revealed by IUVS on MAVEN, Geophys. Res. Lett., 42(21), 9001– 9008, doi:10.1002/2015GL065287.

Chaffin, M.S., Kass, D.M., Aoki, S. *et a.* (2021). Martian water loss to space enhanced by regional dust storms. *Nat Astron* **5,** 1036–1042. https://doi.org/10.1038/s41550-021-01425-w

Chamberlain, J. W. (1963), Planetary coronae and atmospheric evaporation, Planet. Space Sci., 11, 901– 960, doi:10.1016/0032-0633(63)90122-3.

Chassefière, E., and F. Leblanc (2004), Mars Atmospheric escape and evolution: interaction with the solar wind, Planet. Space Sci., 52, 1039– 1058.

Chaufray, J. Y., R. Modolo, F. Leblanc, G. Chanteur, R. E. Johnson, and J. G. Luhmann (2007), Mars solar wind interaction: Formation of the Martian corona and atmospheric loss to space, J. Geophys. Res., 112, E09009, doi:10.1029/2007JE002915.

Chen, J., and P. J. Palmadesso (1986), Chaos and nonlinear dynamics of single-particle orbits in a magnetotaillike magnetic field, J. Geophys. Res., 91 (A2), 1,499-1,508.

Chojnacki, M., McEwen, A., Dundas, C., Ojha, L., Urso, A., & Sutton, S. (2016). Geologic context of recurring slope lineae in Melas and Coprates Chasmata, Mars. Journal of Geophysical Research: Planets, 121, 1204– 1231. https://doi.org/10.1002/2015JE004991

Clancy, R. T., Wolff, M. J., Lefèvre, F., Cantor, B. A., Malin, M. C., & Smith, M. D. (2016). Daily global mapping of Mars ozone column abundances with MARCI UV band imaging. Icarus, 266, 112– 133.

Cloutier, P., McElroy, M., & Michel, F. (1969). Modification of the Martian ionosphere by the solar wind. Journal of Geophysical Research, 74(26), 6215– 6228. https://doi.org/10.1029/JA074i026p06215

Craddock, R. A., and A. D. Howard (2002), The case for rainfall on a warm, wet early Mars, J. Geophys. Res., 107(E11), 5111, doi:10.1029/2001JE001505.

Cravens, T. E., et al. (2017), Hot oxygen escape from Mars: Simple scaling with solar EUV irradiance, *J. Geophys. Res. Space Physics*, 122, 1102– 1116, doi:10.1002/2016JA023461.

Cremades, H., & St. Cyr, O. C. (2006). Coronal mass ejections: Solar cycle aspects. Advances in Space Research, 40(7), 1042– 1048. https://doi.org/10.1016/j.asr.2007.01.088

Crider, D., et al. (2000), Evidence of electron impact ionization in the magnetic pileup bound- ary of Mars, Geophys. Res. Lett., 27, 45–48.

Crider, D. H., Espley, J., Brain, D. A., Mitchell, D. L., Connerney, J. E. P., & Acuna, M. (2005). Mars Global Surveyor observations of the Halloween 2003 solar superstorm's encounter with Mars. Journal of Geophysical Research, 110, A09S21. https://doi.org/10.1029/2001JA010881

Dalgarno, A., McElroy, M. B., & Moffett, R. J. (1963). Electron temperatures in the ionosphere. Planetary and Space Science, 11, 463– 484. https://doi.org/10.1016/0032-0633(63)90071-0

Damiani, A., M. Storini, M. L. Santee, and S. Wang (2010), The hydroxyl radical as an indicator of SEP fluxes in the high-latitude terrestrial atmosphere, Adv. Space Res., 46, 1225–1235, doi:10.1016/j.asr.2010.06.022.

Dartnell, L. R., L. Desorgher, J. M. Ward, and A. J. Coates (2007), Modelling the surface and subsurface Martian radiation environment: Implications for astrobiology, Geophys. Res. Lett., 34, L02207, doi:10.1029/2006GL027494.

Davidson, G. T. (1965), Expected spatial distribution of low-energy protons precipitated in the auroral zones, J. Geophys. Res., 70(5), 1061– 1068.

Delcourt, D. C., Martin, R. F., and F. Alem (1994), A simple model of magnetic moment scattering in a field reversal, Geophys. Res. Lett., 21(14), 1,543-1,546.

Delory, G. T., J. Luhmann, D. Brain, R. Lillis, D. Mitchell, R. A. Mewaldt, and T. Falkenberg (2012), Energetic particles detected by the Electron Reflectometer instrument on the Mars Global Surveyor, 1999–2006, Space Weather, 10, S06003, doi:10.1029/2012SW000781.

Desai, M., and Giacalone, J. (2016). Large gradual solar energetic particle events. Living Reviews in Solar Physics, 13, 3. https://doi.org/10.1007/s41116-016-0002-5

Di Achille, G., and B. M. Hynek (2010), Ancient ocean on Mars supported by global distribution of deltas and valleys, Nat. Geosci., 3, 459– 463, doi:10.1038/NGEO891.

DiBraccio, G. A., Luhmann, J. G., Curry, S. M., Espley, J. R., Xu, S., Mitchell, D. L., Ma, Y., Dong, C., Gruesbeck, J. R., Connerney, J. E. P., Harada, Y., Ruhunusiri, S., Halekas, J. S., Soobiah, Y., Hara, T., Brain, D. A., & Jakosky, B. M. (2018). The twisted configuration of the Martian magnetotail: MAVEN observations. Geophysical Research Letters, 45, 4559– 4568. https://doi.org/10.1029/2018GL077251

Diéval, C., Kallio, E., Stenberg, G., Barabash, S., and R. Jarvinen (2012), Hybrid simulations of proton precipitation patterns onto the upper atmosphere of Mars. Earth Planets Space, 64, 121-134.

Diéval, C., G. Stenberg, H. Nilsson, and S. Barabash (2013), A statistical study of proton precipitation onto the Martian upper atmosphere: Mars Express observations, J. Geophys. Res. Space Physics, 118, 1972– 1983, doi:10.1002/jgra.50229.

Diéval, C., D. D. Morgan, F. Němec, and D. A. Gurnett (2014), MARSIS observations of the Martian nightside ionosphere dependence on solar wind conditions, J. Geophys. Res. Space Physics, 119, 4077– 4093, doi:10.1002/2014JA019788.

Dickeson, Z. I., & Davis, J. M. (2020). Martian Oceans. Astronomy and Geophysics, 61(3), 3.11–3.17. https://doi.org/10.1093/astrogeo/ataa038

Desorgher, L., E. O. Flückiger, M. Gurtner, M. R. Moser, and R. Bütikofer (2005), ATMOCOSMICS: A GEANT4 code for computing the interaction of cosmic rays with the Earth's atmosphere, Int. J. Mod. Phys. A, 20, 6802–6804.

Dolginov, S., Yeroshenko, Y., and L. Zhuzgov (1973), Magnetic field in the very close neighborhood of Mars according to data from the Mars 2 and Mars 3 spacecraft, J. Geophys. Res., 78, 4779–4786.

Dong, C., S. W. Bougher, Y. Ma, G. Toth, A. F. Nagy, and D. Najib (2014), Solar wind interaction with Mars upper atmosphere: Results from the one-way coupling between the multifluid MHD model and the MTGCM model, Geophys. Res. Lett., 41, 2708–2715, doi:10.1002/2014GL059515.

Dong, C., Y. Ma, S. W. Bougher, G. Toth, A. F. Nagy, J. S. Halekas, Y. X. Dong, S. M. Curry, J. G. Luhmann, D. Brain, J. E. P. Connerney, J. Espley, P. Mahaffy, M. Benna, J. P. McFadden, D. L. Mitchell, G. A. DiBraccio, R. J. Lillis, B. M. Jakosky, and J. M. Grebowsky (2015), Multifluid MHD study of the solar wind interaction with Mars' upper atmosphere during the 2015 March 8th ICME event, Geophys. Res. Lett., 42, 9103-9112, doi:10.1002/2015GL065944.

Dong, Y., X. Fang, D. A. Brain, J. P. McFadden, J. S. Halekas, J. E. Connerney, S. Curry, Y. Harada, J. G. Luhmann, and B. M. Jakosky (2015), Strong plume fluxes at Mars observed by MAVEN: An important planetary ion escape channel, Geophys. Res. Lett., 42, 8942– 8950, doi:10.1002/2015GL065346.

Dong, Y., Fang, X., Brain, D. A., McFadden, J. P., Halekas, J. S., Connerney, J. E. P., et al. (2017). Seasonal variability of Martian ion escape through the plume and tail from MAVEN observations. Journal of Geophysical Research: Space Physics, 122, 4009– 4022. https://doi.org/10.1002/2016JA023517

Dresing, N., Gómez-Herrero, R., Heber, B., Klassen, A., Malandraki, O., Dröge, W., and Y. Kartavykh (2014), Statistical survey of widely spread out solar energetic events observed with STEREO and ACE with special attention to anisotropies, Astron. Astrophys., 567, A27, doi: 10.1051/0004-6361/201423789.

Dubinin, E., R. Lundin, O. Norberg, and N. Pissarenko (1993a), Ion acceleration in the Martian tail: Phobos observations, J. Geophys. Res., 98, 3991– 3997, doi:10.1029/92JA02233.

Dubinin, E., Fraenz, M., Woch, F., Duru, F., Gurnett, D., Modolo, R., Barabash, S., and R. Lundin (2009) Ionospheric storms on Mars: Impact of the corotating interaction region, Geophys. Res. Lett., 36, L01105, doi:10.1029/2008GL036559.

Dubinin, E., M. Fraenz, A. Fedorov, R. Lundin, N. Edberg, F. Duru, and O. Vaisberg (2011), Ion energization and escape on Mars and Venus, Space Sci. Rev., 162, 173, doi:10.1007/s11214-011-9831-7.

Dubinin, E., and M. Fraenz (2015), Magnetotails of Mars and Venus, in Magnetotails in the Solar System, edited by A. Keiling, C. M. Jackman, and P. A. Delamere, John Wiley, Hoboken, N. J., doi: 10.1002/9781118842324.ch3.

Dubinin, E., Fraenz, M., Pätzold, M., McFadden, J., Mahaffy, P. R., Eparvier, F., Zelenyi, L.(2017). Effects of solar irradiance on the upper ionosphere and oxygen ion escape at Mars: MAVEN observations. Journal of Geophysical Research: Space Physics, 122, 7142– 7152. https://doi.org/10.1002/2017JA024126

Dubinin, E., Fraenz, M., Pätzold, M., Woch, J., McFadden, J., Fan, K., et al. (2020). Impact of martian crustal magnetic field on the ion escape. Journal of Geophysical Research: Space Physics, 125. 10574– 10579. https://doi.org/10.1029/2020JA028010

Dubinin, E., Sauer, K., Baumgärtel, K., & Lundin, R. (1997). The Martian magnetosheath: Phobos-2 observations. Advances in Space Research, 20(2), 149– 153. https://doi.org/10.1016/S0273-1177(97)00525-5

Dumbović, M., Guo, J., Temmer, M., Mays, M. L., Veronig, A., Heinemann, S. G., Karin, D., Stefan, H., Jasper, H., Christian, M., Tanja, A., Jürgen, H., Saša, B., Konstantin, H., Yuming, W., Lukas, H., Martin, L., & Wimmer-Schweingruber, R. F. (2019). Unusual plasma and particle signatures at Mars and STEREO-A related to CME-CME interaction. The Astrophysical Journal, 880(1), 18. https/doi.org/10.3847/1538-4357/ab27ca

Dundas, C. M. (2020). Geomorphological evidence for a dry dust avalanche origin of slope streaks on Mars. Nature Geoscience, 13, 473– 476. https://doi.org/10.1038/s41561-020-0598-x

Edberg, N. J. T., M. Lester, S. W. H. Cowley, and A. I. Eriksson (2008), Statistical analysis of the location of the Martian magnetic pileup boundary and bow shock and the influence of crustal magnetic fields, J. Geophys. Res., 113, A08206, doi:10.1029/2008JA013096.

Edberg, N. J. T., H. Nilsson, A. O. Williams, M. Lester, S. E. Milan, S. W. H. Cowley, M. Franz, S. Barabash, and Y. Futaana (2010), Pumping out the atmosphere of Mars through solar wind pressure pulses, Geophys. Res. Lett., 37, L03107, doi:10.1029/2009GL041814.

Edgar, B.C., Miles, W.T., and A.E.S. Green (1973), Energy deposition of protons in molecular nitrogen and applications to proton auroral phenomena, J. Geophys. Res., 78, 6595.

Edgar, B.C., Porter, H.S., and A.E.S. Green (1975), Proton energy deposition in molecular and atomic oxygen and applications to the polar cap, Planet. Space Sci., 23, 787.

Ehlmann, B. L., and C. S. Edwards (2014), Mineralogy of the Martian surface, Annu. Rev. Earth Planet. Sci., 42, doi:10.1146/annurev-earth-060313-055024.

Ehlmann, B. L., J. F. Mustard, S. L. Murchie, J.-P. Bibring, A. Meunier, A. A. Fraeman, and Y. Langevin (2011b), Subsurface water and clay mineral formation during the early history of Mars, Nature, 479(7371), 53– 60, doi:10.1038/nature10582.

Eparvier, F. G., Chamberlin, P. C., Woods, T. N., & Thiemann, E. M. B. (2015). The solar extreme ultraviolet monitor for MAVEN. Space Science Reviews, 195(1–4), 293– 301. https://doi.org/10.1007/s11214-015-0195-2

Ergun, R. E., L. Andersson, W. K. Peterson, D. Brain, G. T. Delory, D. L. Mitchell, R. P. Lin, and A. W. Yau (2006), Role of plasma waves in Mars' atmospheric loss, Geophys. Res. Lett., 33, L14103, doi:10.1029/2006GL025785.

Ergun, R. E., et al. (2016), Enhanced O2+ loss at Mars due to an ambipolar electric field from electron heating, J. Geophys. Res. Space Physics, 121, 4668– 4678, doi:10.1002/2016JA022349.

Espley, J. R., W. M. Farrell, D. A. Brain, D. D. Morgan, B. Cantor, J. J. Plaut, M. H. Acuña, and G. Picardi (2007), Absorption of MARSIS radar signals: Solar energetic particles and the daytime ionosphere, Geophys. Res. Lett., 34, L09101, doi:10.1029/2006GL028829.

Espley, J. R. (2018). The Martian magnetosphere: Areas of unsettled terminology. Journal of Geophysical Research: Space Physics, 123, 4521–4525. https://doi.org/10.1029/2018JA025278

Fairén, A. G. (2010), A cold and wet Mars, Icarus, 208, 165– 175.

Fang, X., Liemohn, M. W., Nagy, A. F., Ma, Y., De Zeeuw, D. L., Kozyra, J. U., & Zurbuchen, T. H. (2008). Pickup oxygen ion velocity space and spatial distribution around Mars. Journal of Geophysical Research, 113, A02210. https://doi.org/10.1029/2007JA012736

Fassett, C. I., J. L. Dickson, J. W. Head, J. Levy, and D. R. Marchant (2010), Supraglacial and proglacial valleys on Amazonian Mars, Icarus, 208, 86– 100, doi:10.1016/j.icarus.2010.02.021.

Fassett, C. I., and J. W. Head III (2008), The timing of Martian valley network activity: Constraints from buffered crater counting, Icarus, 195, 61– 89.

Feldman, W. C., et al. (2004), Global distribution of near-surface hydrogen on Mars, J. Geophys. Res., 109, E09006, doi:10.1029/2003JE002160.

Feynman, J., and S. Gabriel (1988), Interplanetary Particle Environment: Proceedings of a Conference, JPL Publ., 88-28.

Fowler, C. M., Agapitov, O. V., Xu, S., Mitchell, D. L., Andersson, L., Artemyev, A., & Mazelle, C. (2020). Localized heating of the Martian topside ionosphere through the combined effects of magnetic pumping by large-scale magnetosonic waves and pitch angle diffusion by whistler waves. Geophysical Research Letters, 47, e2019GL086408. https://doi.org/10.1029/2019GL086408

Fox, J. L., & Dalgarno, A. (1979). Ionization, luminosity, and heating of the upper atmosphere of Mars. Journal of Geophysical Research, 84(A12), 7315– 7333.

Fox, J. L., and A. B. Hać (2009), Photochemical escape of oxygen from Mars: A comparison of the exobase approximation to a Monte Carlo method, Icarus, 204, 527– 544, doi:10.1016/j.icarus.2009.07.005.

Freissinet, C., et al. (2015), Organic molecules in the Sheepbed Mudstone, Gale Crater, Mars, J. Geophys. Res. Planets, 120, 495– 514, doi:10.1002/2014JE004737.

Frey, H. V., S. E. Sakimoto and J. H. Roark (1998), The MOLA topographic signature of the crustal dichotomy boundary zone on Mars, Geophys. Res. Lett., 25(24), 4409– 4412, doi:10.1029/1998GL900095.

Futaana, Y., et al. (2008), Mars Express and Venus Express multi-point observations of geoeffective solar flare events in December 2006, Planet. Space Sci., 56, 873– 880, doi:10.1016/j.pss.2007.10.014.

Gaidos, E., and G. Marion (2003), Geological and geochemical legacy of a cold early Mars, J. Geophys. Res., 108, 5055, doi:10.1029/2002JE002000.

Gaisser, T. K. (1990), Cosmic Rays and Particle Physics, Cambridge Univ. Press, Cambridge, U. K.

Galand, M., J. Lilensten, W. Kofman, and R. B. Sidje (1997), Proton transport model in the ionosphere: 1. Multistream approach of the transport equations, J. Geophys. Res., 102, 22,261–22,272, doi:10.1029/97JA01903.

Gérard, J. -C., Soret, L., Shematovich, V. I., Bisikalo, D. V., and S. W. Bougher (2017), The Mars diffuse aurora: A model of ultraviolet and visible emissions, Icarus, 288, 284-294.

Gopalswamy, N. (2004). A global picture of CMEs in the inner heliosphere. In G. Poletto & S. T. Suess (Eds.), The sun and the heliosphere as an integrated system (Vol. 317, pp. 201). Dordrecht, The Netherlands: Kluwer Academic Publishers. https://doi.org/10.1007/978-1-4020-2831-98

Gopalswamy, N., Akiyama, S., Yashiro, S., Michalek, G., Xie, H., and P. Mäkelä. (2020) Effect of the weakened heliosphere in solar cycle 24 on the properties of coronal mass ejections. J. Phys.: Conf. Ser. 1620, 012005, doi:10.1088/1742-6596/1620/1/012005

Green, A.E.S., and R.J. McNeal (1971), Analytic cross sections for inelastic collisions of protons and hydrogen atoms with atomic and molecular gases. J. Geophys. Res. 76(1):133-144.

Greenwood, J. P., S. Itoh, N. Sakamoto, E. P. Vicenzi, and H. Yurimoto (2008), Hydrogen isotope evidence for loss of water from Mars through time, Geophys. Res. Lett., 35, L05203, doi:10.1029/2007GL032721.

Grießmeier, J. M., et al. (2004), The effect of tidal locking on the magnetospheric and atmospheric evolution of "Hot Jupiters", Astron. Astrophys., 425, 753–762, doi:10.1051/0004-6361:20035684.

Gronoff, G., C. Mertens, J. Lilensten, L. Desorgher, E. Flückiger, and P. Velinov (2011), Ionization processes in the atmosphere of Titan. III. Ionization by high-Z nuclei cosmic rays, Astron. Astrophys., 529, A143, doi:10.1051/0004-6361/201015675.

Gronoff, G., C. S. Wedlund, C. J. Mertens, M. Barthélemy, R. J. Lillis, and O. Witasse (2012), Computing uncertainties in ionosphere-airglow models. II—The Martian airglow, J. Geophys. Res., 117, A05309, doi:10.1029/2011JA017308.

Gronoff, G., R. B. Norman, and C. J. Mertens (2015), Computation of cosmic ray ionization and dose at Mars. I: a comparison of HZETRN and Planetocosmics for proton and alpha particles. Adv. Sp. Res. 55, 1799–1805.

Gruesbeck, J. R., Espley, J. R., Connerney, J. E. P., DiBraccio, G. A., Soobiah, Y. I., Brain, D., Mazelle, C., Dann, J., Halekas, J., & Mitchell, D. L. (2018). The three-dimensional bow shock of Mars as observed by MAVEN. Journal of Geophysical Research: Space Physics, 123, 4542–4555. https://doi.org/10.1029/2018JA025366

Güdel, M. (2007), The Sun in time: Activity and environment, Living Rev. Sol. Phys., 4(3).

Gurnett, D. A., et al. (2008), An overview of radar soundings of the Martian ionosphere from the Mars Express spacecraft, Adv. Space Res., 41, 1335– 1346, doi:10.1016/j.asr.2007.01.062.

Guzman, M., McKay, C. P., Quinn, R. C., Szopa, C., Davila, A. F., Navarro-gonzález, R., & Freissinet, C. (2018). Identification of chlorobenzene in the Viking gas chromatograph-mass spectrometer data sets: Reanalysis of Viking Mission data consistent with aromatic organic compounds on Mars. Journal of Geophysical Research: Planets, 123(7), 1674– 1683. https://doi.org/10.1029/2018JE005544

Haider, S. A., and J. Masoom (2019). Modeling of diffuse aurora due to precipitation of H+-H and SEP electrons in the nighttime atmosphere of Mars: Monte Carlo simulation and MAVEN observation, J. Geophys. Res. Space Physics, 124, 9566-9576, doi:10.1029/2019JA026688.

Halekas, J. S., Taylor, E. R., Dalton, G., Johnson, G., Curtis, D. W., McFadden, J. P., et al. (2015a). The Solar Wind Ion Analyzer for MAVEN. Space Science Reviews, 195(1-4), 125– 151, https://doi.org/10.1007/s11214-013-0029-z

Halekas, J. S., et al. (2015b), MAVEN observations of solar wind hydrogen deposition in the atmosphere of Mars, Geophys. Res. Lett., 42, 8901– 8909, doi:10.1002/2015GL064693.

Halekas, J. S. (2017). Seasonal variability of the hydrogen exosphere of Mars. Journal of Geophysical Research: Planets, 122, 901– 911. https://doi.org/10.1002/2017JE005306

Hamilton D. C. (1977), The radial transport of energetic solar flare particles from 1 to 6 AU. Journal of Geophysical Research 82: 2157– 2169.

Hamilton, D. C. (1988), The radial dependence of the solar energetic particle flux, in Interplanetary Particle Environment: Proceedings of a Conference, edited by J. Feynman, and S. Gabriel, JPL Publ., 88-28, 86.

Harada, Y., Gurnett, D. A., Kopf, A. J., Halekas, J. S., Ruhunusiri, S., DiBraccio, G. A., et al. (2018). MARSIS observations of the Martian nightside ionosphere during the September 2017 solar event. Geophysical Research Letters, doi: 10.1002/2018GL077622.

Harnett, E. M., and R. M. Winglee (2003), The influence of a mini-magnetopause on the magnetic pileup boundary at Mars, Geophys. Res. Lett., 30(20), 2074, doi:10.1029/2003GL017852.
Heber, B., A. Kopp, J. Gieseler, R. Müller-Mellin, H. Fichtner, K. Scherer, M. S. Potgieter, and S. E. S. Ferreira (2009), Modulation of galactic cosmic ray protons and electrons during an unusual solar minimum, Astyrophys. J., 699, 1956– 1963, doi:10.1088/0004-637X/699/2/1956.
Hecht, M. H., et al. (2009), Detection of perchlorate and the soluble chemistry of Martian soil at the Phoenix Lander site, Science, 32, 64– 67, doi:10.1126/science.1172466.
Henriksen, K. (1978), Variations of proton energy and pitch-angle spectra in the upper atmosphere, J. Atmos. Terr. Phys., 41, 633.
Hughes, A., Chaffin, M., Mierkiewicz, E., Deighan, J., Jain, S., Schneider, N., et al. (2019). Proton aurora on Mars: A dayside phenomenon Pervasive in Southern Summer. Journal of Geophysical Research: Space Physics, 124(12), 10533– 10548. https://doi.org/10.1029/2019JA027140
Hughes, A. (2021) Proton aurora at Mars: Assessing the characteristics, variability, and driving mechanisms of a newly discovered phenomenon. PhD thesis, Embry-Riddle Aeronautical University, Daytona Beach.
Hunten, D. M. (1973), The escape of light gases from planetary atmospheres, J. Atmos. Sci., 30, 1481– 1494, doi:10.1175/1520-0469(1973)030<1481:TEOLGF>2.0.CO;2.
Hunten, D. M., Pepin, R. O., & Walker, J. C. G. (1987). Mass fractionation in hydrodynamic escape. Icarus, 69(3), 532– 549. https://doi.org/10.1016/0019-1035(87)90022-4
Jain, S. K., Deighan, J., Schneider, N. M., Stewart, A. I. F., Evans, J. S., Thiemann, E. M. B., et al. (2018). Martian thermospheric response to an X8.2 Solar Flare on September 10, 2017 as seen by MAVEN/IUVS. Geophysical Research Letters, 45. https://doi.org/10.1029/2018GL077731
Jackman, C. H., M. T. DeLand, G. J. Labow, E. L. Fleming, D. K. Weisenstein, M. K. W. Ko, M. Sinnhuber, and J. M. Russell III (2005), Neutral atmospheric influences of the solar proton events in October–November 2003, J. Geophys. Res., doi:10.1029/2004JA010888.
Jakosky, B. (2019). The CO2 inventory on Mars. Planetary and Space Science, 175(1), 52– 59.
Jakosky, B. M., et al. (2015), MAVEN observations of the response of Mars to an interplanetary coronal mass ejection, Science, 350, 0210, doi:10.1126/science.aad3443.
Jakosky, B. M., Slipski, M., Benna, M., Mahaffy, P., Elrod, M., Yelle, R., et al. (2017). Mars' atmospheric history derived from upper-atmosphere measurements of $^{38}Ar/^{36}Ar$. Science, 355(6332), 1408– 1410. https://doi.org/10.1126/science.aai7721
Jakosky, B., Brain, D., Chaffin, M., Curry, S., Deighan, J., Grebowsky, J., Halekas, J., Leblanc, F., Lillis, R., Luhmann, J., et al.. (2018). Loss of the Martian atmosphere to space: Present-day loss rates determined from MAVEN observations and integrated loss through time. Icarus, 315, 146–157. https://doi.org/10.1016/j.icarus.2018.05.030
Jarvinen, R., Brain, D. A., Modolo, R., Fedorov, A., & Holmström, M. (2018). Oxygen ion energization at Mars: Comparison of MAVEN and Mars express observations to global hybrid simulation. Journal of Geophysical Research: Space Physics, 123, 1678– 1689. https://doi.org/10.1002/2017JA024884
Johnson, R. E. (1990), Energetic Charged-Particle Interaction With Atmospheres and Surfaces, Springer, New York. Kasting, J. F. (1991), CO2 condensation and the climate of early Mars, Icarus, 94, 1– 13.
Jokipii, J. R., Levy, E. H., & Hubbard, W. B. (1977). Effects of particle drift on cosmic-ray transport I—General properties, application to solar modulation. The Astrophysical Journal, 213, 861–868. https://doi.org/10.1086/155218

Jolitz, R. D., Dong, C. F., Lee, C. O., Lillis, R. J., Brain, D. A., Curry, S. M., et al. (2017). A Monte Carlo model of crustal field influences on solar energetic particle precipitation into the Martian atmosphere. Journal of Geophysical Research: Space Physics, 122, 5653–5669. https://doi.org/10.1002/2016JA023781

Jolitz, R. D., Dong, C. F., Rahmati, A., Brain, D. A., Lee, C. O., Lillis, R. J., et al. (2021). Test particle model predictions of SEP electron transport and precipitation at Mars. Journal of Geophysical Research: Space Physics, 126, e2021JA029132. https://doi.org/10.1029/2021JA029132

Kahler, S. W., & Vourlidas, A. (2014). Do interacting coronal mass ejections play a role in solar energetic particle events? The Astrophysical Journal, 784(1), 47. https://doi.org/10.1088/0004-637X/784/1/47

Kajdič, P., Sánchez-Cano, B., Neves- Ribeiro, L., Witasse, O., Bernal, G. C., Rojas-Castillo, D., et al. (2021). Interaction of space weather phenomena with Mars plasma environment during solar minimum 23/24. Journal of Geophysical Research: Space Physics, 126, e2020JA028442. https://doi.org/10.1029/2020JA028442

Kallio, E., J. G. Luhmann, and S. Barabash (1997), Charge exchange near Mars: Solar wind absorption and energetic neutral atom production, J. Geophys. Res., 102, 22,183– 22,197, doi:10.1029/97JA01662.

Kallio, E., & Barabash, S. (2000). On the elastic and inelastic collisions between precipitating energetic hydrogen atoms and Martian atmospheric neutrals. Journal of Geophysical Research, 105(A11), 24973– 24996. https://doi.org/10.1029/2000JA900077

Kallio, E., and S. Barabash (2001), Atmospheric effects of precipitating energetic hydrogen atoms on the Martian atmosphere, J. Geophys. Res., 106, 165– 177, doi:10.1029/2000JA002003.

Kallio, E., et al. (2006), Ion escape at Mars: Comparison of a 3-D hybrid simulation with Mars Express IMA/ASPERA-3 measurements, *Icarus*, 182, 350– 359, doi:10.1016/j.icarus.2005.09.018.

Kallio, E., S. McKenna-Lawlor, M. Alho, R. Jarvinen, S. Dyadechkin, and V. V. Afonin (2012), Energetic protons at Mars: Interpretation of SLED/Phobos-2 observations by a kinetic model, Ann. Geophys., 30, 1595–1609, doi:10.5194/angeo-30-1595-2012.

Kella, J., P. J. Johnson, H. B. Pederson, L. Vejby-Christensen, and L. H. Andersen (1997), The source of green light emission determined from a heavy-ion storage ring experiment, Science, 276, 1530– 1533.

Kite, E. S., J.-P. Williams, A. Lucas, and O. Aharonson (2014), Low palaeopressure of the Martian atmosphere estimated from the size distribution of ancient craters, Nat. Geosci., 7(5), 335–339.

Kite, E. S. (2019). Geologic constraints on early Mars climate. Space Science Reviews, 215(1). https://doi.org/10.1007/s11214-018-0575-5

Klein, H. P. (1978), The Viking biological experiments on Mars, Icarus, 34, 666–674.

Klein, K.-L., & Dalla, S. (2017). Acceleration and propagation of solar energetic particles. Space Science Reviews, 212, 1107– 1136.

Klein, K.-L., Trottet, G., Samwel, S., & Malandraki, O. (2011). Particle acceleration and propagation in strong flares without major solar energetic particle events. Solar Physics, 269, 309– 333. https://doi.org/10.1007/s11207-011-9710-0

Kliore, A., D. L. Cain, G. S. Levy, V. R. Eshleman, G. Fjeldbo, and F. D. Drake (1965), Occultation experiment: Results of the first direct measurement of Mars's atmosphere and ionosphere, Science, 149(3689), 1243– 1248, doi:10.1126/science.149.3689.1243.

Kokorowski, M., J.G. Sample, R.H. Holzworth, E.A. Bering, S.D. Bale, J.B. Blake, A.B. Collier, A.R.W. Hughes, E. Lay, R.P. Lin, M.P. McCarthy, R.M. Millan, H. Moraal, T.P. O'Brien, G.K. Parks, M. Pulupa, B.D. Reddell, D.M. Smith, P.H. Stoker, and L. Woodger (2006). Rapid fluctuations of stratospheric electric field following a solar energetic particle event. Geophys. Res. Lett. 33, L20105, doi:10.1029/2006GL027718

Korablev, O., Olsen, K. S., Trokhimovskiy, A., Lefèvre, F., Montmessin, F., Fedorova, A. A., et al. (2021). Transient HCl in the atmosphere of Mars. Science Advances, 7, eabe4386. https://doi.org/10.1126/sciadv.abe4386

Krivolutsky, A.A., Kuminov, A.A., Kukoleva, A.A., Repnev, A.I., Pereyaslova, N.K., and Nazarova, M.N., Solar proton activity during cycle 23 and changes in the ozonosphere: Numerical simulation and analysis of observational data, Geomagn. Aeron. (Engl. Transl.), 2008, vol. 48, no. 4, pp. 432–445.

Krymskii, A. M., T. K. Breus, N. F. Ness, M. H. Acuña, J. E. P. Connerney, D. H. Crider, D. L. Mitchell, and S. J. Bauer (2002), Structure of the magnetic field fluxes connected with crustal magnetization and topside ionosphere at Mars, J. Geophys. Res., 107(A9), 1245, doi:10.1029/2001JA000239.

Kulikov, Y. N., H. Lammer, H. Lichtenegger, T. Penz, D. Breuer, T. Spohn, R. Lundin, and H. K. Biernat (2007), A comparative study of the influence of the active young Sun on the early atmospheres of Earth, Venus, and Mars, Space Sci. Rev., 129, 207– 243, doi:10.1007/s11214-007-9192-4.

Lammer, H., et al. (2012), Variability of solar/stellar activity and magnetic field and its influence on planetary atmosphere evolution, Earth Planets Space, 64, 179– 199.

Lamy, P. L., Floyd, O., Boclet, B., Wojak, J., Gilardy, H., & Barlyaeva, T. (2019). Coronal mass ejections over solar cycles 23 and 24. Space Science Reviews, 215(5), 39. https://doi.org/10.1007/s11214-019-0605-y

Lario, D., A. Aran, N. Agueda, and B. Sanahuja (2007), Radial dependence of proton peak intensities and fluences in SEP events: Influence of the energetic particle transport parameters, Adv. Space Res., 40, 289, doi:10.1016/j.asr.2007.01.057.

Lario, D., Aran, A., Gómez-Herrero, R., Dresing, N., Heber, B., Ho, G., et al. (2013). Longitudinal and radial dependence of solar energetic particle peak intensities: STEREO, ACE, SOHO, GOES, and MESSENGER observations. The Astrophysical Journal, 767(1), 41.

Larson, D. E., et al. (2015), The MAVEN solar energetic particle investigation, Space Sci. Rev., 195, 153– 172, doi:10.1007/s11214-015-0218-z.

Lauro, S. E., Pettinelli, E., Caprarelli, G., Guallini, L., Rossi, A. P., Mattei, E., et al. (2021). Multiple subglacial water bodies below the south pole of Mars unveiled by new MARSIS data. Nature Astronomy, 5(1), 63– 70. https://doi.org/10.1038/s41550-020-1200-6

Lavraud, B., & Larson, D. E. (2016). Correcting moments of in situ particle distribution functions for spacecraft electrostatic charging. Journal of Geophysical Research: Space Physics, 121, 8462– 8474. https://doi.org/10.1002/2016JA022591

Le Chat, G., Issautier, K., & Meyer-Vernet, N. (2012). The Solar Wind Energy Flux. Solar Physics, 279(1), 197– 205. https://doi.org/10.1007/s11207-012-9967-y

Lean, J. L. (1997), The Sun's variable radiation and its relevance for Earth, Annu. Rev. Astron. Astrophys., 35, 33– 67, doi:10.1146/annurev.astro.35.1.33.

Leblanc, F., and R. E. Johnson (2002), Role of molecular species in pickup ion sputtering of the Martian atmosphere, J. Geophys. Res., 107(E2), 5010, doi:10.1029/2000JE001473.

Leblanc, F., J. G. Luhmann, R. E. Johnson, and E. Chassefiere (2002), Some expected impacts of a solar energetic particle event at Mars, J. Geophys. Res., 107(A5), 1058, doi:10.1029/2001JA900178.

Leblanc, F., Modolo, R., Curry, S., Luhmann, J., Lillis, R., Chaufray, J. Y., et al. (2015). Mars heavy ion precipitating flux as measured by Mars Atmosphere and Volatile EvolutioN. Geophysical Research Letters, 42, 9135– 9141. https://doi.org/10.1002/2015GL066170

Leblanc, F., Martinez, A., Chaufray, J. Y., Modolo, R., Hara, T., Luhmann, J., et al. (2018). On Mars's atmospheric sputtering after MAVEN's first Martian year of measurements. Journal of Geophysical Research: Space Physics, 45, 4685– 4691. https://doi.org/10.1002/2018GL077199

Lee, C. O., J. G. Luhmann, I. de Pater, G. M. Mason, D. Haggerty, I. G. Richardson, H. V. Cane, L. K. Jian, C. T. Russell, and M. I. Desai (2010), Organization of energetic particles by the solar wind structure during the declining to minimum phase of solar cycle 23, Sol. Phys., 263, 239–261.

Lee, C. O., Hara, T., Halekas, J. S., Thiemann, E., Chamberlin, P., Eparvier, F., et al. (2017). MAVEN observations of the solar cycle 24 space weather conditions at Mars. Journal of Geophysical Research: Space Physics, 122, 2768– 2794. https://doi.org/10.1002/2016JA023495

Lee, C. O., Jakosky, B. M., Luhmann, J. G., Brain, D. A., Mays, M. L., Hassler, D. M., et al. (2018). Observations and impacts of the 10 September 2017 solar events at Mars: An overview and synthesis of the initial results. Geophysical Research Letters, 45. https://doi.org/10.1029/2018GL079162

Lee, Y., Combi, M. R., Tenishev, V., Bougher, S. W., & Lillis, R. J. (2015). Hot oxygen corona at Mars and the photochemical escape of oxygen: Improved description of the thermosphere, ionosphere, and exosphere. Journal of Geophysical Research: Planets, 120, 1880– 1892. https://doi.org/10.1002/2015JE004890

Levin, G. V., and P. A. Straat (1981), A search for a nonbiological explanation of the Viking Labeled Release life detection experiment, Icarus, 45, 494– 516.

Li, G., Moore, R., Mewaldt, R. A., Zhao, L., & Labrador, A. W. (2012). A twin-CME scenario for ground level enhancement events. Space Science Reviews, 171(1-4), 141– 160. https://doi.org/10.1007/s11214-011-9823-7

Liemohn, M. W., B. C. Johnson, M. Fränz, and S. Barabash (2014), Mars Express observations of high altitude planetary ion beams and their relation to the “energetic plume” loss channel, J. Geophys. Res. Space Physics, 119, 9702– 9713, doi:10.1002/2014JA019994.

Liemohn, M. W., Xu, S. S., Dong, C. F., Bougher, S. W., Johnson, B. C., Ilie, R., & De Zeeuw, D. L. (2017). Ionospheric control of the dawn-dusk asymmetry of the Mars magnetotail current sheet. Journal of Geophysical Research, 122, 6397– 6414. https://doi.org/10.1002/2016JA023707

Lilensten, J., and P.-L. Blelly (2002), The TEC and F2 parameters are tracers of the ionosphere and thermosphere, J. Atmos. Sol. Terr. Phys., 64, 775– 793.

Lillis, R. J., D. L. Mitchell, R. P. Lin, and M. H. Acuña (2008), Electron reflectometry in the Martian atmosphere, Icarus, 194, 544–561, doi:10.1016/j.icarus.2007.09.030

Lillis, R. J., Fillingim, M. O., Peticolas, L. M., Brain, D. A., Lin, R. P., and S. W. Bougher (2009), Nightside ionosphere of Mars: Modeling the effects of crustal fields and electron pitch angle distributions on electron impact ionization, J. Geophys. Res., 114, E11009, doi:10.1029/2009JE003379.

Lillis, R. J., D.A. Brain, G.T. Delory, D.L. Mitchell, J.G. Luhmann, and R.P. Lin (2012), Evidence for superthermal secondary electrons produced by SEP ionization in the Martian atmosphere. J. Geophys. Res. 117, E03004. doi:10.1029/2011JE003932

Lillis, R. J., Robbins, S., Manga, M., Halekas, J. S., & Frey, H. V. (2013). Time history of the Martian dynamo from crater magnetic field analysis. Journal of Geophysical Research: Planets, 118, 1488– 1511. https://doi.org/10.1002/jgre.20105

Lillis, R. J., C. O. Lee, D. Larson, J. G. Luhmann, J. S. Halekas, J. E. Connerney, and B. M. Jakosky (2016). Shadowing and anisotropy of solar energetic ions at Mars measured by MAVEN during the March 2015 solar storm. J. Geophys. Res. 121(4), 2818-2829.

Lillis, R. J., Lee, C. O., Larson, D. E., Luhmann, J. G., Halekas, J. S., Connerney, J. E. P., & Jakosky, B. M. (2017). Photochemical escape of oxygen from Mars: First results from MAVEN in situ data. Journal of Geophysical Research: Space Physics, 122, 3815– 3836. https://doi.org/10.1002/2016JA023525

Lin, R. P. (1974), Non-relativistic solar electrons, Space Sci. Rev., 16, 189-256.

Lindsay, B. G., W. S. Yu, and R. F. Stebbings (2005), Cross sections for charge-changing processes involving kilo-electron volt H and H+ with CO and CO2, Phys. Rev. A, 71, 032705, doi:10.1103/PhysRevA.71.032705.

Lingam, M., C. Dong, X. Fang, B. M. Jakosky, A. Loeb (2018), The propitious role of solar energetic particles in the origin of life, The Astrophysical Journal 853, 10

Liu, Y. D., Zhao, X., Hu, H., Vourlidas, A., & Zhu, B. (2019). A comparative study of 2017 July and 2012 July complex eruptions: Are solar superstorms "perfect storms" in nature? The Astrophysical Journal Supplement Series, 241(2), 15. https://doi.org/10.3847/1538-4365/ab0649

Luhmann, J. G., and J. U. Kozyra (1991), Dayside pickup oxygen precipitation at Venus and Mars: Spatial distributions, energy deposition and consequences, J. Geophys. Res, 96, 5457– 5468.

Luhmann, J. G., R. E. Johnson, and M. H. G. Zhang (1992), Evolutionary impact of sputtering of the Martian atmosphere by O+ pick-up ions, Geophys. Res. Lett., 19, 2151– 2154.

Luhmann, J. G., C. Zeitlin, R. Turner, D. A. Brain, G. Delory, J. G. Lyon, and W. Boynton (2007), Solar energetic particles in near-Mars space, *J. Geophys. Res*., 112, E10001, doi:10.1029/2006JE002886.

Luhmann, J. G., Dong, C. F., Ma, Y. J., Curry, S. M., Xu, S., Lee, C. O., Jakosky, B. M. (2017). Martian magnetic storms. *J. Geophys. Res. Space Physics*,122, 6185–6209, doi:10.1002/2016JA023513

Luhmann, J. G., Mays, M. L., Li, Y., Lee, C. O., Bain, H., Odstrcil, D., et al. (2018). Shock connectivity and the late cycle 24 solar energetic particle events in July and September 2017. Space Weather, 16, 557– 568. https://doi.org/10.1029/2018SW001860

Lummerzheim, D., and J. Lilensten (1994), Electron transport and energy degradation in the ionosphere: Evaluation of the numerical solution, comparison with laboratory experiments and auroral observations, Ann. Geophys., 12, 1039.

Lundin, R., A. Zakharov, R. Pellinen, H. Borg, B. Hultqvist, N. Pissarenko, E. M. Dubinin, S. Barabash, I. Liede, and H. Koskinen (1989), First measurement of the ionospheric plasma escape from Mars, Nature, 341, 609– 612.

Lundin, R., A. Zakharov, R. Pellinen, S. W. Barabasj, H. Borg, E. M. Dubinin, B. Hultqvist, H. Koskinen, I. Liede, and N. Pissarenko (1990), ASPERA/Phobos measurements of the ion outflow from the Martian ionosphere, Geophys. Res. Lett., 17, 873– 876, doi:10.1029/GL017i006p00873.

Lundin, R., et al. (2004), Solar wind-induced atmospheric erosion at Mars: First results from ASPERA-3 on Mars Express, *Science*, 305, 1933– 1936, doi:10.1126/science.1101860.
Lundin, R., H. Lammer, and I. Ribas (2007), Planetary magnetic fields and solar forcing: Implications for atmospheric evolution, Space Sci. Rev., 129, 245– 278, doi:10.1007/s11214-007-9176-4.
Lundin, R., S. Barabash, M. Yamauchi, H. Nilsson, D. Brain (2011), On the relation between plasma escape and the Martian crustal magnetic field, Geophys. Res. Lett., 38, L02102, doi:10.1029/2010GL046019.
Lundin, R., S. Barabash, M. Holmstrom, H. Nilsson, M. Yamauchi, M. Fraenz, and E. M. Dubinin (2008), A comet-like escape of ionospheric plasma from Mars, Geophys. Res. Lett., 35, L18203, doi:10.1029/2008GL034811.
Ma, Y., A. F. Nagy, I. V. Sokolov, and K. C. Hansen (2004), Three-dimensional, multispecies, high spatial resolution MHD studies of the solar wind interaction with Mars, J. Geophys. Res., 109, A07211, doi:10.1029/2003JA010367.
Mahaffy, P. R., et al. (2015), Mars atmosphere. The imprint of atmospheric evolution in the D/H of Hesperian clay minerals on Mars, Science, 347(6220), 412– 414.
Malandraki, O. E., D. Lario, L. J. Lanzerotti, E. T. Sarris, A. Gerranios, and G. Tsiropoula (2005), October/November 2003 interplanetary coronal mass ejections: ACE/EPAM solar energetic particle observations, J. Geophys. Res., 110, A09S06, doi:10.1029/2004JA010926.
Mayyasi, M., Bhattacharyya, D., Clarke, J., Benna, M., Mahaffy, P., Thiemann, E. M. B., et al. (2018). Significant space weather Impact on the escape of hydrogen from Mars. Geophysical Research Letters, 45. https://doi.org/10.1029/2018GL077727
McCauley, J., M. Carr, J. Cutts, W. Hartmann, H. Masursky, D. Milton, R. Sharp, and D. Wilhelms (1972), Preliminary Mariner 9 report on the geology of Mars, Icarus, 17, 289– 327.
McComas, D. J., Angold, N., Elliott, H. A., Livadiotis, G., Schwadron, N. A., Skoug, R. M., & Smith, C. W. (2013). Weakest solar wind of the space age and the current “mini” solar maximum. Astrophysical Journal, 779(1), 2. https://doi.org/10.1088/0004-637X/779/1/2
McElroy, M. B. (1972), Mars: An evolving atmosphere, Science, 175, 443– 445.
McElroy, M. B., Y. L. Yung, and A. O. Nier (1976), Isotopic composition of nitrogen: Implications for the past history of Mars atmosphere, Science, 194, 70– 72.
McGuire, R. E., and T. T. von Rosenvinge (1984), The energy spectra of solar energetic particles, Adv. Space Res. 4(2-3), 117-125.
McKenna-Lawlor, S., V. V. Alfonin, K. I. Gringauz, K. Keckskemety, E. Keppler, E. Kirsch, A. Richter, A. Ruznyuk, K. Schwingenschuh, and D. O'Sullivan (1992), Energetic particle studies at Mars by SLED in PHOBOS-2, Adv. Space Res., 12(9), 231– 241, doi:10.1016/0273-1177(92)90335-U.
McKenna-Lawlor, S., V. V. Afonin, E. Kirsch, K. Schwingenschuh, J. A. Slavin, and J. G. Trotignon (1998), An overview of energetic particles (from 55 keV to >30 MeV) recorded in the close Martian environment and their energization in local and external processes, Planet. Space Sci., 46, 83–102.
McKenna-Lawlor, S., E. Kallio, R. Jarvinen, and V. Afonin (2012), Magnetic shadowing of high-energy ions at Mars and how this effect can be simulated using a hybrid model, Earth Planets Space, 64(2), 247–256.
McNeal, R. J., and J.H. Birely (1973), Laboratory studies of collisions of energetic H+ and hydrogen with atmospheric constituents, Rev. Geophys., 11, 633.

McNeal, R.J. (1970), Production of positive ions and electrons in collisions of 1-25-keV protons and hydrogen atoms with CO, CO2, CH4, and NH3, J. Chem. Phys. 53, 4308.
Melosh, H. J., and I. M. Vickery (1989), Impact erosion of the primordial atmosphere of Mars, Nature, 338, 487– 489.
Mewaldt, R. A., Cohen, C. M. S., Mason, G. M., von Rosenvinge, T. T., Li, G., Smith, C. W., & Vourlidas, A. (2015). Investigating the causes of solar-cycle variations in solar energetic particle fluences and composition. In Proceedings of the 34th International Cosmic Ray Conference, PoS (ICRC2015)030 (1–8).
Mironova, I.A. and I.G. Usoskin, Possible effect of strong solar energetic particle events on polar stratospheric aerosol: A summary of observational results (2014). Environ. Res. Lett. 9(1), 015002. doi:10.1088/1748-9326/9/1/015002
Mironova, I.A., K. L. Aplin, F. Arnold, et al (2015), Energetic particle influence on the Earth's atmosphere. Space Sci. Rev. 194: 1. doi:10.1007/s11214-015-0185-4
Mitchell, D. L., R. P. Lin, C. Mazelle, H. Rème, P. A. Cloutier, J. E. P. Connerney, M. H. Acuña, and N. F. Ness (2001), Probing Mars' crustal magnetic field and ionosphere with the MGS Electron Reflectometer, J. Geophys. Res., 106(E10), 23,419– 23,428, doi:10.1029/2000JE001435.
Mitchell, D. L., et al. (2016), The MAVEN solar wind electron analyzer, Space Sci. Rev., 200, 495 doi:10.1007/s11214-015-0232-1.
Mittelholz, A., Johnson, C. L., Feinberg, J. M., Langlais, B., & Phillips, R. J. (2020). Timing of the Martian dynamo: New constraints for a core field 4.5 and 3.7 Ga ago. Science Advances, 6(18), eaba0513. https://doi.org/10.1126/sciadv.aba0513
Modolo, R., Hess, S., Mancini, M., Leblanc, F., Chaufray, J.-Y., Brain, D., … Mazelle, C. (2016). Mars-solar wind interaction: LatHyS, an improved parallel 3-D multispecies hybrid model. Journal of Geophysical Research: Space Physics, 121, 6378– 6399. https://doi.org/10.1002/2015JA022324
Moore, T. E., W. K. Peterson, C. T. Russell, M. O. Chandler, M. R. Collier, H. L. Collin, P. D. Craven, R. Fitzenreiter, B. L. Giles, and C. J. Pollock (1999), Ionospheric mass ejection in response to a coronal mass ejection, Geophys. Res. Lett., 26, 2339–2342.
Morgan, D. D., D. A. Gurnett, D. L. Kirchner, J. L. Fox, E. Nielsen, and J. J. Plaut (2008), Variation of the Martian ionospheric electron density from Mars Express radar soundings, J. Geophys. Res., 113, A09303, doi:10.1029/2008JA013313.
Morgan, D. D., et al. (2014), Effects of a strong ICME on the Martian ionosphere as detected by Mars Express and Mars Odyssey, J. Geophys. Res. Space Physics, 119, 5891– 5908, doi:10.1002/2013JA019522.
Murakami, S., Sato, T., and A. Hasegawa (1990), Nonadiabatic behavior of the magnetic moment of a charged particle in a dipole magnetic field, Phys. Fluids B, 2 (4), 715-724.
Nagy, A. F., et al. (2004), The plasma environment of Mars, Space Sci. Rev., 111, 33– 114, doi:10.1023/B:SPAC.0000032718.47512.92.
Najib, D., A. F. Nagy, G. Toth, and Y. Ma (2011), Three-dimensional, multifluid, high spatial resolution MHD model studies of the solar wind interaction with Mars, J. Geophys. Res., 116, A05204, doi:10.1029/2010JA016272.
Nakai, Y., T. Shirai, T. Tabata, and R. Ito (1987), Cross sections for charge transfer of hydrogen atoms and ions colliding with gaseous atoms and molecules, At. Data Nucl. Data Tables, 37, 69–101, doi:10.1016/0092-640X(87)90005-2.

Navarro-González, R., E. Vargas, J. de laRosa, A. C. Raga, and C. P. McKay (2010), Reanalysis of the Viking results suggests perchlorate and organics at midlatitudes on Mars, J. Geophys. Res., 115, E12010, doi:10.1029/2010JE003599.

Němec, F., D. D. Morgan, D. A. Gurnett, and F. Duru (2010), Nightside ionosphere of Mars: Radar soundings by the Mars Express spacecraft, J. Geophys. Res., 115, E12009, doi:10.1029/2010JE003663.

Němec, F., D. D. Morgan, D. A. Gurnett, and D. A. Brain (2011), Areas of enhanced ionization in the deep nightside ionosphere of Mars, J. Geophys. Res., 116, E06006, doi:10.1029/2011JE003804.

Němec, F., D. D. Morgan, C. Diéval, D. A. Gurnett, and Y. Futaana (2014), Enhanced ionization of the Martian nightside ionosphere during solar energetic particle events, Geophys. Res. Lett., 41, 793–798, doi:10.1002/2013GL058895.

Newman, J. H., Chen, Y.S., Smith, K.A., and R.F. Stebbings (1986), Differential cross sections for scattering of 0.5-, 1.5-, and 5.0-keV hydrogen atoms by He, H2, N2, and O2, J. Geophys. Res. 91(A8), 8947–8954.

Nier, A. O., W. B. Hanson, A. Seiff, M. B. Mcelroy, N. W. Spencer, R. J. Duckett, T. C. D. Knight, and W. S. Cook (1976), Composition and structure of martian atmosphere—Preliminary results from Viking-1, Science, 193(4255), 786– 788, doi:10.1126/science.193.4255.786.

Nilsson, H., N. J. T. Edberg, G. Stenberg, S. Barabash, M. Holmström, Y. Futaana, R. Lundin, and A. Fedorov (2011), Heavy ion escape from Mars, influence from solar wind conditions and crustal magnetic fields, Icarus, 215, 475– 484, doi:10.1016/j.icarus.2011.08.003.

Nitta, N. V., Liu, Y., DeRosa, M. L., & Nightingale, R. W. (2012). What are special about ground-level events? Flares, CMEs, active regions and magnetic field connection. Space Sci. Rev., 171(1), 61– 83. https://doi.org/10.1007/s11214-012-9877-1.

Noël S., and G. W. Prölss (1993), Heating and radiation production by neutralized ring current particles. J Geophys Res 98:17317–17325.

Norman, R.B., T. C. Slaba, and S. R. Blattnig (2013), An extension of HZETRN for cosmic ray initiated electromagnetic cascades. Adv. Space Res. 51, 2251–2260.

Opgenoorth, H. J., D. J. Andrews, M. Fränz, M. Lester, N. J. T. Edberg, D. Morgan, F. Duru, O. Witasse, and A. O. Williams (2013), Mars ionospheric response to solar wind variability, J. Geophys. Res. Space Physics, 118, 6558–6587, doi:10.1002/jgra.50537.

Owen, T., J. P. Maillard, C. de Bergh, and B. Lutz (1988), Deuterium on Mars: The Abundance of HDO and the Value of D/H, Science, 240, 1767–1770, doi:10.1126/science.240.4860.1767.

Pande, B., Pande, S., Chandra, R., Chandra, and Chandra Mathpal, M. (2018), Solar flares, CMEs and solar energetic particle events during solar cycle 24, Adv. Space Res., 61, 777-785, doi:10.1016/j.asr.2017.11.025

Parker, E. N. (1958), Dynamics of the interplanetary gas and magnetic fields, Astrophys. J., 128, 664, doi:10.1086/146579.

Parker, E. N. (1965), The passage of energetic charged particles through interplanetary space, Planet. Space Sci., 13, 9, doi:10.1016/0032-0633(65)90131-5.

Pepin, R. O. (1994), Evolution of the Martian atmosphere, Icarus, 111, 289– 304.

Pilorget, C., & Forget, F. (2016). Formation of gullies on Mars by debris flows triggered by CO2 sublimation. Nature Geoscience, 9(1), 65– 69. https://doi.org/10.1038/ngeo2619.

Pollack, J. B., J. F. Kasting, S. M. Richardson, and K. Poliakoff (1987), The case for a wet, warm climate on early Mars, Icarus, 71, 203– 224, doi:10.1016/0019-1035(87)90147-3.

Poppe, A. R., Brain, D. A., Dong, Y., Xu, S., & Jarvinen, R. (2021). Particle-in-cell modeling of Martian magnetic cusps and their role in enhancing nightside ionospheric ion escape. Geophysical Research Letters, 48, e2020GL090763. https://doi.org/10.1029/2020GL090763

Porter, H. S., and A. E. S. Green (1975), Comparison of Monte Carlo and continuous slowing-down approximation treatments of 1-keV proton energy deposition in N2, J. Appl. Phys., 46, 5030–5038, doi:10.1063/1.321493.

Potgieter, M. (2013), Solar modulation of cosmic rays, Living Rev. Sol. Phys., 10, 3, doi:10.12942/lrsp-2013-3.

Qin, H., S. Zhang, J. Xiao, J. Liu, Y. Sun, and W. M. Tang (2013), Why is Boris algorithm so good? Phys. Plasmas, 20, 084503.

Rahmati, A., D. E. Larson, T. E. Cravens, R. J. Lillis, P. A. Dunn, J. S. Halekas, J. E. Connerney, F. G. Eparvier, E. M. B. Theimann, and B. M. Jakosky (2015), MAVEN insights into oxygen pickup ions at Mars, Geophys. Res. Lett., 42, 8870, doi:10.1002/2015GL065262.

Rahmati, A., et al. (2017), MAVEN measured oxygen and hydrogen pickup ions: Probing the Martian exosphere and neutral escape, J. Geophys. Res. Space Physics, 122, 3689–3706, doi:10.1002/2016JA023371

Rahmati, A., Larson, D. E., Cravens, T. E., Lillis, R. J., Lee, C. O., & Dunn, P. A. (2020). MAVEN SEP observations of scorpius X-1 X-Rays at mars: A midatmosphere occultation analysis technique. Geophysical Research Letters, 47(21), e88927. https://doi.org/10.1029/2020GL088927

Ramirez, R. M., & Craddock, R. A. (2018). The geological and climatological case for warmer and wetter early Mars. *Nature Geoscience*, 11(4), 230– 237. https://doi.org/10.1555/mars.2013.0002

Ramstad, R., S. Barabash, Y. Futaana, H. Nilsson, X.-D. Wang, and M. Holmstrom (2015), The Martian atmospheric ion escape rate dependence on solar wind and solar EUV conditions: 1. Seven years of Mars Express observations, J. Geophys. Res. Planets, 120, 1298– 1309, doi:10.1002/2015JE004816.

Ramstad, R., S. Barabash, Y. Futaana, H. Nilsson, and M. Holmström (2017), Global Mars-solar wind coupling and ion escape, J. Geophys. Res. Space Physics, 122, 8051–8062, doi:10.1002/2017JA024306

Ramstad, R., Barabash, S., Futaana, Y., Nilsson, H., & Holmström, M. (2018). Ion escape from mars through time: An extrapolation of atmospheric loss based on 10 years of mars express measurements. Journal of Geophysical Research: Planets, 123, 3051– 3060. https://doi.org/10.1029/2018JE005727

Reames, D. V. (2013), The two sources of solar energetic particles, Space Sci. Rev., 175, 53– 92.

Reames, D. V. (2021). Solar Energetic Particles: A Modern Primer on Understanding Sources, Acceleration and Propagation, Lecture Notes in Physics (Vol. 932). Gewerbestrasse, Switzerland: Springer International Publishing.

Rees, M. H. (1989), Physics and Chemistry of the Upper Atmosphere, Cambridge Univ. Press, New York.

Ribas, I., E. F. Guinan, M. Güdel, and M. Audard (2005), Evolution of the solar activity over time and effects on planetary atmospheres. I. High-energy irradiances (1–1700 Å), Astrophys. J., 622, 680– 694, doi:10.1086/427977.

Richardson, I. G. (2004) Energetic particles and corotating interaction regions in the solar wind. Space Sci. Rev. 111: 267-376.

Richardson, I. G. (2018) Solar wind stream interaction regions throughout the heliosphere. Living Rev. Sol. Phys. 15:1 https://doi.org/10.1007/s41116-017-0011-z

Riedler, W., Mohlmann, D., Oraevsky, V. N., Schwingenschuh, K., Eroshenko, Y., Rustenbach, J., Aydogar, O., Berghofer, G., Lichtenegger, H., Delva, M., Schelch, G., Pirsch, K., Fremuth, G., Steller, M., Arnold, H., Raditsch, T., Ayster, U., Fornacon, K.-H., Schenk, H. J., Michaelis, H., Motschmann, U., Roatsch, T., Sauer, K., Schroter, R., Kurths, J., Lenners, D., Linthe, J., Kobzev, V., Styashkin, V., Achache, J., Slavin, J., Luhmann, J. G., & Russell, C. T. (1989). Magnetic fields near Mars: First results. *Nature*, 341, 604.

Ripperda, B., Bacchini, F., Teunissen, J., Xia, C., Porth, O., Sironi, L., Lapenta, G., & Keppens, R.(2018). A comprehensive comparison of relativistic particle integrators. The Astrophysical Journal Supplement Series, 235(1), 21.

Rodriguez, J. A. P., Kargel, J. S., Baker, V. R., Gulick, V. C., Berman, D. C., Fairén, A. G., Linares, R., Zarroca, M., Yan, J., & Miyamoto, H. (2015). Martian outflow channels: How did their source aquifers form, and why did they drain so rapidly? Scientific Reports, 5(1), 13404. https://doi.org/10.1038/srep13404

Rudd, M. E., Kim, Y. K., Madison, D. H., & Gallagher, J. W. (1985), Electron production in proton collisions: Total cross sections. Reviews of Modern Physics, 57, 965– 994.

Rudd, M. E. (1988), Differential cross sections for secondary electron production by proton impact, Phys. Rev. A., 38(12), 6129–6137.

Russell, C., Luhmann. J., Spreiter, J., and S. Stahara (1984), The magnetic field of Mars - implications from gas dynamic modeling, J. Geophys. Res., 89, 2997–3003.

Sauer, K., Bogdanov, A., & Baumgärtel, K. (1995). The protonopause—An ion composition boundary in the magnetosheath of comets, Venus and Mars. *Advances in Space Research*, 16, 2255– 2258.

Schwartz, S. J., Andersson, L., Xu, S., Mitchell, D. L., Akbari, H., Ergun, R. E., et al. (2019). Collisionless electron dynamics in the magnetosheath of Mars. Geophys. Res. Lett., 46, 11,679–11,688. doi:10.1029/2019GL085037

Schwenn, R. (2006), Space weather: The solar perspective, Living Rev. Sol. Phys., 3(2).

Schwenn, R. (2007) Solar wind sources and their variations over the solar cycle. In: Baker D.N., Klecker B., Schwartz S.J., Schwenn R., Von Steiger R. (eds) Solar Dynamics and Its Effects on the Heliosphere and Earth. Space Sciences Series of ISSI, vol 22. Springer, New York, NY. doi:10.1007/978-0-387-69532-7_5

Schneider, N., Deighan, J. I., Jain, S. K., Stiepen, A., Evans, J. S., Stewart, A. I. F., et al. (2015). The discovery of diffuse aurora on Mars. Science, 350, aad0313. https://doi.org/10.1126/science.aad0313

Schneider, N., Jain, S. K., Deighan, J. I., Nasr, C. R., Brain, D. A., Larson, D., et al. (2018). Global aurora on Mars during the September 2017 space weather event. Geophysical Research Letters, 45, doi: 10.1029/2018GL077772.

Shane, A., Liemohn, M., Florie, C., and Xu, S. (2019). Misbehaving high-energy electrons: Evidence in support of ubiquitous wave-particle interactions on dayside Martian closed crustal magnetic fields, Geophys. Res. Lett., 46, doi:10.1029/2019GL084919

Sheel, V., S. A. Haider, P. Withers, K. Kozarev, I. Jun, S. Kang, G. Gronoff, and C. Simon Wedlund (2012), Numerical simulation of the effects of a solar energetic particle event on the ionosphere of Mars, J. Geophys. Res., 117, A05312, doi:10.1029/2011JA017455.

Shematovich, V. I., D. V. Bisikalo, and J.-C. Gérard (1994), A kinetic model of the formation of the hot oxygen geocorona: 1. Quiet geomagnetic conditions, J. Geophys. Res., 99, 23,217– 23,228, doi:10.1029/94JA01769.

Shematovich, V. I., et al. (2011), Protons and hydrogen atoms transport in the Martian upper atmosphere with an induced magnetic field, J. Geophys. Res., 116, A11320, doi:10.1029/2011JA017007.

Slipski, M., and B. M. Jakosky (2016), Argon isotopes as tracers for Martian atmospheric loss, Icarus, 272, 212– 227.

Smart, D. F., and M. A. Shea (2003), Comment on estimating the solar proton environment that may affect Mars missions, Adv. Space Res., 31, 45, doi:10.1016/S0273-1177(02)00655-5.

Smith, E. J., L. Davis, P. J. Coleman, and D. E. Jones (1965), Magnetic field measurements near Mars, Science, 149(3689), 1241– 1242.

Smith, M. D., Bougher, S. W., Encrenax, T., Forget, F., and A. Kleinböhl (2017). Thermal structure and composition. In R. Haberle, R. Clancy, F. Forget, M. Smith, & R. Zurek (Eds.), The atmosphere and climate of Mars, Cambridge Planetary Science (pp. 42–75). Cambridge: Cambridge University Press. doi: https://doi.org/10.1017/9781139060172.004

Spreiter, J. R., A. L. Summers, and A. Y. Alksne (1966), Hydromagnetic flow around the magnetosphere, Planet. Space Sci., 14, 223– 253, doi:10.1016/0032-0633(66)90124-3.

Spreiter, J. R., A. Summers, and A. Rizzi (1970), Solar wind flow past nonmagnetic planets—Venus and Mars, Planet. Space Sci., 18(9), 1281– 1299.

Squyres, S. W., Grotzinger, J. P., Arvidson, R. E., Bell, J. F. III, Calvin, W., Christensen, P. R., Clark, B. C., Crisp, J. A., Farrand, W. H., Herkenhoff, K. E., Johnson, J. R., Klingelhöfer, G., Knoll, A. H., McLennan, S. M., McSween, H. Y. Jr., Morris, R. V., Rice, J. W. Jr., Rieder, R., & Soderblom, L. A. (2004). In situ evidence for an ancient aqueous environment at Meridiani Planum, Mars. Science, 306(5702), 1709– 1714. https://doi.org/10.1126/science.1104559

Sterenborg, M. G., O. Cohen, J. J. Drake, and T. I. Gombosi (2011), Modeling the young Sun's solar wind and its interaction with Earth's paleomagnetosphere, J. Geophys. Res., 116, A01217, doi:10.1029/2010JA016036.

Stevens, M. H., Siskind, D. E., Scott Evans, J., Fox, J. L., Deighan, J., Jain, S. K., and Schneider, N. M. (2019). Detection of the nitric oxide dayglow on Mars by MAVEN/IUVS. J. Geophs. Res. Planets, 124, 1226. https://doi.org/10.1029/2019JE005945

Tanaka, T. (1993), Configurations of the solar wind flow and magnetic field around the planets with no magnetic field: Calculation by a new MHD simulation scheme, J. Geophys. Res., 98, 17,251–17,262, doi:10.1029/93JA01516.

Terada, N., H. Shinagawa, T. Tanaka, K. Murawski, and K. Terada (2009), A three-dimensional, multispecies, comprehensive MHD model of the solar wind interaction with the planet Venus, J. Geophys. Res., 114, A09208, doi:10.1029/2008JA013937.

Thiemann, E. M. B., P. C. Chamberlin, F. G. Eparvier, B. Templeman, T. N. Woods, S. W. Bougher, and B. M. Jakosky (2017), The MAVEN EUVM model of solar spectral irradiance variability at Mars: Algorithms and results, J. Geophys. Res. Space Physics, 122, doi:10.1002/2016JA023512.

Thiemann, E. M. B., Andersson, L. A., Lillis, R., Withers, P., Xu, S., Elrod, M., et al. (2018). The Mars upper ionosphere response to the X8.2 solar flare of 10 September 2017. Geophysical Research Letters, 45. https://doi.org/10.1029/2018GL077730

Thompson, W. R., Shah, M. B., Geddes, J., and H.B. Gilbody (1997), Ionization of atomic oxygen by protons. Phys. B: At. Mol. Opt. Phys. 30 L207.

Tian, F., O. B. Toon, A. A. Pavlov, and H. de Sterck (2005), Transonic hydrodynamic escape of hydrogen from extrasolar planetary atmospheres, Astrophys. J., 621, 1049– 1060.

Trotignon, J., Mazelle, C., Bertucci, C., & Acuña, M. (2006). Martian shock and magnetic pile-up boundary positions and shapes determined from the Phobos 2 and Mars Global Surveyor data sets. Planetary and Space Science, 54(4), 357– 369. https://doi.org/10.1016/j.pss.2006.01.003

Ulusen, D., D. A. Brain, J. G. Luhmann, and D. L. Mitchell (2012), Investigation of Mars' ionospheric response to solar energetic particle events, J. Geophys. Res., 117, A12306, doi:10.1029/2012JA017671.

Ulusen, D., Luhmann, J. G., Ma, Y., and D. A. Brain (2016). Solar control of the Martian magnetic topology: Implications from model-data comparisons. Planet. Space Sci. 128:1-13. doi:10.1016/j.pss.2016.01.007.

Usoskin, I. G., L. Desorgher, P. Velinov, M. Storini, E.O. Flückiger, R. Bütikofer, and G.A. Kovaltsov (2009) Ionization of the Earth's atmosphere by solar and galactic cosmic rays. Acta Geophys. 57, 88–101. doi:10.2478/s11600-008-0019-9.

Vainio, R., et al. (2007), Modeling of solar energetic particles in interplanetary space, in Space Weather: Research Towards Applications in Europe—2nd European Space Weather Week (ESWW2), Astrophys. Space Sci. Libr., 344, p. 27, Springer, Dordrecht, Netherlands.

Vainio, R., Raukunen, O., Tylka, A. J., Dietrich, W. F., & Afanasiev, A. (2017). Why is solar cycle 24 an inefficient producer of high-energy particle events? Astronomy and Astrophysics, 604, A47. https://doi.org/10.1051/0004-6361/201730547.

Vaisberg, O., & Smirnov, V. (1986). The Martian magnetotail. Advances in Space Research, 6(1), 301– 314. https://doi.org/10.1016/0273-1177(86)90046-3

Van Zyl, B. (1978), Charge-state-equilibriated H+/H flux fractions for analysis of the hydrogen aurora, Rep. U AG R-265, Geophys. Inst., Univ. of Alaska, Fairbanks.

Van Zyl, B., Neumann, H., Le, T. Q., and R.C. Amme (1978), H + N2 and H + O2 collisions: Experimental charge-production cross sections and differential scattering calculations, Phys. Rev. A 18(2):506-516.

Van Zyl, B., and H. Neumann (1988), Lyman a emission cross sections for low-energy H and H+ collisions with N2 and O2, J. Geophys. Res, 93(A2):1023-1027.

Van Zyl, B., and T.M. Stephen (2014), Cross sections for electron capture and loss by H+ and H impact on O and O2, J. Geophys. Res. Space Physics 119(8) 6925-6939.

Verkhoglyadova, O. P., G. Li, G. P. Zank, Q. Hu, and R. A. Mewaldt (2012), Radial dependence of peak proton and iron fluxes in solar energetic particle events: Application of the PATH code, Astrophys. J., 757, 75, doi:10.1088/0004-637X/757/1/75.

Vignes, D., Mazelle, C., Rme, H., Acuña, M. H., Connerney, J. E. P., Lin, R. P., Mitchell, D. L., Cloutier, P., Crider, D. H., & Ness, N. F. (2000). The solar wind interaction with Mars: Locations and shapes of the bow shock and the magnetic pile-up boundary from the observations of the MAG/ER Experiment onboard Mars Global Surveyor. Geophysical Research Letters, 27, 49– 52. https://doi.org/10.1029/1999GL010703

Vincendon, M., Pilorget, C., Carter, J., & Stcherbinine, A. (2019). Observational evidence for a dry dust-wind origin of Mars seasonal dark flows. Icarus, 325, 115– 127. https://doi.org/10.1016/j.icarus.2019.02.024

Vervelidou, F., Lesur, V., Grott, M., Morschhauser, A., & Lillis, R. J. (2017). Constraining the date of the Martian dynamo shutdown by means of crater magnetization signatures. Journal of Geophysical Research: Planets, 122, 2294– 2311. https://doi.org/10.1002/2017JE005410

von Clarmann, T., N. Glatthor, M. Hopfner, S. Kellmann, R. Ruhnke, G. P. Stiller, and H. Fischer (2005), Experimental evidence of perturbed odd hydrogen and chlorine chemistry after the October 2003 solar proton events, J. Geophys. Res., 110, A09S45, doi:10.1029/2005JA011053.

Webb, D. F., and R. A. Howard (1994), The solar cycle variation of coronal mass ejections and the solar wind flux, J. Geophys. Res., 99, 4201, doi:10.1029/93JA02742.

Weber, T., Brain, D., Mitchell, D., Xu, S., Connerney, J., & Halekas, J. (2017). Characterization of low-altitude nightside Martian magnetic topology using electron pitch angle distributions. J. Geophys. Res. Space Physics, 122, 9777– 9789. https://doi.org/10.1002/2017JA024491

Weber, T., Brain, D., Mitchell, D., Xu, S., Espley, J., Halekas, J., Lillis, R., & Jakosky, B. (2019). The influence of solar wind pressure on Martian crustal magnetic field topology. Geophys. Res. Lett., 46, 2347– 2354.

Weiss, B. P., Fong, L. E., Vali, H., Lima, E. A., & Baudenbacher, F. J. (2008). Paleointensity of the ancient Martian magnetic field. Geophysical Research Letters, 35(23), https://doi.org/10.1029/2008gl035585

Westall, F., Foucher, F., Bost, N., Bertrand, M., Loizeau, D., Vago, J. L., et al. (2015). Biosignatures on Mars: What, where, and how? Implications for the search for Martian life. Astrobiology, 15(11), 998– 1029. https://doi.org/10.1089/ast.2015.1374

Williams, I.D., Geddes, J., and H.B. Gilbody (1983), Electorn capture, loss, and excitation in collisions of H+, H(1s), H(2s), and H- in atomic oxygen, J. Phys. B: At. Mol. Phys. 17: 1547-1558.

Withers, P., M. O. Fillingim, R. J. Lillis, B. Häusler, D. P. Hinson, G. L. Tyler, M. Pätzold, K. Peter, S. Tellmann, and O. Witasse (2012), Observations of the nightside ionosphere of Mars by the Mars Express Radio Science Experiment (MaRS), J. Geophys. Res., 117, A12307, doi:10.1029/2012JA018185.

Wood, B. E., H. R. Mueller, G. P. Zank, and J. L. Linsky (2002), Measured mass loss rates of solar-like stars as a function of age and activity, Astrophys. J., 574, 412– 425.

Wordsworth, R. D., Kerber, L., Pierrehumbert, R. T., Forget, F., & Head, J. W. (2015). Comparison of "warm and wet" and "cold and icy" scenarios for early Mars in a 3-D climate model. Journal of Geophysical Research: Planets, 120, 1201– 1219. https://doi.org/10.1002/2015JE004787

Wray, J. J., S. L. Murchie, J. L. Bishop, B. L. Ehlmann, R. E. Milliken, M. B. Wilhelm, K. D. Seelos, and M. Chojnacki (2016), Orbital evidence for more widespread carbonate-bearing rocks on Mars, J. Geophys. Res. Planets, 121, 652– 677, doi:10.1002/2015JE004972.

Xu, S., M. W. Liemohn, and D. L. Mitchell (2014), Solar wind electron precipitation into the dayside Martian upper atmosphere through the cusps of strong crustal fields, J. Geophys. Res. Space Physics, 119, 10,100–10,115, doi:10.1002/2014JA020363.

Xu, S., Fang, X., Mitchell, D. L., Ma, Y., Luhmann, J. G., DiBraccio, G. A., et al. (2018). Investigation of Martian magnetic topology response to 2017 September ICME. Geophys. Res. Lett., 45, 7337–7346. https://doi.org/10.1029/2018GL077708

Xu, S., Weber, T., Mitchell, D. L., Brain, D. A., Mazelle, C., DiBraccio, G. A., & Espley, J. (2019). A technique to infer magnetic topology at mars and its application to the terminator region. Journal of Geophysical Research: Space Physics, 124, 1823– 1842. https://doi.org/10.1029/2018JA026366

Xu, S., Mitchell, D. L., McFadden, J. P., Fillingim, M. O., Andersson, L., Brain, D. A., et al. (2020), Inverted-V electron acceleration events concurring with localized auroral observations at Mars by MAVEN. Geophys. Res. Lett., 47, e2020GL087414. doi:10. 1029/2020GL087414

Yung, Y. L., J. S. Wen, J. P. Pinto, M. Allen, K. K. Pierce, and S. Paulson (1988), HDO in the Martian atmosphere—Implications for the abundance of crustal water, Icarus, 76(1), 146– 159, doi:10.1016/0019-1035(88)90147-9.

Zhang, M. H. G., J. G. Luhmann, and A. J. Kliore (1990), An observational study of the nightside ionospheres of Mars and Venus with radio occultation methods, J. Geophys. Res, 95, 17,095–17,102.

Zhang, M. H. G., J. G. Luhmann, S. W. Bougher, and A. F. Nagy (1993), The ancient oxygen exosphere of Mars: Implication for atmospheric evaluations, J. Geophys. Res, 98, 10,915–10,923.

Appendix A

Collisional cross-sections

This section summarizes the collisional processes described by MAVEN and the cross-section sources. Tables are provided for all inelastic processes. If the cross-section was digitized or fitted by a primary reference and unchanged, that primary reference is specified. Otherwise, the specific constraints to determine the cross-section are outlined in the Notes column. The inclusion and exclusion of processes in past publications and the current version is also noted. For example, target excitation processes were used in Jolitz et al. [2017] but have since been excluded due to doubts in the accuracy of those cross-sections. There is no table provided for elastic cross-sections. This is because ASPEN assumes that all elastic cross-sections, regardless of projectile (H^+, H, or H^-) or target (CO_2, N_2, CO, O), have the same cross-section. This approximation was first made by Kallio and Barabash [2001], which used the fitted cross-section for hydrogen atom impact on N_2 from Noel and Prölss [1993] for H^+ and H impact on CO_2, O_2, and N_2. Noel and Prölss [1993] had previously fitted data from Newman et al. [1986]. The original dataset measured 0.5-5 keV hydrogen atoms elastically scattering with H_2, He, N_2, and O_2 [Newman et al. 1986]. No subsequent measurements have been made.

Projectile-Target	Reference	Notes
H^+ - O_2, N_2, CO_2, CO	Rudd et al. [1985]	- Rudd et al. [1985] compiled existing datasets and made fits, which are used in ASPEN.
H^+ - O	-	- Thompson et al. [1997] is the only existing experimental dataset of ionization of O by 34-100 keV H^+ - ASPEN uses the Green and McNeal [1971] formula using coefficients J = 54.15 keV and a = 35 keV, which were determined by fitting the Thompson et al. [1997] data.
H - N_2, O_2	-	- Experiments that measure electron production confound ionization and electron stripping. However, H impact ionization is the only process that produces slow ions, so that can be used as a proxy. - ASPEN uses Basu et al. [1987] data for 1 keV to 300 keV, which subtracted an electron stripping cross-sections for H on O_2 and N_2 [Van Zyl 1978] from a total electron production cross-section [McNeal and Birely 1973] - For below 1 keV, ASPEN uses slow ion production cross-section in electron-producing reactions from Van Zyl et al. [1978].
H - CO, CO_2	-	- Slow ion production cross-sections measured for 1-25 keV H on CO and CO_2 [McNeal 1970] - For below 1 keV, scaled the ion production cross-section for H on O_2 so matched the lowest energy slow ion production cross-sections for CO and CO_2. - For above 25 keV, scaled the ion production cross-section for H on O_2 for CO_2 and the ion production cross-section for H on N_2 for CO.
H - O	McNeal & Birely [1973]	- No experimental data - McNeal and Birely [1973] approximated the process using the semi-empirical formula from Green and McNeal [1971] with parameters that are the averages over all other H-atom ionizations. - This approximation is used in Kallo and Barabash [2001] and Basu et al. [1987].

Table A.1: Ionization cross-sections.

Projectile-Target	Reference	Notes
H, H^+- O, O_2	-	- No experimental data - Basu et al. [1987] uses rescaled electron impact cross sections from Edgar et al. [1975]. The parameters of the rescaling are in Edgar et al. [1975], but do not match Basu et al. [1987]. - Jolitz et al. [2017] used Basu et al. [1987] cross-section. - Process currently disabled in ASPEN due to lack of replicability.
H, H^+ - CO, CO_2	-	- No experimental data for emission other than the UVD from ionized CO_2^+, which must estimated as a subset of ionization. - Jolitz et al. [2017] used the Basu et al. [1987] H, H^+ - O_2 excitation cross-section for the H, H^+-CO_2, CO emission cross-section. - Process currently disabled in ASPEN due to lack of replicability.
H^+ - N_2	Avakyan et al. [1998]	- No experimental data - Basu et al. [1987] used rescaled electron cross-sections from Edgar et al. [1973], but the plot is not replicable using the parameters. - Basu et al. [1987] excitation cross-section used in Jolitz et al. [2017], but subsequently disabled due to lack of replicability. - Avakyan et al. [1998] contains many emission cross-sections, but they have not yet been included
H - N_2	Birely [1974]	- Basu et al. [1987] used the $C^2\Pi_u$ emission cross-section from Birely [1974] as the total excitation cross-section. - Jolitz et al. [2017] used this approximation, but subsequently disabled it due to lack of replicability.

Table A.2: Target excitation cross-sections.

Projectile-Target	Reference	Notes
H^+ - N_2, O_2	Van Zyl [1978]	- Laboratory data and fit compiled in Van Zyl [1978] and reprinted as appendices in Rees [1989] (Fig. A4.8-10). - Previously used in Basu et al. [1987].
H^+ - CO, CO_2	Barnett et al. [1977]	- Jolitz et al. [2017] assumed electron capture cross-section for H^+ on CO_2 was the same as O_2 (as Kallio and Barabash [2001] had assumed) and on CO was the same as on N_2. - Currently ASPEN uses Barnett et al. [1977] cross-sections for 100 eV to 200 keV, and extrapolates the fit upwards/downwards to lower/higher energies.
H^+ - O	Lindsay & Stebbings [2005]	- Jolitz et al. [2017] used the cross-section from Basu et al. [1987], which was determined using data from Williams et al. [1984] and the extrapolation from Van Zyl [1978] for energies above 20 keV. - Lindsay and Stebbings [2005] fitted prior experimental observations, which is used currently in ASPEN. - The most recent dataset suggests these cross-sections might be underestimated [Van Zyl 2014].

Table A.3: Electron capture cross-sections.

Projectile-Target	Reference	Notes
H - O_2, N_2, CO	Nakai et al. [1987]	- Not included in Jolitz et al. [2017] - Compilation in Nakai et al. [1987] synthesized and fitted prior experimental data for impact on O_2 and N_2, which ASPEN currently uses.
H - CO	-	- Not included in Jolitz et al. [2017] - Nakai et al. [1987] fitted data for 2-200 keV H, but cross-sections measured by Lindsay and Stebbings [2005] are higher than the fit at energies below 2 keV - I redrew the fit to incorporate the low energy data following the methodology of Van Zyl [1978], which is the cross-section currently used in ASPEN.
H - CO_2	-	- Not included in Jolitz et al. [2017] - Only one experimental dataset [Lindsay and Stebbings 2005] - Based on the H - O_2 electron attachment cross-section, I made a fit to incorporate this data following the methodology of Van Zyl [1978], which is the cross-section currently used in ASPEN.
H - O	-	- Not included in Jolitz et al. [2017] - Experimental data measured in Van Zyl and Stephen [2014] and Williams et al. [1984] (labeled as H(1s) electron capture) - Made fit using the methodology of Van Zyl [1978], which is the cross-section currently used in ASPEN.

Table A.4: Electron attachment cross-sections.

Projectile-Target	Reference	Notes
H - N_2, O_2	Van Zyl [1978]	- Experimental data compiled and fitted in Van Zyl [1978]. - This fit was previously used in Basu et al. [1987] and is currently used in ASPEN.
H - CO, CO_2	Nakai et al. [1987]	- Jolitz et al. [2017] previously assumed that the cross-section for stripping on CO was equivalent to the cross-section for N_2, and that stripping on CO_2 was equivalent to the cross-section for O_2. - ASPEN currently uses the fit from Nakai et al. [1987], which fitted existing experimental data and holds up for recent data (e.g. Lindsay and Stebbings [2005]).
H - O	-	- Experimental data in Williams et al. [1984] and Van Zyl and Stephen [2014] - Due to systematic errors in Williams et al. [1984], made fit of Van Zyl and Stephen [2014] data for 0.1-2 keV H, extrapolating to lower energies log-linearly and higher energies by scaling the H-O_2 electron stripping cross-section so it matched the highest energy H-O data.

Table A.5: Electron stripping cross-sections.

Projectile-Target	Reference	Notes
H^- - O_2, N_2	Nakai et al. [1987]	- Not included in Jolitz et al. [2017] - ASPEN currently uses the fit from Nakai et al. [1987] from 0.001-1000 keV.
H^- - CO, CO_2	-	- Not included in Jolitz et al. [2017] - The fit from Nakai et al. [1987] is only drawn for 3-30 keV H^- on CO and 20-5000 keV on CO_2. - For CO2, this fit was extended to lower energies by calculating the ratio between the CO_2 and O_2 cross-sections in the overlapping range (~2.8), and scaling the O_2 cross-section for lower energies. - For CO, the fit had to be arbitrarily fitted to ensure it decreased at lower energies, since the recorded cross-section is increasing at low energies.
H^- - O	-	- Not included in Jolitz et al. [2017] - Only laboratory data is from Williams et al. [1984] - Since the systematic errors in Williams et al. [1984] affected all measurements within the study (as outlined by Van Zyl and Stephen [2014]), we calculate the ratio of measured electron stripping cross-section for H^- on O to H^- on O_2 in the same study (~0.6). This factor is then used to scale the Nakai et al. [1987] fit of H^- on O_2. This fit is currently in use in ASPEN.

Table A.6: Electron detachment cross-sections.

Projectile-Target	Reference	Notes
H - O_2, N_2	Van Zyl and Neumann [1988]	- Not included in Jolitz et al. [2017] - ASPEN uses data from Van Zyl and Neumann [1988] for 0.04-10 keV hydrogen atoms, which are log-linearly extrapolated to low and high energies - Also used in Kallio and Barabash [2001]
H - CO, CO_2	-	- Not included in Jolitz et al. [2017] - Only experimental dataset is for 1-25 keV H on CO and CO_2 to produce H(2p) [Birely and McNeal 1972]. - ASPEN uses a cross-section determined from scaling the Lyman alpha emission from H on O_2 to fit the CO and CO_2 data.
H - O	-	- Not included in Jolitz et al. [2017] - No experimental data. - Like other studies (e.g. Kallio and Barabash [2001]), we assume the emission cross-section is equivalent to the cross-section for H impact on O_2.
H^+ - O_2, N_2	-	- Not included in Jolitz et al. [2017] - Must be considered as a subset of charge exchange, since Lyman alpha can only be emitted by an excited hydrogen atom. - Avakyan et al. [1998] compiles and fits prior data. However, this fit is only valid for 0.04-100 keV. If extrapolated to higher energies, the Lyman alpha production cross-section will exceed the electron capture cross-section, which is unphysical. - ASPEN uses the Avakyan et al. [1998] fit with the proviso that the ratio of emission to electron capture is held fixed so the cross-section is that ratio multiplied by the charge-exchange cross-section.
H^+ - CO, CO_2	-	- Not included in Jolitz et al. [2017] - Must be considered as a subset of charge exchange, since Lyman alpha can only be emitted by an excited hydrogen atom. - Data is even sparser, and the Avakyan et al. [1998] fit only extends from 1-25 keV. - Above 25 keV, the data is extrapolated using the scaling method previously used for impact on O_2 and N_2. - Below 1 keV, the oxygen emission cross-section is scaled to fit the data. While this presumes the atomic interaction is similar, it is a sufficient assumption to extend the fit.
H^+ - O	-	- Not included in Jolitz et al. [2017] - Must be considered as a subset of charge exchange, since Lyman alpha can only be emitted by an excited hydrogen atom. - No experimental data. - Like other studies (e.g. Kallio and Barabash [2001]), we assume the emission cross-section is equivalent to the cross-section for H^+ impact on O_2.

Table A.7: Lyman alpha emission cross-section.